
Confocal Microscopy and Spectroscopy of Single Nanomagnets and Quantum Emitters

Von der Universität Bayreuth
zur Erlangung des Grades eines
Doktors der Naturwissenschaften (Dr. rer. nat.)
genehmigte Abhandlung

von
Christian Dicken
aus Viersen

1. Gutachter: Herr Prof. Dr. Markus Lippitz

2. Gutachter: Herr Prof. Dr. Jürgen Köhler

Tag der Einreichung: 29. September 2016

Tag des Kolloquiums: 28. April 2017

Confocal Microscopy and Spectroscopy of Single Nanomagnets and Quantum Emitters

Von der Universität Bayreuth
zur Erlangung des Grades eines
Doktors der Naturwissenschaften (Dr. rer. nat.)
genehmigte Abhandlung

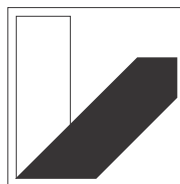
von
Christian Dicken
aus Viersen

Angefertigt am
Max-Planck-Institut für Festkörperforschung in Stuttgart
und dem Lehrstuhl für Experimentalphysik III
der Universität Bayreuth

September 2016



Max Planck Institute
for Solid State Research



Experimental Physics III
University of Bayreuth

ABSTRACT

This thesis is embedded in the realm of single nanoparticle microscopy and spectroscopy. We combine confocal microscopy, ultrafast pulsed lasers and homodyne amplification to make the signature of single nanoparticles and quantum emitters visible. These techniques allow us to observe and manipulate the physical state of quantum dots on picosecond timescales, and we show that the spectral signatures found in our experiments compare well with what we expect from the dynamics of a three-level quantum emitter. These emitters are candidates as nodes of optical networks. Furthermore, we utilize homodyne amplification to analyze the magnetization of single nickel disks and develop a model that is able to predict the optical response of the disks when being embedded in the sample structure. The model allows us to separate the magnetic properties of the nanomagnets from the optical properties of the complete structure.

KURZFASSUNG

Diese Arbeit befasst sich mit der Mikroskopie und Spektroskopie einzelner Nanopartikel und Quantenemitter. Um solche sichtbar zu machen, kombinieren wir konfokale Mikroskopie, ultrakurze Laserpulse und homodyne Verstärkung. Unser System ermöglicht uns beispielsweise, den physikalischen Zustand von einzelnen Quantenpunkten mit einer Auflösung im Pikosekundenbereich zu analysieren und zu kontrollieren. Wir zeigen, dass die spektralen Signaturen im Experiment gut zu dynamischen Prozessen passen, wie wir sie von einem Drei-Niveau Quantenemitter erwarten. Solche Emitter könnten als Knoten in optischen Netzwerken dienen. Desweiteren nutzen wir homodyne Verstärkung, um die Magnetisierung einzelner Nickelscheibchen zu untersuchen. In diesem Rahmen entwickeln wir ein Modell, um die optische Antwort der in die Probenstruktur eingebetteten Scheibchen zu berechnen. Das Modell erlaubt uns, die magnetischen Eigenschaften der Nanomagnete von den optischen Eigenschaften der Gesamtstruktur zu trennen.

PREFACE

The two parts of this thesis, unrelated at first glance, are motivated by the same thing: the physics of single, nanoscopic particles. A single particle always has a different story to tell than many. Its story may be harder to understand, harder to squeeze into theoretical models, but it is also richer in detail. We strive to read that story using farfield optics: with a confocal microscopy system, a single nanoparticle is illuminated and observed at the same time. The tiny fraction of light scattered by the nanoparticle allows us to deduce its physical state and how it evolves with time.

With decreasing size of the nanoobject, the intensity of the scattered light quickly drops below the sensitivity of the detectors or is outshone by background light, rendering the particle invisible to us. Nevertheless, the scattered light can be made visible by making it interfere with a much stronger reference light beam, a concept called *homodyne detection* or *interferometric amplification*: The magnitude of the interferometric signature of the particle is proportional to the magnitude of the reference beam.

In our sample geometries, this concept is implemented by detecting the scattered light together with the light reflected from nearby surfaces, for example of the substrate in which the particle is embedded. Part one of this thesis is concerned with the optimization of interferometric amplification. This is possible by tweaking the phase difference between the scattered electric field and the reference electric field reflected from the interfaces. We exploit the possibility to gain control of the phase difference with a multilayer sample structure and develop a model to describe the optical response of a particle on such a multilayer surface. Originally, this topic arose in the context of magnetometry of single nanomagnets, trying to observe signatures of superparamagnetism. We therefore base our discussion on a particular use case, magnetometry of magnetized nickel nanodisks using an interferometric, confocal Kerr microscope. In such measurements the information about the magnetization is hidden behind the optical properties of the nanomagnet, defined by its size, material and shape. Our model allows us to extract the information about the magnetization from the optical signal of the magnet. We can show that the variation of the measured signal with the disk size is due to changes of the optical properties, in particular the phase of the scattered light. The saturation magnetization essentially is constant over a large interval of disk sizes.

Part one is organized as follows: After a brief motivation, we introduce in chapter 2 the concept of homodyne detection and develop

the idea that transmission microscopy of a single nanoparticle can always be understood as being an interferometric process. Using single nickel disks as example system, we motivate why control of the different phases involved may help to optimize the measured signal. In the form of a multilayer structure that changes the phase of the transmitted light we present a possible technique to exploit this. Using a simple model, the optical properties of the nickel disks and of the multilayer structure are merged to calculate the optical response of the complete system.

In chapter 3 we switch from plane wave illumination to focused Gaussian beams. The length scales of the observed system are neither very large nor very small compared to the wavelength of the used light and render a qualitative modeling difficult. We address the question to which extend and under which conditions the Gaussian beam can still be considered as plane wave when calculating the optical response of the multilayer structure and of the nickel disk. The modifications necessary are used to review the homodyne detection of a nickel disk sitting on a multilayer structure, illuminated with a focused beam.

In chapter 4, we apply homodyne detection to measure the magnetization of single nickel nanodisks. We first introduce the experimental technique and show exemplary measurements of the magnetic hysteresis of single disks. With the help of the Stoner-Wohlfarth model, we show that the disks act as single domain magnets with highly variable properties, emphasizing the importance of single particle measurements. Next, a multilayer structure is used to modify the interferometric amplification of the signal. The dependency of the signal amplitude on the disk diameter is analyzed and compared with the prediction of the model developed in the former chapters.

Finally, we summarize the results of part one in chapter 5.

With farfield optics, not only can we observe the physical state of single nanoparticles, but also manipulate it: Using ultrafast pulsed lasers combined with spectrally resolved homodyne detection [1, 2] we investigate and influence the state of a single self-assembled GaAs-AlGaAs quantum dots. These are candidates to realize an important theoretical concept: the two-level quantum emitter of light, a device with only two allowed quantum states, optically accessible and controllable. From it we could build quantum computers[3, 4], true random number generators[5], flashlights that deliver single photons on demand[6], quantum memories and networks[7, 8], and so on. Part two of the thesis is concerned with the connection between the dynamics of the two-level quantum emitter and the experimental signatures that we expect using spectrally resolved homodyne detection. This connection allows us to judge how close the quantum dots used in our experiments come to the ideal two-level quantum emitter. By considering coherent control experiments [9, 10], we show that the

scattering spectra of the quantum dots agree with the dynamics that we expect of a three-level emitter. Like the two-level emitter, these also could act as a basic element of optical networks. Thus, we also study theoretically, how delocalized states in networks of randomly distributed quantum emitters form and show that they can be influenced and shaped by locally patterning the eigenenergies of the individual quantum emitters. This could help to create first functional quantum networks from high-density quantum dot films. The iterative process of optimizing the properties of quantum dots calls for fast techniques to characterize them. While experiments with ultrafast optical pulses allow access to the quantum dot on picosecond timescales, they are technically demanding and time consuming. Resonant spectroscopy using narrow-line continuous-wave lasers is a good alternative when temporal resolved control of the quantum dot is not required. The temporal resolution is replaced with a high spectral resolution while at the same time the complexity of the experimental setup can be reduced considerably. We thus investigate techniques that allow us to implement spectrally resolved homodyne detection using a continuous-wave diode laser as light source. The focus lies on non-invasive modulation techniques that are necessary for sufficient noise suppression while providing maximal freedom with respect to the sample design.

Putting aside the introduction and summary, part two is organized in three chapters. In chapter 7, we first develop the theoretical formalism to describe the dynamics of the physical state of the quantum emitter. Then we establish the connection to the experimentally accessible quantities, the scattering spectrum of the quantum dot. The scattering spectra expected for absorption bleaching, perturbed induction decay or resonance beating are investigated and compared to the experimental data. Rabi oscillations observed on the dots show an unexpected stretching. We show that the stretched Rabi oscillations can be reproduced in theory by taking into account a strong electric field produced by free photo carriers close to an interface, the so-called Dember field. It changes the optical properties of the quantum dot via Stark's effect.

In chapter 8, we discuss the formation of delocalized states in grids of coupled two-level systems. We start with a simple hybridization model that allows us to visualize the shape of the delocalized grid states. By introducing variance of the eigenenergies of the two-level-systems we influence the shape of the delocalized states. Correlation of the eigenenergies of neighboring two-level-systems can lead to the formation of sub-ensembles. These can be manipulated by controlling the distribution of eigenenergies. Finally, we briefly discuss how the ensemble states could be investigated optically and what the signatures of coupled states are.

In chapter 9 we concentrate on non-invasive modulation techniques for homodyne detection with narrow-line diode lasers. When using homodyne detection, the long coherence length of these lasers imposes the risk of spurious interference, which – when also modulated – enters the signal path. After briefly discussing the signal formation, four different modulation approaches are tried that can be divided into modulation of the laser-emitter energy detuning and modulation of the laser-emitter displacement.

PUBLICATIONS

In scientific journals:

C. Wolpert, **C. Dicken**, L. Wang, P. Atkinson, A. Rastelli, O. G. Schmidt, H. Giessen, H. Schweizer, R. Singh, G. Bester, and M. Lippitz, *Ultrafast switching of localized excitons via transient photo-Dember fields*, in preparation (2016)

C. Dicken, T. Schumacher, D. Wolf, K. Lindfors, H. Giessen, and M. Lippitz, *Homodyne detection of small changes of the optical constants of lossy metal nanoparticles*, in preparation (2016)

C. Wolpert, **C. Dicken**, L. Wang, P. Atkinson, A. Rastelli, O. G. Schmidt, H. Giessen, and M. Lippitz, *Ultrafast coherent spectroscopy of a single self-assembled quantum dot*, *Status Solidi B* **249**, (4), 721–730 (2012)

C. Wolpert, **C. Dicken**, L. Wang, P. Atkinson, A. Rastelli, O. G. Schmidt, H. Giessen, and M. Lippitz, *Transient Reflection: A versatile technique for Ultrafast Spectroscopy of a Single Quantum Dot in Complex Environments*, *Nano Lett.* **12**, (1), 453–457 (2012)

Contributions at international conferences (own):

Talks

C. Dicken, C. Wolpert, K. Lindfors, L. Wang, P. Atkinson, A. Rastelli, O. Schmidt, H. Schweizer, H. Giessen, R. Singh, G. Bester, and M. Lippitz *Ultrafast DC-Stark Switching of a Single Quantum Dot Exciton*, 4th International Workshop on the Optical Properties of Nanostructures, Wrocław/Germany (2016)

C. Dicken, T. Schumacher, D. Wolf, K. Lindfors, and M. Lippitz *Far-field interferometry of weak plasmonic scatterers*, DPG Spring Meeting, Regensburg/Germany (2016)

C. Dicken, T. Schumacher, D. Ullrich, K. Lindfors, and M. Lippitz *The Role of the Scattering Phase in Single Particle Spectroscopy*, DPG Spring Meeting, Regensburg/Germany (2013)

C. Dicken, C. Wolpert, K. Lindfors, L. Wang, P. Atkinson, A. Rastelli, O. Schmidt, H. Schweizer, H. Giessen, R. Singh, G. Bester, and M. Lippitz *Ultrafast Switching of a Single Semiconductor Quantum Dot Exciton*, 11th International Workshop on

Nonlinear Optics and Excitation Kinetics in Semiconductors, Stuttgart/Germany (2012)

C. Dicken, C. Wolpert, K. Lindfors, L. Wang, P. Atkinson, A. Rastelli, O. Schmidt, H. Schweizer, H. Giessen, R. Singh, G. Bester, and M. Lippitz *Ultrafast Switching of a Single Semiconductor Quantum Dot Exciton*, DPG Spring Meeting, Berlin/Germany (2012)

Posters

C. Dicken, A. Neufeld, C. Wolpert and M. Lippitz, *Dual Color Transient Absorption Spectroscopy with two synchronized GHz-Oscillators*, DPG Spring Meeting, Berlin/Germany (2015)

C. Dicken, K. Lindfors, M. Hentschel, and M. Lippitz, *Kerr Microscopy of Magnetic Nanostructures*, DPG Spring Meeting, Dresden/Germany (2011)

Contributions at international conferences (others):

Talks

C. Wolpert, **C. Dicken**, K. Lindfors, L. Wang, P. Atkinson, A. Rastelli, O. Schmidt, H. Giessen, and M. Lippitz *Nonlinear Spectroscopy of Single Quantum Dots*, ICOOPMA12, Nara (2012)

C. Wolpert, **C. Dicken**, L. Wang, P. Atkinson, A. Rastelli, O. Schmidt, H. Giessen, and M. Lippitz *Ultrafast Spectroscopy of Single Quantum Dots*, 4th International Workshop on Positioning of Single Nanostructures, Lake Como (2011)

M. Pfeiffer, K. Lindfors, C. Wolpert, **C. Dicken**, P. Atkinson, M. Beyoucef, A. Rastelli, O. G. Schmidt, H. Giessen, and M. Lippitz *Ultrafast Spectroscopy of Coupled Quantum Dots*, 4th International Workshop on Positioning of Single Nanostructures, Lake Como (2011)

Posters

J. Koller, T. Schumacher, **C. Dicken**, D. Wolf, A. Köhler, and M. Lippitz, *Coupling of an organic cyanine dye with a plasmonic structure*, DPG Spring Meeting, Berlin/Germany (2015)

CONTENTS

Preface vii

I	OPTIMIZATION OF DIFFERENTIAL TRANSMISSION IN CONFOCAL MICROSCOPY	1
1	INTRODUCTION	3
2	LIGHT TRANSMISSION AS INTERFEROMETRIC PROCESS	7
2.1	Transmission measurements imply homodyne mixing	7
2.2	The scattered field of a small disk in an effective medium	11
2.3	Differential transmission of a small particle	13
2.4	Phase control with a multilayer reflector	14
3	THE EFFECTS OF FOCUSING AND LIMITED SPOT SIZE	19
3.1	Review of Gaussian beams	19
3.2	Wavefront error at the focal plane of a Gaussian beam	21
3.3	Modeling the shadow of a particle in a Gaussian beam	24
3.4	Differential reflection of a particle on a multilayer using a Gaussian beam	28
3.5	Summary	30
4	CONFOCAL KERR MICROSCOPY OF NICKEL NANODISKS	33
4.1	Confocal Kerr Interferometer	35
4.1.1	Why Sagnac interferometers?	35
4.1.2	The optical path of the interferometer	36
4.1.3	Signal detection and modulation principle	38
4.1.4	Confocal imaging	42
4.2	Kerr rotation of a single nickel nanodisk	43
4.2.1	Magnetic anisotropy and particle hysteresis	43
4.2.2	Size dependency of the magneto-optic effect	49
4.3	Adaption of the model to the setup	54
4.4	Comparison of experimental data and the model	58
5	SUMMARY AND CONCLUSION	65
II	DYNAMICS AND COHERENT CONTROL OF QUANTUM EMITTERS	69
6	INTRODUCTION	71
7	TRANSIENT SPECTROSCOPY OF SINGLE SEMICONDUCTOR QUANTUM DOTS	73
7.1	Dynamics of the V-atom under pulsed excitation	74
7.1.1	Von-Neumann equation of a V-atom	76
7.1.2	Bloch vector representation	80
7.1.3	A detuned V-atom pumped with a $\pi/2$ -pulse	83
7.1.4	From time traces to spectra	86
7.1.5	First test case: Groundstate bleaching and perturbed induction decay	89

7.1.6	Second test case: Response beating	94
7.2	Perturbation of a two-level-system by ultrafast charge carrier dynamics	99
7.2.1	Model of the Dember field amplitude	101
7.2.2	The Dember effect and Rabi oscillations	105
7.2.3	Comparison of theory and experimental data	111
7.2.4	Outlook	111
8	DELOCALIZED STATES OF AN INHOMOGENEOUS EMITTER NETWORK	115
8.1	Formation of delocalized states	116
8.2	Delocalization and static spectral variance	120
8.3	Optical excitation of an ensemble	123
8.4	Summary and Outlook	127
9	MODULATION TECHNIQUES FOR CW-SPECTROSCOPY OF SINGLE QUANTUM DOTS	129
9.1	Experimental setup and signal formation	130
9.2	Wavelength modulation of light source and quantum dot	133
9.3	Position modulation of laser spot and quantum dot	138
9.4	Summary	146
10	SUMMARY AND CONCLUSION	149
III	APPENDIX	153
A	THE JACOBI-ANGER EXPANSION	155
B	NOISE SUPPRESSION BY MODULATION	157
B.1	Amplitude modulation and lock-in detection	158
B.2	Noise suppression by fast scan	161
	BIBLIOGRAPHY	165

LIST OF FIGURES

Figure 2.1	Beam path of a Mach-Zehnder interferometer.	8
Figure 2.2	Transmission experiment as Mach-Zehnder interferometer.	9
Figure 2.3	Polar diagrams of the detected intensity	10
Figure 2.4	Geometry of the FEM simulation	11
Figure 2.5	Magnitude and phase of σ of nickel disks and gold disks	12
Figure 2.6	Scattering amplitude of a nickel disk in vacuum	13
Figure 2.7	Sketch a interferometer with a multilayer reflector	15
Figure 2.8	Contributions to the scattered field of a particle in front of a reflector	16
Figure 2.9	Phase and magnitude of the reflection coefficient of a dielectric slab on a mirror	17
Figure 2.10	Dependency $\Delta\phi$ and $ \mathbf{E}_s $ with respect to ϕ_{ref} .	18
Figure 3.1	Phase fronts and waveform error of a Gaussian beam	21
Figure 3.2	Illustration of the shadowing of a Gaussian beam	26
Figure 3.3	Shadow factors vs. disk diameter and wavelength	27
Figure 3.4	$\Delta\phi$ and $\Delta I/I$ with respect to disk diameter and layer thickness. Polar diagram of $\Delta I/I$.	29
Figure 4.1	Illustration of the magnetization of a particle in an external field.	33
Figure 4.2	Kerr rotation and intensity contrast of a nickel disk array	34
Figure 4.3	Sketch of the beam path of a Sagnac interferometer	36
Figure 4.4	Sketch of the experimental setup.	37
Figure 4.5	Representation of the setup with symmetric paths for both beams.	39
Figure 4.6	Illustration of the modulation principle in the Sagnac interferometer	40
Figure 4.7	Implementation of confocal imaging	42
Figure 4.8	Experimental setup for the measurements of magnetic hysteresis.	44
Figure 4.9	Illustration of the hysteresis measurement procedure	44
Figure 4.10	Example of a magnetic field ramp cycle during a hysteresis measurement.	45

Figure 4.11	The Stoner-Wohlfarth model	46
Figure 4.12	Magnetic hysteresis measurements of single nickel disks.	47
Figure 4.13	Sketch of the sample structure and SEM images of disk arrays.	49
Figure 4.14	Darkfield images of multilayer samples.	51
Figure 4.15	Illustration of the Kerr rotation and intensity fitting routine.	52
Figure 4.16	Nominal versus experimental disk diameters	53
Figure 4.17	2D Kerr rotation and intensity contrast maps of nickel disks of decreasing diameter.	54
Figure 4.18	Kerr rotation and intensity contrast with respect to disk diameter	55
Figure 4.19	Illustration of the optical setup used to derive mathematical expressions for the measured signals	56
Figure 4.20	Limits of the small angle approximation used in eq. 4.31	58
Figure 4.21	Fit results excluding specular reflections at the reflector.	61
Figure 4.22	Fit results including specular reflections at the reflector.	62
Figure 4.23	Polar diagram of the Kerr rotation and intensity contrast	62
Figure 4.24	Comparison of size dependency of Kerr rotation and intensity contrast for different spacer layer heights	63
Figure 7.1	Sketch of the exciton formation in quantum dots	75
Figure 7.2	Conceptual sketch of transient pump-probe spectroscopy	76
Figure 7.3	Luminescence emission spectrum and level scheme of a quantum dot	77
Figure 7.4	Conceptual illustration of the Bloch sphere	81
Figure 7.5	Pseudo-Bloch vector traces of an V-atom after a $\pi/2$ -pulse	84
Figure 7.6	Time traces of the density matrix elements of a V-atom after double pulse excitation	85
Figure 7.7	$\Delta I/I$ spectra calculated from the density matrix elements	87
Figure 7.8	Illustration of two classes of transient pump-probe experiments defined by the polarization of the incoming pulses	88
Figure 7.9	Pseudo Bloch vector traces of ground state bleaching and perturbed induction decay	89

- Figure 7.10 Comparison of the simulated pump-probe spectra with the experimental data 91
- Figure 7.11 Polarization trace and spectra of a perturbed induction decay of an exciton 92
- Figure 7.12 Illustration of polarization retrieval in the X_2 exciton 93
- Figure 7.13 Quantum beats seen in measured $\Delta I/I$ spectra of two slightly detuned exciton transitions 95
- Figure 7.14 Illustration of the beating mechanism against the optical field 96
- Figure 7.15 Simulated differential reflection spectra showing quantum beats in dependency of the pump-probe delay. 97
- Figure 7.16 Horizontal crosssections of the spectra shown in fig. 7.15 98
- Figure 7.17 Rabi oscillations of an exciton resonance measured in a ground state bleaching experiment and illustration of the Dember effect 100
- Figure 7.18 Dependency of the Dember field on the pulse area and different parameters 104
- Figure 7.19 Illustration of the pulse sequence and polarizations of the simulated stretched Rabi oscillation experiment 106
- Figure 7.20 comparison of the impact of detuning, dephasing and oscillator strength reduction on the pump process 107
- Figure 7.21 **a** shows the motion of \vec{M} during the pump process. It moves in the u - w plane on the curve indicated by the dashed line, depending on the evolution of $\Omega(t)$ and $\delta(t)$. The Bloch vector \vec{S} moves in a plane perpendicular to \vec{M} if the precession frequency is large compared to the change of \vec{M} with time. **b** Shown is the small temporal lag of the detuning δ due to the Dember field with respect to the optical pumping with the Rabi frequency Ω . If Ω and δ are of the same order, the effective motion of \vec{M} resembles a rotation from the u -axis to the w -axis. 108
- Figure 7.22 Simulated Rabi stretching for different values of α and F_m 109
- Figure 7.23 comparison of the simulated and measured Rabi oscillations 110
- Figure 7.24 Images of pillars milled in a semiconductor substrate 112

Figure 7.25	Images of pillars milled in a semiconductor substrate covered with PMMA	113
Figure 8.1	Schematic sketch of a two-level-system	117
Figure 8.2	Illustration of the composition of the coupling matrix J	118
Figure 8.3	Eigenstates of a rectangular grid of two-level-system with a $1/d^3$ -interaction	120
Figure 8.4	Degradation of a delocalized state with increasing $\Delta\omega/\omega_c$	121
Figure 8.5	Dependency of the participation ratio N_j on $\Delta\omega/\omega_c$	122
Figure 8.6	Participation ratio of a grid of two-level-systems with correlated eigenenergies.	124
Figure 8.7	Real part of delocalized eigenvectors and excitation probability	125
Figure 9.1	Simplified sketch of the continuous-wave spectroscopy setup.	131
Figure 9.2	Signal formation in continuous-wave spectroscopy	132
Figure 9.3	Background modulation of due to laser emission frequency modulation	134
Figure 9.4	Sample structure for strain-modulation	135
Figure 9.5	Strain-tuning of exciton luminescence emission spectrum	136
Figure 9.6	Spatial map of the differential intensity on top of a GaAs membrane	137
Figure 9.7	Strain-bias dependent differential intensity on a AlGaAs membrane	137
Figure 9.8	Spectrum and confocal maps of $\Delta I/I$ of the bare substrate with laser focus position modulation	139
Figure 9.9	Confocal map of $\Delta I/I$ due to modulation of the laser focus position with dithering of the laser emission wavelength	140
Figure 9.10	Fringe amplitude versus dither amplitude of the laser emission frequency	141
Figure 9.11	Sample design and electronics for spatial modulation of the sample	142
Figure 9.12	$\Delta I/I$ of the bare substrate while modulating the sample position with a piezo actuator	143
Figure 9.13	Noise spectrum of the detected intensity	144
Figure 9.14	Luminescence emission spectrum and modulated luminescence count rate of a quantum dot exciton due to spatial modulation	145
Figure 9.15	$\Delta I/I$ spectra of single quantum dot excitons	146
Figure B.1	Comparison of flicker noise and shot noise	158

Figure B.2	Lock-in modulation illustrated in the frequency domain	159
Figure B.3	Illustration of fast scan principle	161
Figure B.4	Effect of data reordering in a fast scan measurement	162

LIST OF TABLES

Table 3.1	Comparison of the relative amplitude and the focal shift of a beam after k internal reflections in the multilayer.	24
Table 4.2	Fit parameter values	61
Table 7.1	Theoretical estimation of the resonance shift δ and the oscillator strength f in the presence of an electric field parallel to the growth direction.	105

Part I

OPTIMIZATION OF DIFFERENTIAL
TRANSMISSION IN CONFOCAL MICROSCOPY

INTRODUCTION

WHY SINGLE NANOMAGNETS? Magnetism is one of the most important phenomena of nature. From large planetary scales down to microscopically small structures the action of magnetism is found. In the bodies of living organisms we find these very different worlds acting together, allowing a bird to find its way on a journey of thousands of kilometers[11]. The bird does sense the magnetic field of the earth, an ability commonly called magneto-reception. Remarkably, even though magneto-reception has been observed in many different animals for half a decade, it is yet unclear which are the mechanisms that allow the animals to sense the magnetic field[12, 13]. In the beaks of pigeons and other birds, complex structures of magnetite particles were found[14]. Bacteria and insects also are known to incorporate magnetite particles and align their movement relative to magnetic field[15, 16]. But by which means they allow the pigeon to feel the magnetic field is an open question. Studies on this subject try to establish a link between the behavior of the animals and the physical properties of the magnetite nanoparticles[17]. For example[18], pulsed magnetic fields are applied to the head of the pigeon, reorienting the magnetization in the magnetic particles. The bird loses its ability to correctly navigate with the help of the magnetic field, but it recovers within a certain time. The recovery time should be linked to the magnetic properties that allow the bird to sense the magnetic field. For example, superparamagnetic particles would show different time constants compared to single domain magnets[14]. It is essential to characterize the magnetic structures that can be found in the animals. Johnson and Lohrmann stated[19], that *„attempts to locate magnetite in animals have been impeded by several factors, the first of which is that the crystals are small (50 nm diameter) and difficult to resolve microscopically.“* This is just one example where methods are required that allow the detection and characterization of small magnetic structures.

WHY FAR FIELD OPTICS? There is different methods that allow the detection of small nanomagnets. The size regime between $0.01 - 1\mu\text{m}$ in particular is interesting because here single domain magnetization and superparamagnetic behavior can be observed. The advantage of optical methods is the combination of high temporal and spatial resolution. Magnetometers based on magneto-optics with pulsed light sources reach temporal resolutions in the femtosecond regime and allow to investigate high-speed magneto-dynamics. Recently, the magneto-dynamics of sub-100 nm particles have been measured with

a pulsed Kerr magnetometer based on simple far-field optics[20]. The spatial resolution of far field optics is limited to about $\lambda/2$. Spatial resolutions down to 200 nm are common in Kerr magnetometers working close to ultra-violet range[21]. This restriction may be overcome with near-field optics, that allows spatial resolutions below 100 nm. However, compared to near-field techniques, far-field optics is much easier to implement and for many applications, a spatial resolution of a few hundred nanometers is sufficient. For example, with nowadays technology it is possible to fabricate single nanomagnets such that they are separated enough to be resolved by far-field microscopy.

INTERACTION OF PLANE WAVES WITH NANOOBJECTS IS SMALL
 We use a very sensitive optical interferometer developed by Xia et al. to measure the magnetization of nanoparticles[22]. They have shown that Kerr rotations on the order of μrad can be measured on ferromagnetic films. Switching from bulk materials and films to single nanoparticles, a great deal of measurement performance is due to the sample design. A careful sample design allows us to increase the interaction of far-field optical modes with nanoobjects and thus to increase the sensitivity of the setup to the particle magnetization. The interaction with light is usually small because the k-space spectrum of a sub-wavelength nanoobject contains a large number of evanescent modes that do not propagate into the far-field. A possible solution to this are optical antennas that work as a bridge between far-field modes and near-field modes. There are many examples for antenna enhanced far-field optics[23] and also for antenna enhanced Kerr microscopy[24]. Using an antenna is like confining the electro-magnetic energy of the far-field to a sub-wavelength volume. Another option is to increase the interaction time of the far-field modes with the nanoobject by using optical cavities[25, 26]. They store electro-magnetic energy for a longer time in the vicinity of the nanoparticle.

In this work we investigate another approach that allows for the tweaking of the optical response of the sample, using neither antennas nor optical cavities. We exploit the interferometric nature of far-field scattering experiments and take control of the phase difference between scattered and transmitted fields. The test case of our investigations is the Kerr rotation of nickel disk, which are easy to fabricate and pattern with electron beam lithography. The phase difference is controlled by means of a dielectric multilayer system that is used as substrate of the nickel disks.

In the course of our investigations we develop a model that synthesizes the optical response of the complete nanostructure from the optical response of its constituents. This allows us to work with tools and methods that are optimized for simulating the optics of the individual constituents, making the design and optimization of such structures very simple and flexible.

Furthermore the model solves a basic problem of Kerr magnetometry of single nanoobjects, namely that the information about the magnetic properties is intermixed with the optical properties of the nanoobject. Size, shape and environment of a particle obscure the direct link between the Kerr rotation angle and magnetization because the signal is diluted depending on the scattering amplitude of the nanoobject. We separate the intrinsic Kerr rotation angle from the scattering amplitude. To proof the validity of the model and its limits we compare its prediction with Kerr rotation measurements of single nickel disks on a multilayer substrate.

Excluding introduction and conclusion, the text is organized in three chapters. In chapter 2 we start by emphasizing the interferometric character of transmission experiments using the example of nickel disks. We discuss a method that allows us to tweak the phase difference between scattered and transmitted light, not with a typical interferometer, but by with a multilayer reflector as sample substrate. We put together the individual optical responses of the nanoobject and the reflector to synthesize the total response of the structure.

In chapter 3 we discuss the usage of focused beams and how they influence the measurement. We show that for our systems, the disks are effectively illuminated by plane waves and use a model by Nahm and Wolfe to describe the shadow of the nickel disks in a Gaussian beam.

In chapter 4 we present measurements of the Kerr rotation and differential reflection of single nickel nanodisks. We show that they indeed behave like individual nanomagnets and that their Kerr rotation signal strongly depends on their size, obscuring the underlying magnetic properties. We show that the data can be described by the model and that we are able to track down unexpected phenomena found in the measurement to be optical effects unrelated to magnetism.

LIGHT TRANSMISSION AS INTERFEROMETRIC PROCESS

In this chapter we discuss the idea that optical transmission is an interferometric process. As with any interferometer we like to exploit the phase sensitivity and tweak the phase working point such that it fits our needs best. In the first section we briefly introduce homodyne mixing, that is, mixing of two signals of the same frequency. Any optical interferometer where the interfering beams are derived from the same light source performs homodyne mixing. The concept is introduced in sec. 2.1, where we also motivate why control of the phases of electric fields is important in transmission experiments. In sec. 2.2 and sec. 2.3 we investigate the optical properties of single nickel disks and how they influence transmission experiments in the context of homodyne mixing. In sec. 2.4 we introduce a possible technique to actually control the phase of the light scattered by a single particle with a multilayer substrate.

2.1 TRANSMISSION MEASUREMENTS IMPLY HOMODYNE MIXING

If two time-dependent signals are multiplied to generate a third one, we say that the input signals are mixed. Mixing shifts spectral power to frequencies not present in the input signals. The new frequencies are sums and differences of any pair of the input frequencies.

Often the input signals are modulated. If the modulation frequency of both signals is derived from the same source we speak of homodyne mixing. The advantage is that any fluctuation of the source is imposed on both signals. Any difference in the signals must be due to something other than the source. One of the inputs is usually called the *reference* while the other is simply named the *signal*. We make the signal interact with some physical system that we want to study. If the system is linear, then it merely changes the phase and the amplitude of the signal by $\Delta\phi$ and α respectively. Finally, the signal and the reference are mixed and the output of the mixing process recorded. The outcome of the mixing is

$$\begin{aligned} \text{out}(t) &= \overbrace{\sin(\omega t)}^{\text{reference}} \cdot \overbrace{\alpha \sin(\omega t + \Delta\phi)}^{\text{signal}} \\ &= \frac{\alpha}{2} (\cos(-\Delta\phi) - \cos(2\omega t + \Delta\phi)) \end{aligned} \quad (2.1)$$

$\Delta\phi$ and α provide the physical information we are interested in.

The constant offset $-\cos \Delta\phi$ in eq. 2.1 is the essence of homodyne mixing. We deduce from it the changes made to the signal relative

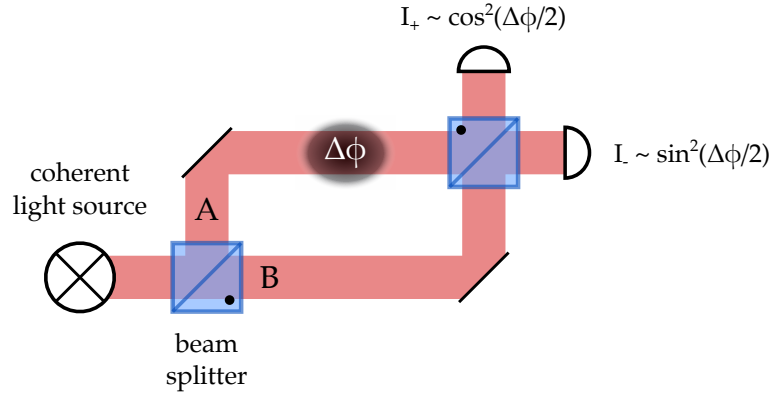


Figure 2.1: Beam path of a Mach-Zehnder interferometer.

to the reference. The sum frequency component $\cos(2\omega t + \Delta\phi)$ is removed with a low pass filter. To determine both parameters α and $\Delta\phi$, the experiment is repeated with an artificial phase shift of 90° between the signal and the reference.

In optics, homodyne mixing can be realized in Mach-Zehnder interferometers (figure 2.1). The input signals are the electric field amplitudes of coherent laser beams, $\mathbf{E}_{A,B} = |\mathbf{E}| \exp i\omega t$. They are derived from the laser source by a 50% beam splitter and propagate along the optical paths A and B. The sample is put into path A and induces a phase difference $\Delta\phi$ between the beams. Then the beams are superposed by a second 50% beam splitter. The reflections on the beam splitter interfaces add additional phase shifts to the two beams. Consequently, at one of the output ports of the second beam splitter the electric field amplitudes are added. At the other one they are subtracted. The emerging beams are fed to non-linear transformers, the photo diodes.

Feeding the sum of two signals to a non-linear transformer is called additive mixing. Compared to pure multiplicative mixing as described by eq. 2.1, the output contains products of each input with itself. The output voltages I_{\pm} of the photo diodes are proportional to the electric field magnitude squared,

$$\begin{aligned}
 I_{\pm} &= |\mathbf{E}_A \pm \mathbf{E}_B|^2 \\
 &= |\mathbf{E} \cdot (1 \pm e^{i\Delta\phi})| \propto \begin{cases} \cos^2 \frac{\Delta\phi}{2}, & + \\ \sin^2 \frac{\Delta\phi}{2}, & - \end{cases} \quad (2.2)
 \end{aligned}$$

The phase shift $\Delta\phi$ due to the sample can be derived from I_{\pm} .

The optical transmission of a small particle in a light beam can be understood just like that. Imagine the electric field of the beam being split into a reference part \mathbf{E}_r and a signal part \mathbf{E}_s , as illustrated by figure 2.2. The signal interacts with the particle while the reference does not. There is no beam splitters, though, and no spatial separation

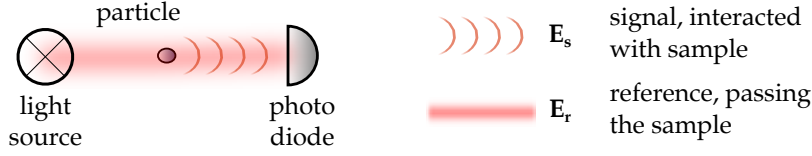


Figure 2.2: A simplified sketch of a transmission experiment. The light scattered by the particle can be understood as the signal path of a Mach-Zehnder interferometer. The light passing the particle unhindered can be understood as the reference of the interferometer. The particle is a linear system that modifies the signal with respect to the reference.

of the two parts. At some point after the interaction region, a detector is placed to mix the reference and the signal.

The particle acts like a linear system if the light intensities are low. The spectral components of the incident light are scaled and phase shifted when interacting with it,

$$\mathbf{E}_s(\omega) = \sigma(\omega) \cdot \mathbf{E}_o(\omega), \quad \sigma(\omega) = \sigma(\omega) \cdot e^{i\Delta\phi(\omega)} \quad . \quad (2.3)$$

The complex scale factor σ is called the scattering amplitude of the particle. \mathbf{E}_s is the scattered electric field of the particle.

The photo diode does additive mixing as in the Mach-Zehnder interferometer. Its output is

$$\begin{aligned} I &= |\mathbf{E}_r + \mathbf{E}_s|^2 \\ &= |\mathbf{E}_o|^2 |1 + \sigma|^2 \\ &= |\mathbf{E}_o|^2 [1 + \sigma^2 + 2\sigma \cos \Delta\phi] \end{aligned} \quad (2.4)$$

The result is similar to the Mach-Zehnder interferometer, except that we have no control over the total phase difference and only one output port.

Interpreted as a function of σ alone (considering $\Delta\phi$ as a parameter), eq. 2.4 describes a parabola,

$$I_{\Delta\phi}(\sigma) \propto (\sigma + \cos \Delta\phi)^2 + \sin^2 \Delta\phi \quad . \quad (2.5)$$

$\Delta\phi$ determines the position $(x, y)_a$ of the apex, which itself moves on a parabola,

$$y_a = 1 - x_a^2, \quad x_a = -\cos \Delta\phi \quad . \quad (2.6)$$

Figure 2.3a visualizes this. When $\Delta\phi$ is tuned from 0 to π , then the apex moves on the parabola indicated by the dashed line. The position of the apex determines the slope of $I_{\Delta\phi}(\sigma)$ at small values of σ . When the apex is located at $\sigma = 0$, the slope is zero. Consequently, a small particle is nearly invisible if $\Delta\phi = \pm \frac{\pi}{2}$.

We can visualize eq. 2.5 for all values of $\Delta\phi$ in a polar diagram, see figure 2.3b. The radial axis represents σ and the azimuthal axis represents $\Delta\phi$. Each cut along the radial axis corresponds to a parabola like

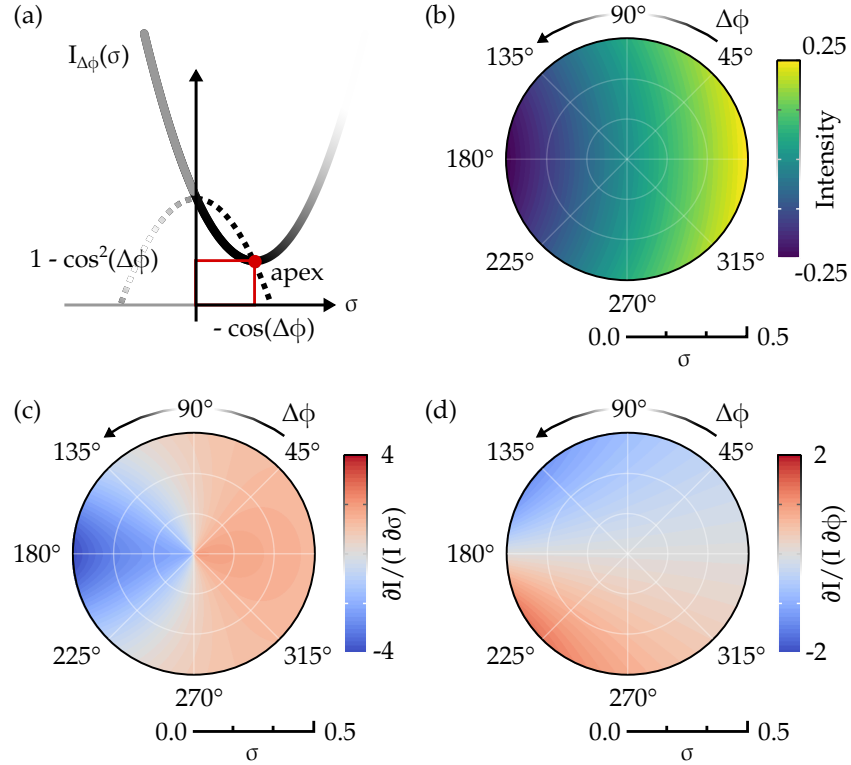


Figure 2.3: **a** The detected intensity $I_{\Delta\phi}(\sigma)$ can be understood as a parabolic function of the scattering magnitude σ of the nanoparticle. The position of the apex of the parabola is determined by the phase difference $\Delta\phi$ of the scattered field and the reference field. **b** The detected intensity can be visualized in a polar diagram where the azimuthal axis corresponds to the phase $\Delta\phi$ and the radial axis corresponds to the magnitude of the scattered electric field. **c,d** shown is the relative change of the detected intensity if the magnitude or the phase is changing.

shown in fig. 2.3a. The polar diagram gives us an overview of how the transmitted intensity changes around a particular value of σ . We can look for good working points in the diagram, depending on what we want to measure. Maybe we want to use the particle as a probe of the environment, want to detect a particle on some background or discriminate particles with respect to some physical property (like magnetization, size, shape). All this boils down to a single thing. *We want to detect changes of σ , that is, σ or $\Delta\phi$.* Lets see how these changes are reflected by equation 2.4. Its partial derivative with respect to σ and $\Delta\phi$ is

$$\frac{1}{I} \frac{\partial I}{\partial(\Delta\phi)} = \frac{2\sigma \sin \Delta\phi}{1 + \sigma^2 + 2\sigma \cos \Delta\phi} \quad (2.7)$$

$$\frac{1}{I} \frac{\partial I}{\partial \sigma} = \frac{2\sigma + 2 \cos \Delta\phi}{1 + \sigma^2 + 2\sigma \cos \Delta\phi} \quad (2.8)$$

These equations are visualized in polar diagrams presented in figures 2.3c and d. They show that a small change of either $\Delta\phi$ or σ is

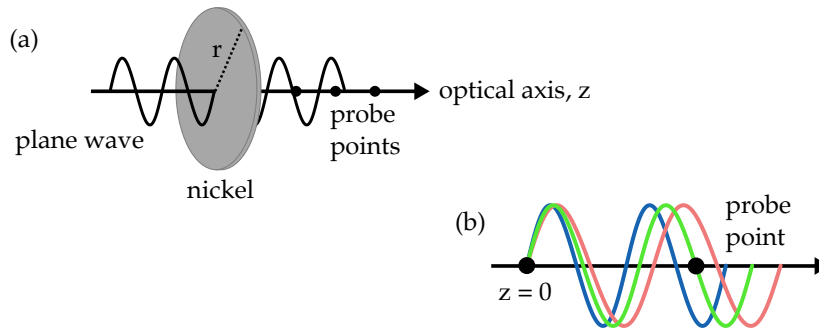


Figure 2.4: **a** A disk is illuminated with a linearly polarized plane wave and scatters a fraction σ of it. The disk axis and the propagation direction of the plane wave fall together. The electric field is probed at separate points on the optical axis. **b** The phase of the electric field at the probe points depends on the wavelength and the distance between the disk plane and the probe point.

reflected well in the transmitted intensity only for certain regions in the diagram. In an interferometer we could add an offset to $\Delta\phi$ by adjusting the length of the optical paths to move into these regions. In a transmission experiment we cannot do that. Happily there is a special sample geometry that works like an interferometer and allows us to manipulate the phase. We discuss it in section 2.4.

Before we come to this we need to know σ for the particular particle we like to study. And we need to know how σ changes in a particular experiment. In this work, we want to discriminate nickel disks with respect to their size and with respect to their magnetization. Hence, in the next section we address these questions by calculating the scattering amplitude of small nickel disks illuminated by a plane wave.

2.2 THE SCATTERED FIELD OF A SMALL DISK IN AN EFFECTIVE MEDIUM

Different methods are available to determine the electric field scattered by a small particle. For spheroids, analytical expressions for the polarizability can be found [27, 28]. For spheres we can use Mie theory [28, 29].

We employ COMSOL, a numerical finite element solver, providing high flexibility in implementing complex geometries without periodic boundaries. An isolated structure in an infinite universe is simulated using a finite volume enclosed in perfectly matched layers.

The geometry is sketched in figure 2.4a. The disk is placed in an effective medium with refractive index N_{eff} . The optical constants of nickel are taken from Johnson and Christy [30]. The plane wave comes from the left. The optical axis is normal to the disk plane. The polarization is linear.

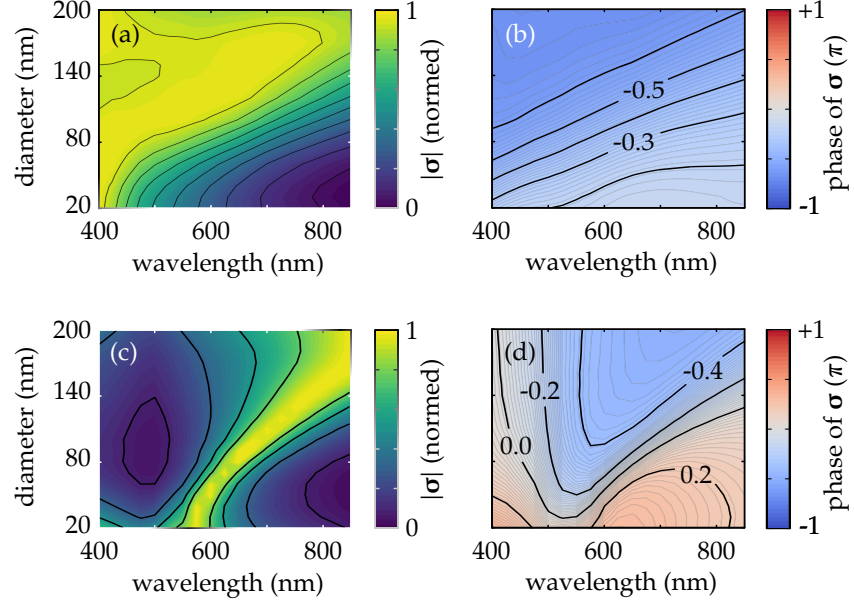


Figure 2.5: **a** shows the magnitude of the scattering amplitude σ of nickel disks with respect to the wavelength and the disk diameter. For each diameter, the magnitude is normalized to the spectral maximum. **wb** shows the phase of σ . **c** and **d** show the same for gold disks.

The scattered field is the total field minus the incident field. It is represented by a complex number, $\sigma = \sigma \exp(i\phi_{\text{scat}})$. We probe it in forward direction at points on the optical axis. It is sufficient to probe only the forward direction because the disk is too thin to be sensitive to the propagation direction of the plane wave. The scattered field therefore has a mirror symmetry with respect to the disk plane.

The probe points are located in some distance to the disk plane to avoid the near field region. Consequently there is some wavelength dependent phase added to σ proportional to the optical path between the disk plane and the probe points (see fig. 2.4b). We remove the offset by multiplying σ with a complex exponential,

$$\sigma(\lambda)_{\text{corr}} = \sigma(\lambda, z_{\text{probe}}) \cdot e^{-2\pi i \cdot N_{\text{eff}} \cdot \frac{z_{\text{probe}}}{\lambda}} . \quad (2.9)$$

In the following, if not declared otherwise, the label σ always refers to the offset corrected scattering amplitude σ_{corr} , as defined by eq. 2.9.

σ depends on the wavelength of the incident plane wave and the radius r of the disk. Figures 2.5a,b show this dependency in terms of its magnitude $|\sigma|$ and of its phase ϕ_{scat} . The spectral maximum of the magnitude shifts red as the disk diameter increases. The phase follows this general pattern. This is due to particle plasmon resonances that change with the particle shape. Metals with lower damping show similar but more pronounced behavior. Figures 2.5c and d show the magnitude and phase of σ of gold disks for comparison. In the next section we substitute $\sigma(\lambda, r)$ into eq. 2.4 and estimate the outcome of a transmission experiment.

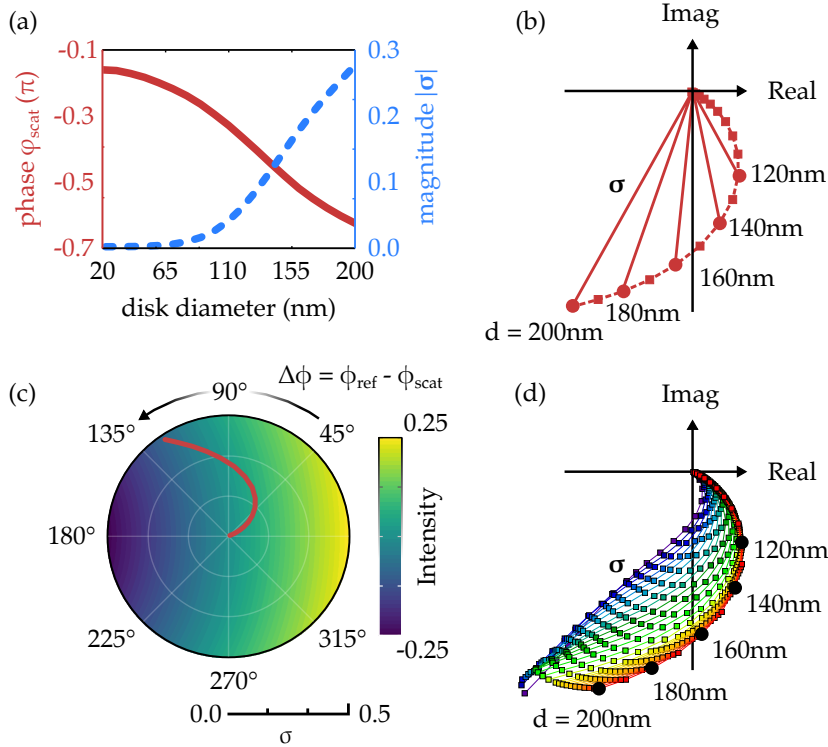


Figure 2.6: **a** Shown is the dependency of σ and ϕ_{scat} of nickel disks at $\lambda = 800 \text{ nm}$. **b** The pairs σ and ϕ_{scat} visualized as a path $\sigma(\phi_{\text{scat}})$ in the complex plane for different disk diameters at $\lambda = 800 \text{ nm}$. **c** The path shown in **b** can be transferred directly to the polar intensity diagram. **d** The path $\sigma(\phi_{\text{scat}})$ depends on the wavelength. The wavelength is marked by the line color.

2.3 DIFFERENTIAL TRANSMISSION OF A SMALL PARTICLE

Given σ in dependency of the disk radius and wavelength, we can determine in which region of the polar diagrams in fig. 2.3 we are. In the experiments described later we use a wavelength of $\lambda = 800 \text{ nm}$. Figure 2.6a shows the magnitude σ and phase ϕ_{scat} taken from the corresponding cross sections in figures 2.5a,b. Figure 2.6b shows the same cross section represented as a path in the complex plane, in the following termed $\sigma(\phi_{\text{scat}})$. This curve can be transferred to the polar diagrams of $I_{\Delta\phi}(\sigma)$ using eq. 2.5, as is shown in figure 2.6c.

Moving outwards along the path in the polar diagrams, the radius of the disks increases. Discriminating disks with respect to their radius is easy if the path goes close to the gradient of the polar diagram 2.6c. In our example this is true for small disks and for large disks. If the disks are small, then the transmitted intensity changes because the magnitude of σ changes. If the disks are large, then the intensity changes because the phase of σ changes. This behavior is also wavelength dependent, as can be deduced from figure 2.6d, showing how $\sigma(\phi_{\text{scat}})$ depends on the wavelength. In the near infrared (de-

noted by red colors), the phase of $\sigma(r)$ changes gradually with the disk radius. At the blue end of the spectrum (denoted by blue colors) the phase changes significantly at smaller diameters, but is approximately constant above 80 nm. Only the magnitude changes.

We are working in the near infrared. There is an intermediate interval of diameters where the path $\sigma(\phi_{\text{scat}})$ evolves nearly perpendicular to the gradient of the polar diagram. No discrimination of disks with different sizes is possible in this interval. It would be convenient if we could rotate the path $\sigma(\phi_{\text{scat}})$ as a whole such that it goes along a gradient path for the particle configuration of interest. The rotation is the same as adding a phase difference between the scattered electric field and the background electric field passing the disk. The next section discusses how this could be done by placing a reflector behind the particle.

2.4 PHASE CONTROL WITH A MULTILAYER REFLECTOR

In the former chapters we stated that a transmission experiment is essentially an interferometric process. The transmitted light is a superposition of a signal electric field and a reference electric field that interfere with each other. Just as with a real interferometer the light intensity at the detector is influenced by the phase difference between the interfering fields. But unlike with a real interferometer we cannot control it because the optical path of the forward scattered light and the light that passed the particle is the same. There is different methods that circumvent this issue. Most of them separate the optical path between the reference electric field and the scattered field before the interaction takes place [31–33], like it is done in the Mach-Zehnder interferometer described in section 2.1. This kind of separation, although necessary, is a drawback. Asynchronous fluctuations of the optical paths are reflected in the detected intensity. The length of the separated optical paths should therefore be as small as possible.

Our solution is to observe the backscattered light instead of the forward scattered light. Its optical path is intrinsically separated from the forward passed light. We let the forward passed light acquire additional phase by traveling some optical path and then merge it again with the backscattered light simply using a mirror. The arrangement is shown in figure 2.7a. The resulting phase difference is defined by the distance between the particle and the mirror. The distance h needs to be on the order of the wavelength to add a phase of 2π . The overall separation of the optical paths can thus be made very small. Similar geometries are used in interferometric scattering microscopy (iSCAT), where interference between light reflected from an interface and the light scattered by particles on the interface is used to enhance the image contrast[34]. A possible implementation of the concept that allows us to control of the distance between particle and mirror is

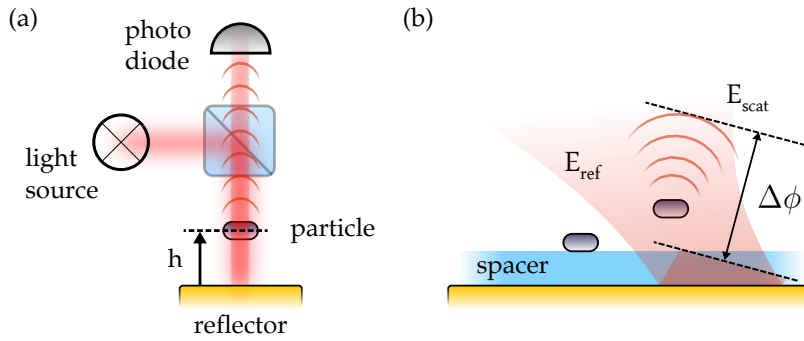


Figure 2.7: **a** The backward scattered light and the forward passed light are merged with a reflector in some distance h behind the particle. **b** The distance between the reflector and the particle is controlled with a transparent spacer. Its thickness controls the phase difference between the backscattered field and the reference field that passes the particle.

shown in figure 2.7b. A simple transparent layer is evaporated on the mirror. The thickness of the spacer layer controls the phase difference $\Delta\phi$ of the reference light and the scattered light.

At this point we may ask some basic questions: What happens to the forward scattered light? Does the reflected light interact with the particle a second time? Does the particle interact with its dipole image? It is not easy to get definite answers to these questions. The big challenge is the intermediate character of the length scales involved. The observed disks are neither very small nor very large compared to the wavelength of the light. The distance between particles and interfaces is also neither large nor small. A quantitatively correct approach requires us to solve Maxwell's equations for the complete structure numerically. However, our goal is to get a qualitative, intuitive picture. We like to separate the problem into smaller pieces that give a better insight of the different physical mechanisms involved here. So, instead of resorting to numerical calculation, we start with the most simple answers to the posed questions and extend the model in combination with further experiments.

An intuitive model of the electric field returning from a scatterer sitting on top of a reflecting interface is presented by Nahm and Wolfe [35]. The model also addresses the questions stated above. Nahm and Wolfe take into account effects of multiple interactions and obstruction of the passed light by the particle. The incident plane wave is divided in two parts: One is scattered by the particle directly, the other one is first reflected by the mirror and then scatters. In the same way they divide the scattered fields. The backward scattered light reaches the detector directly. The forward scattered light is reflected by the mirror and then reaches the detector. All four parts are illustrated in figure 2.8. The first case is the direct scattering of the incident beam. In the second and third case, either the incident wave or the scattered field is reflected by the mirror once, and thereby ac-

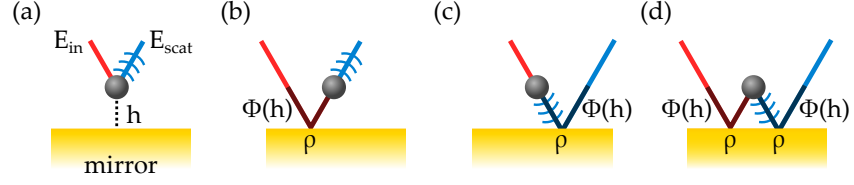


Figure 2.8: From **a–d**, this figure sketches the possible optical paths that contribute to the total scattered field. They correspond to the equations 2.10a to d. ρ is the reflection coefficient of the mirror. ϕ is the phase due to the optical path between the mirror and the particle. h is the distance between the mirror and the particle. The figure is drawn with oblique incidence angle for clarity. The equations refer to normal incidence.

quires some phase ϕ due to the additional path. Moreover, we have to take into account the complex reflection coefficient ρ of the mirror. In the fourth case, both the excitation light and the scattered light are reflected by the mirror. They sum up to the total scattered field. The model assumes that the particle does not interact with its own mirror image. Additionally it assumes that the particle blocks a fraction of the passing fields to guarantee energy conservation. In formulas the four contributions read [36],

$$\begin{aligned}
 \mathbf{E}_{s,1} &\propto \boldsymbol{\sigma} \\
 \mathbf{E}_{s,2} &\propto \rho \cdot F(\boldsymbol{\sigma}) \cdot \boldsymbol{\sigma} \cdot e^{4\pi i \cdot \frac{h}{\lambda}} \\
 \mathbf{E}_{s,3} &\propto \rho \cdot F(\boldsymbol{\sigma}) \cdot \boldsymbol{\sigma} \cdot e^{4\pi i \cdot \frac{h}{\lambda}} \\
 \mathbf{E}_{s,4} &\propto \rho^2 \cdot F^2(\boldsymbol{\sigma}) \cdot \boldsymbol{\sigma} \cdot e^{8\pi i \cdot \frac{h}{\lambda}}
 \end{aligned} \tag{2.10}$$

ρ is the reflection coefficient of the mirror and $\boldsymbol{\sigma}$ is the scattering coefficient of the particle. $F(\boldsymbol{\sigma})$ describes the partial blocking of the incident and scattered fields by the particle. $F(\boldsymbol{\sigma})$ decreases when the particle cross section increases. The exponential phase factor takes into account the optical path between the mirror and the particle. The path is traversed twice, hence the factor 4π . Note that we assume normal incidence of the plane waves.

We implement the arrangement in fig. 2.7b using a transparent dielectric spacer made of silicon oxide between the disks and the mirror. The spacer layer and the mirror form a multilayer structure. The disks sit directly on top of it. The phase shift due to the distance between the mirror and the disk is absorbed into the reflection coefficient ρ_L of the multilayer structure. ρ_L can be determined using the transfer-matrix method [37, 38]. Our structure corresponds to a single slab with refractive index n_L enclosed by half-spaces of air and gold. One finds [37]

$$\rho_L = \frac{\rho_1 + \rho_2 \cdot e^{-2i\phi_L}}{1 + \rho_1 \cdot \rho_2 \cdot e^{-2i\phi_L}}, \quad \phi_L = 2\pi \frac{n_L d}{\lambda} \quad . \tag{2.11}$$

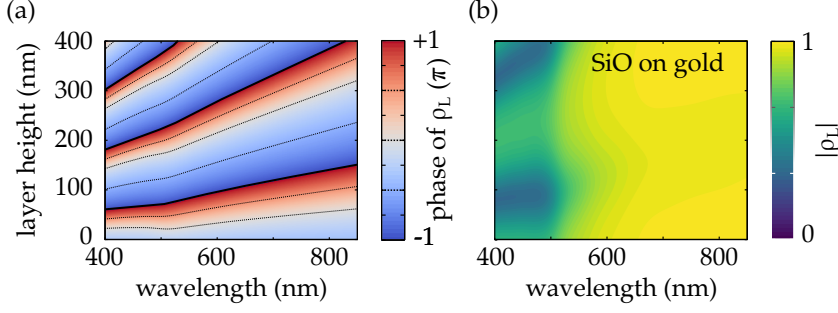


Figure 2.9: **a** and **b** show the phase and the magnitude of the reflection coefficient ρ_L of a gold mirror covered with a silicon oxide layer. Both depend on the wavelength and the thickness of the SiO layer.

ρ_1 is the reflection coefficients of the interfaces between the air and the dielectric. ρ_2 is the reflection coefficient of the interface between the dielectric and the gold mirror,

$$\begin{aligned}\rho_1 &= \frac{n_{\text{air}} - n_L}{n_{\text{air}} + n_L} \quad , \\ \rho_2 &= \frac{n_L - n_{\text{Au}}}{n_L + n_{\text{Au}}} \quad .\end{aligned}\tag{2.12}$$

n_x denotes the complex refractive index of material x . ρ_L depends on λ and the layer thickness h . This dependency is illustrated in figures 2.9a and b, showing the phase and the magnitude of ρ_L respectively.

Except for the D-band absorption range of gold the magnitude of ρ_L is close to one. We could replace it by silver or aluminum if a high reflectivity is desired for wavelengths less than 600 nm. Within the shown wavelength interval, the phase tunes over a 2π -cycle for layers thinner than 400 nm. That is to say, we can shift the phase of an incident wave to any value and at the same time preserve its magnitude.

The total scattered field is the sum of the contributions denoted in eq. 2.10, multiplied with the incident field

$$\begin{aligned}\mathbf{E}_s &= \sum_i \mathbf{E}_{s,i} \\ &= (1 + 2\rho_L F(\boldsymbol{\sigma}) + \rho_L^2 F^2(\boldsymbol{\sigma})) \cdot \boldsymbol{\sigma} \cdot \mathbf{E}_{\text{in}}\end{aligned}\tag{2.13}$$

The reference field is the incident field reflected at the multilayer structure,

$$\mathbf{E}_r = \rho_L \cdot \mathbf{E}_{\text{in}}$$

If the particle is very large and completely shadows the incident beam, $F(\boldsymbol{\sigma})$ is zero. In this case \mathbf{E}_s is not dependent on ρ_L , allowing us to adjust the phase difference $\phi_L - \phi_{\text{scat}}$ between \mathbf{E}_r and \mathbf{E}_s to take any value. If the particle is small, then the freedom to manipulate the phase is limited because the secondary scattered waves are

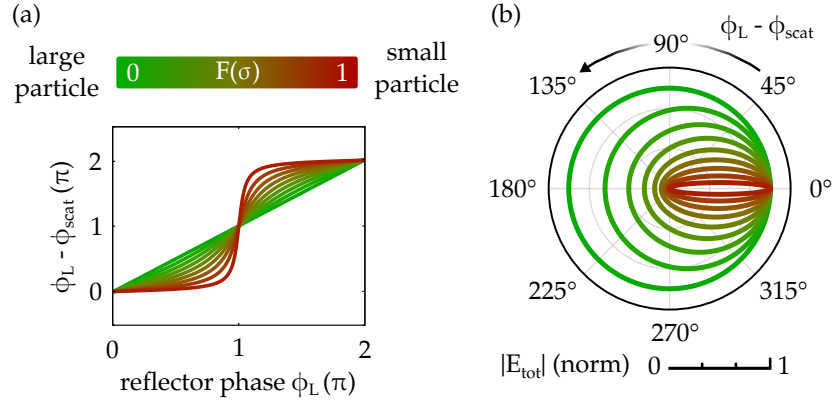


Figure 2.10: **a** shows the phase difference $\Delta\phi = \phi_{ref} - \phi_{scat}$ as a function of the reference phase ϕ_{ref} . **b** shows $|E_s|$ with respect to $\Delta\phi$ in a polar diagram.

also phase shifted by the reflector. It depends mostly on the product $\rho_L \cdot F(\sigma)$ which phase differences are accessible to us.

In fig. 2.10a the phase difference $\Delta\phi = \phi_L - \phi_{scat}$ is plotted against the phase shift ϕ_L induced by the reflector. Differently colored curves correspond to different values of $F(\sigma)$. From red to green the particles get larger. At first glance it seems that by tuning ρ_L , $\Delta\phi$ can take any value between 0 and 2π independent of the particle size. Only the slope around $\phi_L = \pi$ increases. But it turns out that, if the particles are small, the magnitude $|E_s|$ is diminished for most values of $\phi_L - \phi_{scat}$ due to destructive interference of the backscattered light and the reflected, phase shifted forward scattered light. That is emphasized in fig. 2.10b, which shows $|E_s|$ as a function of $\Delta\phi = \phi_L - \phi_{scat}$. If the particle is small, the scattering magnitude is small except for a narrow interval around $\Delta\phi = 0$. The interval grows with the shadowing of the particle until in the limit of a very large particle, $|E_s|$ does not depend on $\Delta\phi$ anymore because the specular reflections are suppressed by shadowing. The shadowing factors are thus significant parameters that determine the effectiveness of the reflector as a phase shifting element. A model for the estimation of $F(\sigma)$ is discussed in the next chapter.

THE EFFECTS OF FOCUSING AND LIMITED SPOT SIZE

So far we have been concerned with plane wave illumination. In the experiment the light used to excite the nickel disks is tightly focused. In contrast to plane waves, the energy of such a spatially limited beam is finite. The nickel disk draws part of that energy from the beam mode and reduces the amplitude of the reference field \mathbf{E}_r , which was assumed to be constant. Furthermore, we used a plane wave to calculate the scattering amplitude of the nickel disks and the complex reflectivity of the multilayer structure. A focused beam in general has a large number of spatial frequencies (or curved wavefronts). We have to investigate whether or not we can approximate the incident light as a plane wave in our system.

In the following discussion we use the Gaussian beam model and start with a brief review of its properties. Then we investigate whether the curvature of the wavefronts is low enough to justify the plane wave approximation. The shadowing of the beam by a particle is discussed next and we finish by reviewing the interferometric response of a disk in front of a multilayer illuminated by a Gaussian beam.

3.1 REVIEW OF GAUSSIAN BEAMS

The Gaussian beam is a solution to the paraxial Helmholtz equation [39]. It is a plane wave $\exp(ikz)$ traveling along the z -axis with a Gaussian intensity profile in the x - y -plane. In polar coordinates ($r = \sqrt{x^2 + y^2}, z$) the Gaussian beam is defined as

$$\begin{aligned} G(r, z) &= U(r, z) \cdot \exp(ikz) \\ &= \frac{A}{q(z)} \cdot \exp\left(-ik\frac{r^2}{2q(z)}\right) \cdot \exp(ikz), \quad q(z) = z - iz_0 \quad . \end{aligned} \quad (3.1)$$

$U(r, z)$ is a complex envelope function that describes the lateral profile of the beam. The two free parameters are the amplitude A and the so called Rayleigh range z_0 . It defines the width of the Gaussian beam in the focal plane and its divergence. To separate the magnitude and the phase of U , $q(z)$ is usually redefined in terms of two new functions $R(z)$ and $w(z)$,

$$\frac{1}{q(z)} = \frac{1}{R(z)} + i\frac{\lambda}{\pi w^2(z)} \quad . \quad (3.2)$$

Substituting into eq. 3.1 we get

$$G(r, z) = i \frac{A \cdot w_0}{z_0 \cdot w(z)} \cdot \exp\left(-\frac{r^2}{w^2(z)}\right) \cdot \dots \cdot \dots \times \exp\left(i\pi \frac{r^2}{\lambda R(z)} - i \tan^{-1}\left(\frac{z}{z_0}\right) + ikz\right) . \quad (3.3)$$

The first exponential in eq. 3.3 is the magnitude profile of the electric field in a given x-y plane. The function $w(z)$ is thus identified as the lateral $1/e$ beam width at a position z on the optical axis. $w^{-1}(z)$ also defines the longitudinal profile on the optical axis. The second exponential determines the phase of the electric field in the x-y plane and along the z-axis respectively. $R(z)$ is the radius of curvature of the wavefronts. $R(z)$ and $w(z)$ can be expressed in terms of the Rayleigh range z_0 ,

$$R(z) = z \cdot \left(1 + \frac{z_0^2}{z^2}\right) , \quad (3.4)$$

$$w(z) = w_0 \cdot \sqrt{1 + \frac{z^2}{z_0^2}} , \quad (3.5)$$

$$w_0 = \sqrt{\frac{\lambda z_0}{\pi}} . \quad (3.6)$$

The term

$$\zeta(z) = -\tan^{-1}\left(\frac{z}{z_0}\right) . \quad (3.7)$$

is called Gouy phase[40, 41]. It implies that the phase of a Gaussian beam at some position z on the optical axis differs from the phase of a plane wave $\exp(ikz)$ by $-\tan^{-1} \frac{z}{z_0}$. In particular, far away from the focal plane the Gaussian beam has a phase difference of $\pm\pi/2$ compared to a plane wave. The Gouy phase is implemented in our model by multiplying an additional phasor $\exp(-i\pi/2)$ to the reference plane wave amplitude \mathbf{E}_r , an approach commonly used in the literature[31, 34].

To summarize, the relevant implications to our model are:

- The second exponential implies that the phase of the electric field is not constant on the surface of a large disk and of the reflector. How large is the wavefront error for our system?
- The lateral confinement of the electric field due to the first exponential implies a finite energy content. Part of this energy is removed from a beam by a disk within it. One says that the particle casts a shadow.
- We have to add the far-field Gouy phase to the reference plane wave used in our model, $\mathbf{E}_r \rightarrow \mathbf{E}_r \cdot \exp(-i\pi/2)$.

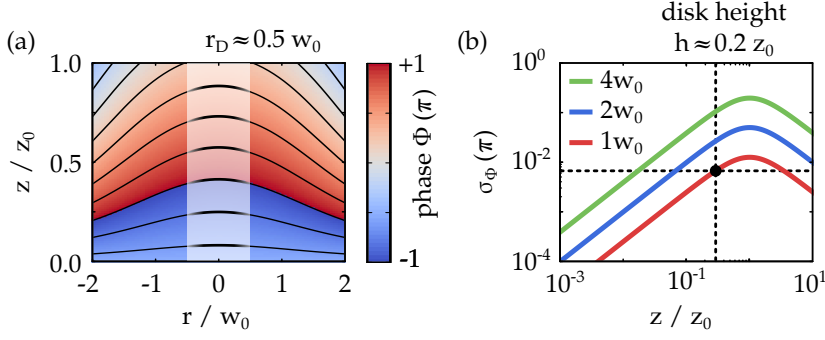


Figure 3.1: **a** Shown is the phase of a Gaussian beam at the points (r, z) . The radial axis is normed to the beam waist w_0 . The z axis is normalized to the Rayleigh range z_0 . The disks we use are typically well below a radius of $0.5w_0$. This region is marked by the white shade. **b** Shown is the standard deviation σ_ϕ of the phase along the radial axis in units of π . A different color refers to a different radial interval over which the deviation is calculated. The red curve corresponds to the interval marked in part a of the figure. The height of our structures is typically below 100 nm which is $0.2z_0$.

In the next sections we discuss if the wavefront error due to the curved wavefronts of the Gaussian beam is small enough to justify the plane wave approximation for our kind of structure. Afterwards we investigate the shadowing of the spatially confined beam by the investigated particles and its influence on the phase control mechanism of the multilayer reflector.

3.2 WAVEFRONT ERROR AT THE FOCAL PLANE OF A GAUSSIAN BEAM

When calculating the reflection coefficient of the multilayer reflector we assumed that the incident field is a plane wave propagating perpendicular to the layer structure. In the same way, we assumed that the nickel disks are illuminated by plane waves. The wavefronts of a Gaussian beam, however, are curved. We check now that close to the focal plane the approximation of the Gaussian electric fields as a plane wave is valid. First we check this with respect to the nickel disks. Afterwards we handle the multilayer reflector.

The phase of the electric field $G(r, z)$ of a Gaussian beam is illustrated in dependency of r and z in fig 3.1a. The r -axis is normalized to the beam waist w_0 in the focal plane and the z -axis is normalized to the Rayleigh range z_0 . The black line mark cross sections of constant phase. The shaded area marks the radial interval that corresponds to the maximum size of the nickel disks we use in our experiments. The curvature of a wavefront determines the wavefront error in the corresponding x - y plane. In the focal plane the wavefronts are flat. Hence,

the thinner an object is and the closer to the focal plane it is located, the smaller is the wavefront error on its surface.

But how thin is thin enough? The answer depends on the diameter of the nickel disks. Close to the optical axis the phase Φ of G is approximately a quadratic function of the radial coordinate. Except for an offset depending on the z -coordinate we have

$$\Phi(r, z = \text{const}) \propto \frac{\pi \cdot r^2}{\lambda \cdot R(z)} .$$

Then, in the limit of a disk with a radius r_D such that $r_D^2 \ll \lambda \cdot R$, we have $\Phi \approx \text{const}$ on the disk surface. Since $R(z)$ gets smaller if z increases, a disk with large diameter must be close to the focal plane to keep this approximation valid.

We use the standard deviation $\sigma_\phi(z)$ of Φ on a specified radial interval, corresponding to the diameter of the nickel disks, to quantify the wavefront error in a distance z from the focal plane. Figure 3.1b shows $\sigma_\phi(z)$ for three different radial intervals. The red curve corresponds to the interval $r \in [-w_0/2, w_0/2]$ as is marked in fig. 3.1a by the gray shade. The maximum is for all curves at $z = z_0$ where wavefront curvature is maximal. For structures with diameters less than w_0 and heights less than $0.2z_0$ the deviation is below 1%. In praxis, with the disk sizes and heights we use, this is sufficiently small.

In the next paragraph we discuss the validity of the plane wave approximation with respect to the multilayer reflector. The following argumentation shows that the multilayer structure, although in principle extended in z -direction and supporting multiple reflections, can be reduced to act like a bare mirror surface in the focal plane of the Gaussian.

The multilayer reflector in essence splits the single incident Gaussian beam into several copies. These copies are due to the multiple reflections at the interfaces and have different focal planes. We can use the ABCD-Method [42] to see this by means of an example. The ABCD-Method is used in paraxial ray optics to describe the propagation of a ray through an optical system. An optical element is characterized by a 2x2 matrix, the so called ray-transfer matrix,

$$M = \begin{pmatrix} A & B \\ C & D \end{pmatrix} . \quad (3.8)$$

These matrices describe how the parameters of a ray are changed by an optical element. In standard ray optics this is the distance of the ray from the optical axis and its inclination. The ABCD-Method also applies to Gaussian beams and describes the change of the q -parameter when the beam propagates through an optical system. If

an optical element is defined by M , then the q -parameters q_1 and q_2 of the incident and the outgoing beam are related by [42]

$$q_2 = \frac{A \cdot q_1 + B}{C \cdot q_1 + D} . \quad (3.9)$$

The reflector is a dielectric slab between air and a mirror. It is described by three subsequent optical elements, namely the interface between air and the dielectric, the propagation over a distance d inside the dielectric slab and the reflection at the gold surface. The ABCD-matrices are

$$M_1 = \begin{pmatrix} 1 & 0 \\ 0 & \frac{n_a}{n_d} \end{pmatrix}, \quad \text{an interface between two media} \quad (3.10)$$

$$M_2 = \begin{pmatrix} 1 & \frac{d}{n_d} \\ 0 & 1 \end{pmatrix}, \quad \text{propagation over a distance } d \quad (3.11)$$

$$M_3 = \begin{pmatrix} 1 & 0 \\ 0 & 1 \end{pmatrix}, \quad \text{reflection at a planar mirror} . \quad (3.12)$$

n_a and n_d are the refractive indices of air and the dielectric. To get the matrix of the complete optical system, the ray-transfer matrices of subsequent optical elements are concatenated. The passage through the multilayer system consists of several different optical paths, depending on the number of internal reflections the beam undergoes. For each path we have to calculate the ray-transfer matrix separately. The matrix for a single reflection at the gold mirror is

$$\begin{aligned} M &= M_1' \cdot M_2 \cdot M_3 \cdot M_2 \cdot M_1 \\ &= \begin{pmatrix} 1 & 2d \frac{n_a}{n_d} \\ 0 & 1 \end{pmatrix} . \end{aligned} \quad (3.13)$$

Note that the dielectric layer and the air-dielectric interface are passed twice and that for the second passage of the air-dielectric interface we have to swap the refractive indices in the ray-transfer matrix, indicated by the prime added to the matrix label M_1 . Using eq. 3.9, we compute the new q -parameter,

$$q_2 = q_1 + 2d \frac{n_a}{n_d} \quad (3.14)$$

$$\Rightarrow q_2(z) = q_1(z + z'), \quad z' = 2d \frac{n_a}{n_d} , \quad (3.15)$$

since $q(z) = z + iz_0$. The beam envelope is translated along the z -axis by $2d \frac{n_a}{n_d}$. All other parameters stay constant. Each additional internal reflection at the dielectric-air interface adds another copy of the beam shifted along the z -axis. For k internal reflections the shift is

$$z'_k = 2kd \frac{n_a}{n_d} .$$

The insight is that the multilayer systems produces copies of the incident Gaussian beam with shifted focal planes. The focal shift grows with the number of internal reflections. If it is larger than the Rayleigh range, then the wavefronts are curved significantly already within the multilayer structure. We need to check that these copies are negligible. The k -th copy experiences k internal reflections in the multilayer. Its magnitude is reduced by a factor [37]

$$\rho_k = (-\rho_1)^k \cdot (1 - \rho_1)^2 \cdot \rho_2^{k+1} \quad , \quad (3.16)$$

where $\rho_{1,2}$ are the Fresnel coefficients of the air-dielectric and dielectric-gold interface for normal incidence as defined in eq. 2.12, page 17. Table 3.1 shows the magnitude of ρ_k and the focal shift z' for up to five internal reflections in a silicon oxide slab on a gold mirror¹. The focal shift z'_k is normed to the Rayleigh range of a Gaussian beam with a numerical aperture of NA=0.65 at 800 nm.

Order k	0	1	2	3	4	≥ 5
ρ_k	0.923	0.220	0.052	0.012	0.003	$< 10^{-4}$
z'_k/z_0	0.20	0.40	0.60	0.80	1.01	1.21

Table 3.1: Comparison of the relative amplitude and the focal shift of a beam after k internal reflections in the multilayer.

Obviously, only copies with less than two internal reflections contribute significantly. For those, the focal shift is less than $0.5z_0$. The integrated contribution of higher order copies is below 7%. We conclude that for our structures we can approximate the incident field as a plane wave when calculating the optical response of the particle and the multilayer reflector.

3.3 MODELING THE SHADOW OF A PARTICLE IN A GAUSSIAN BEAM

In section 2.4 we use the approach by Nahm and Wolfe [35] to describe the light scattered by a particle in front of a planar reflector. They also address the issue of energy conservation. A beam of finite spatial extend carries a finite amount of energy. A scatterer placed in the beam removes a certain fraction of it by scattering and absorption. The intensity of the passed light must decrease accordingly. If the incident field is a plane wave, then the optical theorem states[43] that the total cross section (scattering plus absorption) of the particle is proportional to the imaginary part of the scattering amplitude in the forward direction. From the cross section of the particle, we

¹ At a wavelength of 800 nm the refractive indexes of silicon oxide is $n_{\text{SiO}} = 1.63$ as determined by ellipsometry. For gold we use data from Johnson and Christy [30], so $n_{\text{Au}} = 0.14 + 4.91i$

can compute by how much it reduces the integrated intensity caught by a screen in a far distance. In our case, a system with multiple reflections, multiple scattering processes and focusing the optical theorem cannot be applied in this way. Nahm and Wolfe suggest that the amount of energy removed from the background beam by each scattering process is determined by the geometrical shadow of the particle as emphasized in figure 3.2a. The particle blocks the area C of the beam intensity profile I_b . The transmitted power is the total intensity minus the intensity integrated over C. Assuming that the particle has a circular cross section and is in the center of the beam profile (compare with fig. 3.2b), the integrated power relative to the total power P is

$$\begin{aligned}\alpha &= \frac{1}{P} \int_C |G(\mathbf{r})|^2 \cdot dA \\ &= \frac{1}{P} \int_0^{r_d} |G(r, z=0)|^2 r \cdot dr \cdot d\theta \\ &= 1 - \exp\left(-\frac{2r_d^2}{w_0^2}\right) \quad ,\end{aligned}\tag{3.17}$$

where r_d is the radius of the cross section C, and w_0 is the beam waist of the Gaussian beam in the focal plane (eq. 3.6). Therefore the passed intensity is $1 - \alpha = \exp(-\frac{2r_d^2}{w_0^2})$. If applied to field amplitudes instead of intensities, we have to use the square root of these expressions. The equations 2.10 change to

$$\begin{aligned}\mathbf{E}_{s,1} &\propto \boldsymbol{\sigma} \quad , \\ \mathbf{E}_{s,2} &\propto \rho \cdot \sqrt{1-\alpha} \cdot \boldsymbol{\sigma} \cdot e^{4\pi i \cdot \frac{h}{\lambda}} \quad , \\ \mathbf{E}_{s,3} &\propto \rho \cdot \sqrt{1-\alpha} \cdot \boldsymbol{\sigma} \cdot e^{4\pi i \cdot \frac{h}{\lambda}} \quad , \\ \mathbf{E}_{s,3} &\propto \rho^2 \cdot (1-\alpha) \cdot \boldsymbol{\sigma} \cdot e^{8\pi i \cdot \frac{h}{\lambda}} \quad .\end{aligned}\tag{3.18}$$

In the same way the background field \mathbf{E}_r is obstructed twice when passing the particle and its mirror image.

$$\mathbf{E}_r = (1 - \alpha) \cdot \rho \cdot \exp(-i\pi/2) \cdot \mathbf{E}_{in} \quad .\tag{3.19}$$

The total field now reads

$$\begin{aligned}\mathbf{E}_{tot} &= [(1 - \alpha) \cdot \rho \cdot \exp(-i\pi/2) \\ &\quad + (1 + 2\rho \cdot \sqrt{1-\alpha} + \rho^2 \cdot (1-\alpha)) \cdot \boldsymbol{\sigma}] \cdot \mathbf{E}_{in} \\ &= \left[(1 - \alpha) \cdot \rho \cdot \exp(-i\pi/2) + (1 + \rho \cdot \sqrt{1-\alpha})^2 \cdot \boldsymbol{\sigma} \right] \cdot \mathbf{E}_{in} \quad .\end{aligned}\tag{3.20}$$

As we said before (see sec. 2.4), the shadow factors play a crucial role for the application of a multilayer reflector as a phase controlling

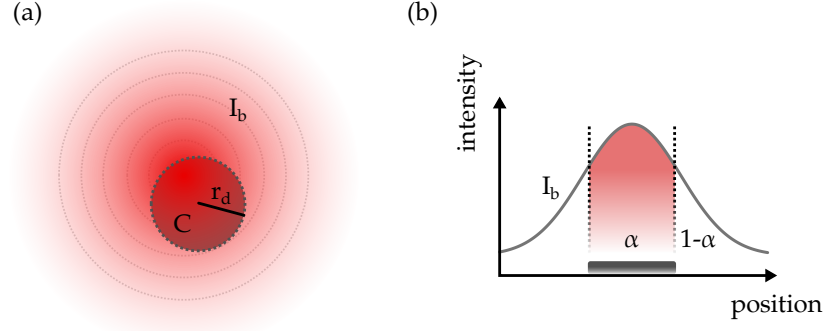


Figure 3.2: **a** A particle casts a shadow that is proportional to the integrated intensity $\int_C I_B$ blocked by its cross section C . **b** The problem is reduced to one dimension if the particle is located in the center of the beam. α is the intensity blocked by the particle, normalized to the total intensity. $1 - \alpha$ is the fraction passing the particle.

element. We want to estimate how large α is in our system. The cross section C is the extinction cross section C_{ext} of the disk for a given geometrical size and wavelength. We use the extinction cross section because it is the effective area of the disk as seen by a plane wave. The effective radius of a disk that we have to substitute into eq. 3.17 is

$$r_{\text{eff}} = \sqrt{\frac{C_{\text{ext}}}{\pi}} . \quad (3.21)$$

The beam width w_0 depends on the numerical aperture of the objective used in the experiment and the wavelength. It is given by [42]

$$w_0 = \frac{\lambda}{\pi \cdot \text{NA}} . \quad (3.22)$$

Figure 3.3a shows $\sqrt{1 - \alpha}$ for different geometrical sizes of the nickel disks. Different line colors correspond to different wavelengths as indicated by the color bar.

In the near infrared shadowing is not significant for sub-100 nm particles. $\sqrt{1 - \alpha}$ is larger than 75%. In the blue wavelength range shadowing sets in earlier but will not block the specular reflections and forward scattered light. We stated already in section 2.4 that the forward scattered light locks the phase of the reference field and the total scattered field, reducing the effectiveness of the reflector as phase shifting device. The shadowing factors given by eq. 3.17 can now be used to estimate the optical response of a nickel disk for different multilayer phase shifts. Figure 3.3b shows the magnitude of $E_s = \sum E_{s,i}$ of nickel disks with respect to the phase difference $\Delta\phi = \phi_{\text{ref}} - \phi_{\text{scat}}$. The wavelength is 800 nm. Red to green colors designate small to large disk diameters. For σ we substituted the optical response of the nickel disks from the FEM calculations (see fig. 2.5, page 12). The phase shift of the reflector we varied from 0 to 2π by

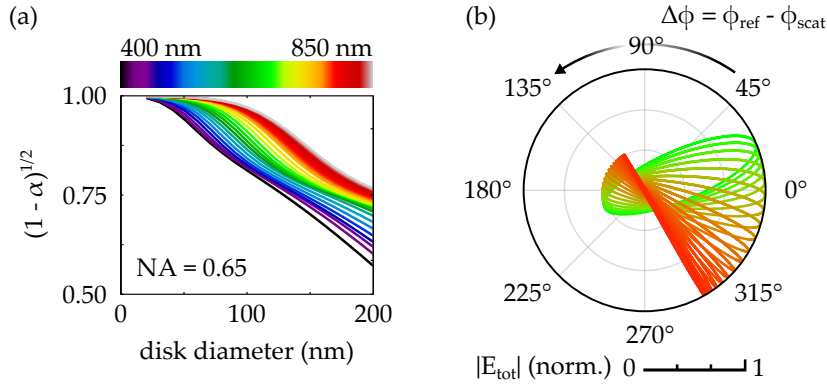


Figure 3.3: **a** The shadow factors $\sqrt{1 - \alpha}$ plotted with respect to disk diameter and wavelength. **b** The magnitude of \mathbf{E}_s with respect to the phase difference $\Delta\phi = \phi_{\text{ref}} - \phi_{\text{scat}}$ at a wavelength of 800 nm. The disk diameter increases from red to green color. For each particle size, the phase shift of the reflector is tuned from 0 to 2π .

tuning its thickness. For small disk diameters, the phase difference of \mathbf{E}_s and \mathbf{E}_r is pretty much a constant. The phase of \mathbf{E}_s is locked to the phase of \mathbf{E}_r because the specular reflections contribute a large fraction to the total scattered light.

According to this model the multilayer reflector would not separate the optical paths of the reference field and the scattered field very well, especially for small particles. However, we heavily simplify a rather complicated system:

- geometrical optics is applied to a sub-wavelength system
- it is assumed that the scattered light has the same shadow factor as the Gaussian beam
- possible coupling between the mirror and the particle is ignored

Furthermore we will see in chapter 4 that the model also fails to describe experimental data when we include any forward scattered contributions and indirectly scattered light. For this reason we will for the moment assume that the scattered light is given by

$$\mathbf{E}_s = \sigma \cdot \mathbf{E}_{\text{in}} \quad , \quad (3.23)$$

and that the shadow of the particle only affects the reference field. Together with the Gouy phase shift it is given by

$$\mathbf{E}_r = \sqrt{1 - \alpha} \cdot \rho_L \cdot \exp(-\pi/2) \cdot \mathbf{E}_{\text{in}} \quad . \quad (3.24)$$

The total field is then given by

$$\mathbf{E}_{\text{tot}} = \left(\sqrt{1 - \alpha} \cdot \rho_L \cdot \exp(-\pi/2) + \sigma \right) \cdot \mathbf{E}_{\text{in}} \quad . \quad (3.25)$$

3.4 DIFFERENTIAL REFLECTION OF A PARTICLE ON A MULTI-LAYER REFLECTOR WITH GAUSSIAN BEAM ILLUMINATION

In chapter 2.1 we calculated the differential transmitted intensity, the phase response and the amplitude response of a single particle illuminated by a plane wave. We found out that all these quantities are sensitive to the phase difference between the reference field and the scattered field. The multilayer reflector allows us to tweak the phase difference to some extent. In this section we review the optical response of a nickel disk, taking into consideration that it is put onto a multilayer reflector and not into vacuum. We use eq. 3.25 to describe the total field at the detector and tune the phase difference by assuming a certain spacer layer thickness. In the calculations the operation wavelength is 800 nm. We use gold as a mirror material and silicon oxide as spacer layer². The scattering amplitude σ of the nickel disk is taken from the FEM simulations (review fig. 2.5, page 12). The shadow factor α of the reference field is given by equation 3.17. The effective area of the disk is the extinction cross section determined by the FEM simulation.

Figure 3.4a shows the phase difference $\Delta\phi = \phi_{\text{ref}} - \phi_{\text{scat}}$ for different spacer layer heights. We see that the multilayer reflector adds the expected phase bias ϕ_{ref} to the scattering phase ϕ_{scat} . For a constant layer thickness, the equi-phase lines are bent because the scattering phase changes with the size of the disks. For certain layer thicknesses (e.g. $h \approx 150$ nm) it seems that this bending is flattened out a little. This is because ϕ_{ref} does not change linearly with the thickness of the spacer layer. Close to a layer thickness of 150 nm the slope is highest. The phase shift induced by the reflector repeats every 270 nm of layer thickness. Compare this with the Rayleigh range of our system which is about 600 nm. If we like to exploit the full 2π phase difference interval we come close to a structure height of $0.5 \cdot z_0$, where the phase fronts of the incident field are not flat anymore. The angular spectrum of the Gaussian should be taken into account in this case.

Figure 3.4b shows the change of total intensity, $|\mathbf{E}_{\text{tot}}|^2/|\mathbf{E}_{\text{tot},0}|^2 - 1$, when the particle is put into the beam. Like $\Delta\phi$, it depends on the spacer layer thickness. The path of maximum change for a given diameter is marked by the solid lines. It is impossible to optimize the change of the total intensity for all disk diameter at the same time with a single spacer layer thickness. For larger particles, the thickness of the spacer layer must increase. However, the dashed line indicates that a linear increasing layer thickness approximates the optimal layer thickness quite well. In practice a layer with continuously increasing

² The refractive index of gold at 800 nm is $n_{\text{Au}} = 0.15 + 4.91i$ and determined by interpolation of experimental data taken from [30]. The refractive index of silicon oxide was determined by ellipsometry and is 1.65.

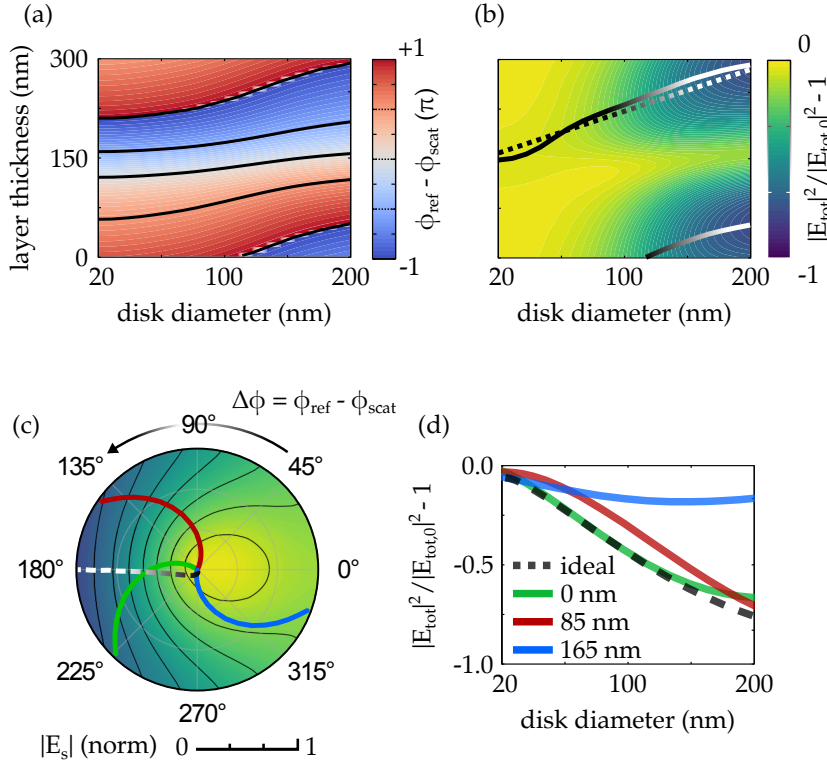


Figure 3.4: **a** and **b** show the dependency of $\Delta\phi$ and $\Delta I/I$ on the disk diameter and the thickness of the spacer layer. The solid lines in **b** mark the path maximum transmission contrast. The dashed line is a linear approximation. **c** is a polar diagram of $\Delta I/I$ with respect to $\Delta\phi$ and the magnitude of E_s . The cross sections mark spacer layer heights of 0 nm (green), 85 nm (red) and 165 nm (blue). The dashed line corresponds to the path of maximum contrast **d** shows the cross sections along the marked paths in **c**.

thickness can be fabricated on a single substrate by thermal evaporation combined with a cover that is slowly removed from the sample. The layer thickness is proportional to the integrated exposure time of the uncovered area. In this way, any monotonously increasing thickness profile can be realized. Figure 4.14 in chapter 4 shows dark-field microscopy images of a sample that was fabricated this way.

For a better comparison with the results in section 2.1, we visualize the change of the intensity again in a polar diagram shown in figure 3.4c. The phase difference $\Delta\phi$ for a given spacer layer thickness is used as azimuthal coordinate. The radial coordinate is $|E_s|$. Due to shadowing of the Gaussian beam, E_r depends on E_s . Accordingly, the differential intensity is no longer a parabolic function of $|E_s|$, as was the case in section 2.1. In contrast to plane wave illumination, the equi-intensity curves are thus bend much stronger (compare with fig. 2.3, page 10). We can use that to our advantage, making the path $\sigma(\phi_{\text{scat}})$ go close to a gradient in the polar diagram by adjusting

the multilayer properties: $\sigma(\phi_{\text{scat}})$ tends to bend against the equi-intensity lines for phase differences from 0° to 180° and tend to bend along the equi-intensity lines for phase differences from 180° to 360° .

This behavior is visualized in the polar diagram by the three colored paths which correspond to the optical response of nickel disks for fixed heights of the dielectric layer of 0 nm, 85 nm and 165 nm. The dashed line corresponds to the path of maximum transmission contrast as marked in figure 3.4b. The red path crosses the equi-intensity lines nearly at right angles and is rather sensitive to changes of the disk radius. It turns out, that especially for small nickel disks, a bare mirror without dielectric spacer already provides a very good intensity contrast. For disks larger than 200 nm a dielectric spacer may provide advantages.

3.5 SUMMARY

In the present chapter we described a method that allows us to exploit the interferometric nature of transmission experiment by separating the phase of the two interfering fields, namely the field scattered by the particle and the field passing the particle. The separation is achieved using a multilayer structure that is placed behind the particle. The optical response is determined in two steps. First we calculate the optical properties of the particle and the multilayer reflector separately. Then we combine the results to construct the optical response of the complete system. The joint between the reflector and the nanoobject is eq. 3.20, which makes assumptions about how the electric fields of the scattered light and the reflected light must be merged to describe the complete structure. Most important is the process of multiple scattering and how the particle obscures the beam that is used as a reference. To describe the latter, we assume that the particle casts a shadow that is proportional to its effective area. The energy withdrawn from the incident light is proportional to the integrated intensity that falls on the particle cross section.

The combination of these separate results is challenging because we are in a regime of neither very small nor very large particles. The usual approximations may not work reliably. For example, we have seen that the reflector does not work if we take into account specular reflections of the reference field and forward scattered light. In this case the phase of the reference field and the scattered field is locked as in an ordinary transmission experiment. In spite of this, we will see in the next chapter that the model does describe experimental data well if these contributions are neglected.

What is a possible explanation for this? It is clear that the forward scattered field must exist. Yet, we made several assumptions in our model that to this date we have not tested in experiment. Especially the shadow of a particle in a Gaussian beam may not be suited to

describe the optics of our sub-wavelength structure. A more sophisticated model that includes the angular spectrum of the incident and scattered light might resolve this issue and will be integrated into the model in the future.

A possible coupling of the metal particle with the gold mirror and the spacer layer is not addressed in this work. Especially for very thin layers we have to consider a possible coupling of plasmonic resonances. Up to now we found no indication for a direct coupling of the nickel disks with the gold film down to spacer layer heights of 75 nm. In the next chapters we will see that the experimental data is fit well without assuming a coupling in the model. The situation may be different when thinner spacers and materials with more pronounced resonances are used.

All these questions can be addressed by simulating the complete structure with numerical tools. It is clear that our model cannot compete quantitatively with a numerical solution of the problem. However, goal of this model is to gain a qualitative insight with a few basic assumptions. Effects on the optical response of the complete structure can be clearly addressed to the individual parts of the system, yielding an intuitive picture of the relevant parameters. Additionally it is very flexible concerning the means by which the optical response of the nanoparticle and the reflector are determined. Very simple and fast methods such as Mie theory or a Clausius-Mosotti type of model can be utilized for the particle response. The methods used can be refined step by step as needed to get a more realistic picture. In the next chapter we will apply the described model to magnetized nickel disk on a multilayer reflector, and show that it is able to predict the radius dependence of the Kerr rotation of the disks correctly.

CONFOCAL KERR MICROSCOPY OF NICKEL NANODISKS

The model described in the former chapters was originally developed to understand the dependency of the magneto-optic Kerr Effect (MOKE) on the size of individual nanomagnets that we observed in our experiments. MOKE refers to the phase shift of circularly polarized light that is reflected by a magnetized ferromagnet. The sign of the phase shift depends on the handedness of the wave. The magnitude of the phase shift depends on the magnetization of the ferromagnet at its surface. In effect, the polarization of a linearly polarized light beam will be rotated by an angle ϕ_k proportional to the magnetization \mathbf{M} of the illuminated surface. Depending on the angle of incidence, different components of the magnetization vector contribute. For normal incidence only the component vertical to the surface is relevant. This configuration is called polar MOKE, as opposed to longitudinal MOKE for parallel incidence of the light. Longitudinal MOKE is sensitive to the parallel component of the magnetization. Our experimental setup is restricted to polar MOKE measurements.

Closely related to MOKE is Faraday's effect. It is a polarization rotation of linearly polarized light when passing through a paramagnetic, transparent material such as fused silica. Faraday's effect is used in optical isolators in which the polarization rotation is used to block unwanted back-reflections from optical elements. Both MOKE and Faraday's effect are used to investigate the magnetic properties of functional materials. Detailed information about the microscopic origins of MOKE and Faraday's effect can be found in [44–46].

We observed that the Kerr rotation of sub-wavelength nickel disks does depend on the disk diameter. Similar effects have been observed by other groups[25, 47]. This can be partly attributed to the dilution of the optical signal when nano particles are observed. Hence, if the

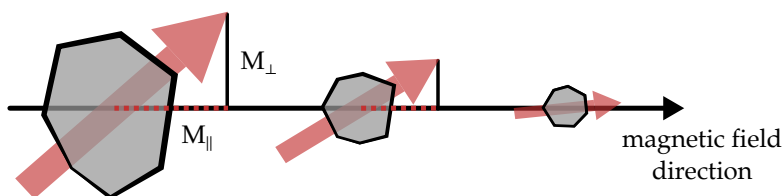


Figure 4.1: The polarity of the magnetization is always positive with respect to the external magnetic field, if the field strength is larger than the coercive field strength.

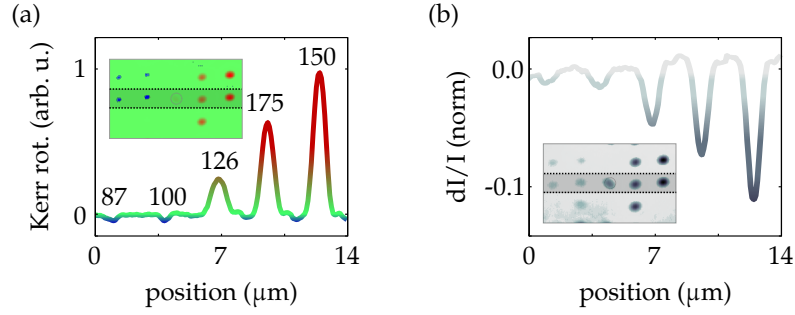


Figure 4.2: **a** Shows the Kerr rotation of nickel disks on a SiO-gold multilayer and **b** shows the corresponding differential intensity. The insets show the corresponding 2D scan of the disk array. From left to right the diameter of the disks increases. The numbers at the peaks denote the disk diameters in nanometers. The line graphs are the averaged horizontal cross sections marked by the shaded rectangle in the inset. The color gradient corresponds to the color map of the 2D scan.

Kerr rotation of a particle is understood merely as a measure of magnetization, the experimental results seem to contradict magnetic theory. Consider for example a ferromagnetic particle in a magnetic field (see fig. 4.1). The external field magnetizes the particle. Possible magnetization anisotropies may prevent us to magnetize the particle completely along the field axis. Nevertheless, if the field strength is larger than the coercive field strength, the parallel component of the magnetization will always be positive with respect to the external magnetic field, independently of the particle size. Yet, we observed sign reversal of the Kerr rotation of single nickel disks with diameters below 120 nm. Figure 4.2a and b show the Kerr rotation and the differential intensity of nickel disks on a gold mirror covered with a 75 nm thick SiO spacer layer. The numbers at the peaks denote the disk radius in nanometers and the inset shows a 2D picture of the disk array. The graph corresponds to the cross sections along the x -axis averaged in the shaded area. As expected, the differential intensity increases with the diameter of the disks. However, at a diameter of around 120 nm the Kerr rotation changes its sign from negative to positive. This indicates that the direct relation of Kerr rotation and magnetization is lost. Lindfors et al. have observed similar contrast reversals in scattering experiments of gold nanostructures on reflecting surfaces[34].

It turns out that this is the result of the interferometric nature of far field particle microscopy. With the methods described in the former chapters we can restore the link between Kerr rotation and magnetization. To show this we investigate in the following the size dependency of nickel disks experimentally and use our model to explain the data. First, we describe in the next section the experimental technique. Then, in sec. 4.2, the magnetic hysteresis and size dependency of the Kerr rotation of single nickel disks is investigated. Finally, in

sec. 4.3 and 4.4 we compare the data to our model to explain the mechanisms of the size dependency.

4.1 CONFOCAL KERR INTERFEROMETER

Typically, Kerr rotation is measured directly using polarization optics. However, if very high precision and sensitivity is required, the phase shift can be determined with interferometers. We performed our measurements with a zero-loop-area Sagnac interferometer described by Xia et al [22]. In contrast to Kerr magnetometers based on polarization optics, Sagnac interferometers reject polarization rotation due to optical activity or birefringence. Additionally, low frequency noise is rejected by a sophisticated modulation scheme. Measurement of the absolute Kerr rotation angle of a magnetized film with microrad resolution is possible [22]. Parts of the following discussion are already covered in greater detail in [48] and repeated here for convenient reading.

4.1.1 *Why Sagnac interferometers?*

This type of common-path interferometer was invented by Georges Sagnac [49]. Its optical path is a loop in which light can propagate in opposite directions. It is especially suited to detect magnetization-induced phase shifts because it is insensitive to phase shifts with time-inversion symmetry, which is most non-magnetic sources of phase shifts. Figure 4.3a shows a sketch of a Sagnac interferometer. The loop is created by a beam splitter. The reflected beam propagates in the loop clockwise, the transmitted beam propagates counter-clockwise. Parasitic phase differences observed in other interferometer types are eliminated because the optical path of both beams is the same except for the propagation direction. The phase shifts due to MOKE and Faraday's effect do depend on the propagation direction and are thus visible in Sagnac interferometers. A transparent sample is put inside the loop as indicated. The quarter-wave-plates are used to make the polarization of the light circular. A second beam splitter is necessary when opaque samples must be investigated in reflection (see for example the works of Dodge et al[50].).

A phase difference is also induced if the interferometer rotates as a whole. The optical path is shortened for the beam that propagates against the rotation and it is elongated for the beam that propagates along with the rotation. The total phase shift depends linearly on the rotation speed and the area A enclosed by the loop. This is used in interferometric fiber gyroscopes to measure absolute rotation speeds. The effective area of these interferometers is made very large by using fibers with lengths of several kilometers, winded in coils. In magnetometry the effective area of the loop must be zero to eliminate phase

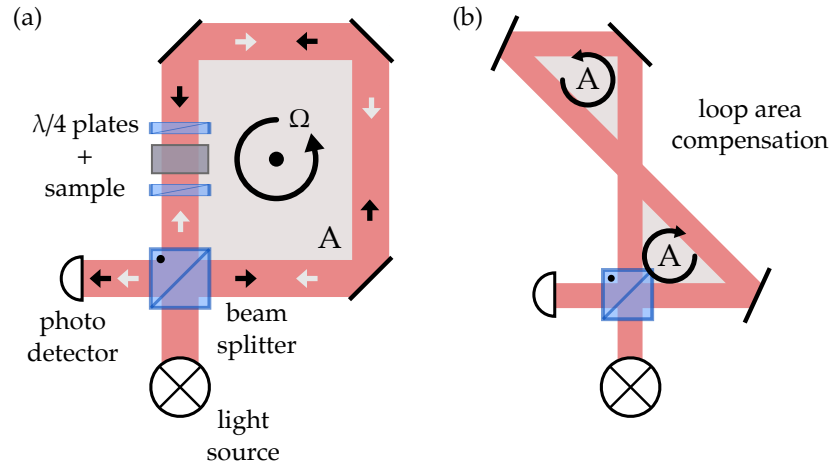


Figure 4.3: A Sagnac interferometer is based on an optical loop in which light can propagate in opposite directions. **a** shows a setup which is sensitive to rotation of the whole setup. The beam circulating with the same handedness as the rotation (black arrows) travels a longer optical path than the other one (white arrows). The path difference is proportional to the area A enclosed by the loop and the rotation frequency ω . A transparent sample can be placed inside the loop. To measure MOKE or Faraday rotation, quarter-wave-plates are used to change into circular polarization. **b** shows a setup that is insensitive to rotations. By forming two loops with opposite handedness, the path difference of the two counter-propagating beams is compensated. The enclosed areas A of the loops must be identical.

shifts due to rotations. This can be done by forming a double loop with the shape of the digit eight (see fig. 4.3b). The exact shape is not important, but the areas of the two loops must be identical. In this case the phase difference acquired in one of the loops is compensated by the other. The principle of zero loop area is also used in our setup, but the implementation is different.

4.1.2 The optical path of the interferometer

We will first describe the optical path of our setup and show that it is an implementation of the zero-area Sagnac interferometer, as illustrated in figure 4.3a. Then we discuss the modulation technique and derive a relation between the detected intensity and Kerr rotation.

Figure 4.4a shows a simplified sketch of the setup with the most important optical elements. The beam passes a polarizer, an electro-optical modulator and a quarter-wave-plate. Afterwards it is reflected from the sample and passes the same optical elements in reversed order. An avalanche photo diode (APD) operated in proportional mode is used to measure the intensity of the returning light.

Figure 4.4b shows that the polarizer splits the incoming beam into orthogonally polarized components and feeds them to distinct optical

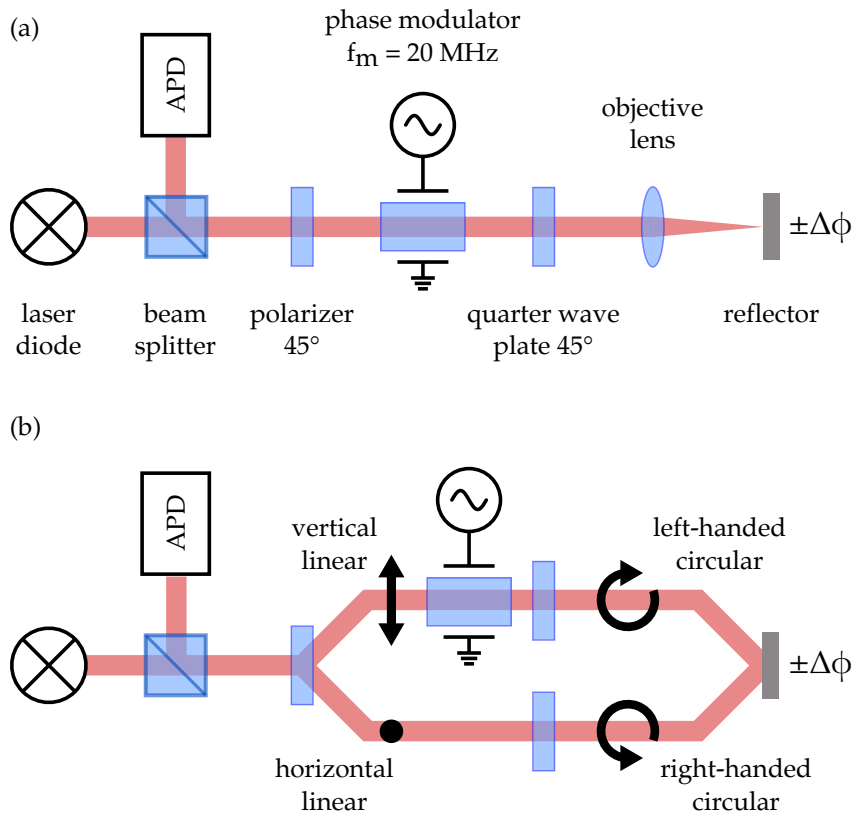


Figure 4.4: Simplified sketch of the Sagnac interferometer. **a** shows the true optical path. **b** emphasizes that the optical path is a loop formed by two orthogonal polarization axes. Two independent beams can travel in opposite direction through the loop. The sample acts as a reflector and is magnetized by an external magnetic field. When the circularly polarized beams hit the reflector, it induces a phase difference proportional to the magnetization. The sign depends on the handedness of the incoming light and is thus opposite for the two beams.

paths. Consider the vertical polarized component. As indicated in the figure, it propagates along the upper path. It passes a high frequency electro-optical modulator which induces a periodic phase shift. The modulator acts on the vertical polarization axis only and its effect is described later in detail. The combination of the wave plate and the reflector forms the return point. It guarantees that the polarization of the light is rotated by 90° : The 45° quarter-wave-plate transforms the vertical polarization to left-handed circular polarization. The handedness flips upon reflection from the sample and the polarization is transformed to horizontal instead of vertical when the wave plate is passed the second time. The beam then returns to the polarizer on the bottom path in figure 4.4b. In this way a loop is formed.

Consider now the horizontal component of the incoming beam. It propagates in the loop in the exact reverse order. Hence, when both beams reach the polarizer again they traveled on the same optical path with opposite propagation direction. In contrast to fig. 4.3, the

vanishing loop area is not achieved by matching counter-oriented loops, but by folding the beam path onto itself. This scheme is easy to implement with fiber optics and much less vulnerable to thermal drifts or vibrations. Single mode fibers can be used to allow only a single optical mode in the loop. This ensures that the beams travel exactly along the same path.

4.1.3 Signal detection and modulation principle

To avoid low frequency noise a phase modulation technique is applied using the electro-optic modulator shown in figure 4.4. We said before that the interferometer is not sensitive to phase shifts with time-reversal symmetry. A static phase shift has thus no effect on the detected signal because both of the counter-propagating beams are shifted. In contrast, a dynamic phase shift on one of the polarization axes within the round-trip time of the loop is not compensated. If there is such a phase shift, the polarization of the returning beam will be slightly elliptical and partly blocked at the polarizer. The detected intensity decreases accordingly. For optical path lengths of a few meters the round-trip time is some hundred nanoseconds, corresponding to frequencies in the MHz-range. We use a resonant electro optical modulator to generate HF phase modulations,

$$\phi_m(t) = \phi_{m,0} \cos \omega_m t \quad . \quad (4.1)$$

The modulation frequency ω_m is matched to the round-trip time of the loop such that the beams reach the modulator with a time difference $T_m/2 = \pi/\omega_m$. Because $\phi_m(t + T_m/2) = -\phi_m(t)$, the phase difference between the returning beams is $2\phi_m(t)$. The polarization of the resulting electric field at the polarizer oscillates periodically between circular and linear states. The intensity transmitted by the polarizer changes accordingly due to partial blocking of the elliptically polarized states.

The detection of Kerr rotation is based on the following statement: *The oscillation of the detected intensity with the modulation frequency ω_m is zero unless there is an additional phase offset ϕ_k due to some magnetized material.* We proof this by calculating the detected intensity with Jones vector calculus. To simplify the abstraction, we switch to an equivalent representation of the setup, shown in figure 4.5. In this representation, we neglect the first half of the optical path and the quarter wave plate. Instead, we consider only the returning, linearly polarized beams. They have a small phase shift $\pm\phi_k$ due to the interaction with the sample. Although in reality the two beams pass the electro-optic modulator at different times and positions in their loops, we can make use of $\phi_m(t + T_m/2) = -\phi_m(t)$ to shift the modulator to the same position in the loop for both beams. The optical path is now symmetric for the two components except for the polarity of the

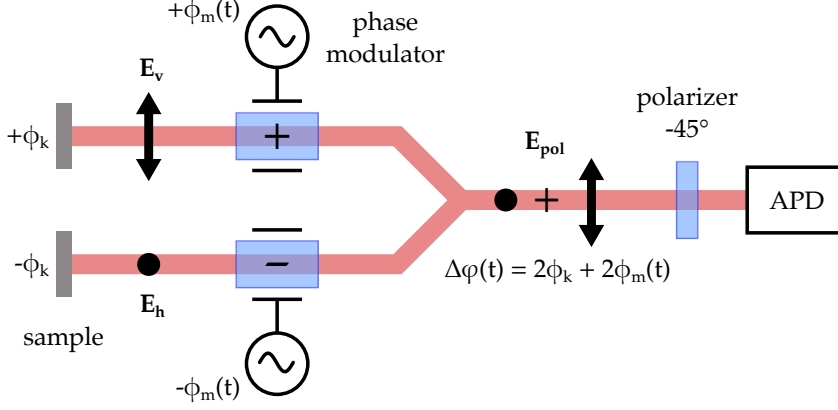


Figure 4.5: This equivalent representation of the setup is used to simplify the calculation of I_{APD} . See text for details. We imagine the two counter-propagating beams in fig. 4.4 as being created at the sample with linear polarization and a small phase shift $\pm\phi_k$ due to MOKE. Both beams are phase shifted by $\pm\phi_m(t)$ using the electro optic modulator before they are superimposed in front of the polarizer. The polarizer projects both components to the same polarization axis. The beam paths are symmetric, but the phase shifts have opposite sign. The total phase shift is $\Delta\phi = 2\phi_k + 2\phi_m(t)$.

phase shifts. When the beams are recombined at the polarizer, the total phase difference is $2\phi(t) = 2\phi_k + 2\phi_m(t)$. The total electric field at the APD is given by

$$\begin{aligned} \mathbf{E}_{\text{APD}}(t) &= \frac{1}{2\sqrt{2}} \cdot \overbrace{\begin{pmatrix} +1 & -1 \\ -1 & +1 \end{pmatrix}}^{J_{\text{pol}}} \cdot \overbrace{\begin{pmatrix} e^{i\phi(t)} \\ -e^{-i\phi(t)} \end{pmatrix}}^{\mathbf{E}_{\text{pol}}} \\ &= \frac{\cos \phi(t)}{\sqrt{2}} \cdot \begin{pmatrix} 1 \\ -1 \end{pmatrix}, \end{aligned} \quad (4.2)$$

where J_{pol} is the Jones matrix of a -45° polarizer and \mathbf{E}_{pol} represents the polarization state of the incoming electric field in terms of its vertical and horizontal component. The complex exponentials introduce the phase difference of $2\phi(t)$ between the counter-propagating beams. The polarizer projects both components of \mathbf{E}_{pol} to the same polarization axis. The intensity is

$$\begin{aligned} I_{\text{APD}}(t) &= \mathbf{E}_{\text{APD}}^\dagger(t) \cdot \mathbf{E}_{\text{APD}}(t) \\ &= \cos^2 \phi(t) \\ &= \frac{1 + \cos 2\phi(t)}{2}. \end{aligned} \quad (4.3)$$

Substituting $\phi(t)$ we then finally have

$$I_{\text{APD}}(t) = \frac{1 + \cos(2\phi_k + 2\phi_{m,0} \cos \omega_m t)}{2}. \quad (4.4)$$

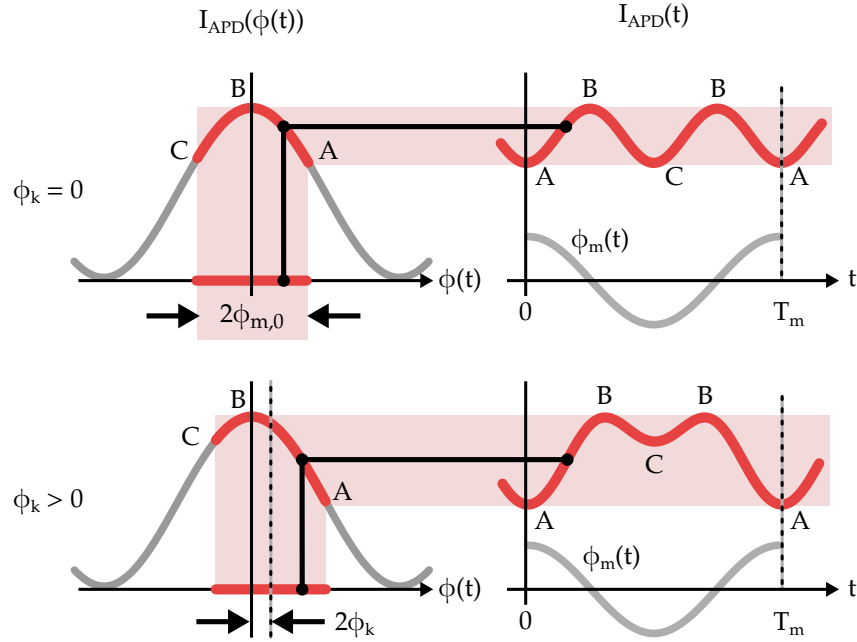


Figure 4.6: This figure illustrates the modulation principle of the Sagnac interferometer. The right part shows the dependency of I_{APD} on the angle $\phi = \phi_k + \phi_m$. The left size shows temporal evolution of I_{APD} if ϕ_m is modulated at a frequency ω_m . In the top row the Kerr rotation angle ϕ_k is zero. In the lower part ϕ_k is finite.

The argument of the cosine function oscillates with period $T_m = 2\pi/\omega_m$ and magnitude $2\phi_{m,0}$ around a constant offset $2\phi_k$. The behavior of I_{APD} is visualized in figure 4.6. The left part shows the intensity I_{APD} as a function of ϕ . The angular interval covered by $\phi(t)$ is marked red on the ϕ -axis. If $\phi_k = 0$, it is symmetric around zero (upper part), otherwise it is shifted by $2\phi_k$ and the symmetry is lost (lower part).

On the right side the corresponding temporal evolution of $I_{APD}(t)$ is shown for a single modulation cycle. If $\phi_k = 0$, the temporal pattern repeats twice per modulation cycle due to the identical heights of the points A ($t = 0$) and C ($t = T_m/2$). Hence the spectral power at frequency $2\omega_m$ is high and at frequency ω_m it is zero.

On the lower row the same is shown for some finite Kerr phase shift $\phi_k > 0$. The range covered by $\phi(t)$ shifts slightly and is no longer symmetric around zero. This lifts the degeneracy between points A and C and the temporal intensity pattern now repeats only once per modulation cycle. The Signal power at frequency $2\omega_m$ drops while at frequency ω_m it rises. Please note that in the figure ϕ_k is of the same order as $\phi_{m,0}$ to make the effect visible. In practice ϕ_k is by a factor of 10^3 or more smaller than $\phi_{m,0}$ and the change of signal power at the second harmonic can be neglected.

Now we show that *the ratio of the signal powers at the two frequencies ω_m and $2\omega_m$ is a measure of the phase shift ϕ_k* . This can be seen easily for small modulation amplitudes if in eq. 4.3 we approximate the cosine up to second order in $\phi(t)$, that is $\cos(\phi(t)) \approx 1 - \phi(t)^2$. Omitting all time-independent factors and using the identity $2 \cos^2 x = 1 + \cos 2x$ we get

$$I_{APD}(t) \approx -\phi_{m,0}^2 \cos(2\omega_m t) - 4\phi_{m,0}\phi_k \cos(\omega_m t) \quad . \quad (4.5)$$

The signal magnitudes at ω_m and $2\omega_m$ are

$$\begin{aligned} I_{1\omega_m} &= 4\phi_{m,0}\phi_k \\ I_{2\omega_m} &= \phi_{m,0}^2 \quad . \end{aligned} \quad (4.6)$$

Taking the ratio of the powers we find a direct correspondence with the Kerr phase shift,

$$\frac{I_{1\omega_m}}{I_{2\omega_m}} = 4 \frac{\phi_k}{\phi_{m,0}} \Rightarrow \phi_k = \frac{\phi_{m,0}}{4} \frac{I_{1\omega_m}}{I_{2\omega_m}} \quad . \quad (4.7)$$

It is important to note that the result does not depend on the total intensity of the detected light, which makes the technique very robust and makes absolute measurements of ϕ_k possible. Assuming shot noise limited operation and $I_{1\omega_m} \ll I_{2\omega_m}$, it turns out that the relative error of the measured Kerr phase shift can be reduced by making the modulation depth $\phi_{m,0}$ large,

$$\frac{\Delta\phi_k}{\phi_k} = \sqrt{I_{1\omega_m}^{-1} + I_{2\omega_m}^{-1}} \approx \sqrt{\frac{1}{4\phi_{m,0}\phi_k}} \quad . \quad (4.8)$$

In this case we have to use the exact result for $I_{APD}(t)$ and extract the signal powers from eq. 4.4 by Fourier transformation,

$$\begin{aligned} I_{1\omega_m} &= \mathcal{F}\{I_{APD}(t)\}(\omega_m) \\ I_{2\omega_m} &= \mathcal{F}\{I_{APD}(t)\}(2\omega_m) \quad . \end{aligned} \quad (4.9)$$

Noticing that all time-dependent terms of eq. 4.4 are of the form $g(t) = A \cos(\beta \cos \omega_m t + \alpha)$, we can use the Jacobi-Anger expansion [51] to get the Fourier transform coefficients at ω_m and $2\omega_m$. The theorem states that (see also appendix A)

$$\mathcal{F}\{g(t)\}(\omega) = -\sqrt{2\pi} \cdot A \cdot \begin{cases} J_1(\beta) \sin(\alpha), & \text{if } \omega = \omega_m \\ J_2(\beta) \cos(\alpha), & \text{if } \omega = 2\omega_m \end{cases} \quad . \quad (4.10)$$

J_1 and J_2 are the Bessel functions of the first kind [51]. Applying the Jacobi-Anger theorem to eq. 4.4 we get

$$\begin{aligned} I_{1\omega_m} &= \sqrt{2\pi} \cdot J_1(2\phi_{m,0}) \sin 2\phi_k \\ I_{2\omega_m} &= \sqrt{2\pi} \cdot J_2(2\phi_{m,0}) \cos 2\phi_k \quad . \end{aligned} \quad (4.11)$$

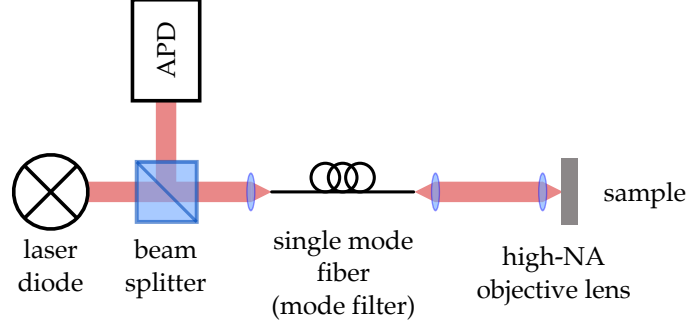


Figure 4.7: The confocal imaging in the Sagnac interferometer is realized using single mode fibers as mode filters.

and eq. 4.7 is replaced by the correct expression for ϕ_k ,

$$\phi_k = \frac{1}{2} \tan^{-1} \left(\frac{J_2(2\phi_{m,0}) I_{1\omega_m}}{J_1(2\phi_{m,0}) I_{2\omega_m}} \right) . \quad (4.12)$$

As before, the total intensity does not need be known to determine ϕ_k . Since in practice $\phi_k \ll \pi$, we can approximate $\tan x \approx x$ to get again a linear relation between $I_{1\omega_m}/I_{2\omega_m}$ and ϕ_k ,

$$\phi_k \approx \frac{1}{2} \frac{J_2(2\phi_{m,0}) I_{1\omega_m}}{J_1(2\phi_{m,0}) I_{2\omega_m}}, \quad \phi_k \ll \pi . \quad (4.13)$$

The signal powers at the two frequencies are measured with lock-in amplifiers that act as high-Q band passes, rejecting noise at other frequencies. The width of the pass band is typically 10-100 Hz which corresponds to a $Q \approx 2M - 200k$ at 20 MHz. Modulation frequencies much lower than 20 MHz are sufficient in principle since typical $1/f^\alpha$ -noise usually is important only up to a few kHz. However, to match the modulation period T_m to the round-trip time of the loop, we have to use frequencies in the MHz range.

4.1.4 Confocal imaging

The interferometer is equipped with a confocal imaging system using single mode fibers as mode filters and a high-NA microscope objective for illumination and imaging of the sample (see fig. 4.7). The sample is mounted on a 3-axes linear stage. The nanostructure on the sample is brought roughly into focus using micrometer screws. Fine adjustment of the working distance and automated scanning of the illuminated spot is achieved using a computer controlled steerable scan mirror in front of the objective and a piezo actuator that moves the objective along the optical axis (not shown in the sketch). The lateral range of the laser scanner is about $100 \times 100 \mu\text{m}^2$. We use a superluminescent diode with a center emission wavelength of 796 nm as

light source. At this wavelength the spatial resolution with a 0.7NA objective is approximately 700 nm.

A typical measurement consists of scanning the laser focus laterally along the sample to get a spatially resolved map of the reflected intensity. For each focus position, the detected signal power is demodulated at frequencies ω_m and $2\omega_m$ and recorded. Figure 4.2 on page 34 shows a typical example of such a scan.

4.2 KERR ROTATION OF A SINGLE NICKEL NANODISK

In the last section we described a confocal Kerr interferometer, enabling us to measure the Kerr rotation of nanoparticles with microrad angular resolution. In this section we first present magnetic hysteresis measurements on single nanodisks in the sub-100 nm regime. Then we analyze the dependency of the Kerr rotation on the disk diameter and use the model described in the last sections to show that the dependency is a purely optical effect.

4.2.1 *Magnetic anisotropy and particle hysteresis*

We use an electro magnet to generate a variable magnetic field for hysteresis measurements. Figure 4.8 shows a sketch of the arrangement. The sample is mounted directly on the pole of the magnet. On the lateral scale of the observed nanostructures the magnetic field can be assumed to be homogeneous. The current in the coils is generated with a voltage controlled power supply driven with a ramp generator at a frequency of 1 mHz. The magnetic field also leaks into the microscope objective which can be used as a field probe by observing its Faraday rotation at non-magnetic spots on the sample.

The hysteresis measurement procedure for a single particle is as follows: The magnetic field is slowly ramped at a rate of approximately $40\mu\text{T/s}$. At the same time the signal powers $I_{1\omega_m}$ and $I_{2\omega_m}$ are measured on the particle itself and additionally at two separate reference spots on the bare, non-magnetic substrate (see fig. 4.9a). In the following these measurement are labeled *sig*, *ref_A* and *ref_B*. The measurements at the different spots are performed in turns (see fig. 4.9b). The integration time at each spot is typical on the order of a few seconds.

The reference signal is due to Faraday rotation in the objective and is therefore a linear function of the magnetic field strength B at the sample. This means that we can use the reference signal as field probe. The calibration factor that relates $I_{1\omega_m}/I_{2\omega_m}$ at the reference spots and the magnetic field B is determined in two steps: First, $I_{1\omega_m}/I_{2\omega_m}$ is measured as a function of the magnet drive voltage. Then the sample is replaced with a Hall probe magnetometer and the magnetic field is also measured as a function of the magnet drive voltage U_{mag} .

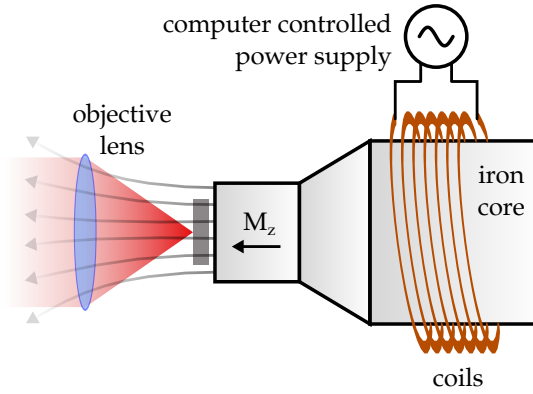


Figure 4.8: Sketch of the experimental arrangement for the measurement of magnetic hysteresis. The magnetic field is generated with an electro magnet and homogeneous on the length scale of the nanostructures. It extends into the objective lens which can be used as a field probe by Faraday’s effect. The current source is driven by a ramp generator.

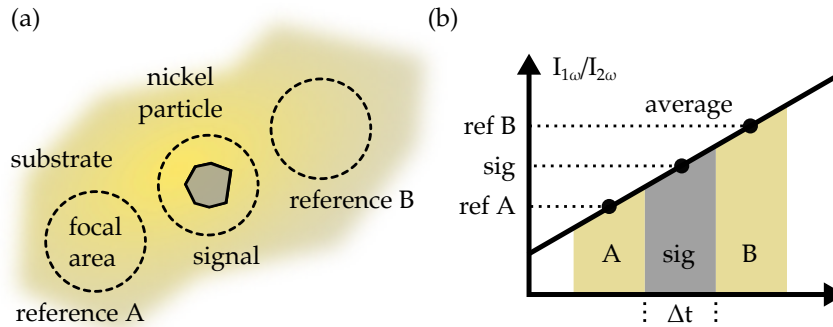


Figure 4.9: **a** Shown is a sketch of the spatial arrangement of the reference and signal measurements to determine the magnetic hysteresis. The reference spots are well separated from the nickel disks. See the text for details. **b** The temporal evolution of a measurement cycle: The magnetic field is ramped linearly and continuously in time. The Kerr signal $I_{1\omega_m}/I_{2\omega_m}$ thus increases. Subsequently the focal spot is switched between point A, the nickel disks and point B. On each position the $I_{1\omega_m}/I_{2\omega_m}$ is averaged over a given time interval.

We can then establish a linear relation between B and the reference signal,

$$B = \frac{\Delta B}{\Delta U_{mag}} \cdot \frac{\Delta U_{mag}}{\Delta ref} \cdot ref + ref_{off} \quad (4.14)$$

where ref_{off} is an offset determined from the reference signal at the extremal electro magnet drive voltages $\pm U_{max}$. Notice that this method has the advantage of being insensitive to the hysteresis of the iron core.

Figure 4.10a shows on the left a typical example of $I_{1\omega_m}/I_{2\omega_m}$ during a linear ramp cycle of the magnet drive voltage. The gray curve

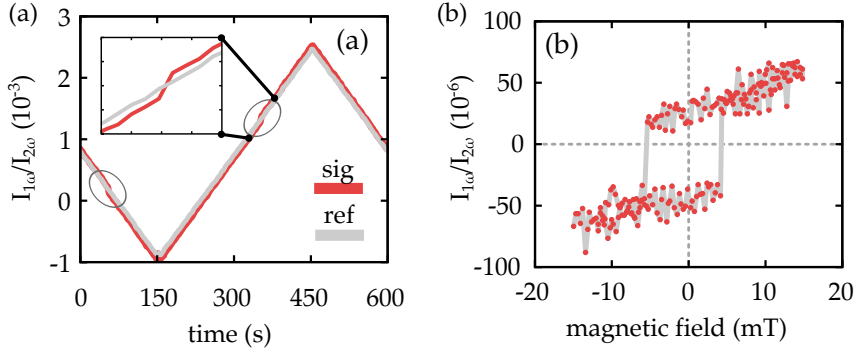


Figure 4.10: **a** shown is the reference and the signal of a complete ramp cycle of the magnetic field during a hysteresis measurement of a single nickel disk. The inset shows the switch point where the magnetization of the nickel disk reverses its sign. **b** From the data on the left graph the hysteresis of the particle is calculated by subtracting the reference from the signal.

is the background level estimated from the average of ref_A and ref_B . The red curve is the on-particle signal level for a nickel disk with a diameter of 90 nm and a height of 27 nm. The substrate is a 100 nm gold layer on SiO_2 . The main contribution to both curves is Faraday rotation of the objective lens which follows the magnetic drive voltage in a linear fashion. The on-particle signal, however, has jumps at certain drive voltages that switch it from below to above the background level and vice versa. At these drive voltages the particle magnetization flips due to the external magnetic field. The inset shows a magnified range around the switch point. The particle hysteresis is extracted by subtracting the background level from the signal level. The result is the particle hysteresis as shown in figure 4.10b. The abrupt switching of the magnetization indicates the existence of only a single magnetic domain. On the other hand the hysteresis is not flat above the switching points, as one would expect of a single domain magnet. This might be due to a slight calibration mismatch for different spots on the sample.

To get a basic understanding of the hysteresis curves, we imagine the nickel disks as spheroids with an uni-axial magnetic anisotropy due to the shape of the magnet. Shape anisotropy is due to reduced magneto-static energy for a certain distribution of magnetic poles on the surface of the magnet. Magnetization along the long axis of the spheroid is preferred. The preferred axis for magnetization is called *easy axis*. Any axis orthogonal to the easy axis is called *hard axis*.

A widely used theory of the magnetization of single domain magnets with uni-axial anisotropy in external magnetic fields is the Stoner-Wohlfarth model [52]. It states that the direction of the magnetization vector is stable if there is no torque acting on it. The torque is calculated from the derivative of the magnetic energy E_{mag} with respect to the orientation of the magnetization vector \mathbf{M} . Fig-

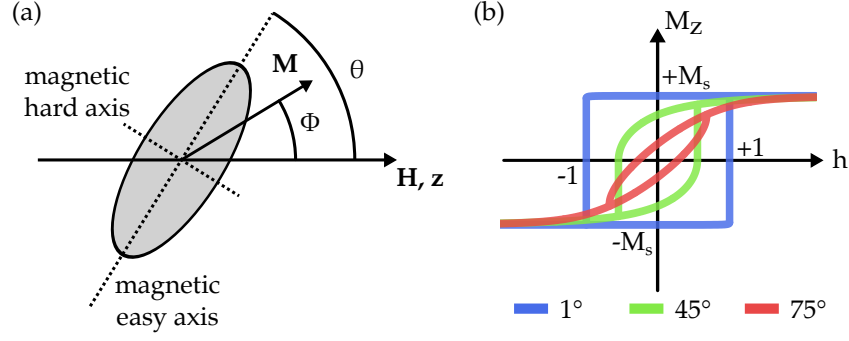


Figure 4.11: **a** The Stoner-Wohlfarth model describes a single domain magnet with a uni-axial magnetic anisotropy. The angle θ is the inclination of the magnetic easy axis and the magnetic field. The angle Φ is the inclination of the magnetization vector \mathbf{M} and the magnetic field axis. **b** shows hysteresis curves of single domain magnets with different orientations θ of the magnetic easy axis, predicted by the Stoner-Wohlfarth model. The corresponding values of θ are shown in the legend. The horizontal axis is the normalized magnetic field strength h as described in the text. The vertical axis shows the z -component of the magnetization.

Figure 4.11a introduces the relevant quantities. The external magnetic field $\mathbf{H} = |\mathbf{H}| \cdot \mathbf{e}_z$ defines the z -axis of the system. The angle between the magnetization vector \mathbf{M} and the z -axis is ϕ . The angle between the easy axis of the magnet and the z -axis is θ . The energy of the system can be expressed in terms of ϕ and θ ,

$$E_{\text{mag}} = K_u V \sin^2(\phi - \theta) - \mu_0 V |\mathbf{M}| |\mathbf{H}| \cos \phi \quad . \quad (4.15)$$

Here $K_u \cdot V$ is the energy contribution due to the magnetic anisotropy for a magnet with volume V , and $\mu_0 V |\mathbf{M}| |\mathbf{H}|$ is the energy contribution due to the interaction of the magnetic moment and the external field. μ_0 is the vacuum permeability. Note that for single domain magnets $|\mathbf{M}| = M_s$. Defining a normalized field strength $h = \mu_0 |\mathbf{M}| |\mathbf{H}| / 2K_u$ and a normalized magneto-static energy $\eta = E / 2K_u V$, eq. 4.15 can be rewritten,

$$\eta = \frac{1}{2} \sin^2(\phi - \theta) - h_0 \cos \phi \quad . \quad (4.16)$$

At a stable equilibrium orientation of the magnetization the first derivative of the energy with respect to ϕ is zero while the second derivative is positive,

$$\frac{d\eta}{d\phi} = \frac{1}{2} \sin(2\phi - 2\theta) + h \sin \phi = 0 \quad , \quad (4.17)$$

$$\frac{d^2\eta}{d\phi^2} = \cos(2\phi - 2\theta) - h \cos \phi > 0 \quad . \quad (4.18)$$

For a given angle θ of the easy axis, we calculate h from eq. 4.17,

$$h(\phi) = -\frac{1}{2} \frac{\sin(2\phi - 2\theta)}{\sin \phi} \quad , \quad (4.19)$$

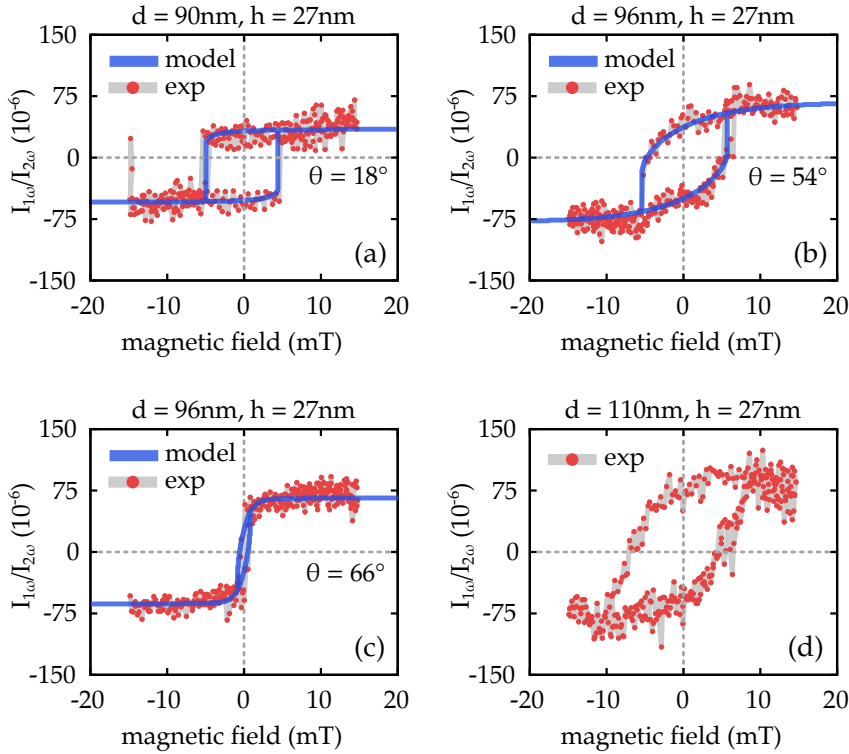


Figure 4.12: Magnetic hysteresis measurements of different nickel disks. The diameter and height of each disk is denoted in the figure title. To each the Stoner-Wohlfarth model was fitted by tuning the angle of the magnetic soft axis θ . The hysteresis of figure d is not described by the model.

subject to the constraint equation 4.18. By plotting $h(\phi)$ against the z-component of the magnetization, $M_z = |\mathbf{M}| \cdot \cos \phi$ we get the hysteresis curves of the single domain magnet. Figure 4.11b shows calculated hysteresis curves of a single domain magnet for different angles of the easy magnetic axis. The magnetization is always aligned parallel to the field axis if the magnetic easy axis and the magnetic field axis fall together. For $|h| \leq 1$ there is two solutions ϕ_{\pm} that fulfill equation 4.18. In this case the particle shows a magnetic hysteresis. For $|h| > 1$ only one stable orientation exists. If the easy axis is tilted, the region with two stable solutions shrinks until at $\theta = \pi/2$ there is only one stable solution for all magnetic field magnitudes. The particles show no hysteresis in this case.

We fit the Stoner-Wohlfarth model to the measured hysteresis by adjusting the tilt angle θ of the easy axis and finding appropriate values for the saturation magnetization M_s (in units of the Kerr rotation) and the anisotropy constant K_u . The choice of the anisotropy constant and the saturation magnetization effectively scales the normalized magnetic field axis, $H = \frac{2K_u}{\mu_0 M_s} h = \alpha h$. α can be deduced from the experimentally measured magnetic field H_{flip} at which the

magnetization of the particle flips. By definition, $h = 1$ at the flip point, so $H_{\text{flip}} = \frac{2K_u}{\mu_0 M_s} = \alpha$.

Using α , we can compare the anisotropy parameters K_u of two particles,

$$\frac{\alpha_1}{\alpha_2} = \frac{K_{u,1} M_{s,2}}{K_{u,2} M_{s,1}} . \quad (4.20)$$

Figure 4.12 shows a collection of hysteresis curves for a number of particles. The particles were positioned close together to ensure comparable field strength. Subfigures 4.12a to c show the hysteresis of four particles of similar size. Nevertheless, we observe quite diverse behavior. Table 4.1 collects the scale factors and tilt angles used to adapt the model to the measured hysteresis. The saturation magnetizations are of the same order.

Particle	α (arb. u.)	M_s (arb. u.)	θ (deg)
(a)	8	40	18
(b)	10.5	75	54
(c)	1	65	66

Table 4.1: The parameters used to fit the Stoner-Wohlfarth model to the hysteresis curves in fig. 4.12a to c.

Using eq. 4.20 we can estimate the difference in the magnetic anisotropy, for example for particles (b) and (c) we have

$$\frac{\alpha_b}{\alpha_c} = \frac{K_{u,b} M_{s,c}}{K_{u,c} M_{s,b}} \Rightarrow 10.5 = \frac{K_{u,b} 65}{K_{u,c} 75} \Rightarrow K_{u,b} \approx 12 K_{u,c} . \quad (4.21)$$

The comparable low shape anisotropy of particle C corresponds to the observed low coercive field strength and indicates a rather sphere-like shape. Particles A and B have similar anisotropy constants. However, the magnetic easy axis of particle B seems to be tilted, resulting in the gradually decreasing magnetization before it flips completely. The tilt of the easy axis may be a result of a distortion of the particle shape or rupture of the particle during the lift-off process. The hysteresis curves shown in figs. 4.12a to c is in contrast to the hysteresis curve shown in figure 4.12d, which belongs to a nickel disk with 110 nm diameter (red). The height is the same as for the other particles. The 110 nm disk shows a hysteresis, but lacks a switching point, showing that it is not a single domain state.

The analysis emphasizes the importance of single particle measurements to discriminate the properties of nominally similar structures. This is helpful for the optimization of manufacturing processes and, in combination with other measurement techniques, allows the direct relation of cause and effect of various observed properties. In an ensemble measurement, these relations would be averaged out.

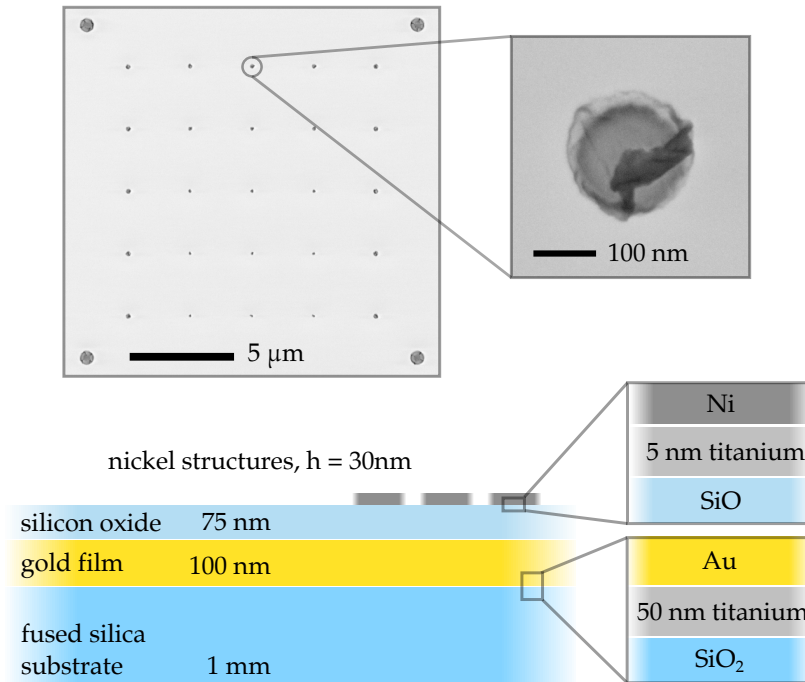


Figure 4.13: Sketch of the sample structure. A 50 nm thick titanium adhesion layer and an opaque gold film of 100 nm is evaporated onto a fused silica substrate. In a second step, a silicon oxide layer is evaporated. Finally, nickel structures are written to the top of the silicon oxide in a standard electron beam lithography procedure. Titanium is again used for better adhesion of nickel to the silicon oxide. On the top of the figure, SEM images of the fabricated disk arrays are shown.

4.2.2 Size dependency of the magneto-optic effect

We have seen that far-field Kerr microscopy is a potential technique, enabling magnetic hysteresis measurements on the single particle level. But the information is intermixed with the optical properties of the investigated object. One of the most crucial parameters that determine these properties is the particle shape and its size. We indicated already in the introduction, that the Kerr rotation of a nickel nanodisk does reverse its sign if their diameter drops below some threshold even though the magnetization of a nanoparticle is aligned along the external magnetic field. In this section we show details of this experiment and present experimental data on the size dependency of the Kerr rotation. Afterwards we show that the data can be explained with the model that was developed in the last chapter.

The sign change of the Kerr rotation was observed with nickel disks on a multilayer reflector. To analyze this behavior we fabricated arrays of disks with diameters between 50 nm and 200 nm on a multilayer structure made from a gold mirror and a 75 nm silicon oxide spacer layer.

A schematic sketch of the sample structure is depicted in the lower part of figure 4.13. The individual layers were created by thermal evaporation. To increase the adhesion between the gold film and fused silica and between the nickel and silicon oxide we used layers of titanium. We chose titanium as adhesion layer because the standard choice for this procedure, chromium, is known to show anti-ferromagnetic behavior[53]. Titanium is a diamagnet. In general we chose diamagnetic metals to exclude possible ferromagnetic interactions with nickel. The nickel disks were fabricated with electron beam lithography. The solubility of a resist layer (PMMA) is changed locally with a focused electron beam. At the exposed areas the resist is removed with a solvent. Afterwards nickel is evaporated on top of the structured resist. It covers both, the remaining resist film and the holes created by the solvent. Afterwards the remaining resist is removed with another solvent, taking with it all the nickel on top. Only the nickel in the former holes is left on the surface. This process is called lift-off.

The fabricated nickel nanostructures were checked and characterized using scanning electron microscopy (SEM). The upper part of fig. 4.13 shows an typical overview of a disk array recorded with SEM. In the corners large markers were written for orientation. The central three rows are nickel disks with decreasing diameter (from top to bottom). The distance between the individual disks is $3\mu\text{m}$, which is larger than the optical resolution of our confocal microscope. The inset shows a zoom on one of the marker disks with a diameter of 200 nm. It can be seen that the quality of the disks is not very good. Until now no procedure was found to produce reliably high quality nickel disks using EBL. Most often the disks are simply ripped off the surface or ruptured during lift-off as can be seen in the inset. A considerable amount of fencing[54] is seen, even though a secondary resist was used to prevent this. Additionally, SiO tends to build up tension if large areas of the SiO_2 substrate are covered with it. Often the complete film will disrupt and get opaque when the sample is mounted or otherwise strained. We therefore tried other materials as spacer layer such as PC403, which is a photo-polymer that can be spin-coated. However, thickness control is limited with spin-coating and it turns out that the sample quality is worse. The best approach is to evaporate the SiO only to small parts of the substrate, leaving free any part that touches the sample holder.

The SEM measurements must be done after the optical measurements because the samples are contaminated with carbon that changes the optical properties. We post-select the optical measurements that were performed on destroyed disks and exclude them from further evaluation.

The height of the silicon oxide spacer was controlled by evaporating at a constant rate for a certain time. By covering parts of the

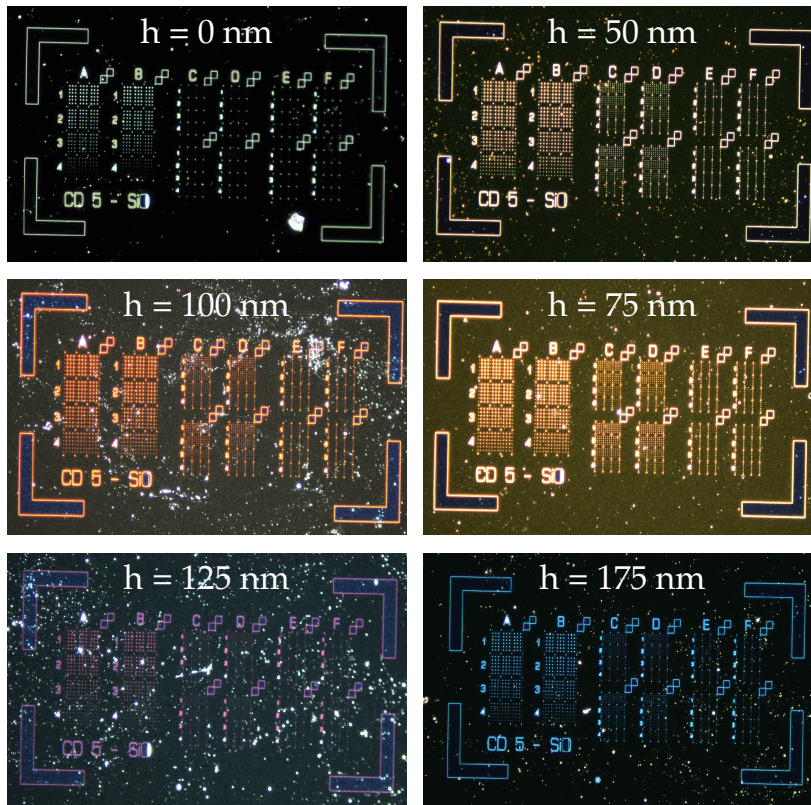


Figure 4.14: Darkfield microscope images of the sample structure on different spacer layer heights. The height is denoted in nanometers on each image.

substrate while evaporating the silicon oxide and moving the cover after specified time intervals, several layers of different height can be realized on one sample. The nickel structures are then written to the particular areas on the substrate. Figure 4.14 shows dark-field microscopy images of such structures that were written to areas with different spacer layer heights. The height of the layer is denoted on each image. Note how the color of the scattered light changes with the spacer layer height.

The disks were driven into magnetic saturation with a permanent magnetic field of 0.5 T. Confocal maps of the Kerr rotation and the intensity contrast were recorded with the setup described in section 4.1. To determine the dependency of the Kerr rotation and the intensity contrast on the disk diameter, nearby disks were scanned while keeping the magnetic field and the optical configuration constant. A typical scan of an array was shown in fig. 4.2.

With the current setup, an absolute measurement of the Kerr rotation is not possible due to the Faraday rotation of the microscope objective. The Kerr rotation of a nickel disk is therefore understood relative to the background, at positions where no magnetic material is present on the sample surface. The same is true for the intensity

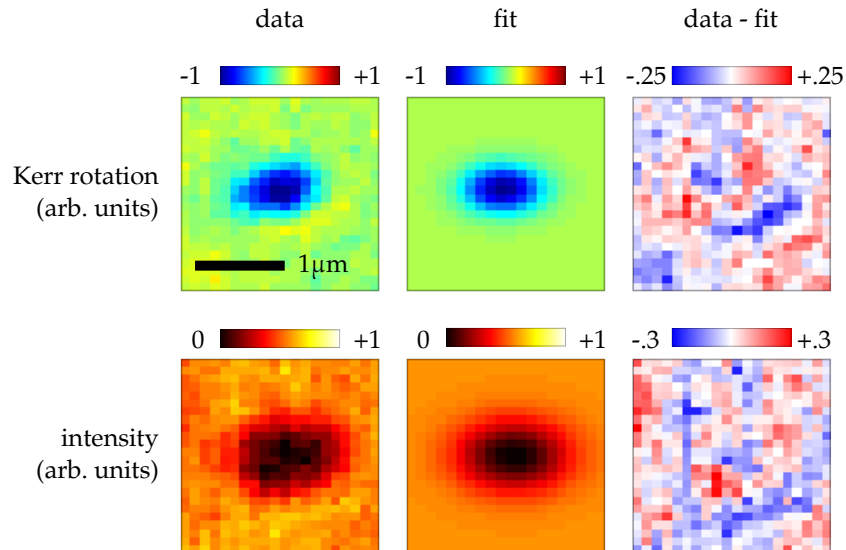


Figure 4.15: This figure shows on the left measured Kerr rotation maps and intensity maps of a 90 nm nickel disk. The color maps are normalized to the maximum for comparison. In the middle the fitted Gaussians are shown. On the right the residuals, data - fit, are shown.

signal. In what follows we will always consider the contrast with respect to the background next to the particle. The signature of a disk in a 2D scan is a Gaussian since the particles are much smaller than the spot size.

To get the Kerr rotation of an individual disk, the relevant section of a 2D scan is first offset corrected and detrended. Then a Gaussian is fitted to the peak. Its amplitude is taken to be the Kerr rotation of the disk. The same procedure is applied to the intensity map. Figure 4.15 shows the different steps of the analysis. On the left we see the Kerr rotation map and the intensity map of a 90 nm nickel disk. In the middle, the fitted Gaussian is shown and on the right the difference of the data and the fit is shown. In general, the intensity signature is very well fitted by a Gaussian. The Kerr rotation map often shows features that deviate from a Gaussian. A possible explanation is a slight misalignment of the two circular polarized beams.

The sensitivity to Kerr rotation of the setup itself is in the microrad range and much smaller than the signal due to the particles. Main sources of error are the particle shape and size. Nominally the particles should be disks, but the SEM images reveal that their real shape may differ significantly from disks and therefore they may have significantly different optical properties. Because the particles are not round we cannot determine their effective diameter from the lateral extensions. In this case it is not clear what the diameter of the particle should be if it is elliptical or bend. We use the surface area A_s of the

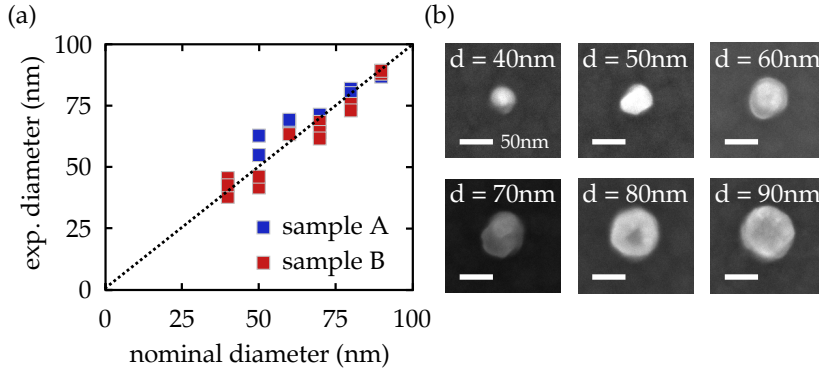


Figure 4.16: **a** Shown is the diameter of nickel disks as determined by scanning electron microscopy against the nominal diameter. Not shown are larger disks for which the deviation is negligible ($d > 100$ nm). Blue and red markers refer to different samples. **b** Shows scanning electron microscopy images of nickel disks of various diameter. Note how the shape gets irregular when the disks get smaller.

particle in the SEM images and define the radius of the particle to be that of a disk with the same surface area,

$$r_{\text{disk}} = \sqrt{\frac{A_s}{\pi}} \quad (4.22)$$

Figure 4.16 shows on the right a comparison of the nominal radius of the disks as specified by the lithography design and the radius as measured by SEM and equation 4.22. The measurements were taken from two different samples and the measurements corresponding to one or the other sample are marked in different colors. Especially for smaller disks the spread is high. With increasing diameter the spread gets smaller, because the surface-to-circumference ratio increases. Above 100 nm the difference between the nominal diameter and the real diameter is negligible. On the left side some examples of measured disks are shown. Nominally large disks are indeed round. The smaller the particle, the more irregular the shape is.

We measured the Kerr rotation of disks with diameters between 40 nm and 180 nm. Only one sample provided high enough quality to measure the Kerr rotation in this size regime. Figure 4.17 shows the corresponding scans. We see that the sign of the Kerr rotation flips at a disk diameter of 100 nm. The intensity drops monotonically and does not show a sign flip.

To extract the Kerr rotation and intensity signal strength we apply the method described above. The diameters of the disk are determined from the corresponding SEM images. Figure 4.18a and b show the Kerr rotation and the intensity with respect to the experimentally determined diameter. We applied logarithmic scale to make the signal evolution for small diameters better visible.

In figure 4.18c and d we plotted the same data as in a and b, but this time only the absolute values and in double logarithmic represen-

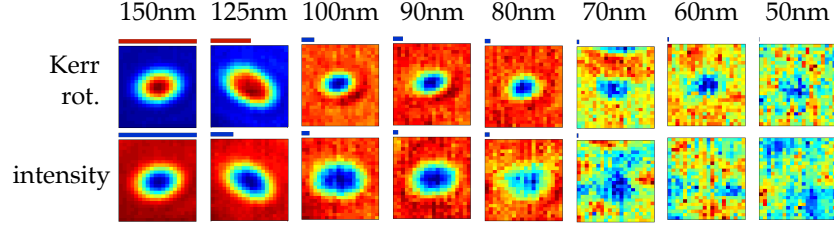


Figure 4.17: Shown are Kerr rotation maps and intensity maps of nickel disks on a reflector with a 75 nm silicon oxide spacer and gold mirror. The top row shows the Kerr rotation and the lower row shows the reflected intensity. The bars on top of the figures indicate the relative signal strength, normed to the largest disk. The color indicates positive (red) and negative sign (blue).

tation. We see that the Kerr rotation and the intensity actually follow the same power law, which corresponds roughly to the diameter to the fourth power ($m = 4.4$), that is, the volume squared. This indicates that in this size regime pure scattering is dominating the optical signal and that the interference term discussed in the last chapters plays a minor role (it goes roughly linearly with the volume). Interestingly, the sign change of the Kerr rotation can be tracked down to be an interference effect, related to the change of the scattering phase of the disks with increasing disk diameter. This we will see in the following sections where we apply the model developed in the first chapter to our experiment. The next step is to develop a connection between the electric fields E_s and E_r that we can describe with our model, and the Kerr rotation signal $I_{1\omega_m}/I_{2\omega_m}$ that we measure with our setup.

4.3 ADAPTION OF THE MODEL TO THE SETUP

We have seen in section 4.1 that for a homogeneous magnetization within the focal spot, a direct relation between the Kerr rotation angle and $I_{1\omega_m}/I_{2\omega_m}$ may be established:

$$\frac{I_{1\omega_m}}{I_{2\omega_m}} = \frac{J_1(2\phi_m)}{J_2(2\phi_m)} \cdot \tan(2\phi_k) \quad . \quad (4.23)$$

ϕ_m is a well known constant and no sample related quantity enters the expression. We can indeed say that $I_{1\omega_m}/I_{2\omega_m}$ is the Kerr rotation due to the magnetized film at this position. If, on the other hand, a particle smaller than the focal spot area is observed, only part of the incident light interacts with the particle. The signal at the 1st harmonic frequency is diluted and the direct correspondence between $I_{1\omega_m}/I_{2\omega_m}$ and the Kerr rotation of the particle is lost.

We derive now an expression for $I_{1\omega_m}/I_{2\omega_m}$ that includes the signal dilution. We use the model described in the former chapters to

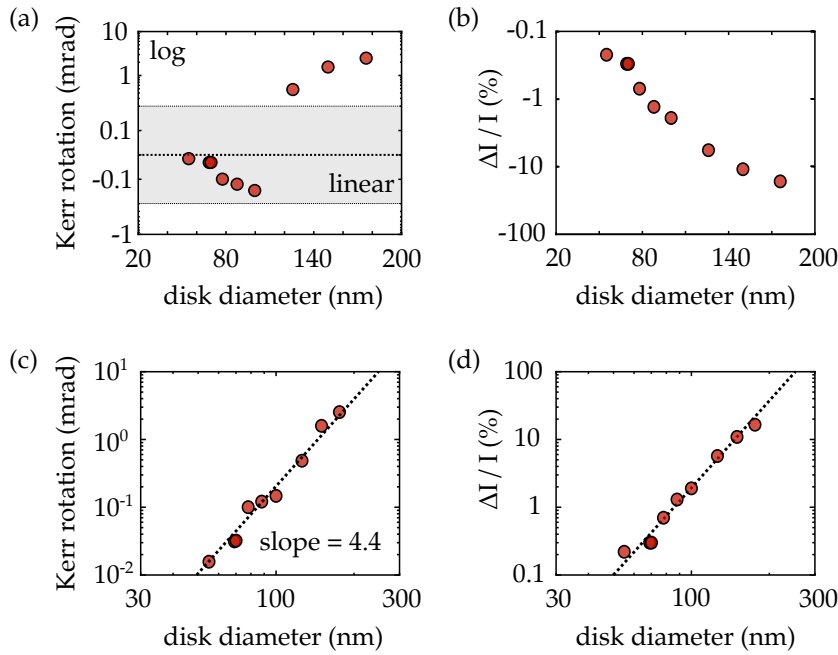


Figure 4.18: **a** Shown is the Kerr rotation of single nickel disks on a reflector made from gold and a 75 nm silicon oxide layer. Large signal amplitudes are plotted in log-scale for better visibility. **b** Shown is the corresponding intensity of the same disks. The largest disks show approximately 20% intensity drop. In **c** and **d** the absolute values of graphs **a** and **b** are shown respectively in a double logarithmic fashion. The dashed line is a guide to the eye and indicates a slope of 4.40 and is the same in both graphs.

calculate the electric field reflected by the sample. We have to perform the following steps:

- represent the electric field coming from the sample as the superposition of a component interacting with magnetized material and a background component left unchanged
- apply Jones formalism to describe the propagation through optical elements of the setup
- perform a Fourier analysis of the detected intensity to get the power at the first and second harmonic of the modulation frequency

Figure 4.19 shows a schematic sketch of the relevant optical components. The electric field coming from the sample is composed of orthogonally polarized components named E_v and E_h . They represent the two light beams traveling in the Sagnac interferometer in opposite directions and interact with the sample independently. Each is a coherent superposition of scattered and reflected light. Only the scattered part interacts with magnetized material. Before reaching the

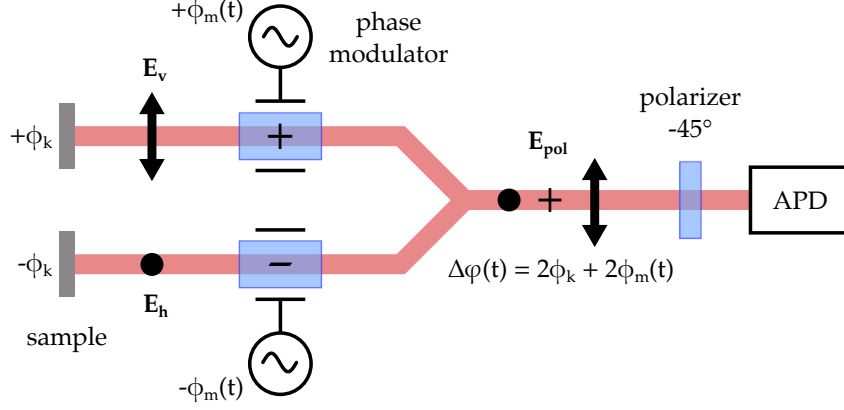


Figure 4.19: This equivalent representation of the setup is used to simplify the calculation of I_{APD} . See text for details. We imagine the two beams counter-propagating in the Sagnac-interferometer (review fig. 4.4) as being created at the sample with linear polarization and a small phase shift $\pm\phi_k$ due to MOKE. Additionally, the beams acquire a phase shift of $\pm\phi_m(t)$ due to the electro-optic modulator. The polarizer projects both components to the same polarization axis. The beam paths are symmetric, but the phase shifts have opposite sign. The total phase shift is $\Delta\phi = 2\phi_k + 2\phi_m(t)$.

photo diode the two beams are projected to the same polarization axis so that they can interfere.

The expression of $E_{v,h}$ is our starting point:

$$E_{v,h} = \pm [\mathbf{E}_r + \mathbf{E}_s \cdot e^{\pm i\phi_k}] \cdot e^{\pm i\phi_m(t)} \cdot \mathbf{e}_{v,h} \quad , \quad (4.24)$$

where $\mathbf{e}_{v,h}$ correspond to the Jones vectors of horizontal and vertical polarization. The field \mathbf{E}_s describes light that interacts with the magnetized particle. It is phase shifted by Kerr's effect, hence the multiplication with the phasor $\exp(\pm i\phi_k)$. The field \mathbf{E}_r does not interact with the magnetized part of the sample. Another phasor $\exp(i\phi_m(t))$ is applied to take the periodic phase modulation of the beams into account. The phase shift ϕ_k is of opposite sign for the vertical and horizontal component, as is the phase shift $\phi_m(t) = \phi_{m,0} \cos \omega_m t$ due to the electro-optic modulation. Additionally, the horizontal component undergoes a phase shift of 180° under reflection by the sample. We assumed that the reflection and scattering coefficients are the same for both polarizations except for Kerr's effect. This is true in theory due to the symmetry of the structure but may not hold true in practice.

The projection of $E_{v,h}$ by the -45° -polarizer may be expressed using the Jones matrix

$$J_{pol} = \begin{pmatrix} +1 & -1 \\ -1 & +1 \end{pmatrix} \quad , \quad (4.25)$$

so we have

$$\begin{aligned}\mathbf{E}_{\text{APD}} &= \mathbf{J}_{\text{pol}} \cdot (\mathbf{E}_{\text{v}} + \mathbf{E}_{\text{h}}) \\ &= 2 \cdot [\mathbf{E}_{\text{r}} \cos \phi_{\text{m}}(t) + \mathbf{E}_{\text{s}} \cos(\phi_{\text{k}} + \phi_{\text{m}}(t))] \cdot (\mathbf{e}_{\text{v}} - \mathbf{e}_{\text{h}}).\end{aligned}\quad (4.26)$$

The detected intensity I_{det} is

$$\begin{aligned}I_{\text{det}}(t) &= \mathbf{E}_{\text{APD}}^* \cdot \mathbf{E}_{\text{APD}} \\ &= 4 [|\mathbf{E}_{\text{r}}|^2 \cos^2 \phi_{\text{m}}(t) + |\mathbf{E}_{\text{s}}|^2 \cos^2(\phi_{\text{k}} + \phi_{\text{m}}(t)) \\ &\quad + 2\Re\{\mathbf{E}_{\text{r}}\mathbf{E}_{\text{s}}^*\} \cos \phi_{\text{m}}(t) \cos(\phi_{\text{k}} + \phi_{\text{m}}(t))].\end{aligned}\quad (4.27)$$

\mathbf{E}^* denotes complex conjugation and transposition. In the next step we use the trigonometric identities $2 \cos(x) \cos(y) = \cos(x+y) + \cos(x-y)$ and $2 \cos^2 x = 1 + \cos(2x)$ to simplify the result. Additionally we omit any term constant in time as we are interested in the signal power at high frequencies only. To indicate this we use the label I_{AC} instead of I_{det} ,

$$\begin{aligned}I_{\text{AC}}(t) &= 2|\mathbf{E}_{\text{r}}|^2 \cos 2\phi_{\text{m}}(t) + 2|\mathbf{E}_{\text{s}}|^2 \cos(2\phi_{\text{k}} + 2\phi_{\text{m}}(t)) \\ &\quad + 4\Re\{\mathbf{E}_{\text{r}}\mathbf{E}_{\text{s}}^*\} \cos(\phi_{\text{k}} + 2\phi_{\text{m}}(t)).\end{aligned}\quad (4.28)$$

Using the Jacobi-Anger theorem again (review eq. 4.10, page 41) we get

$$\begin{aligned}I_{1\omega_{\text{m}}} &= -2\pi|\mathbf{E}_{\text{s}}|^2 J_1(2\phi_{\text{m},0}) \sin 2\phi_{\text{k}} \\ &\quad - 4\pi\Re\{\mathbf{E}_{\text{r}}\mathbf{E}_{\text{s}}^*\} J_1(2\phi_{\text{m},0}) \sin \phi_{\text{k}},\end{aligned}\quad (4.29)$$

$$\begin{aligned}I_{2\omega_{\text{m}}} &= -2\pi|\mathbf{E}_{\text{r}}|^2 J_2(2\phi_{\text{m},0}) - 2\pi|\mathbf{E}_{\text{s}}|^2 J_2(2\phi_{\text{m},0}) \cos 2\phi_{\text{k}} \\ &\quad - 4\pi\Re\{\mathbf{E}_{\text{r}}\mathbf{E}_{\text{s}}^*\} J_2(2\phi_{\text{m},0}) \cos \phi_{\text{k}}.\end{aligned}\quad (4.30)$$

It can be seen that $I_{1\omega_{\text{m}}} \rightarrow 0$ if $|\phi_{\text{k}}| \rightarrow 0$, as expected. The signal power has an interferometric signature $\Re\{\mathbf{E}_{\text{r}}\mathbf{E}_{\text{s}}^*\}$ at both frequencies. For $I_{1\omega_{\text{m}}}/I_{2\omega_{\text{m}}}$ we have

$$\frac{I_{1\omega_{\text{m}}}}{I_{2\omega_{\text{m}}}} = \frac{J_1(2\phi_{\text{m},0})}{J_2(2\phi_{\text{m},0})} \cdot \frac{|\mathbf{E}_{\text{s}}|^2 \sin 2\phi_{\text{k}} + 2\Re\{\mathbf{E}_{\text{r}}\mathbf{E}_{\text{s}}^*\} \sin \phi_{\text{k}}}{|\mathbf{E}_{\text{r}}|^2 + |\mathbf{E}_{\text{s}}|^2 \cos 2\phi_{\text{k}} + 2\Re\{\mathbf{E}_{\text{r}}\mathbf{E}_{\text{s}}^*\} \cos \phi_{\text{k}}}.\quad (4.31)$$

For $|\mathbf{E}_{\text{r}}| \rightarrow 0$ the result simplifies to eq. 4.23 as it should. For small Kerr rotation angles $\phi_{\text{k}} \ll \pi$ we may apply approximations, namely $2 \sin \phi_{\text{k}} \approx \sin 2\phi_{\text{k}}$ and $1 \approx \cos \phi_{\text{k}} \approx \cos 2\phi_{\text{k}}$. This yields an expression that allows for a very intuitive interpretation of the signal dilution,

$$\frac{I_{1\omega_{\text{m}}}}{I_{2\omega_{\text{m}}}} = \frac{J_1(2\phi_{\text{m},0})}{J_2(2\phi_{\text{m},0})} \cdot \tan 2\phi_{\text{k}} \cdot \frac{|\mathbf{E}_{\text{s}}|^2 + \Re\{\mathbf{E}_{\text{r}}\mathbf{E}_{\text{s}}^*\}}{|\mathbf{E}_{\text{r}}|^2 + |\mathbf{E}_{\text{s}}|^2 + 2\Re\{\mathbf{E}_{\text{r}}\mathbf{E}_{\text{s}}^*\}},\quad (4.32)$$

The result corresponds to eq. 4.23, except for the last product term. It describes the dilution of Kerr's effect in terms of the optical properties of the sample alone. Equation 4.32 states that the ratio $I_{1\omega_{\text{m}}}/I_{2\omega_{\text{m}}}$ expected for a particle is by a factor

$$\Delta_{\text{opt}} = \frac{|\mathbf{E}_{\text{s}}|^2 + \Re\{\mathbf{E}_{\text{r}}\mathbf{E}_{\text{s}}^*\}}{|\mathbf{E}_{\text{r}}|^2 + |\mathbf{E}_{\text{s}}|^2 + 2\Re\{\mathbf{E}_{\text{r}}\mathbf{E}_{\text{s}}^*\}}\quad (4.33)$$

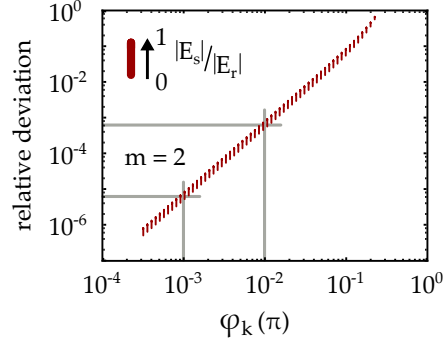


Figure 4.20: Relative deviation of eq. 4.31 and 4.32 with respect to the Kerr rotation angle ϕ_k . The red bars mark the variation when the magnitude of E_s is increased from 10^{-3} to E_r .

smaller compared to that of the bulk material, assuming that the phase shift due to the magnetized material is the same. We can use the model developed in chapter 3 to calculate Δ_{opt} for our experimental arrangement. This allows the prediction of the signal detected with the confocal Sagnac interferometer.

LIMITS OF THE SMALL ANGLE APPROXIMATION The deviation of eq. 4.32 from eq. 4.31 increases with the Kerr rotation angle ϕ_k . Figure 4.20 shows the normed difference of the full and approximated form,

$$\frac{|I_{1\omega_m}/I_{2\omega_m} - I_{1\omega_m}/I_{2\omega_m \text{ approx}}|}{|I_{1\omega_m}/I_{2\omega_m}| + |I_{1\omega_m}/I_{2\omega_m \text{ approx}}|}, \quad (4.34)$$

in dependency of ϕ_k on a double-logarithmic scale. The deviation also depends on the ratio of $|E_r|$ and $|E_s|$ as is indicated by a vertical bar. However, this dependency is negligible. The slope indicates that the deviation increases quadratically with ϕ_k . The Kerr rotation of the structures investigated by us is 10 mrad or less. In this range the deviation is on the order of 10^{-4} to 10^{-3} , which is below the resolution limit of the setup.

4.4 COMPARISON OF EXPERIMENTAL DATA AND THE MODEL

With the modification described in the last section we are able to simulate the Kerr rotation and the intensity contrast detected with the Sagnac interferometer. We will first compare the data with the model, ignoring the forward scattered light. In the second step we will take the forward scattering and specular reflections into account and again compare the model prediction with the data.

The equations that are fitted to the data are eq. 4.30 and eq. 4.32. The expression for $I_{1\omega_m}/I_{2\omega_m}$ is taken directly because it is background free,

$$\frac{I_{1\omega_m}}{I_{2\omega_m}} = \frac{J_1(2\phi_{m,0})}{J_2(2\phi_{m,0})} \cdot \tan 2\phi_k \cdot \frac{|\mathbf{E}_s|^2 + \Re\{\mathbf{E}_r \mathbf{E}_s^*\}}{|\mathbf{E}_r|^2 + |\mathbf{E}_s|^2 + 2\Re\{\mathbf{E}_r \mathbf{E}_s^*\}} \quad (4.35)$$

The intensity at the second harmonic $I_{2\omega_m}$ always has an offset due to the mirror reflection. Since the data is offset corrected we fit to it the difference $\Delta I_{2\omega_m} = I_{2\omega_m} - I_{2\omega_m}^0$, where $I_{2\omega_m}^0$ is the second harmonic signal strength without the particle, $\mathbf{E}_s \rightarrow 0$. That is,

$$\begin{aligned} \Delta I_{2\omega_m} &= I_{2\omega_m} - I_{2\omega_m}^0 \\ &= 2\pi \cdot J_2(2\phi_{m,0}) [|\mathbf{E}_r|^2 + |\mathbf{E}_s|^2 + 2\Re\{\mathbf{E}_r \mathbf{E}_s^*\}] - \\ &\quad - 2\pi \cdot J_2(2\phi_{m,0}) |\mathbf{E}_r^0|^2 \quad . \end{aligned} \quad (4.36)$$

\mathbf{E}_r^0 is the reference field when no particle is present ($\sigma \rightarrow 0$).

When the forward scattered light and specular reflections are ignored, \mathbf{E}_r and \mathbf{E}_s are given by eq. 3.24 and 3.23 (see page 27 in section 3.3),

$$\mathbf{E}_r = \sqrt{1 - \alpha} \cdot \rho_L \cdot \exp\left(-\frac{\pi}{2}\right) \cdot \mathbf{E}_{in} \quad , \quad (4.37)$$

$$\mathbf{E}_s = \sigma \cdot \mathbf{E}_{in} \quad , \quad (4.38)$$

and the reference field without particle reads

$$\mathbf{E}_r^0 = \rho_L \cdot \exp\left(-\frac{\pi}{2}\right) \cdot \mathbf{E}_{in} \quad . \quad (4.39)$$

The reflection coefficient ρ_L of the multilayer is given by eq. 2.11, page 16. The shadow factor α is given by eq. 3.17, page 25. The scattering amplitude σ of disks with the experimentally measured diameters is determined by interpolation of the FEM simulations, see section 2.2.

The fit parameters of the model are the amplitude \mathbf{E}_{in} of the incident field and the Kerr rotation angle ϕ_k . ϕ_k is assumed to have the same value for all disk diameters. This is reasonable since it was shown that the saturation magnetization of nanocrystals is approximately constant in this size regime[55, 56]. Exceptions may be the largest particles observed by us. They show a strong anisotropy, the easy axis being within the disk plane. With our electro magnet, which delivers a maximum field strength of 20 mT at the sample, we were not able to saturate disks larger than 120 nm. However, in this experiment a permanent magnet was used with a field strength of 500 mT at the sample.

The waist of the Gaussian beam – used to calculate α – can be determined theoretically from the numerical aperture of the objective used during the measurements or experimentally from the intensity profile

of a small particle. We use a microscope objective with a numerical aperture of $NA = 0.65$. The theoretical beam waist is[42]

$$w_0 = \frac{\lambda}{\pi \cdot NA} = \frac{800 \text{ nm}}{\pi \cdot 0.65} \approx 392 \text{ nm} \quad .$$

Based on fitting a Gaussian $\exp(-2\rho^2/w_0^2)$ to the intensity profiles of five different particles we find a larger experimental beam waist of

$$w_0^{\text{exp}} = (540 \pm 20) \text{ nm} \quad .$$

We use its nominal value of 75 nm for the height of the silicon oxide spacer layer. The other quantities necessary to calculate ρ_L are the refractive indexes of gold and silicon oxide. They are taken from the literature [30, 57] and are $n_{Au} = 0.15 + 4.9i$ and $n_{SiO} = 1.93$ at a wavelength of 800 nm.

We use the method of least squares to fit the data to the model. Both the Kerr rotation and the intensity are a strong function of the disk diameter, rising approximately with the forth power. The data thus spreads over several orders of magnitude. We use logarithmic scaling to guarantee that the fit converges to the data not only for large disks. A probabilistic optimizer is used to minimize the residuals

$$R_{I_{2\omega_m}} = \sum (\ln(\Delta I_{2\omega_m})^{\text{exp}} - \ln(\Delta I_{2\omega_m})^{\text{theo}})^2 \quad , \quad (4.40)$$

$$R_{K_{err}} = \sum (\ln(\Delta I_{1\omega_m}/I_{2\omega_m})^{\text{exp}} - \ln(\Delta I_{1\omega_m}/I_{2\omega_m})^{\text{theo}})^2 \quad . \quad (4.41)$$

Figure 4.21 compares the results of three different fit configurations, termed A, B and C. Fit A uses the theoretical value for the beam waist, $w_0 = 394 \text{ nm}$. Fit B allows the beam waist to be optimized within the experimental bounds $w_0 = (540 \pm 40) \text{ nm}$. Fit C allows both the beam waist and the spacer layer thickness to be optimized freely. For each configuration the optimization is repeated a hundred times to get a statistical distribution of the optimized fit parameter values. In the figure, the results of all runs are plotted on top of each other with a high level of transparency. The color density thus gives a feeling of the distribution of the individual runs. The spread of the distribution of course increases with the number of fit parameters. Table 4.2 shows a summary of the fit parameter values. They are the average values of the different runs. The bound is an estimate taken from the standard deviation of the distribution.

The Kerr rotation is fitted by all configurations comparably well. Significant differences we find at the intensity contrast. Fit B has the highest deviation from the data. Fit A is better and the data is fit best when the layer thickness and the beam waist are free parameters. Note, however, that the optimized value for the layer height corresponds to the nominal value. It is mainly the much smaller value of

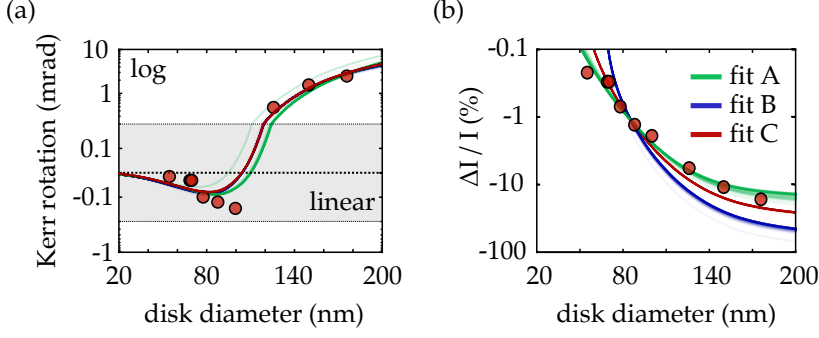


Figure 4.21: **a** and **b** show the fit results for $I_{1\omega_m}/I_{2\omega_m}$ and $I_{2\omega_m}$ when specular reflections are ignored. Fits A, B and C refer to different fit configurations as described in the text.

Fit	$h_{\text{SiO}}(\text{nm})$	$w_0(\text{nm})$	$\phi_k(\text{mrad})$	$ \mathbf{E}_{\text{in}} ^2(\text{arb.u.})$
A	75 (f)	394 (f)	-15 ± 1	$(14 \pm 1) \cdot 10^{-3}$
B	75 (f)	521 ± 2	-15 ± 1	$(31 \pm 2) \cdot 10^{-3}$
C	76 ± 1.2	279 ± 18	-13 ± 1	$(6 \pm 1) \cdot 10^{-3}$

Table 4.2: Optimized fit parameter values for the fit configurations A, B and C. The suffix (f) denotes that the parameter is fixed to this value. The error range corresponds to the standard deviation of 100 fit runs.

the beam waist that leads to a better fitting. The optimal value is considerably smaller than the theoretical and experimentally measured one. This is equivalent to a larger shadow factor and indicates that the particle obstructs the incident beam stronger than estimated. The results supports the assumption that the method used to determine the shadow factor may not be suited for our nanoscale system.

Now we like to include also specular reflections and the forward scattered light. We switch to the complete expression for the scattered electric field,

$$\begin{aligned} \mathbf{E}_r &= (1 - \alpha) \cdot \rho_L \cdot \exp\left(-\frac{\pi}{2}\right) \cdot \mathbf{E}_{\text{in}} \quad , \\ \mathbf{E}_s &= \left(1 + \rho \cdot \sqrt{1 - \alpha}\right)^2 \cdot \boldsymbol{\sigma} \cdot \mathbf{E}_{\text{in}} \quad . \end{aligned} \quad (3.20 \text{ revisited})$$

Figure 4.22 shows the fit results with multiple scattering and specular reflections for three fit configurations. Fit D uses the nominal spacer layer height of 75 nm and a free beam waist. Although there is good agreement for the intensity contrast, the Kerr rotation does not agree with the model. The model does only agree well with the data if the spacer layer thickness is left a free parameter. This is the case for fit E and fit F. In fit E the beam waist is left a free fit parameter. In fit F it is restricted to the experimental bounds. Both fit the data comparably well, but both converge only for spacer layer heights of about 20 nm, which is considerably smaller than the nominal value of 75 nm.

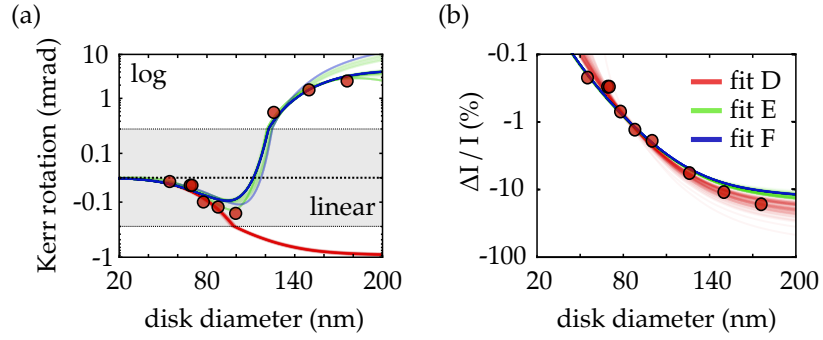


Figure 4.22: **a** and **b** show the fit results for $I_{1\omega_m}/I_{2\omega_m}$ and $I_{2\omega_m}$, including specular reflections. Fit D, E, and F refer to different fit configurations as described in the text.

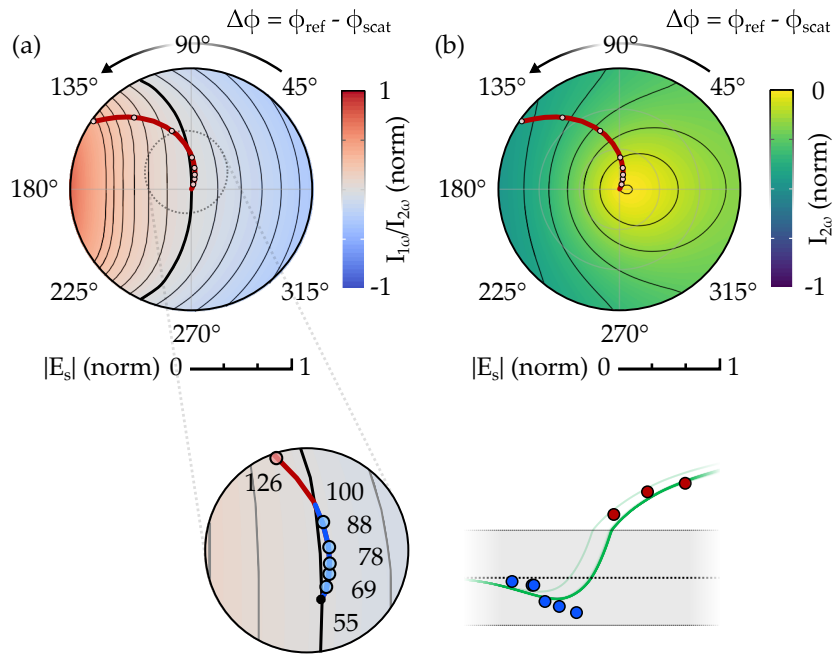


Figure 4.23: **a** and **b** show the polar diagrams of $I_{1\omega_m}/I_{2\omega_m}$ and $I_{2\omega_m}$. The azimuthal axis corresponds to the phase difference $\Delta\phi = \phi_{ref} - \phi_{scat}$. The radial axis corresponds to $|E_s|$. Marked in red is the path on which the intensity evolves with increasing disk diameter when a spacer height of 76 nm is used. The dots indicate where the disks observed in experiment are located. The inset shows a zoom of the polar diagram and the cut along the marked path for comparison.

We can use the optimized parameter values to predict the interferometer response when other spacer layer heights are used. We set $\omega_0 = 279$ nm, $\phi_k = -13$ mrad and $|E_{in}|^2 = 6 \cdot 10^{-3}$. The spacer layer height we tune from 0 to 300 nm and calculate $I_{2\omega_m}$ and $I_{1\omega_m}/I_{2\omega_m}$. Figures 4.23a and b show the resulting polar diagrams of $I_{1\omega_m}/I_{2\omega_m}$ and $I_{2\omega_m}$. The radial axis corresponds to the magnitude

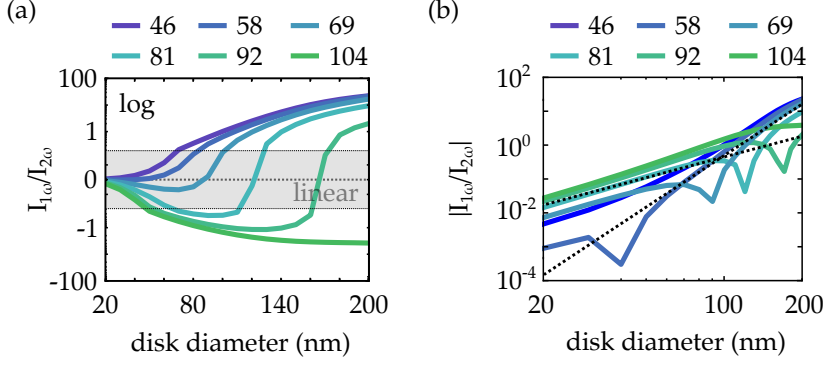


Figure 4.24: **a** Shown is the evolution of $I_{1\omega_m}/I_{2\omega_m}$ with the disk diameters for different spacer layer thicknesses. The height of the spacer layer for each curve is denoted above the graph in units of nanometers. **b** The absolute values of the curves in the right graph in a double logarithmic scale. The slope of the curves is two for small diameters. The offset does change with the spacer layer height according to eq. 4.35.

of the scattered field, $|\mathbf{E}_s|$. The azimuthal axis is the phase difference $\Delta\phi = \phi_{\text{ref}} - \phi_{\text{scat}}$. The color scale of both plots is normalized. The red curve marks the path with a fixed spacer layer height of 76 nm and increasing disk diameter. The dots on the path mark the radial position that corresponds to the experimental diameters. The inset at the bottom is a zoom to the center area. The diameters of the disks are denoted in nanometers next to the dots.

The model predicts correctly the experimentally observed sign reversal of $I_{1\omega_m}/I_{2\omega_m}$. We see that it is indeed related to the phase difference between \mathbf{E}_r and \mathbf{E}_s . The sign of $I_{1\omega_m}/I_{2\omega_m}$ changes because $\Delta\phi$ increases with the diameter of the disks and at some point the zero line is crossed. It is a purely optical effect (remember that in the model ϕ_k is assumed to be constant for each diameter). The diameter at which the sign reversal occurs can be controlled with the spacer layer thickness. Figure 4.24a shows the predicted evolution of $I_{1\omega_m}/I_{2\omega_m}$ for a number of different spacer layer heights. The actual heights are denoted in the legend in units of nanometers. With increasing height of the spacer layer the diameter, at which the sign flip occurs, increases. This is because the phase difference decreases and the curved path marked in red in fig. 4.23 rotates clockwise.

Figure 4.24b shows the absolute value of $I_{1\omega_m}/I_{2\omega_m}$. Note that the slope of all curves is approximately two before the sign flip occurs. In this region we can neglect the pure scattering term in eq. 4.35. This is in contrast to our experimental data which shows a much larger slope of 4.4 also for smaller particles. Once again this could be due to inaccurate model of the shadow factor, which is the only quantity that may change the scaling of the interference term.

SUMMARY AND CONCLUSION

We showed that we can use the interferometric nature of confocal transmission experiments to our advantage, taking control of the phase difference of the contributing electric field with a multilayer substrate. The multilayer structure can be as simple as a dielectric spacer on top of a mirror, its height determining the phase difference between light reflected by the mirror and light scattered by the nanoobject on top of the dielectric.

A major part of the text discussed how the electric fields returning from the sample upon illumination with a Gaussian beam can be computed. The intermediate character of the involved length scales, that is to say, the sizes of the disks relative to the wavelength and laser spot and the distance between the particle and the interfaces of the multilayer substrate, requires simulation of the complete sample structure with a numerical solver. Nevertheless, we developed an ansatz that treats the multilayer structure and the particle separately, allowing great flexibility considering the tools used to compute the optical responses. The reflectivity of the multilayer structure is calculated with a simple T-matrix approach. The nanodisks are treated using a numerical FEM solver, but depending on the geometry, other tools such as Mie theory can be used. The results of the separate computations are combined by superposition, weighting each electric field to take into account the shadow of the particle and second-order scattering processes.

Given this model, we demonstrated that a multilayer reflector does allow for a tweaking of the phase difference only, if the light scattered by the particle in forward direction (towards the mirror), is blocked to a large extent by shadowing. This is equivalent to ignore the forward scattered light and second order scattering processes. Otherwise the efficiency of the method is heavily reduced due to destructive interference of the forward scattered light and the backward scattered light. Comparison of the model prediction and measurements of the Kerr rotation of single nickel nanodisks indicates that multiple scattering and the forward scattered light is indeed negligible. Why this is the case remains an open question and subject of further investigations.

Additionally, the model was used to extract the magnetization of a single, magnetized nickel disks on top of a dielectric layer by observing the change of the overall intensity returning from the sample. The intensity change is due to the phase shift of light scattered by a magnetized object. However, when observing nanoparticles, the intensity does also change with its geometry, orientation and size. Us-

ing our model we showed that it is possible to distinguish between these different contributions and extract the true magnetization. In this context it was possible to show that the saturation magnetization of nickel disks is essentially constant for diameter-to-height ratios between 2 and 8.

Additionally, we were able to record the magnetic hysteresis of single nickel nanodisks. A comparison with the Stoner-Wohlfarth model indicates single domain magnetization. From the hysteresis we are able to deduce the saturation magnetization and the orientation of the easy axis. Our technique, combined with the model and the multilayer substrate, may open a new possibility to study single nanomagnets using simple far-field optical microscopy.

Part II

DYNAMICS AND COHERENT CONTROL OF
QUANTUM EMITTERS

INTRODUCTION

If the optics of a nanoobject cannot be explained by classical theories but only with quantum mechanics, we speak of a quantum emitter. In contrast to classical emitters, the state spectrum of a quantum emitter may be discrete. As a consequence, it is often possible to restrict optical transitions in the system to a single pair of quantum states. This involves an important advantage: We can model the physics of such an emitter with a very basic and well-understood conceptual quantum system, the two-level-system. Those are the sound theoretical basis of a number of today's technologies such as spin resonance techniques, single photon sources[58, 59] or the upcoming concept of quantum information processing[3, 4, 60, 61].

Atoms and molecules can function as two-level-systems, but with advances in fabrication technology on the nanoscale, artificial two-level-systems can be build, for example, in the form of semiconductor quantum dots. These are small bits of a low-band-gap semiconductor embedded in a high-band-gap host semiconductor[62, 63]. Within the quantum dot, electrons and holes can be trapped, the spatial confinement of the wavefunction leading to the formation of discrete states necessary for two-level-systems. These structures have advantages over atoms. Being embedded within a host material, they are chemically stable and no special measures are necessary to hold them in place. They have many degrees of freedom regarding their properties and can be designed to fit particular needs[62].

Within the context of quantum information processing, the dynamics of the quantum dot state are of particular importance. The protocols used in quantum information theory involve preparation of a particular state of a two-level-system and a subsequent sequence of manipulations[64]. While all this happens, the information stored in the quantum state is subject to the degrading interaction with the host material. Eventually the information is read. Preparation and manipulation of the quantum dot state are done using short optical pulses[65, 66], which at the same time provide temporal resolution necessary to operate on the two-level-system before the information stored within it degrades. Our task, and the topic of this part of the thesis, is to develop the experimental tools to perform these operations and measurements, and to develop the connection to the theoretical models we have of the emitters and their interaction with light.

Of the experimental tools, we have recently demonstrated [1, 2] transient pump-probe spectroscopy and coherent control of a single self-assembled quantum dot with a non-invasive, far-field spec-

troscopy technique. In chapter 7 we show, based on the experimental data, that the self-assembled quantum dots we use behave like two-level-systems, and establish the link between the dynamics of the quantum dot state and the optical spectra of scattered laser pulses as observed in the experiment. This allows us to characterize and quantify the properties of the quantum dots, required to successively improve their performance. In this context, we also show that a major deviation of our quantum dots from the theory of two-level-systems, stretched Rabi cycles, can be attributed to the creation of a photo carrier cloud close to the dot.

With a future transition from single emitters to emitter networks in mind, we study in chapter 8 a special type of emitter network, namely an ensemble of randomly distributed semiconductor quantum dots. It has been shown[67] that delocalized states exist within such ensembles, that is to say, states that indeed spread over a kind of network. We study the influence of the local distribution of eigenenergies on the network quantum states and show that, depending on the correlation between the eigenenergies of neighboring emitters, sub-networks can form in the ensemble. This gives first hints on how such networks can be made by manipulating the local energy landscape.

To realize this vision, the quality and properties of the emitters must be improved successively and step-by-step. To increase the options we have in studying single quantum emitters, we plan to integrate a continuous-wave laser spectroscopy experiment into our setup. We require a design that allows maximum flexibility in sample design. In particular, we require that it is not necessary to change the sample structures in order to perform measurements in the setup. This is also the main challenge: Single emitter spectroscopy usually demands for modulation techniques that suppress noise and these often require modification of the sample structure. For example Stark-shift modulation of the exciton resonances of single quantum dots was successful implemented [68, 69], but requires electrodes close to the quantum dots to provide the electric field. To prevent such modification, we investigate in chapter 9 four different approaches for a modulation technique that imposes as few restrictions on the sample design as possible. We show that spatial modulation of the sample position is the most promising route to go, presenting also preliminary experimental data on single emitter measurements.

TRANSIENT SPECTROSCOPY OF SINGLE SEMICONDUCTOR QUANTUM DOTS

Mimicking two-level-systems well, quantum dot excitons can take the role of qubits, the basic element of quantum information processing. In this context, we investigate how the state of a semiconductor quantum dot exciton can be controlled and evaluated on ultrafast timescales with pulsed laser light. The general scheme of such processes is always the same: The quantum state of a dot is prepared or manipulated with one or several subsequent light pulses. Between the pulses, the state is allowed to evolve freely. Aside from manipulating the quantum dot, the pulses carry information about it to the outside world and can be used to deduce the state, for example by observing the absorption spectrum.

We have recently demonstrated coherent control of single self-assembled GaAs/AlGaAs quantum dots with far-field pump-probe spectroscopy [70]. In this chapter we describe the formalism used to establish the connection between the theory of the dynamics of the so-called V-atom, which is a special type of three-level-system, and the scattering spectra observed in the experiment. Not only is this important to understand and predict the dynamics of a V-atom when it is excited with a certain pulse sequence, but also it is necessary to deduce unknown parameters of the real sample from the experimental data, such as relaxation rates of coherence and the excited states.

The outline of this chapter is as follows: In section 7.1 we first introduce the Hamiltonian and the density matrix of a V-atom that is excited by a classical optical field and develop a convenient representation of its dynamics. Then the formalism is used to reproduce a number of test cases that have been investigated experimentally with the transient pump-probe setup described in [70], namely absorption bleaching, perturbed induction decay (both in sec. 7.1.5), and quantum beating (sec. 7.1.6). The test cases show that the quantum dots we use act close to theory. For each test case we discuss the dynamics that are associated with characteristic signatures found in the experimental data. In section 7.2 we discuss the power dependence of absorption bleaching. The quantum dots we use show a significant deviation of the observed Rabi cycles from theory. By including into the model of our system a DC-electric field induced by photo carriers, we show that the deviation can be qualitatively traced back to a modification of the optical properties of the emitter via Stark's effect.

The text at hand focuses on the the main contribution of the author, which is the theoretical reproduction, analysis and interpretation of

the measured data. Although the author contributed significantly to the experimental work discussed in the following, the data recording and the implementation of the optical setup was mainly done by our former PhD student Christian Wolpert. He covers in his thesis [70] the measurement technique, sample fabrication, and the experimental realization of the test cases named above. The measured data presented here is understood to originate from close collaboration with Christian Wolpert and we introduce only those parts that are necessary to understand the text.

7.1 DYNAMICS OF THE V-ATOM UNDER PULSED EXCITATION

Transient pump-probe experiments are a versatile tool to study the dynamics of single quantum emitters and, in particular, their coherent interaction with light pulses. In contrast to continuous-wave irradiation, light pulses allow us manipulate the quantum dot in restricted time windows, much shorter than typical relaxation processes within the dot. Additionally, complex pulse sequences allow us not only to study the quantum dots, but also to control the interaction of the dot with subsequent pulses and by that implement protocols, to be used for example in quantum information processing devices. In order to achieve this, we must know in detail how the internal dynamics of the quantum dot translate to experimentally observable properties. In this section we study the dynamics of a special type of three-level-system, the V-atom or V-level-system, under pulsed excitation and how the dynamics translate to scattering spectra recorded with a spectrometer. In the V-atom, the upper two levels have nearly the same energy and a direct transition between them is forbidden. Excitation transfer is mediated via the ground state. This is the case for the dots we use, motivating the choice of the V-atom in our studies.

The self-assembled GaAs/AlGaAs-quantum dots we use were designed and prepared in the group of Oliver G. Schmidt in Dresden [71]. Their structure is sketched in figure 7.1a. The lower AlGaAs-barrier, sitting on a GaAs substrate, contains nano-holes that are filled by growing a GaAs wetting layer on top. The filled holes form the quantum dots. Then follows the upper AlGaAs-barrier, the thickness of which can be chosen to be about 30-100 nm. A GaAs-capping layer prevents oxidation of the AlGaAs. The shape of the quantum dots resembles one half of a heavily oblate ellipsoid. The extension along the growth direction (z-axis) is about 3 nm. The extension in the sample plane (x- and y-axis) is about 60 nm. The formalism that describes the formation of excitons in such dots is presented in great detail by Bayer et al. in [72]: We can define four neutral exciton states from the combination of the single particle spin eigenstates of the electron ($S_z = \pm 1/2$) and the hole ($J_{h,z} = \pm 3/2$) caught in the dot. Two of the combinations have angular momentum z-projections $|J_{ex,z}| = 2$,

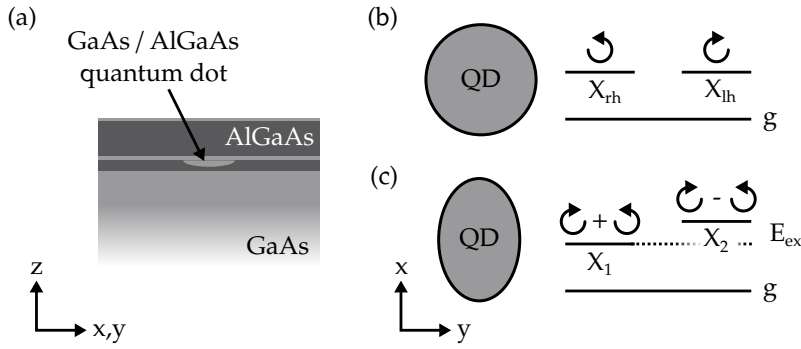


Figure 7.1: This figure illustrates the formation of excitons with linear selection rules in the used quantum dots. **a** shows the semiconductor heterostructure in which the quantum dots are embedded. The substrate is made from GaAs. Then comes a 10 nm thick AlGaAs layer which forms the lower barrier. It is fabricated such that it contains circular dips, which are covered with a GaAs wetting layer. The filled dips form the actual quantum dot. The upper barrier is again made from AlGaAs. Another thin GaAs capping layer prevents oxidation. **b** shows the level scheme of the bright excitons in a circular quantum dot, termed X_{lh} and X_{rh} . They couple to circularly polarized light of left and right handedness respectively. **c** In an elliptical dot, X_{lh} and X_{rh} are coupled via exchange interaction. They hybridize to form new eigenstates X_1 and X_2 , which couple to light polarized along the long and the short axis of the ellipsis.

hence do not couple to the optical field and are called dark excitons. They take no part in the further discussions. The other two combinations yield $J_{ex,z} = \pm 1$, hence couple to circularly polarized light of left and right handedness respectively. They are called bright excitons, labeled X_{lh} and X_{rh} .

The excitons are subject to exchange interaction[72]. If the quantum dot is circular (see fig. 7.1b), X_{lh} and X_{rh} are degenerate eigenstates of the exchange Hamiltonian, but if the quantum dot is elliptically (see fig. 7.1c), X_{lh} and X_{rh} couple and hybridize. The new eigenstates, termed X_1 and X_2 , are the symmetric superpositions $(X_{lh} \pm X_{rh})/\sqrt{2}$. The spin z-projection of the hybridized excitons is $J_{ex,z} = 0$, hence they couple to light polarized linearly along the two axes of the ellipsis. Their energy differs by the exchange energy, which is about $50 - 150 \mu\text{eV}$ in our quantum dots.

With X_1 and X_2 , the transition dipoles $\vec{\mu}_1$ and $\vec{\mu}_2$ are associated. The dipoles are oriented orthogonal to each other along the two axes of the ellipsis formed by the quantum dot boundary. They are excited by – and emit into – orthogonally linearly polarized optical modes.

Figure 7.2 shows a simplified sketch of the experiment. The quantum dot is illuminated with two orthogonally polarized, pulsed laser beams derived from the same light source. The beams, called pump beam and probe beam, are delayed with respect to each other by a time Δt_p . Δt_p is controlled by us and may assume positive and nega-

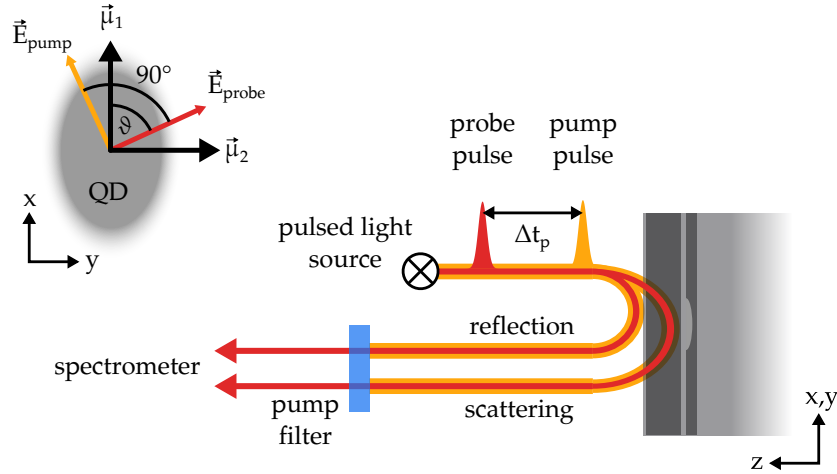


Figure 7.2: The figure illustrates the principle of a transient pump-probe measurement as described in the text. In the lower part of the figure, the beam path and the sample structure is sketched. In the upper left part the orientations of the optical polarization of the pump beam and the probe beam relative to the exciton dipole moments are shown.

tive values, determining the pulse order. When reaching the sample, part of the light is reflected from the sample surface, and another part is scattered back by the quantum dot. Both parts are detected with a spectrometer. The pump beam is blocked with a polarization filter before reaching the spectrometer. This and the polarization is the only principal distinction between the pump beam and the probe beam. The axes of the dipole moments and the axes of the pulse polarization make an angle of ϑ , as shown by the inset in the upper left corner of figure 7.2. The choice of ϑ is free to us and defines the type of experiment that we like to carry out. If $\vartheta = 0, \pi/2, \dots$, then each of the incident beams interacts with only one of the excitons. If $\vartheta = \pm\pi/4$, then each beam interacts with both excitons.

In the next subsection we introduce the formalism to describe the dynamics of a V-atom excited in this way. It is based on the density operator approach. Its dynamics is covered by the Von-Neumann equation.

7.1.1 Von-Neumann equation of a V-atom

The formalism used to describe the dynamics has two ingredients: The first one is the abstraction of a quantum dot interacting with a classical light field, described by a Hamiltonian. The second one is the introduction of the density operator and an ensemble representation of the dynamics, describing the averaging process that is performed in our experiments due to the integration over many repetitions of the pulse sequence.

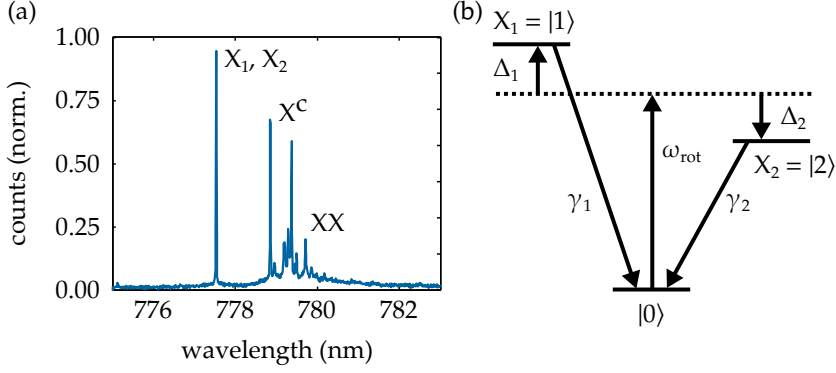


Figure 7.3: **a** A typical low temperature luminescence spectrum of the self-assembled quantum dots used in our experiment. The marked transitions correspond to the exciton transitions ($X_{1,2}$), trions (X_c) and bi-excitons (XX). **b** Simplified level scheme of the quantum dot. $|1\rangle$ and $|2\rangle$ correspond to the excitons X_1 and X_2 . ω_{rot} is the excitation laser center frequency used for the rotating frame approximation, from which the excitons are detuned by the frequencies Δ_1 and Δ_2 . γ_1 and γ_2 are the relaxation rates of the excitons back into the ground state.

We first start with the abstraction of the quantum dot, of which we show a typical luminescence spectrum in figure 7.3a. The quantum dot shows a number of resonances, excitons (X_1, X_2), charged excitons (X^c), and bi-excitons (XX). The laser light is resonant with X_1 and X_2 , which are distinct by a small energy splitting on the order of $100 \mu\text{eV}$ (not resolved in the graph). X_1 and X_2 have orthogonal optical selection rules and a direct transition between them is dipole forbidden. The other transitions, charged excitons and bi-excitons, are energetically well separated and are not excited. They take no part in the dynamics of our experiment and are ignored.

We thus describe the quantum dot as a V-atom, the states being the crystal ground state $|0\rangle$ and the two excitons $X_1 = |1\rangle$ and $X_2 = |2\rangle$. The dynamics of such a system are conveniently described in a coordinate frame rotating with a frequency ω_{rot} close to the eigenfrequencies of the excitons and the optical field, a method called rotating wave approximation [73]. We choose ω_{rot} to be identical with the frequency of the optical field. All other frequencies are defined relative to ω_{rot} . Figure 7.3b shows the resulting level scheme with the parameters used later on. The eigenenergies of the excitons are Δ_1 and Δ_2 , their decay rates into the crystal ground state are γ_1 and γ_2 . There is no direct coupling between the excitons. The Hamiltonian, also defined in the rotating coordinate system, reads

$$\hat{H} = \hbar\Delta_1\sigma_{11} + \hbar\Delta_2\sigma_{22} + [\hbar\Omega_1\sigma_{10} + \hbar\Omega_2\sigma_{20} + \text{h.c.}] \quad . \quad (7.1)$$

The projection operators σ_{ij} are defined in the eigenstate basis of the V-atom,

$$\sigma_{ij} = |i\rangle \langle j| \quad , \quad (7.2)$$

so $\sigma_{10} = |1\rangle \langle 0|$ describes a transition from the crystal ground state to the exciton X_1 . The first two terms of eq. 7.1 are the eigenenergies of the excitons. The terms containing the Rabi frequencies $\Omega_i(t) = \hbar^{-1} \cdot \vec{\mu}_i \cdot \vec{E}(t)$ define the interaction energy of the transition dipole moment $\vec{\mu}$ and the classical, time-dependent electric field $\vec{E}(t)$ of the laser pulses. For example, the Rabi frequency of a transition dipole $\vec{\mu}$ due to a Gaussian pulse at time t_p with $1/e^2$ -duration τ_p reads

$$\Omega(t) = \vec{\mu} \cdot \vec{E}_p \cdot \exp\left(-\frac{(t-t_p)^2}{2 \cdot \tau_p^2}\right) \cdot \exp(-i\omega_p t) \quad . \quad (7.3)$$

The vector product term on the left is the projection of the electric field amplitude vector to the transition dipole orientation of the exciton transition. The exponential in the middle defines the envelope function of the pulse and the rightmost exponential is an oscillatory term due to the detuning ω_p of the pulse carrier frequency from the rotating frame frequency. If several pulses are interacting with a transition, then the total Rabi frequency is the sum of the individual contributions. In the following, if not explicitly stated otherwise, we set $\omega_p = 0$ and the pump pulse and probe pulse are always meant to be defined according to equation 7.3.

Although we use a single quantum dot, we create a statistical ensemble by repeating the experiment many times. Fluctuations partly diminish the correlation between the individual trials. The quantum state of an statistical ensemble is defined by the density operator $\hat{\rho}$, which describes the intrinsic statistics of quantum mechanics and the classical statistics due to lack of information at the same time. Given $\hat{\rho}$, we can compute the expectation values of observables that we want to study. For an ensemble of quantum systems, the density operator is defined as [74]

$$\hat{\rho} = \sum_i p_i \cdot |\psi_i\rangle \langle \psi_i| \quad , \quad (7.4)$$

where p_i is the probability to find a randomly picked ensemble member in the pure state state $|\psi_i\rangle$. Given an orthonormal basis $|n\rangle$, the matrix representation of $\hat{\rho}$ is

$$\hat{\rho} = \sum_{nm} \sum_i p_i \psi_{ni} \psi_{mi}^* |n\rangle \langle m|, \quad \psi_{ki} = \langle k | \psi_i \rangle \quad . \quad (7.5)$$

To determine the optical emission of the excitons we need to know the expectation value of the transition dipole operator, $\hat{V} = \hat{\mu} \cdot \hat{E}$, where $\hat{\mu} = e \cdot \hat{x}$ is the dipole moment operator. The ensemble average of the

observable $\hat{\Theta}$ (or any operator) can be computed from the density matrix as

$$\langle \hat{\Theta} \rangle = \text{tr}\{\hat{\rho}\hat{\Theta}\} = \sum_i \sum_k \hat{\rho}_{ik} \hat{\Theta}_{ki} \quad . \quad (7.6)$$

So the ensemble average of \hat{V} is given by

$$\langle \hat{V} \rangle = \text{tr}\{\hat{\rho} \cdot \hat{\mu} \cdot \hat{\mathbf{E}}\} \propto \sum_i \sum_k \hat{\rho}_{ik} \langle k | \hat{x} | i \rangle \quad . \quad (7.7)$$

As $\langle i | \hat{x} | i \rangle = 0$ for any i , the ensemble average of \hat{V} is entirely determined by the off-diagonal elements of $\hat{\rho}$. For this reason, an off-diagonal elements are commonly termed *polarizations* in optics. The diagonal elements ρ_{ii} are termed *populations*, because they define how many of the ensemble members, on average, are found in state $|i\rangle$ of the basis set.

In an ensemble of classical, oscillating dipoles the off-diagonal elements of $\hat{\rho}$ would be a measure of phase stability of the oscillation. If the off-diagonal elements are zero, the phases of the individual members are random. The optical emission would be incoherent. Hence, even if the excited states of an ensemble are strongly populated and many members may decay into their ground state via optical emission, coherent radiation is only found when the polarization is not zero.

In the Heisenberg picture, the dynamics of the density matrix elements can be expressed with the Hamiltonian of the ensemble members by

$$\frac{d\hat{\rho}}{dt} = -i [\hat{\rho}, \hat{\mathbf{H}}] + L\hat{\rho} \quad . \quad (7.8)$$

This equation is commonly called Von-Neumann equation or master equation. In our case, \mathbf{H} is given by eq. 7.1. The damping operator $L\rho$ describes phenomenologically the decay of populations and polarizations. Population decay involves energy loss, e.g., decay of the quantum dot into its ground state. Polarization decay involves elastic scattering processes that randomize the quantum phase of individual ensemble members.

The damping operator elements are constructed from the phenomenological exciton population decay rates $\gamma_{1,2}$ and the pure dephasing rates $\gamma'_{1,2}$, associated with the two exciton transitions $X_{1,2}$. If we express the density matrix as a vector

$$\hat{\rho} = (\rho_{00}, \rho_{10}, \rho_{20}, \rho_{01}, \rho_{11}, \rho_{21}, \rho_{02}, \rho_{12}, \rho_{22})^T \quad , \quad (7.9)$$

and use the abbreviations

$$\alpha_j = \gamma_j, \quad \beta_j = \frac{\gamma_j}{2} + \gamma'_j \quad , \quad (7.10)$$

then we may write [75]

$$\mathbf{L}\hat{\rho} = (\mathbf{L}_1 + \mathbf{L}_2) \cdot \hat{\rho} \quad , \quad (7.11)$$

with the two matrices given by

$$\mathbf{L}_1 = \begin{pmatrix} 0 & 0 & 0 & 0 & \alpha_1 & 0 & 0 & 0 & 0 \\ 0 & -\beta_1 & 0 & 0 & 0 & 0 & 0 & 0 & 0 \\ 0 & 0 & 0 & 0 & 0 & 0 & 0 & 0 & 0 \\ 0 & 0 & 0 & -\beta_1 & 0 & 0 & 0 & 0 & 0 \\ 0 & 0 & 0 & 0 & -\alpha_1 & 0 & 0 & 0 & 0 \\ 0 & 0 & 0 & 0 & 0 & -\beta_1 & 0 & 0 & 0 \\ 0 & 0 & 0 & 0 & 0 & 0 & 0 & 0 & 0 \\ 0 & 0 & 0 & 0 & 0 & 0 & 0 & -\beta_1 & 0 \\ 0 & 0 & 0 & 0 & 0 & 0 & 0 & 0 & 0 \end{pmatrix} \quad , \quad (7.12)$$

$$\mathbf{L}_2 = \begin{pmatrix} 0 & 0 & 0 & 0 & 0 & 0 & 0 & 0 & \alpha_2 \\ 0 & 0 & 0 & 0 & 0 & 0 & 0 & 0 & 0 \\ 0 & 0 & -\beta_2 & 0 & 0 & 0 & 0 & 0 & 0 \\ 0 & 0 & 0 & 0 & 0 & 0 & 0 & 0 & 0 \\ 0 & 0 & 0 & 0 & 0 & 0 & 0 & 0 & 0 \\ 0 & 0 & 0 & 0 & 0 & -\beta_2 & 0 & 0 & 0 \\ 0 & 0 & 0 & 0 & 0 & 0 & -\beta_2 & 0 & 0 \\ 0 & 0 & 0 & 0 & 0 & 0 & 0 & -\beta_2 & 0 \\ 0 & 0 & 0 & 0 & 0 & 0 & 0 & 0 & -\alpha_2 \end{pmatrix} \quad . \quad (7.13)$$

Before we proceed with the solution of the master equation we want to introduce Bloch vectors as a convenient way to visualize the resulting dynamics of the V-atom. We first introduce Bloch vectors of two-level-systems, and then develop a similar concept for the V-atom.

7.1.2 Bloch vector representation

The state of a two-level-system can be represented either by the density matrix or by a three dimensional vector $\vec{S} = (u, v, w)$, called *Bloch vector*. Given the two available states $|0\rangle$ and $|1\rangle$, \vec{S} is defined in terms of the density matrix elements,

$$\begin{aligned} u &= \rho_{10} + \rho_{01} = 2\Re\{\rho_{10}\} \\ v &= i(\rho_{10} - \rho_{01}) = -2\Im\{\rho_{10}\} \\ w &= \rho_{11} - \rho_{00} \quad . \end{aligned} \quad (7.14)$$

We see from the equations that the u- and v-component refer to the polarization of the ensemble while the w-component refers to the

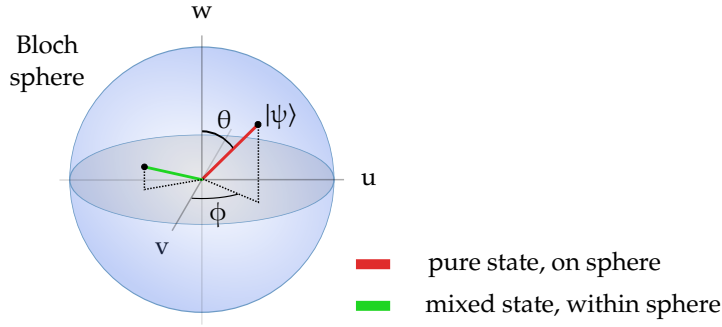


Figure 7.4: Conceptual illustration of the Bloch sphere and the definition of the polar angle θ and the azimuthal angle ϕ . The red vector lies on the surface of the sphere and refers to a pure quantum state. The green vector lies within the sphere and refers to a mixed state.

population. \vec{S} is usually depicted in a 3-dimensional coordinate system, the w -component commonly taken as the up-down component as shown in figure 7.4. By definition, \vec{S} is always located within a sphere of radius 1, called *Bloch sphere*. Pure quantum states all lie on the Bloch sphere. Each point on the sphere identifies with a coherent superposition $|\psi\rangle = A|0\rangle + B|1\rangle$. The complex coefficients A and B depend on the polar angle θ and the azimuthal angle ϕ of the Bloch vector, as depicted in the figure. Up to constant factors we have

$$|\psi(\phi, \theta)\rangle = \sin\left(\frac{\theta}{2}\right)|0\rangle + \cos\left(\frac{\theta}{2}\right)\exp(i\phi)|1\rangle \quad . \quad (7.15)$$

If the Bloch vector ends in the south pole, then the probability to find a randomly picked ensemble member in the ground state is one. If the Bloch vector ends in the north pole, then the probability to find a randomly picked ensemble member in the excited state is one. If the Bloch vector tip ends in a point on the equator, then the ensemble members are in a coherent superposition $|\psi\rangle \propto |0\rangle + \exp(i\phi)|1\rangle$.

For a detailed description of the concept of Bloch vectors, have a look at the great book *Optical resonance and two-level atoms* by Allen and Eberly[73]. To understand the behavior of the Bloch vector in the following discussion, it is enough to investigate three facts about Bloch vector dynamics. Have a look on equation 7.16,

$$\frac{d\vec{S}}{dt} = \vec{M} \times \vec{S}, \quad \vec{M} = (\Omega, 0, \delta) \quad . \quad (7.16)$$

It describes the motion of the Bloch vector of a loss-less two-level-system, detuned from the rotating frame frequency by δ , while being illuminated with an optical field with Rabi frequency Ω . Equation 7.16 can be deduced from the corresponding master equation [73] and is called the *optical Bloch equation*. Mathematically it is equivalent to the precession of a spin due to a magnetic field, which generates a torque that changes the angular momentum. In our case the torque

on \vec{S} is generated by the detuning and the interaction with the optical field.

Let δ be finite for the moment and $\Omega = 0$. Then \vec{M} points along the w -axis and its magnitude is δ , that is to say, the Bloch vector of a detuned two-level-system rotates with the detuning frequency around the w -axis. This is the first fact. Now let Ω be finite and $\delta = 0$. Then \vec{M} points along the u -axis with magnitude Ω , that is to say, the Bloch vector of a two-level-system driven by an optical field rotates with the Rabi frequency around the u -axis. This is the second fact. Combining both motions, the Bloch vector rotates around \vec{M} with an effective frequency $\sqrt{\Omega^2 + \delta^2}$.

The third fact relates to decay processes, which add another set of terms to equation 7.16. They are deduced from the population and polarization decay rates $\alpha = \gamma$ and $\beta = \gamma/2 + \gamma'$ as defined in equation 7.10. By substitution in to eq. 7.14 we get

$$\begin{aligned}\dot{u} &= -\beta u \quad , \\ \dot{v} &= -\beta v \quad , \\ \dot{w} &= -\alpha(w + 1) \quad .\end{aligned}\tag{7.17}$$

which means that polarization decay reduces the length of the Bloch vector perpendicular to the w -axis while population decay draws the w -component to the south pole, where $w = -1$.

Bloch vector dynamics are always a mixture of these three types of movements. With this in mind it is easy to say what happens during the excitation of a two-level-system with a pulse much shorter than relaxation and precession due to detuning: When starting with an ensemble of two-level-systems in the ground state, coherent interaction with the resonant light pulse rotates the Bloch vector around the u -axis, the rotation speed at time t being determined by the instantaneous Rabi frequency $\Omega(t)$. The so-called *pulse area* Φ is the time-integral of $\Omega(t)$,

$$\Phi = \int_{-\infty}^{\infty} dt \cdot \Omega(t) \quad .\tag{7.18}$$

It can be understood as the total rotation angle of the Bloch vector around the u -axis during the interaction with the light pulse¹. The latter is therefore conveniently defined by its pulse area, which is given in radian, e.g., a $\pi/2$ -pulse rotates the Bloch vector by 90° .

Because the mapping between the density matrix and the Bloch sphere is bijective, Bloch vectors can be used to define uniquely the state of an ensemble of two-level-systems. Additionally, Bloch vectors are very intuitive when being concerned with dynamics of the

¹ Note that this is only true if the pulse is much shorter than any other dynamical process in the two-level-system.

ensemble. How can we transfer the concept of Bloch vectors to a V-atom, obviously having more density matrix entries than eq. 7.14 can handle? We do this by defining for each excited level its own pseudo-Bloch vector. The vector orientations will be coupled to each other via the conservation of the total population, $\text{Tr}\rho = 1$, that is to say, arbitrary orientations of the two pseudo-Bloch vectors do not necessarily describe a valid state of an ensemble of V-atoms. We loose the bijective mapping. So we shall *not* use pseudo-Bloch vectors to define the state of the ensemble, but we shall only use them to visualize the state of the ensemble. Although with this they lack a great strength of Bloch vectors of two-level-systems, pseudo-Bloch vectors are very helpful to visualize the reaction of the V-atom to the incident light pulses. Additionally, keeping in mind the three facts about Bloch vector behavior, it is easy to spot and understand both, similarities and differences between two-level-systems and the V-atom.

The definition of the u- and v-components of the pseudo-Bloch vector stay the same. The w-component is redefined and understood as the difference of the population in the associated exciton and the populations in all other states, that is to say, the w-component of the pseudo-Bloch vector of exciton X_j is given by

$$w_j = \rho_{jj} - \sum_{i \neq j} \rho_{ii} = 2\rho_{jj} - 1 \quad , \quad (7.19)$$

where we used the conservation of the total populations. This merely ensures the meaning of the w-component as a measure of the population of the exciton.

7.1.3 A detuned V-atom pumped with a $\pi/2$ -pulse

Let us now consider as an example a V-atom with excitons X_1 and X_2 . We let X_1 be detuned slightly from the rotating coordinate frame. The pump pulse shall interact with X_1 only and has a pulse area of $\pi/2$. The probe pulse shall interact with X_2 only and has a pulse area of $3/2\pi$. It arrives some time after the pump pulse. Within between the pulses, the system is allowed to evolve and relax. Initially, the system is in the ground state.

We use the ODE113 solver for ordinary differential equation provided by MATLAB to integrate the Von-Neumann equation of this system. The resulting dynamics of the pseudo-Bloch vectors is depicted in figures 7.5a and b. In graph (a), the Bloch vector trace of X_1 , the pumped exciton, is shown. The red and green sections of the traces mark the arrival of the pump pulse and the probe pulse respectively. The pump pulse rotates the Bloch vector of X_1 by an angle of $\approx 90^\circ$, close to the equator. Afterwards the state evolves freely, spiraling around the w-axis due to the detuning between X_1 and the rotating frame combined with continuous decay of the polarization.

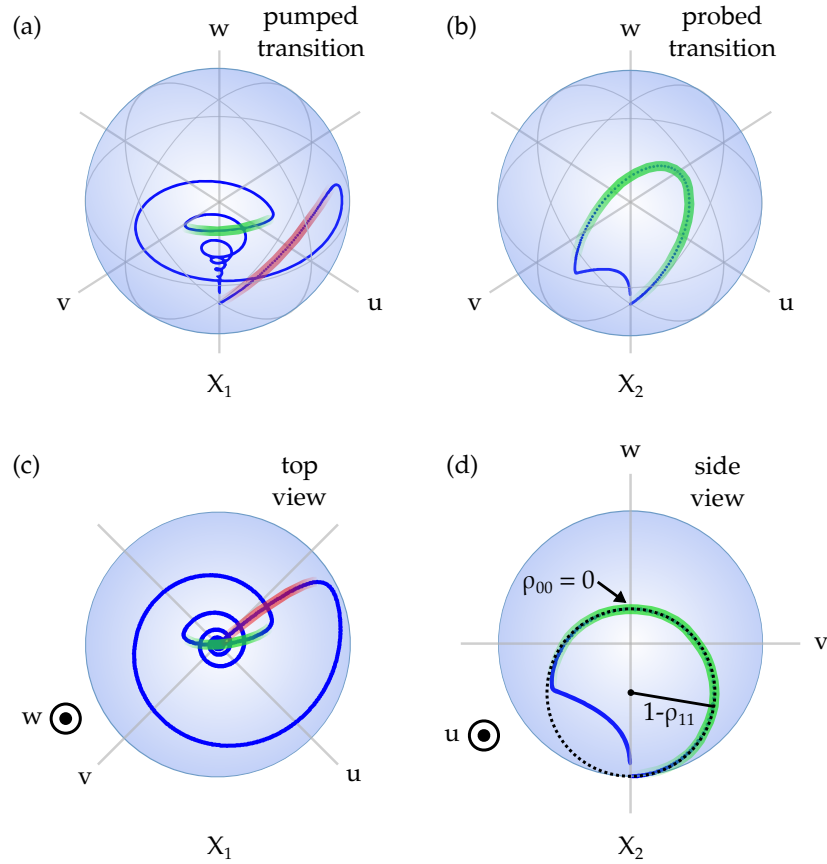


Figure 7.5: **a** and **b** show the traces of the pseudo Bloch vectors of the X_1 and X_2 transitions. The arrival time of the pump pulse is marked in red. The arrival of the probe pulse is marked in green. **c** and **d** show the top view of (a) and the side view of (b) respectively. The Bloch vector of X_2 moves on a circle with radius $1 - \rho_{11}$. When it crosses the w -axis, ρ_{00} is zero.

Up to now, the behavior is equivalent to a pumped two-level-system as discussed in the last subsection.

After a while, the probe pulse with a pulse area of $3/2\pi$ arrives and shuffles population into the X_2 state as indicated by the Bloch vector trace in figure 7.5b. As in a two-level-system, the Bloch vector is rotated by an angle of $3/2\pi$. But because X_1 is already populated and because the total population is conserved, it does not rotate on a sphere with radius 1, but on a sphere with radius $1 - \rho_{11}$, see figure 7.5d.

During the probe process the ground state population is temporary depleted. In effect, even though X_1 does not directly interact with the probe pulse, the polarization between X_1 and the groundstate is diminished. This is emphasized in fig. 7.5c, which shows a top view of the X_1 Bloch vector trace. It can be seen that when the probe pulse arrives, the X_1 vector is drawn exactly through the w -axis. The X_1

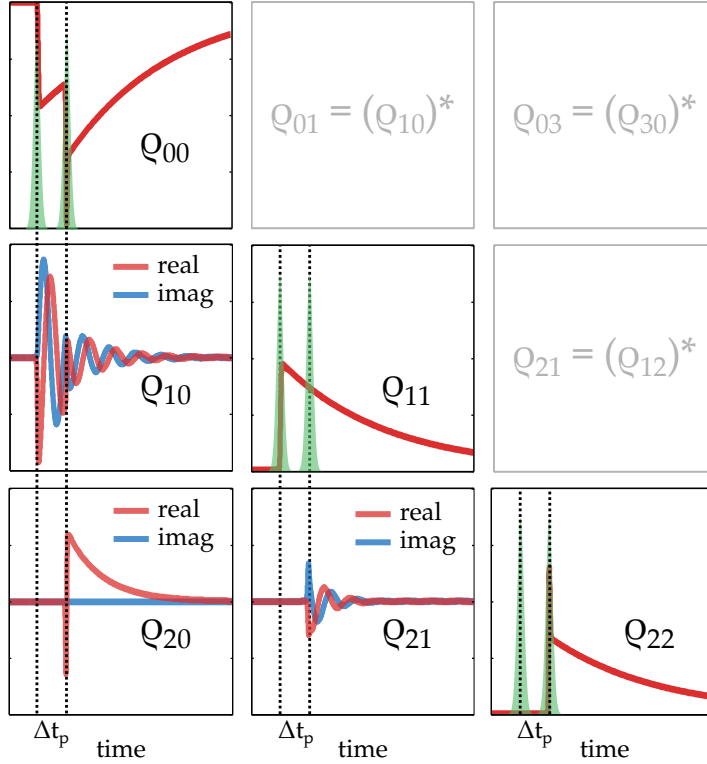


Figure 7.6: Time traces of the V-atom density matrix elements due to a double pulse excitation as described in the text. The plots are arranged like the matrix elements. The diagonal plots show populations and have a range of 0 to 1. The off-diagonal plots polarizations and have a range of -0.5 to 0.5 and show both, the real part and the imaginary part of the density matrix elements. The omitted plots in the upper left are the complex conjugates of the transpose plots. The pulse arrival times are indicated by the shaded area and the dashed lines.

and X_2 Bloch vectors pass the w -axis in the same moment, when all the population is within the excited state and the ground state is depleted.

The corresponding time traces of the density matrix elements are shown in figure 7.6. The plot positions correspond to the position of the matrix elements. Since the density matrix is symmetric, only three of the off-diagonal elements are shown. The graphs show both, real and imaginary part, as the off diagonal elements are complex numbers in general. The arrival times of the light pulses are marked by the dashed lines. We see how the pump pulse increases the population ρ_{11} while at the same time reducing the ground state population. Since the interaction is coherent, polarization ρ_{01} is induced. Both, populations and polarizations decay exponentially with their respective rates. The X_1 polarization is modulated. This corresponds to the Bloch vector rotation due to the detuning from the rotating frame. When the probe pulse arrives, not only is polarization induced be-

tween the ground state and X_2 , but also between X_1 and X_2 . This is due to the coherence between the pump pulse and the probe pulse: Ensemble members that get excited by either of the pulses inherit the phase reference of the electric field. No coherence could be induced between X_1 and X_2 if the light pulses would be incoherent or if the dephasing time of X_1 is shorter than the delay between the pulses.

We can compute the emission spectrum of the quantum dot from the time traces of the density matrix elements. The next paragraph describes the procedure we use.

7.1.4 From time traces to spectra

Considering the emission of radiation, the V-atom is two oscillating dipoles. The emitted field is proportional to the imaginary part of the corresponding off-diagonal element of $\hat{\rho}$ [76], which is an approximation only valid at frequencies close to ω_{rot} . The Fourier transform yields the scattering spectra. In the experiment, the light emitted by the dipole interferes with the probe pulse reflected by the sample surface (review fig. 7.2). The detected intensity in the frequency domain is thus

$$\begin{aligned} I_{\text{det}}(\omega) &= \left| \vec{\mathbf{E}}_{\text{probe}}(\omega) + \vec{\mathbf{E}}_{\text{QD}}(\omega) \right|^2 \\ &= |\vec{\mathbf{E}}_{\text{probe}}(\omega)|^2 + |\vec{\mathbf{E}}_{\text{QD}}(\omega)|^2 \\ &\quad + 2\Re\{\vec{\mathbf{E}}_{\text{probe}}(\omega) \cdot \vec{\mathbf{E}}_{\text{QD}}^*(\omega)\} \quad . \end{aligned} \quad (7.20)$$

The pure scattering term $|\vec{\mathbf{E}}_{\text{QD}}(\omega)|^2$ is so small that it can be omitted. To get rid of the probe contribution $|\vec{\mathbf{E}}_{\text{probe}}(\omega)|^2$, a reference measurement is subtracted. The reference measurement is performed by switching the pump pulse off. Hence, we do not detect the absolute scattering spectrum of the quantum dot, but the difference of the scattering spectrum when the pump is switched on. The spectral difference is normalized to the spectral sum of the two measurements. In total we have,

$$\begin{aligned} \frac{\Delta I(\omega)}{I(\omega)} &= \frac{I_{\text{on}}(\omega) - I_{\text{off}}(\omega)}{I_{\text{on}}(\omega) + I_{\text{off}}(\omega)} \\ &\approx \frac{\Re\{\vec{\mathbf{E}}_{\text{probe}}(\omega) \cdot (\vec{\mathbf{E}}_{\text{QD}}^{\text{on}}(\omega) - \vec{\mathbf{E}}_{\text{QD}}^{\text{off}}(\omega))^*\}}{2|\vec{\mathbf{E}}_{\text{probe}}(\omega)|^2} \quad , \end{aligned} \quad (7.21)$$

where we omitted the insignificant contributions of the quantum dot in the denominator.

The probe pulse is a Gaussian, defined by

$$\vec{\mathbf{E}}_{\text{probe}}(t) = \vec{\mathbf{E}}_0 \cdot \exp\left(-\frac{(t-t_p)^2}{2 \cdot \tau_p^2}\right) \cdot \exp(-i\omega_p t) \quad , \quad (7.22)$$

where $\vec{\mathbf{E}}_0 = E_0 \cdot \vec{\mathbf{e}}_p$ is a constant defining the peak amplitude and polarization direction of the electric field. If we set the rotating frame

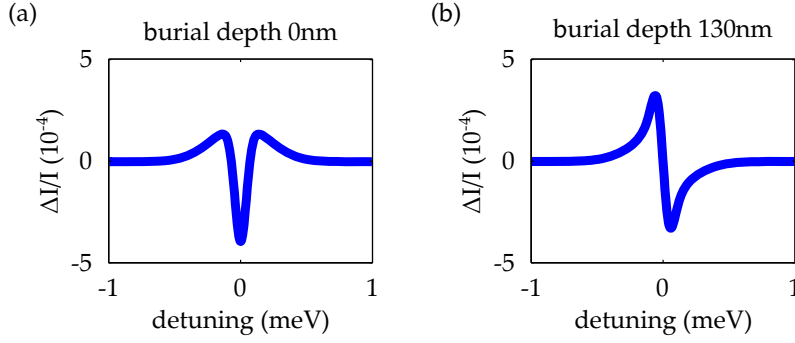


Figure 7.7: This figure shows the differential intensity spectra corresponding to the time traces presented in figure 7.6. The difference between **a** and **b** is the burial depth of the quantum dots, resulting in a different lineshape due to interference with another phase difference.

frequency to be identical with the pulse carrier frequency, then $\omega_p = 0$ and the pulse spectrum is given by

$$\vec{E}_{\text{probe}}(\omega) = E_0 \cdot \vec{e}_p \cdot \tau_p \cdot \exp(-i\omega t_p) \cdot \underbrace{\exp\left(-\frac{\tau_p^2}{2}\omega^2\right)}_{\approx 1} . \quad (7.23)$$

The second exponential, the spectral envelope of the Gaussian, is approximately constant on the scale of the quantum dot resonance width and can be omitted. The first exponential is a spectral phase modulation due to the temporal shift of the Gaussian with respect to the laboratory time frame. $\vec{E}_{\text{QD}}(\omega)$ carries the same phase modulation, which cancels in the product terms of equation 7.21. That is to say, by observing not only the scattered light of the quantum dot, but also the probe light, we automatically translate the quantum dot emission to $t = 0$.

$\vec{E}_{\text{QD}}(\omega)$ is the superposition of the dipole emissions of both excitons. It can be expressed in terms of the expectation value of the transition dipole operator, which is determined by the imaginary part of the polarizations [76]. The dipoles emit radiation polarized according to their orientation, denoted by the unit vectors \vec{e}_i . We have

$$\vec{E}_{\text{QD}}(\omega) \propto \mathcal{F}[\mathcal{I}\{\rho_{01}(t) \cdot \vec{e}_1 + \rho_{02}(t) \cdot \vec{e}_2\}](\omega) . \quad (7.24)$$

Substituting into eq. 7.21, we get

$$\frac{\Delta I(\omega)}{I(\omega)} = \frac{\Re\{\exp(-i\omega t_p) \cdot \vec{e}_p \cdot \mathcal{F}[\mathcal{I}\{\rho_{01}(t) \cdot \vec{e}_1 + \rho_{02}(t) \cdot \vec{e}_2\}]\}}{|\vec{E}_0 \cdot \tau_p|} . \quad (7.25)$$

Finally, the limited resolution of the spectrometer used in the experiment is included by convolving the calculated spectra with the

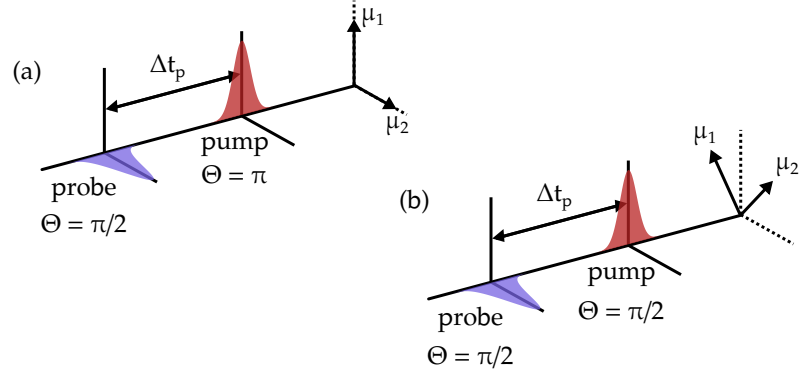


Figure 7.8: **a** In the first class of experiments the pulses are aligned parallel to the dipole orientations. Each pulse interacts with only one exciton. The pulse areas in the experiments are fixed to the shown values. We analyze the behavior of the V-atom in dependence of the pump-probe-delay Δt_p . **b** In the second class the pulses are polarized at an angle of 45° with respect to the dipole orientations. Each pulse interacts with both excitons.

instrumental response function, which is a Gaussian with spectral width of approximately ten times the linewidth of the excitons. Figure 7.7 shows differential intensity spectra of the X_2 polarization time trace $\rho_{02}(t)$ shown in figure 7.6. The two curves differ by the phase of the probe light reflected by the semiconductor surface. In fig. 7.7a, the phase difference is zero, which corresponds to quantum dots sitting right at the surface. In fig. 7.7b the quantum dots are buried 130 nm below the semiconductor surface, corresponding to the the samples that we use in the experiment. At a wavelength of 720 nm and a AlGaAs semiconductor matrix with a refractive index of $n_{\text{AlGaAs}} = 3.45$, the phase due to the additional optical path is

$$\phi = 2\pi \cdot \frac{2 \cdot n_{\text{AlGaAs}} \cdot d_{\text{QD}}}{\lambda} = 0.49\pi \quad , \quad (7.26)$$

where d_{QD} means the burial depth of the quantum dots.

Now that we did establish a connection between the dynamics of the V-atom and the experimentally accessible transient pump-probe spectra, we want to check if the self-assembled GaAs/AlGaAs-quantum dots we use come close to theoretical V-atoms. To do this, and as proof-of-concept of our measurement technique, we performed a number coherent control experiments [1, 2, 70]. In the following, we reproduce the experimental results with the theory described above. We establishing a relation between features found in the dynamics of the system and features found in the differential reflection spectra.

We start with a brief introduction of the test cases, which are divided in two distinct classes: In the first class, one exciton of the V-atom is used to monitor the state of the other exciton, which im-

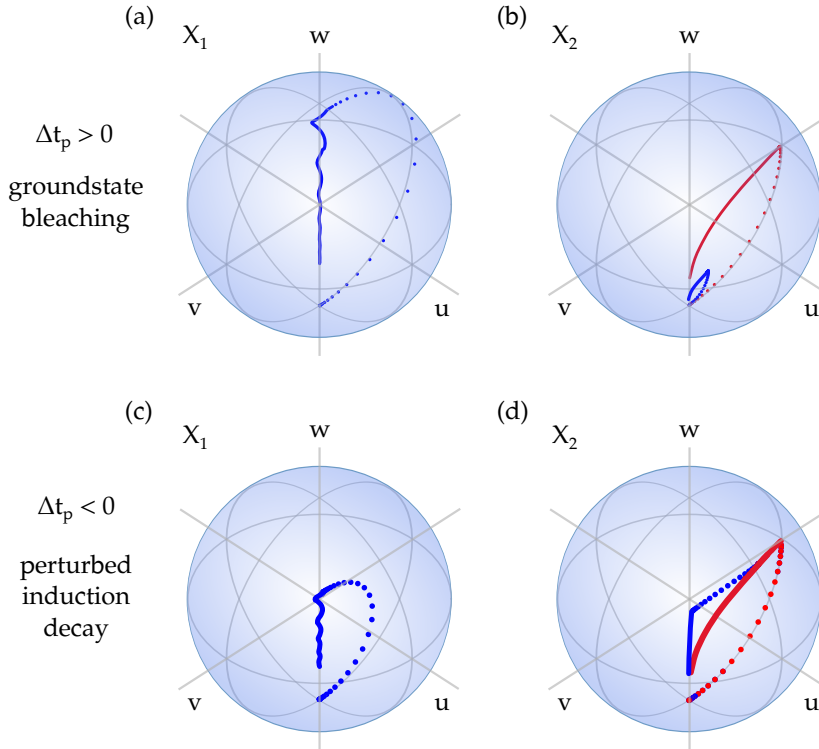


Figure 7.9: **a** and **b** show the pseudo Bloch vector traces of X_1 and X_2 in the case of a positive pump-probe delay. This process is called ground state bleaching. X_1 is first pumped with a π -pulse, then X_2 is probed with a $\pi/2$ -pulse. The red traces show the case without pump pulse, blue traces show the case with pump pulse. **c** and **d** show the pseudo Bloch vector traces of X_1 and X_2 in the case of a negative pump-probe delay. This process is called perturbed induction decay (PID). X_2 is first probed with a $\pi/2$ -pulse, then X_1 is pumped with a π -pulse.

plements a qubit. On the qubit, we perform coherent operations with the pump pulse. Only the monitor exciton is probed. This configuration, illustrated in fig. 7.8a, allows us to study the decay of population and polarization within one of the excitons.

In the second class of experiments, both excitons are pumped and probed (see fig. 7.8b). The polarizations of the optical fields are at an angle of 45° with respect to the dipole orientations, that is to say, the excitons play equivalent roles. This configuration allows us to study beating processes based the simultaneous evolution of the two excitons.

7.1.5 First test case: Groundstate bleaching and perturbed induction decay

In the first class, we distinguish positive and negative pump-probe delays, where positive means that the pump pulse arrives first. At pos-

itive delays, population decay is studied. The pump pulse performs a coherent operation on the state of the qubit exciton X_1 , creating polarization and population according to the chosen pulse area. The polarization that a subsequent probe pulse induces in the monitor exciton X_2 depends on the remaining ground state population, and thus on the state of X_1 . Figure 7.9a and b shows the pseudo Bloch vector traces of the pumped exciton X_1 and the probed exciton X_2 . Blue traces refer to the case with the pump pulse switched on. The red traces show the case with the pump pulse switched off. Consider the blue traces first: The X_1 vector quickly rotates around the u-axis to the north pole when the pump pulse arrives with a pulse area of π . The ground state population is depleted. Then we probe X_2 with a $\pi/2$ -pulse, but because the ground state is still nearly depleted, the X_2 Bloch vector moves on a sphere with effective radius $1 - \rho_{11} \approx 0$ (review fig. 7.5d). Accordingly, the X_2 Bloch vector barely leaves the south pole (blue trace in fig. 7.9b) and the quantum dot emission due to the X_2 polarization is strongly suppressed. For this reason, the process is called *ground state bleaching*. The Bloch vector trace of X_2 expected without pump pulse is shown in red for comparison. If the pump-probe delay is large, the ground state refills partly due to the decay of the X_1 population and the X_2 emission rises again. By measuring the differential intensity on X_2 in dependence of the pump-probe delay, we can determine the decay rate of the X_1 population back into the ground state.

At negative delays, when the probe pulse comes first, polarization decay in the X_2 exciton is studied. It works the other way round: The probe pulse first induces polarization in X_2 . A subsequent pump pulse on the X_1 exciton then perturbs the exponential decay of the X_2 polarization. This is commonly called *perturbed induction decay* (PID). Figures 7.9c and d show the pseudo Bloch vectors in a PID experiment, the blue traces denoting again the pumped case, the red curves the unpumped case. We see that the trace of the X_2 Bloch vector significantly changes, if the pump is switched on. In this particular case, X_2 is probed with a $\pi/2$ -pulse. Afterwards the groundstate population is depleted by pumping the X_1 exciton with a π -pulse. Consequently, the X_2 polarization is completely diminished, drawing the Bloch vector to the w-axis and inducing characteristic spectral features in the differential intensity signal. By observing the dependency on the pump-probe delay of those features, we can determine the polarization decay rate of the X_2 exciton.

We investigated groundstate bleaching and PID experimentally by measuring the differential intensity while tuning the pump-probe delay in a single sweep from negative to positive values. We use single GaAs/AlGaAs quantum dots as described in section 7.8. The experimental configuration is as in the examples above: X_1 is pumped with a pulse area of π , X_2 is probed with pulse area of $\pi/2$. We sweep the

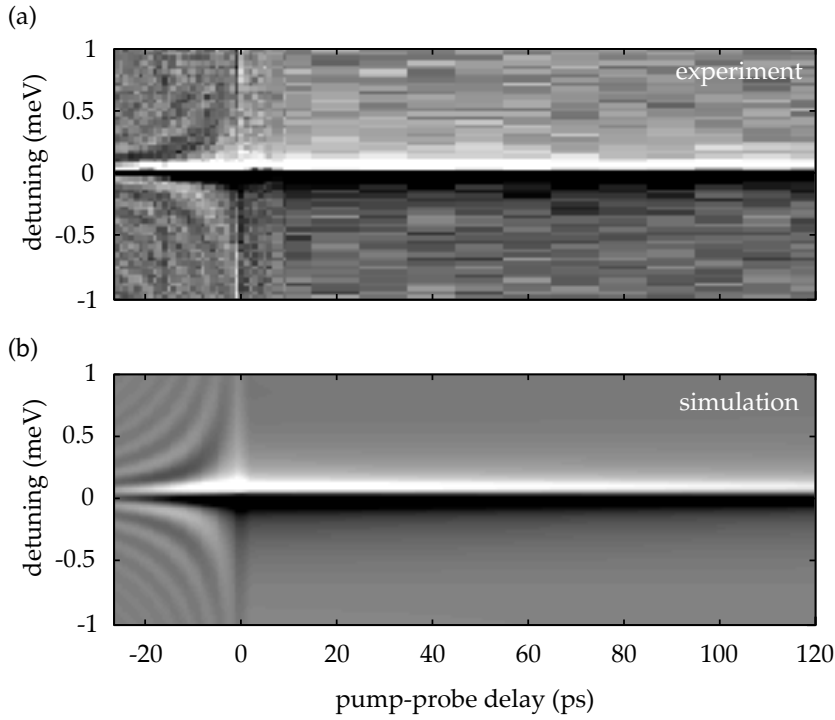


Figure 7.10: Comparison of the simulated pump-probe spectra with the experimental data. **a** shows the dependency of the differential intensity spectra on the pump-probe delay as found in the experiment. **b** is the reproduction of the spectra using the theory.

pump-probe delay from -50 ps to 120 ps. The population lifetime of the excitons is known to be on the order of 200–300 ps and the coherence lifetime is known to be on the order of 50–100 ps. The measured differential intensity spectra are shown in figure 7.10a. Each vertical cross section corresponds to one spectrum, taken at the pump-probe delay given by the horizontal axis.

The fringes at negative pump-probe delays are due to perturbed induction decay. Their frequency increases with the pump-probe delay while their amplitude decreases due to the exponential decay of the X_2 polarization. At positive delays we see ground state bleaching, the signature of which is a single resonance line, the amplitude corresponding to the population remaining in X_1 at the given pump-probe delay. The dispersive appearance of the resonance is due to the burial depth of the quantum dots, as discussed in subsection 7.1.4. Figure 7.10b shows a reproduction of the spectra using the theory described above. We tweak the polarization and population decay rates and a general scaling factor for the dipole moments to match the data and the theoretical prediction. We get a good match with a population half-lifetime of 230 ps and a polarization half-lifetime of 90 ps. They are the same for both excitons.

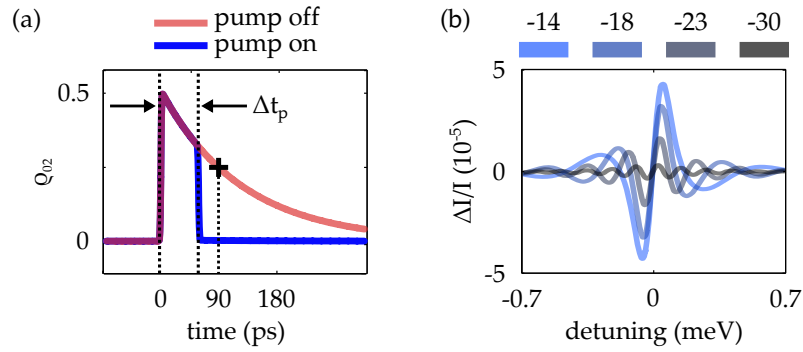


Figure 7.11: This figure illustrates the origin of the fringes in perturbed induction decay spectra. **a** shows the polarization time trace $\rho_{02}(t)$ of the probed exciton with and without pump pulse. The arrival time of the probe pulse and the pump pulse are marked by the dashed lines. The probe pulse comes first. The cross marks the half-lifetime of the exponential. **d** shows the corresponding differential intensity spectra at different pump-probe delays. The delay is denoted in picoseconds in the legend. It affects the periodicity of the fringes.

The agreement of the simulated spectra and the experimental data is very good, allowing us to deduce the temporal dynamics in the real quantum dot from the simulations. For example, by comparing the measured and the simulated spectra and investigating the associated dynamics of the density matrix elements, we can explain the fringes found in the experimental data at negative pump-probe delays. First note that, without a pump pulse, the polarization in X_2 follows an exponential function, as illustrated by the red curve in figure 7.11a. Its Fourier transform is simply a Lorentzian without fringes, as seen for example at positive delays. When the pump pulse is switched on, the exponential decay of the polarization is interrupted because the ground state is depleted. The resulting polarization trace, roughly spoken, is a scaled exponential multiplied with a rectangular window function of width Δt_p (see the blue curve in fig. 7.11). Multiplication of two functions in the time domain means convolution in the frequency domain, so the spectrum is a Lorentzian convolved with the Fourier transform of a rectangle, which is a sinc-function. The periodicity of the sinc-function is determined by the width of the rectangle. This is why the fringe periodicity increases with larger pump-probe delays.

In contrast to dephasing due to noise, in the case of PID the polarization of X_2 is not diminished due to random processes, but because the ground state population is depleted by a coherent interaction. If the ground state population is restored coherently, we may restore also the polarization of the X_2 transition. This can be done by applying a second pump pulse to X_1 that refills the ground state. Figures 7.12a and b show in the upper part the Bloch vector traces

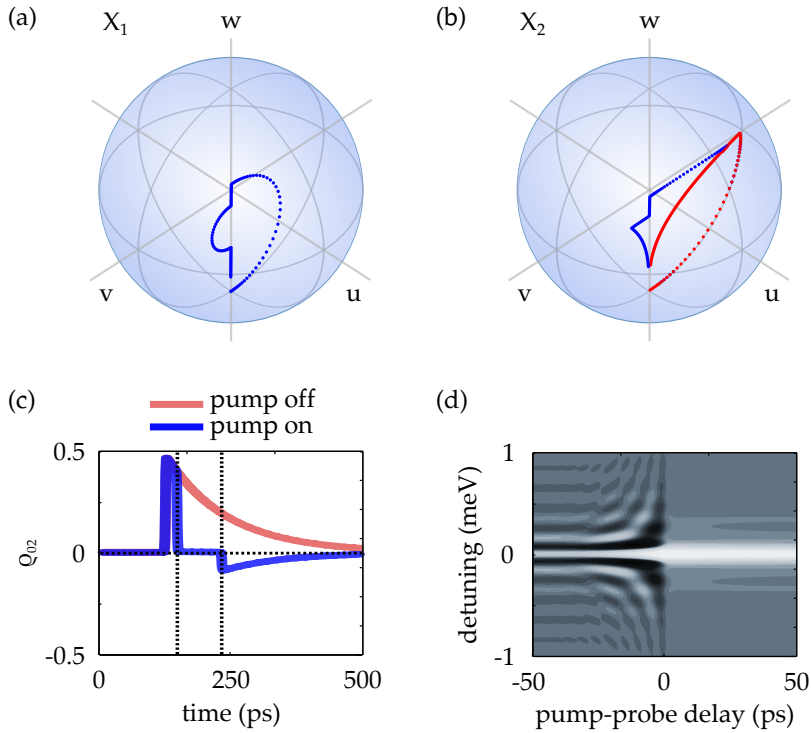


Figure 7.12: Illustration of polarization retrieval in the X_2 exciton. The probe pulse induces a polarization in X_2 . The pump pulse arrives 25 ps later and shuffles the remaining ground state population into the X_1 exciton, diminishing the polarization in X_2 . The polarization is restored by another pump pulse after 100 ps. **a** and **b** show the pseudo Bloch vectors of the X_1 and X_2 transition. Blue traces mark the pumped case, red traces mark the unpumped case. **c** shows the associated time trace of the X_2 polarization. The arrival times of the pump pulses are marked by dashed lines. **d** shows the differential intensity spectra in dependency on the delay between the probe pulse and one of the pump pulses.

of X_1 and X_2 for the case of a $\pi/2$ -probe pulse applied to X_2 and two subsequent π -pump pulses applied to X_1 . Figure 7.12c shows the corresponding X_2 polarization time trace. Red traces refer again to the case without pump pulses, showing a normal exponential decay of the X_2 polarization. When the pump pulses are active, the first π pump pulse shuffles the remaining ground state population into X_1 , diminishing the X_2 polarization just as it was the case in the former PID example. The Bloch vector of X_2 is drawn to the w -axis accordingly. However, after some time, we apply the second π pump pulse, shuffling some of the X_1 population back into the ground state. This restores the X_2 polarization, except for the fraction that is destroyed by decay processes. We see that the Bloch vector of X_2 is pushed away from the w -axis again.

Figure 7.12d shows the resulting differential intensity spectra in dependence of the delay between the probe pulse and one of the pump pulses. The delay between the probe and the second pump pulse is

fixed to 20 ps. We see that within the delay interval $-20 - 0$ ps, there is a double modulated structure, which is the superposition of $\text{sinc}(\omega)$ and a modulated $\exp(-\omega t_p)/\omega$ function, the Fourier transforms of a rectangle and a time shifted signum-function, which resembles the polarization trace in figure 7.12c.

7.1.6 Second test case: Response beating

Let us now switch to an experiment of the second class, pumping and probing both excitons (review fig. 7.8). This is realized by rotating the optical polarization of all beams by 45° and has been performed by Christian Wolpert and coworkers [1, 70]. We use a pulse area of $\pi/2$ for both the pump pulse and the probe pulse. The studied system is a single, self-assembled GaAs/AlGaAs quantum dot with two exciton resonances X_1 and X_2 . The resonances are detuned from each other by approximately $96 \mu\text{eV}$. Differential intensity spectra are measured in dependence of the pump-probe delay. The resulting experimental data is presented in figure 7.13a. We observe signatures of response beating, that is to say, the magnitude of the differential intensity oscillates as a function of the pump-probe delay. The blue dots in figure 7.13b shows the amplitude of the signal determined by fitting two equally strong resonances to the data [70]. The solid line is a least-squares fit of an exponential superimposed by an cosine. The period of the beating is 43 ps and fits the energy detuning between the excitons. The decay time of the exponential corresponds to the population decay time. This suggests that the beating is related to interference of the excitons. In what follows we clarify the origin of these oscillations.

In our experiment, response beating may be caused by coherence between the light field and the excitons or by coherence between the excitons alone. Isn't this the same? The answer is no, because the excitons may loose coherence with the light field while maintaining coherence between themselves. As a consequence, there is two distinct beating processes that may be observed.

Whenever an exciton interacts twice with the optical field, the coherence between the exciton and the field comes into play which is known as Ramsey interference [9]. The polarization revival discussed in the former subsection is an example, and another one would be an exciton pumped and probed directly with a detuned light field. Such a process shows a beating of the exciton resonance with the detuning frequency from the optical field.

The underlying mechanism is illustrated in fig. 7.14, showing the polarization and the Bloch vector dynamics of a single exciton that is first probed by a $\pi/2$ -pulse and then pumped with another $\pi/2$ -pulse. The studied exciton is detuned slightly from the optical field. The second exciton is switched off by setting the dipole moment to

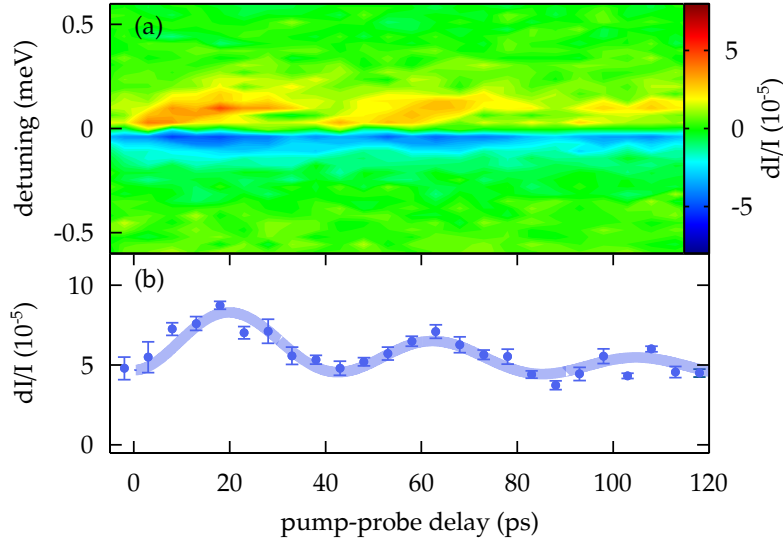


Figure 7.13: When pumping and probing both excitons in a V-atom, the differential intensity shows a beating with the pump-probe delay, superimposed on the exponential decay of the population. **a** shows an example of measured data. **b** shows the amplitude of the signal as determined by fitting two equally strong resonances to the data (dots with error bars). The solid line is a fit of an exponential decay with an added sinusoid. See [70] for detail on the measurement and data evaluation.

zero. Figures 7.14a and b show the dynamics for a pump-probe delay that corresponds to one fourth of the beating period. The red curves show the unpumped case, the blue curves the pumped case. After the probe pulse induces the initial population and polarization in the exciton, the Bloch vector spirals around the w -axis according to the detuning and exponential decay. Upon the arrival of the pump pulse, the Bloch vector would be rotated around the u -axis. However, at that moment the Bloch vector is nearly parallel to the u -axis and thus does not change significantly. As a result, the polarization trace is the same no matter if there is a second pulse or not (see figure 7.14b). The differential intensity is thus zero.

If the pump-probe delay is one-half the detuning period, the situation is different, as shown in figures 7.14c and d. When the pump pulse arrives, the Bloch vector points along the v -axis and does change significantly upon rotation around the u -axis. The polarization trace does change accordingly. The resulting differential intensity spectra calculated from the polarization time trace of a single, detuned exciton is shown in figure 7.15a. In this particular case, the detuning of the exciton is chosen to be 0.33 meV, or 80 MHz. The beating with a period of 12.5 ps is clearly visible. The population and polarization lifetimes have been increased to make the beating better visible. In fact, what really interferes in this process is the two laser pulses. We can think of the quantum dot as a mediator, storing the

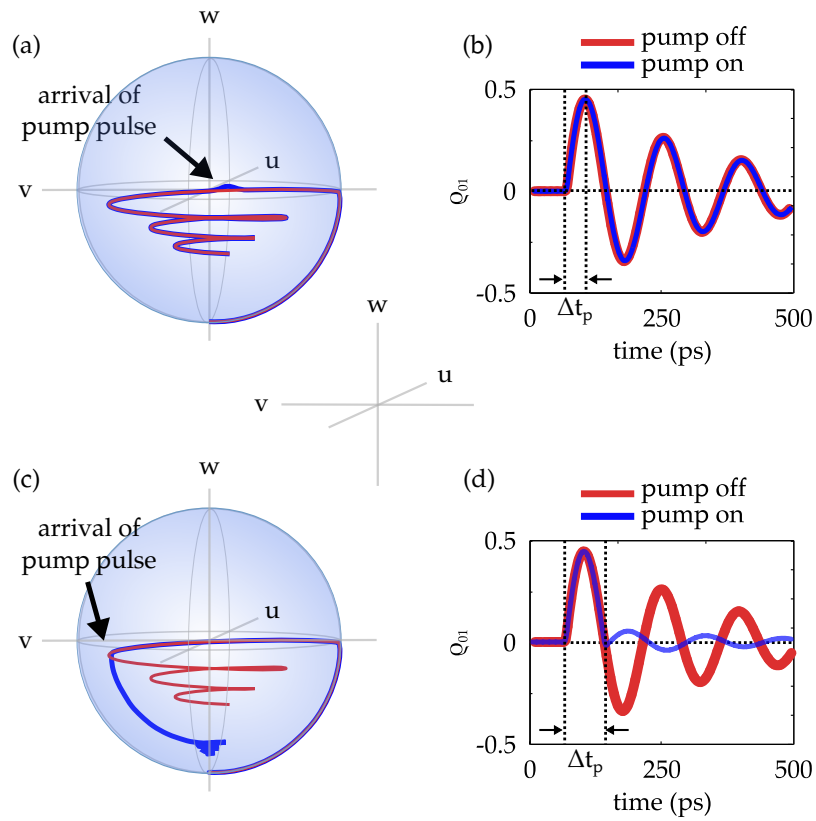


Figure 7.14: This figure demonstrates the beating mechanism due to interference of the detuned exciton wave function and the probe pulse electric field. Blue colors refer to the pumped case, red colors refer to the unpumped case. **a** Time trace of the pseudo-Bloch vector when the pump-probe delay is one-fourth of the detuning period. There is nearly no change to the ensemble state. **b** Comparison of the corresponding polarization time traces. The arrival time of the two light pulses is marked by the dashed lines. Δt_p is the pump-probe-delay. **c** and **d** show the same for a pump-probe delay of one-half the detuning period. The change to the ensemble state is maximal.

phase of the pump pulse for comparison with the phase of the probe pulse at a later time. Due to dephasing and population decay the beating of course gets weaker when Δt_p increases.

In the experiment, this type of beating is not visible, as it averaged out due to jitter of the pulse phase and because the acousto-optic modulators used to gate the pulses introduce a difference of the carrier frequencies of the pump pulse and the probe pulse by several MHz. Without special measures for stabilization of the optical path, the pump pulse and the probe pulse are practically incoherent to each other. Nevertheless we see in the data a beating if two excitons are illuminated at the same time, the beating period corresponding to the

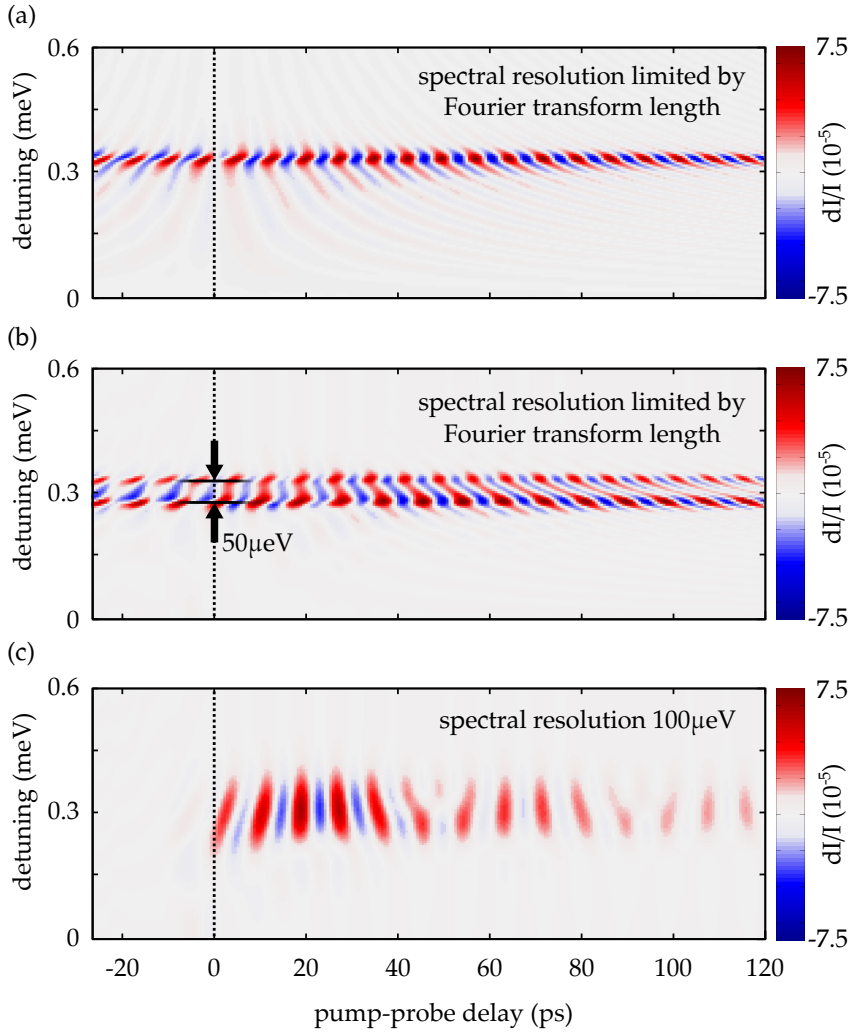


Figure 7.15: Simulated differential reflection spectra showing quantum beats in dependency of the pump-probe delay. **a** shows the resonance of a single exciton detuned by $330 \mu\text{eV}$ from the optical field. The resonance beats with a period of 12.5 ps . The spectral resolution is limited by the temporal length of the data set. **b** shows the same for two excitons, detuned by $55 \mu\text{eV}$ with respect to each other. This adds another resonance to the spectrum. In **c** the spectral resolution is limited to $100 \mu\text{eV}$. The detuning between the resonances is not resolved anymore. The coherent emissions of the excitons interfere and lead to a beating with a period of 75 ps .

detuning between the excitons. Such a beating can also be found in the simulations, superimposed on the beating with the pulse phase.

Figure 7.15b shows the differential intensity spectrum of two exciton transitions that are detuned to each other. Both are pumped and probed with $\pi/2$ pulses. The relative detuning of the excitons is $55 \mu\text{eV}$, corresponding to a beating period of 75 ps . The detunings of the excitons with respect to the electric field are $275 \mu\text{eV}$ and $330 \mu\text{eV}$,

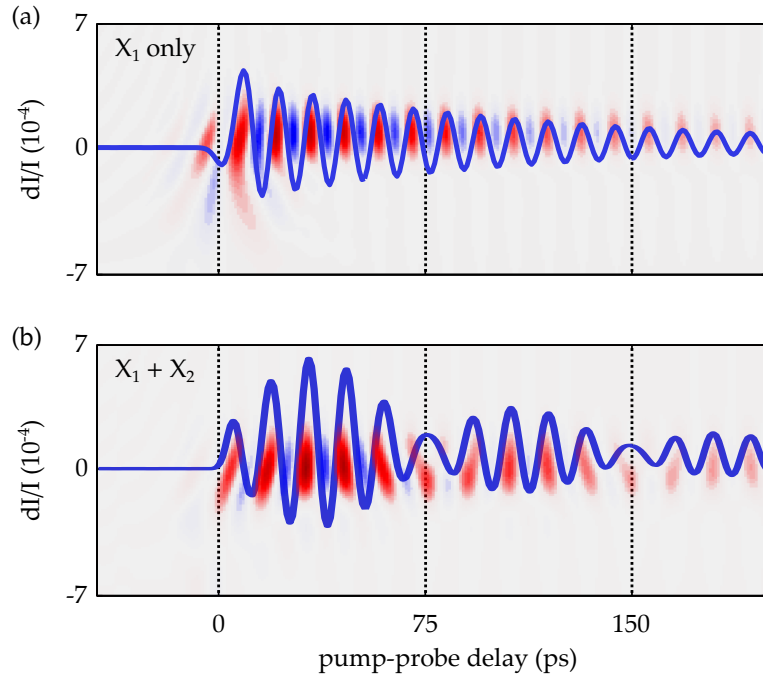


Figure 7.16: Horizontal crosssections of the spectra shown in figure 7.15. In the background, the color-coded spectra are shown for comparison. **a** shows the cross section in the case of a single exciton: a modulated exponential decay. The spectral resolution is set to $100 \mu\text{eV}$. **b** shows the cross section in the case of two detuned excitons that are not individually resolved: A beating is imposed on the modulation.

corresponding to a beating period of 15 ps and 12.5 ps . The spectrum resolution, in this plot limited by the length of the Fourier transform, is good enough to separate the resonances, each of which beats with its detuning frequency against the light field. It can be seen that at certain pump-probe delays the beats are in phase while for others they are out of phase. When spectrally not resolved, the emissions of the excitons interfere constructively when in-phase and interfere destructively when out-of-phase. The period of this interference corresponds to the relative detuning of the excitons. That is shown in fig. 7.15c, in which the resolution of the spectrum is limited to $100 \mu\text{eV}$. Instead of two separate beatings, we see one double-modulated resonance. For comparison, fig. 7.16 shows the average of the color plots along the spectral axis. When there is only one exciton (see part (a) of the figure), an exponential decay modulated with the detuning frequency is found. When there is two excitons (see part (b)), the modulation does beat with the detuning difference frequency. This is what we observe in the experiment. Christian Wolpert showed in his thesis, that the beating period observed experimentally in the pump-probe spectra fits well with the detuning of the excitons. To finally prove that the excitons do beat with respect to each other but not individually against the electric field of the probe pulse, we could increase the de-

tuning until the exciton resonances can be resolved. Then, if they do not show a beating, we could exclude a stable phase relation between the excitons and the probe pulse.

7.2 PERTURBATION OF A TWO-LEVEL-SYSTEM BY ULTRAFAST CHARGE CARRIER DYNAMICS

We have seen in the last chapter that the investigated quantum dots mimic a V-atom quite well, enabling us to establish complex schemes of coherent control in theory and realizing them experimentally. However, we observed that the data stops fitting the theory when we gradually increase the pulse area. In theory, when pumping a two-level-system with a pulse area Φ , the Bloch vector will rotate by that angle, its z-component given by

$$S_z = \sin^2 \Phi \quad . \quad (7.27)$$

We thus expect a 2π periodicity in any measurement that depends only on the population of the excited state, a phenomenon generally known as Rabi oscillation². An example is the groundstate bleaching experiment described in section 7.1.5. We expect that the differential intensity measured on the probed exciton is directly proportional to the population of the pumped exciton, that is to say

$$\frac{\Delta I}{I} \propto \sin^2 \Phi \quad . \quad (7.28)$$

However, this is not what we observe. Figure 7.17a shows the differential intensity on resonance recorded in a ground state bleaching experiment on a single GaAs/AlGaAs quantum dot while gradually increasing the pulse area of the pump pulse (in the following denoted *power sweep*). The probe pulse area is held constant at $\pi/2$. The theory agrees with the data within the first 2π cycle, but then the Rabi cycles found in the experiment seem to stretch. Note that the modulation depth of the Rabi oscillation stays the same.

The favorite explanation for this behavior is the presence of charge carriers in the vicinity of the quantum dot, created in the GaAs substrate by the pump laser pulse. The creation of free carriers close to the quantum dot is possible due to the very thin lower AlGaAs barrier and the close-by GaAs substrate, where unbound carrier states exists at the laser frequency. This is illustrated in figure 7.17b. The incident laser pulse, resonant to the exciton, is absorbed by the GaAs substrate and electron-hole pairs are created below the quantum dot. The charge clouds change the properties of the quantum dot by inducing a net electric field. The required charge separation is due to the reflection of the charge carriers at the GaAs/AlGaAs interface

² The term *Rabi oscillation* originally refers to the continuous rotation of the Bloch vector upon coherent illumination of a two-level-system with a CW-laser.

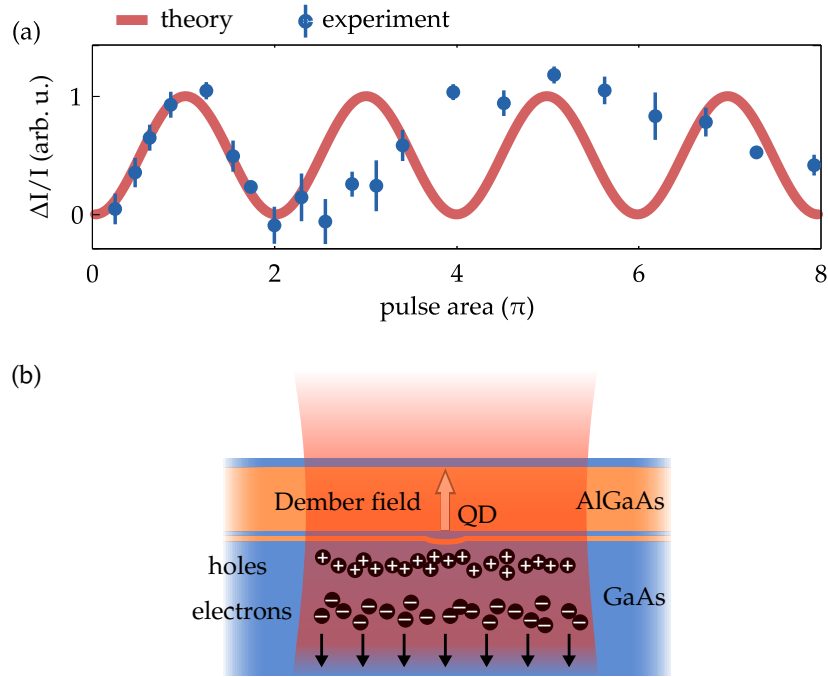


Figure 7.17: **a** This graph shows the differential intensity of an exciton resonance in a ground state bleaching experiment in dependence of the pump pulse area. The theory predicts a $\sin^2 \Phi$ dependence on the pulse area Φ (red curve). In the experiment, we see a stretching of the second Rabi cycle (blue points). **b** Sketch of the Dember effect, which is assumed to be the origin of the stretching seen in (a). The quantum dot is embedded in a GaAs/AlGaAs heterostructure. The lower AlGaAs-barrier is very thin (10 nm). Below, in the GaAs substrate, free photo charge carriers are created by the laser pulse. The carriers, electrons and holes, are reflected at the GaAs/AlGaAs interface and diffuse away from it. Since the electrons are much faster, two separate charge clouds form and induce a net electric field, the Dember field. It changes the optical properties of the quantum dot via DC-Stark effect.

and different diffusion speeds of electrons and holes. The electrons are considerably faster and diffuse down into the substrate while the holes stay close to the interface. An electric field orthogonal to the interface builds up between the centers-of-charge. This mechanism is named *Dember effect* after Harry Dember, who discovered the effect in 1931 [77]. The electric field is called *Dember field*. It was studied extensively by Dekorsy et al. using reflective electro-optic sampling (REOS) [78], measuring the change of reflectivity of a semiconductor surface due to the electric field. The Dember field has amplitudes on the order of tens of kV/cm [79], it rises within a few hundred femtoseconds and decays exponential afterwards, the decay time in general depending on the particular photo carrier dynamics within the sample [79].

We showed [70] the existence of the Dember field in our samples in a separate experiment and found that the Dember field directly manipulates the quantum dot via the quantum-confined Stark effect, shifting the resonance energy and reducing the transition dipole moment of the exciton [80, 81]. We like to see whether these effects lead, in theory, to the observed stretching of the Rabi cycles by including a time dependent detuning and dipole moment into the density matrix formalism described in section 7.1. This involves two steps. First, we model the dynamics of the Dember field in terms of a rate equation for the photo carrier number. Second, the change of the optical properties of the quantum dot due to the Dember field must be estimated. This was done in collaboration with the Group of Gabriel Bester at the Max-Planck-Institute of Solid State Research in Stuttgart. The master equation of the system is then solved with the dynamically changing optical properties. Finally, the results are compared with the data.

7.2.1 Model of the Dember field amplitude

For the time being we assume that the Dember field amplitude $F_D(t)$ is proportional to the number of photo carrier pairs $N(t)$ at time t , requiring that the charge clouds do not significantly change their shape and position as time goes on. Modeling the movement and shape of the charge clouds is a topic of future investigations and not covered in this work. For $N(t)$, we can setup a rate equation. Photo carrier pairs are created by absorbing a fraction of the pump pulse photons, the number of pairs created in a time interval dt being proportional to the intensity $I(t)$ of the pulse and the number of available valence band electrons. We assume that initially there is N_m valence band electrons available to create photo carrier pairs. The number of remaining valence band electrons at time t is thus $N_m - N(t)$. Additionally, we assume that within each time interval, a fraction γ_D of the existent photo carrier pairs recombines. In total, in a time interval dt , $N(t)$ changes by

$$\frac{dN}{dt} = \underbrace{-\gamma_D \cdot N(t)}_{\text{relaxation}} + \underbrace{\alpha \cdot I(t) \cdot \left(1 - \frac{N(t)}{N_m}\right)}_{\text{creation}} , \quad (7.29)$$

where α is a measure of how many pairs are created per incident power unit. Given $N(t)$, we define the Dember field amplitude F_D as

$$F_D(t) = f_0 \cdot N(t) , \quad (7.30)$$

where f_0 is a proportionality factor that may depend on the geometry of the sample, its material composition, the exact distribution of the charge clouds and how they change over time. As discussed above we take it as a constant for the time being, giving $F_D(t)$ the same proper-

ties as $N(t)$. Substituting eq. 7.30 into eq. 7.29 we get the differential equation for $F_D(t)$,

$$\frac{dF_D}{dt} = -\gamma_D \cdot F_D(t) + \alpha \cdot f_0 \cdot I(t) \cdot \left(1 - \frac{F_D(t)}{F_{max}}\right) . \quad (7.31)$$

We may give an intuitive meaning to α by expressing $I(t)$ in terms of the Rabi frequency, $I(t) = E(t)^2 = \hbar^2/\mu^2 \cdot \Omega(t)^2$, and absorbing all the constants including f_0 into α . If the optical field, and hence $\Omega(t)$, has the form of a Gaussian of duration τ_p and area Φ we have

$$\int_{-\infty}^{\infty} \Omega(t) dt = \Phi \Rightarrow \int_{-\infty}^{\infty} \Omega(t)^2 dt = \frac{\Phi^2}{\sqrt{4\pi\tau_p^2}} . \quad (7.32)$$

Then α , expressed in units of

$$[\alpha] = \frac{kV}{cm} \cdot \frac{\sqrt{4\pi\tau_p^2}}{(2\pi \text{ rad})^2} , \quad (7.33)$$

is the Dember field strength created by a pump pulse with pulse area 2π rad and duration τ_p (ignoring saturation and recombination). In the following, we will abbreviate the unit of α as $kV/cm/cycle^2$, where implicitly the normalization with the pulse duration is included. In summary, we redefine eq. 7.31 as

$$\frac{dF_D}{dt} = -\gamma_D \cdot F_D(t) + \alpha \cdot \Omega(t)^2 \cdot \left(1 - \frac{F_D(t)}{F_{max}}\right) . \quad (7.34)$$

Equation 7.34 is a ordinary linear differential equation with variable coefficients,

$$y' + h(t) \cdot y = g(t) , \quad (7.35)$$

where

$$\begin{aligned} y(t) &= F(t) , \\ h(t) &= \gamma_D + \frac{\alpha}{F_m} \cdot \Omega(t)^2 , \\ g(t) &= \alpha \cdot \Omega(t)^2 . \end{aligned} \quad (7.36)$$

The formal solution to eq. 7.35 is

$$\begin{aligned} y(t) &= \left(\int_0^t g(t') \cdot \exp\left(\int_0^{t'} h(t'') dt''\right) dt' \right) \times \dots \\ &\quad \times \exp\left(-\int_0^t h(t') dt'\right) . \end{aligned} \quad (7.37)$$

We use the ODE113 numerical solver provided by MATLAB to evaluate eq. 7.29 on a appropriate set of trial points. When simulating

the dynamics of the V-atom, we linearly interpolate the data set as needed to integrate the master equation. Figure 7.18 summarizes the properties of $F_D(t)$ as defined by equation 7.34. Graph (a) compares $F_D(t)$ for different pump pulse areas in a semi-logarithmic representation. As expected, the peak Dember field amplitude F_p is a non-linear function of the pulse area, which is indicated by the formation of a plateau during the pump process. Afterwards, the field decays exponentially, the slope being proportional to the recombination rate γ_D . Figure 7.18b compares $F_D(t)$ for different values of the recombination rate γ_D . For lifetimes on the order of the pulse duration τ_p , $F_D(t)$ essentially follows the pulse envelope $\Omega(t)^2$ and can be considered as a delta spike on typical relaxation times of the quantum dot. For recombination times long compared to the pulse duration, the dynamics is essentially a step-like rise of $F_D(t)$ and subsequent exponential decay. Figures 7.18c and d demonstrate the influence of F_m and α on the peak amplitude F_p . As expected, F_p is proportional to F_m when driven into saturation. α determines how fast F_p rises with the pulse area. These two parameters are very important since they mainly define the power dependence of the Dember field peak amplitude, and hence the power dependence of the exciton optical properties.

The next step is to translate the Dember field strength into changes of the exciton resonance energy $\hbar\omega$, changes of the dephasing rate γ' and changes of the dipole moment μ , denoted respectively by δ , Γ and κ . We define

$$\hbar\omega(t) = \hbar\omega_0 + \delta(F_D(t)) \quad , \quad (7.38)$$

$$\gamma'(t) = \gamma'_0 + \Gamma(F_D(t)) \quad , \quad (7.39)$$

$$\mu(t) = \mu_0 \cdot \kappa(F_D(t)) \quad , \quad (7.40)$$

where δ_0 , μ_0 and γ'_0 denote the initial values of the parameters without Dember field. To estimate the values of δ and κ with respect to F_D , the optical properties of our sample structure were simulated by Ranber Singh in the group of Gabriel Bester at the Max-Planck-Institute of Solid State Research, performing ab-initio calculations of the resonance energy and the oscillator strength f of the exciton in the presence of an external electric field. They used an atomistic pseudopotential approach [82]. The structural properties of our sample structure were determined on nominally identical samples by AFM measurements [71]. Table 7.1 shows the calculated values of δ and the relative oscillator strength f/f_0 for different electric fields parallel to the growth direction. f_0 is the oscillator strength without electric field. The negative field amplitudes correspond to a field pointing downwards, based on the fact that the negative charges move away from the quantum dot.

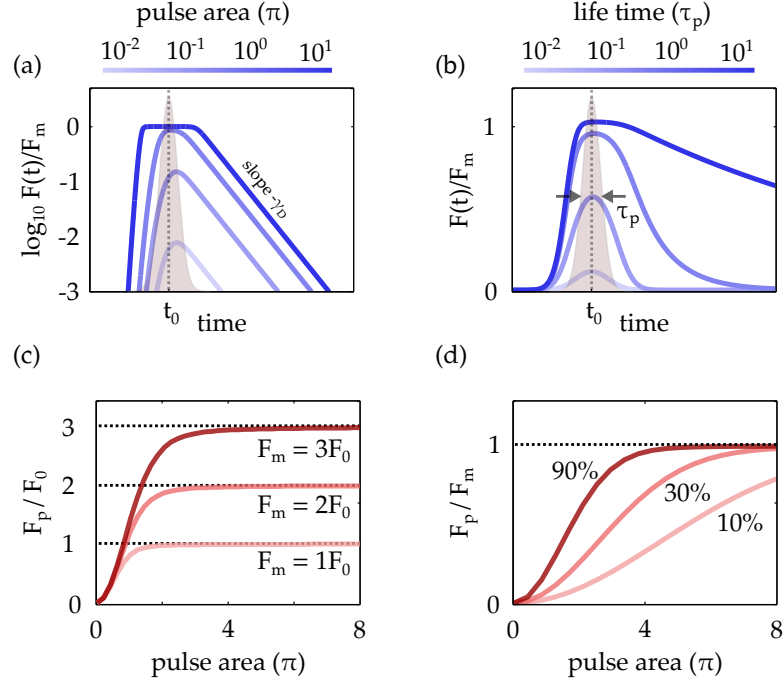


Figure 7.18: **a** This graph demonstrates the non-linear dependence of the Dember field amplitude F_D on the pump pulse area. The different curves denote different pulse areas, as indicated by the color bar. The scaling of the y-axis is logarithmic. The arrival time and width of the pump pulse is indicated by the red shade. **b** The graph illustrates the dynamics of the Dember field amplitude for different photo carrier lifetimes, given in units of the pulse duration τ_p . The arrival time of the laser and its width are indicated by the red shade. **c** Shown is the dependency of the peak Dember field amplitude F_p on the pulse area for three different values of the maximum photo carrier number, $F_m = F_0, 2F_0, 3F_0$. **d** Shown is the dependency of the peak Dember field amplitude F_p on α . The values of α is denoted in fractions of F_m next to the curves. For example, a value of 90% means $\alpha = 0.9 \cdot F_m/\text{cycle}^2$.

δ and f have a quadratic dependency on the field amplitude due to lack of a permanent dipole moment. Fitting second order polynomials yields

$$\delta(F) = -0.23 \mu\text{eV} / \left(\frac{\text{kV}}{\text{cm}} \right)^2 \cdot (F + 17.86 \text{ kV/cm})^2 - 74.6 \mu\text{eV} \quad (7.41)$$

$$\frac{f(F)}{f_0} = -7.23 \cdot 10^{-6} \cdot (F - 138.8 \text{ kV/cm})^2 + 1.14 \quad (7.42)$$

From $\frac{f}{f_0}$, we get the change of the dipole moment by taking the square root,

$$\kappa = \frac{\mu}{\mu_0} = \sqrt{\frac{f}{f_0}} \quad (7.43)$$

F_z (kV/cm)	δ (μeV)	f/f_0 (%)
0	0	100
-10	28.3	98.47
-20	19.6	96.76
-40	-12.5	90.08
-50	-152.3	87.77
-60	-334.0	85.25
-70	-559.6.0	82.54
-80	-830.0	79.56
-90	-1146.6	76.28
-100	-1507.0	72.49

Table 7.1: Results of the atomistic pseudo-potential simulation of the resonance shift δ and relative oscillator strength f/f_0 for a given DC-electric field F_z oriented parallel to the growth direction (z-axis).

The dephasing Γ is due to the fluctuation of the Stark shift with the Dember field amplitude,

$$\begin{aligned} \Gamma(F) &= \left| \frac{d\delta}{dF} \right| \cdot \Delta F \\ &= 0.46 \mu\text{eV} \cdot F \cdot \Delta F \end{aligned} \quad (7.44)$$

where ΔF is the fluctuation of the Dember field amplitude, being dependent on the fluctuation of the photo carrier number and their random movement. Knowing the Dember field amplitude due to the pump pulse, its value is substituted into equations 7.42–7.44. We then evaluate the master equation of the V-atom, see equation 7.8, page 79.

7.2.2 The Dember effect and Rabi oscillations

We investigate individually the impact of δ , κ and Γ on the Rabi cycles seen in a ground state bleaching measurement to find out which of them yields a stretching of the Rabi cycles. The experimental arrangement is sketched in figure 7.19a. The orthogonally polarized pulses arrive at a fixed delay Δt_p . The X_1 exciton transition is pumped with a variable pulse area Φ . The groundstate population is measured by probing the monitor exciton X_2 with a pulse area of $\pi/2$. The pump pulse area is increased gradually from zero to 8π . For each value, the peak amplitude of the differential intensity spectrum is extracted and displayed against the pulse area, see figure 7.19b. We change only the optical properties of the pumped X_1 exciton. The pump probe delay is chosen such that it is at least three times the lifetime of the Dember field.

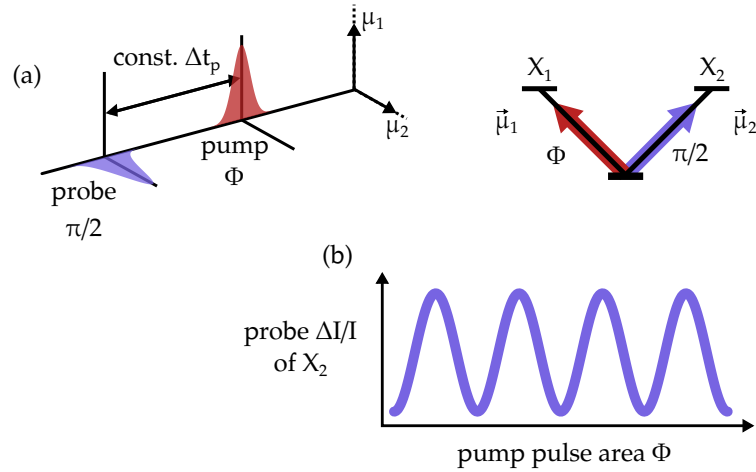


Figure 7.19: **a** Illustration of the pulse sequence and polarizations of the simulated experiment. The pump pulse is aligned to the X_1 -transition and has a variable pulse area. The probe pulse is aligned to the X_2 -transition and has a fixed pulse area of $\pi/2$. The pump-probe-delay Δt_p is also held constant. **b** For each pump pulse area, a differential intensity spectrum is calculated, its resonance peak height extracted and plotted against the pulse area.

7.2.2.1 Detuning and Dephasing

We first investigate the impact of detuning. We substitute $\delta(t)$, as defined by eq. 7.42, into the master equation and calculate differential intensity spectra as described in section 7.1. The dipole moment and the dephasing rate we leave unchanged. Figure 7.20a shows the Bloch vector evolution of an exciton pumped with a pulse area of 3π , detuned by the Dember field as defined by equation 7.34. The saturation field strength is set to $F_m = 100$ kV/cm and α is 125 kV/cm/cycle². At the given pulse area, the peak field strength is -92 kV/cm and the peak detuning is -1.2 meV. In saturation, the peak detuning is -1.5 meV. The Bloch vector initially rotates around the u -axis, as it would without the Dember field, but quickly starts to deviate. The exciton phase relative to the optical field runs off. This has large impact especially in the tail of the pulse where the pump rate is low while the detuning is large due to the persistence of the Dember field.

Figure 7.20b presents the corresponding power sweeps of the differential intensity. For small peak detuning (blue curve), the signal is still modulated, but never reaches the maximum and minimum values again. Comparing with fig. 7.20a we see that this is due to the Bloch vector missing the poles of the Bloch sphere. Note that there is no stretching of the Rabi oscillation due to the detuning. For large detuning (red curve), the differential signal settles at a value close to one half of the maximum value. We can understand why this is by considering again the loss-less optical Bloch equation, describing the

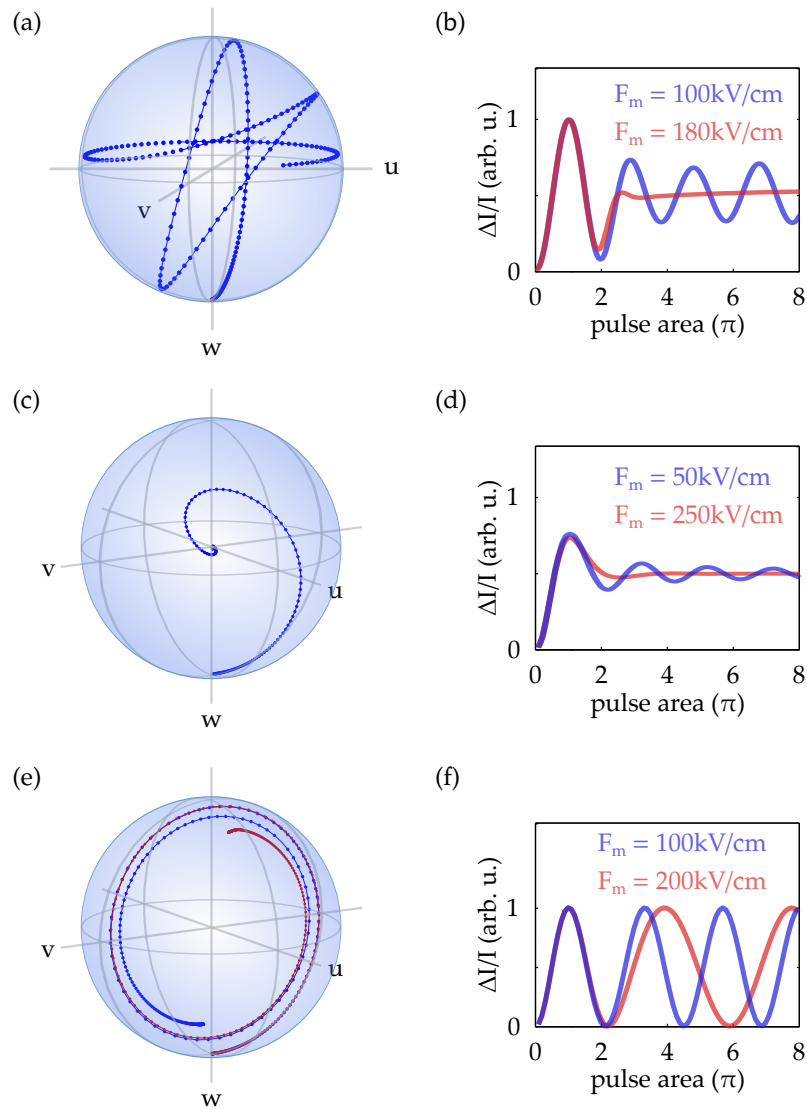


Figure 7.20: This figure compares from top to bottom the impact of detuning, dephasing and a change of the dipole moment during the pump process, induced by the Dember field. **a**, **c** and **e** show the Bloch vector traces. Without the Dember field, the pump pulse would rotate the Bloch vector around the u-axis with the vector tip nearly on the surface of the sphere. The Dember field significantly alters the trace. In the case of dipole moment change, the effect is merely to slow down the evolution. Two curves with a different value of α are shown for comparison. **b**, **d** and **f** show for these cases the dependency of the peak spectral differential intensity on the pulse area. Each plot shows two curves for comparison of different saturation limits.

change of the Bloch vector \vec{S} due to the optical torque generated by \vec{M} ,

$$\frac{d\vec{S}}{dt} = \vec{M} \times \vec{S}, \quad \vec{M} = (\Omega, 0, \delta) \quad . \quad (7.16 \text{ revisited})$$

Without the Dember field, \vec{M} points along the u -axis, merely changing its magnitude during the pump-process. This leads to the usual Rabi cycles with the Bloch vector rotating around the u -axis in the v - w -plane. In contrast, when there is a Dember field, \vec{M} will first point along the u -axis and then starts to move gradually to the w -axis as indicated by figure 7.21a. This is because the detuning due to Stark's effect follows the optical pumping with a small temporal lag, see figure 7.21b. If the change of \vec{M} is slow compared to the precession of \vec{S} , then \vec{S} will always move in a plane going through the origin and being orthogonal to \vec{M} . This plane follows the change of \vec{M} , which finally must point along the w -axis due to the long persistence of the detuning compared to the optical field. In this way, the Bloch vector will always rotate in the equatorial plane after the pump process, giving rise to the differential intensity signal shown in figure 7.20b. This process is similar to *adiabatic following* as described by Allen and Eberly in [73], although in their case, the Bloch vector is nearly parallel to \vec{M} .

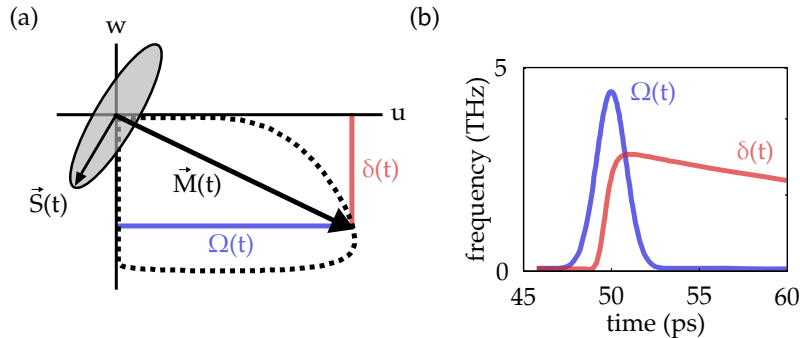


Figure 7.21: **a** shows the motion of \vec{M} during the pump process. It moves in the u - w plane on the curve indicated by the dashed line, depending on the evolution of $\Omega(t)$ and $\delta(t)$. The Bloch vector \vec{S} moves in a plane perpendicular to \vec{M} if the precession frequency is large compared to the change of \vec{M} with time. **b** Shown is the small temporal lag of the detuning δ due to the Dember field with respect to the optical pumping with the Rabi frequency Ω . If Ω and δ are of the same order, the effective motion of \vec{M} resembles a rotation from the u -axis to the w -axis.

As said, the movement of \vec{M} must be slow compared to the precession. Otherwise the precession plane will no longer go through the origin as is the case for small peak detunings due to the dember field (see fig. 7.20b).

The outcome for increased dephasing is similar, although the mechanism is different. The coherence of the exciton is destroyed already

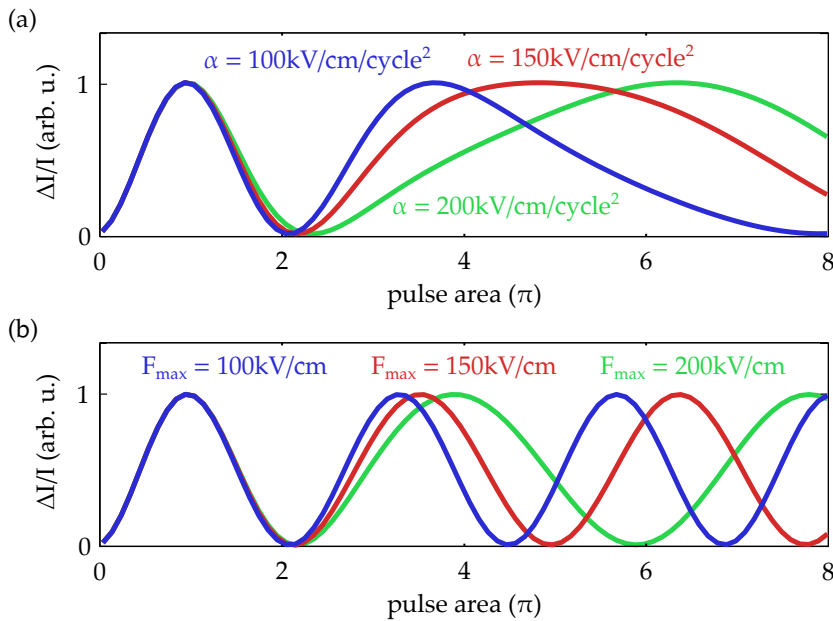


Figure 7.22: **a** The graph compares Rabi cycle stretching with different values of α . The larger α is, the faster the stretching sets in. **b** The graph compares Rabi cycle stretching with different values of the maximum photo carrier number F_{m} . α was chosen such that saturation sets in already in the first Rabi cycle. After saturation, the stretching does not further increase with the pulse area.

during the pump process, which means that the Bloch vector spirals towards the center of the Bloch sphere (see fig. 7.20c). As consequence, the peak differential intensity will always settle at a value of 0.5. For small peak dephasing (blue curve in fig. 7.20d), there is still some modulation, which is diminished with increasing pulse area. In the limit of very large dephasing we have a situation similar to incoherent pumping with a population limit of 0.5 (red curve).

7.2.2.2 Reduction of the dipole moment

A pure stretching is only found when the Dember field reduces the dipole moment of the exciton. This merely scales the effective pulse area of the pump pulse. Figure 7.20e compares the Bloch vector traces of two excitons whose dipole moment is reduced by the Dember field. The saturation field strength of the two cases is $F_{\text{m}} = 100 \text{ kV/cm}$ (blue curve) and $F_{\text{m}} = 200 \text{ kV/cm}$, corresponding to a dipole moment of $\mu = 0.85 \mu_0$ and $\mu = 0.56 \mu_0$. Consequently, the total rotation angle of the red trace angle is smaller compared to the blue trace. The Rabi cycles seen in the differential intensity (fig. 7.20) are stretched accordingly. The modulation depth is the same as without the Dember field, as neither the interaction phase nor the dephasing rate is affected by the change of μ . Thus, the effect seen in the data may be the result of a

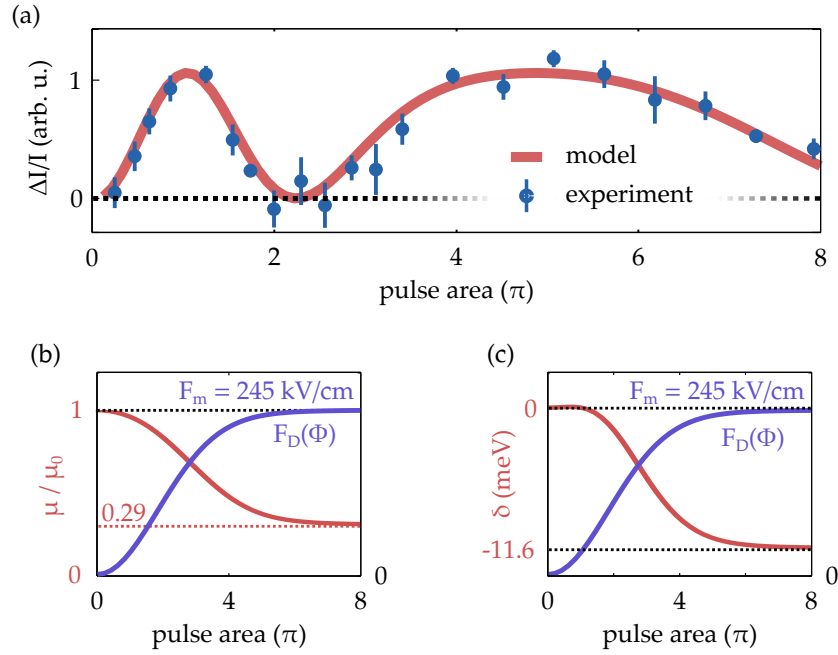


Figure 7.23: **a** Shown is a comparison of the model prediction and the experimentally observed Rabi cycles. The saturation field strength is 243.5 kV/cm . The detuning and the dephasing due to the Dember field were switched off. **b** Shown is the dipole moment with respect to the pump pulse area (red scale) that we use to reproduce the data in (a). The blue curve indicates the corresponding Dember field amplitude. **c** The graph shows the detuning (red curve) with respect to the pulse area, as would be expected for the Dember field amplitude (blue curve) we use to reproduce the data in (a).

diminished dipole moment alone. The onset and amount of stretching depends strongly on α and F_m . Figure 7.22a and b compare stretched Rabi cycles for different values of α and F_m respectively. Note how the value of α does control the acceleration of the stretching. F_m limits the stretching to a certain value. After saturation, the Rabi cycle period is constant.

Note that in the ground state bleaching experiment, the probe pulse absorption is determined by the remaining population of the pumped exciton, which during the free decay of the exciton is not altered by the mere presence of an external DC electric field. It is the preparation of the initial excited state during the interaction with the pump pulse that is altered by the Dember field, agreeing with the fact that we find no systematic dependency of the Rabi cycle stretching on the pump-probe delay [70].

7.2.3 Comparison of theory and experimental data

Figure 7.23a shows a comparison of the model prediction and the data, done by adapting F_m and α . We ignore in this case the detuning and dephasing by the Dember field. The parameters we set to $\alpha = 143.5 \text{ kV/cm/cycle}^2$ and $F_m = 243.5 \text{ kV/cm}$. The half-life time of the Dember field is 100 ps and the duration of the pump pulse and the probe pulse is 2 ps. The corresponding Dember field amplitude and the dipole moment are presented with respect to the pulse area in figure 7.23b. Note that a reduction of the dipole moment by 70% is necessary to match the data, requiring the high value of $F_m \approx 250 \text{ kV/cm}$. At this field strength we must extrapolate the value of μ from the calculated values in table 7.1. Assuming that the extrapolation is correct, we also would expect a detuning close to -12 meV (see fig. 7.23c), which is not in agreement with the data. Moreover, Christian Wolpert et al. directly measured the power-dependent detuning of the quantum dot due to the Dember field by pumping the substrate alone [70] in a dual color pump-probe experiment. The outcome of these measurements show that, if table 7.1 is correct, the Dember field strength must be on the order of only a few tens kV/cm in our samples. At these field strengths, the stretching of the Rabi cycle is negligible. A stronger impact of the Dember field we can only obtain when we assume that the field is tilted [70]. Since the confinement potential of the electron wavefunction and the hole wavefunction is much weaker in the lateral direction, the Stark effect is stronger. However, the detuning would also increase accordingly. The careful conclusion from the fit is that the data may be explained by a reduction of the dipole moment due to the Dember field, but is not consistent with the properties of the quantum dot that we estimate theoretically.

7.2.4 Outlook

Our results show that the Dember field alters the optical properties of the quantum dot significantly. We have shown that in principle, the observed experimental data can be explained by a reduction of the dipole moment of the pumped exciton due to the Dember field. However, given the estimated response of our quantum dot to electric fields, unreasonably high Dember field amplitudes of 250 kV/cm are necessary to achieve the reduction at a vertically oriented field. It was shown that the Stark effect is much stronger when the field is tilted [70], yet, due to the symmetry of our structure there is no reason to assume that there is such a tilting. The main question that should be addressed is thus whether the values given in table 7.1 agree with the properties of the real dots. Both the optical properties of the quantum dot in presence of an electric field and the strength of the Dember field should be investigated experimentally.

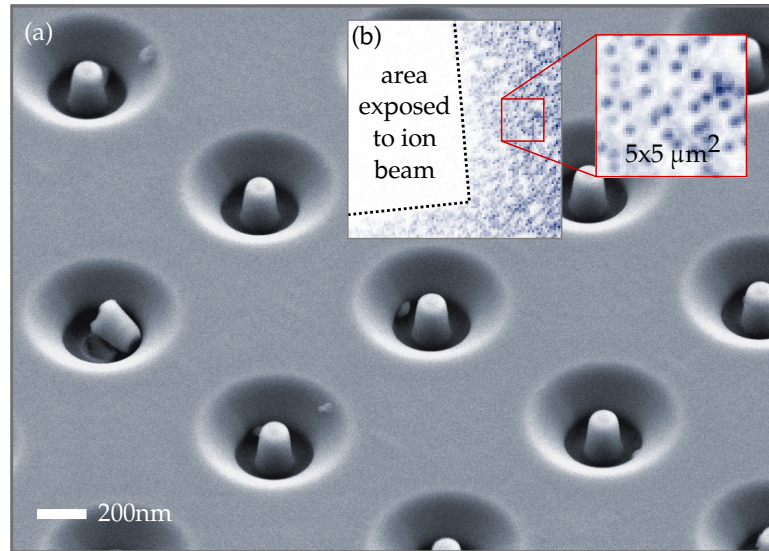


Figure 7.24: **a** A scanning electron microscope image of pillars manufactured by focused ion beam milling. The diameter of the pillars is 150 nm. **b** shows a confocal scan of the quantum dot luminescence emission. The area enclosed by the dashed lines was exposed to the gallium beam. Obviously both the quantum well and the quantum dots are destroyed in this region. A zoom to a $5 \times 5 \mu\text{m}^2$ area shows that the luminescence emission comes from single emitters.

Additionally, we can make use of the fact that the effect of the Dember field on the quantum dot must depend on the shape of the charge clouds and their relative position and investigate how a tilting of the field may affect the quantum dot properties. We have taken a first step into this direction by embedding the quantum dots in slim pillars instead of bulk material. This is done by removing the material around the quantum dot with a focused ion beam. The pillars are produced with several diameters and arranged in a regular pattern. The quantum dots are distributed randomly and a tilted field is expected when the quantum dot by chance is located off-center. An scanning electron microscopy image of the resulting samples is shown in figure 7.24a. The shown pillars have a diameter of 150 nm. However, it turns out that the quantum dots are destroyed by gallium contamination due to the ion beam and do not show any optical emission anymore. This is illustrated in fig. 7.24b, which shows an overlay of a bright field microscope image of the structure and a luminescence map of the same area. The inset shows that in the area illuminated by the ion beam, no luminescence is observed. At other areas, the emission of single quantum dots is found (see inset). It seems that the quantum dots are destroyed even when they are not directly illuminated by the ion beam. The same is true for the quantum well. Even the GaAs substrate luminescence is greatly diminished.

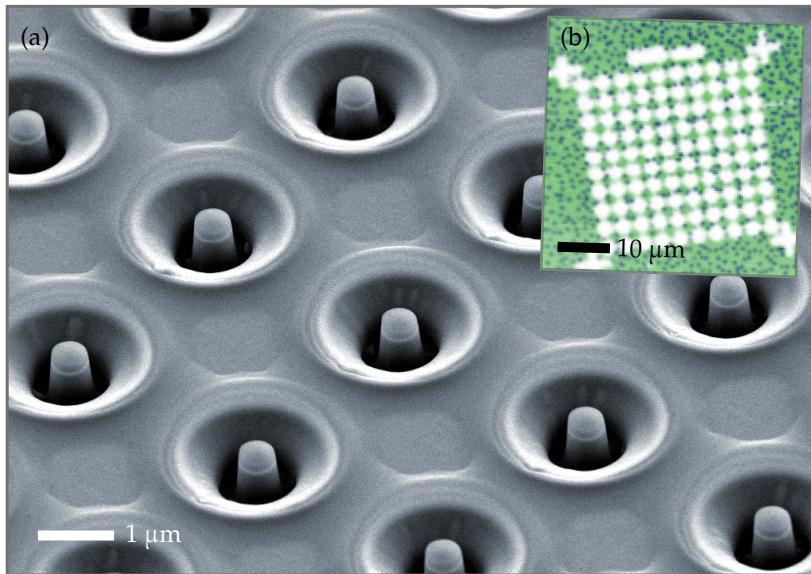


Figure 7.25: **a** A scanning electron microscope image of pillars manufactures with a PMMA capping layer to protect the quantum dots from gallium ions. The PMMA layer is visible on top of the pillars and on the sample surface. **b** shows confocal scans of the quantum well luminescence emission (green) and the quantum dot luminescence emission (dark blue) on the pillar structure.

To protect the quantum dots during the ion beam milling we spin-coated a 75 nm thick PMMA capping layer on top of the sample before the milling process. The idea is that the PMMA shall block indirect illumination by the nearby gallium beam. Figure 7.25a shows a scanning electron microscope image of the resulting structure. The leftovers of the PMMA layer are visible on top of the pillars and the nearby sample surface. After fabrication, the leftover PMMA is removed with acetone. Figure 7.25b indicates that the protection layer has a clear effect on the luminescence. Shown is again the overlay of a bright field microscope image of the structure and a luminescence map. Both the quantum well emission (green) and the quantum dot emission (dark blue) are shown. Compared to the sample without protection layer, quantum dots very close to the directly illuminated area do survive the milling process. Nevertheless, from within the pillars, we observe neither from the quantum well nor the quantum dot any emission. The probability that just by chance none of the observed pillars contains a quantum dot is very low. We observed structures of various diameters and on none we observed any emission from the quantum dots in the pillars. Also, the lack of quantum well emission indicates that the quantum dots are destroyed.

A possible alternative to focused ion beam milling is reactive ion etching, which implies a pre-structuring of a PMMA layer on the sam-

ple surface and subsequent etching. This technique has successfully been tested on other devices and could be used on future samples.

DELOCALIZED STATES OF AN INHOMOGENEOUS
EMITTER NETWORK

Up to now, we considered single, isolated quantum dots. Their optical properties are nowadays well understood and we have seen in the former sections that in experiments they behave as expected. The next step is the combination of individual quantum dots to form an optical quantum network, its quantum state extending over all the constituents of the network. The creation of quantum networks is desired because they open a new field, quantum information processing. However, the question which type of system is the best to create such networks is not answered. Single quantum dots embedded in a semiconductor matrix are a promising candidate since they provide high stability and are easily linked to the outside world by optics and electronics. Yet, although it is possible to create quantum dots of very high quality, it is challenging to form networks: The emitters must maintain coherence over substantial periods of time while coupling via routing elements, the latter specifically designed and positioned with respect to the emitters with nanometer precision. Much effort is put into technologies to master these challenges. For example, Pfeiffer et al. recently showed that with multi-step electron beam lithography, metallic nanoantennas can be placed with an accuracy of 11 nm on top of semiconductor quantum dots [83].

But networks can, alternatively, be formed also without a controlled routing. A direct, coherent coupling and formation of a delocalized state within an ensemble of randomly distributed semiconductor quantum dots was already shown by Scheibner et al., observing the narrowing of the ensemble emission linewidth with the number participating emitters [67], similar to J-aggregates. It was done by etching parts of the substrate away, restricting the ensemble size and thus changing the properties of the delocalized state. So an alternative approach to study ensemble networks could be to structure the shape of a randomly distributed ensemble of semiconductor quantum dots, for example by etching away certain parts, locally implanting defects or by placing plasmonic near field antennas in close proximity of the dots to locally enhance or suppress a coupling. In this section we begin to investigate how the delocalized states of an ensemble depend on the local environment and how the local distribution of emitter eigenenergies does affect the ensemble states. Furthermore, we investigate how the ensemble could be studied or manipulated using optics. We start with the introduction of the formalism to describe the delocalized states, inspired by the work of Cho[84]. Then

we study the delocalized states of a rectangular grid of semiconductor quantum dots, subject to inhomogeneity of their local environment, by solving the eigenvalue problem of the time-independent Hamiltonian. In particular, we use the participation ratio to quantify how much a state is delocalized over the network. Finally, we discuss how a coupled ensemble can be studied optically by calculating the transition dipole moments of the delocalized states.

8.1 FORMATION OF DELOCALIZED STATES

The interaction of light with semiconductor quantum dots is well understood. As we have seen in the last sections, it can be modeled by a V-atom, or in the ideal case of only one exciton resonance, as two-level-system. Hence, the straight forward approach to model the optical response of a coupled ensemble of quantum dots would be to describe it in terms of the optical response of an ensemble of coupled two-level-systems. We first look for the delocalized states of the ensemble, without optical excitation. Afterwards, the two-level-system interaction with the optical field can be transformed into the delocalized state picture to find out how the ensemble interacts with laser pulses and so on.

For semiconductor quantum dots, the two-level-system states would be the crystal ground state $|0\rangle$, and the occupied state $|1\rangle$, with an electron-hole pair populating the S-shell states (see fig. 8.1). An optical excitation, for example a short laser pulse with a pulse area of π , just switches between the states. This is the link of the ensemble to the outside world. For example, a single two-level-system can be addressed with a near-field-probe or a plasmonic antenna [85, 86]. In the following we understand the states $|0\rangle$ and $|1\rangle$ as number states, counting the number of excitations in the two-level-system. So $|0\rangle$ means no excitation, $|1\rangle$ means one excitation, and $|n\rangle$ would correspond to n excitations within the two-level-system. If the excitation is fermionic, a maximum of only one excitation is allowed per two-level-system. The usage of number states seems unnecessary, but it has the advantage that the formalism is easily extended to bosonic two-level-systems, such as optical resonators.

The transition between the number states is described by the ladder operators,

$$\begin{aligned} |n+1\rangle &\propto \hat{a}^\dagger |n\rangle, & 0 &= \hat{a}^\dagger |n_{\max}\rangle, \\ |n\rangle &\propto \hat{a} |n+1\rangle, & 0 &= \hat{a} |0\rangle. \end{aligned} \quad (8.1)$$

By definition, an excited fermionic two-level-system cannot be further excited. Furthermore, occupation cannot be removed from a two-level-system in the ground state. Any physical process that changes the number state of a two-level-system is described in terms of the ladder operators. For example, we can express an interaction J_{ab} that pe-

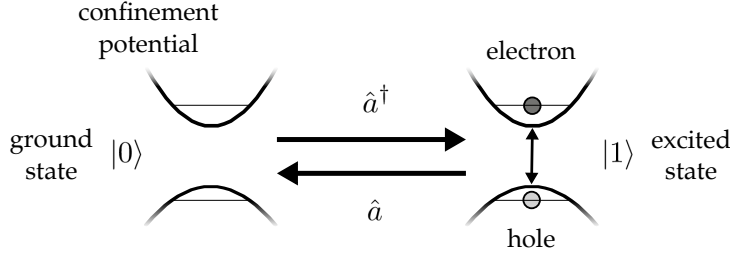


Figure 8.1: Illustration of states in a quantum dot two-level-system. If the two-level-system is in the groundstate $|0\rangle$, no electron-hole-pair exists. If the two-level-system is in the excited state $|1\rangle$, a single electron hole pair occupies the S-shell states defined by the confinement potential. Transitions between the ground state and the excited state are described by the operators \hat{a}^\dagger and \hat{a} that act on the ground state and excited state vectors.

periodically exchanges the occupation of two two-level-system a and b at a rate ω_{ab} by

$$\begin{aligned} \hat{J}_{ab} &= \hbar\omega_{ab} \cdot (\hat{a}_a^\dagger \hat{a}_b + \hat{a}_a \hat{a}_b^\dagger) \\ &\rightarrow \hat{J}_{ab} |0_a, 1_b\rangle = \hbar\omega_{ab} \cdot |1_a, 0_b\rangle \quad . \end{aligned} \quad (8.2)$$

The product state $|1_a, 0_b\rangle$ means that two-level-system a is occupied with one excitation while two-level-system b is not occupied.

A ensemble of two-level-systems is represented by the product state of the individual two-level-system number states. In principle and without restriction, each of the ensemble members can be occupied or not. However, in the context of optical excitation, a multi-photon-process would be necessary to excite delocalized states with more than one occupied two-level-system. For the present, basic discussion this is not important and we restrict the number of occupied two-level-systems in the ensemble to one, reducing the dimensionality of the Hilbert space and making the formalism much simpler. However, we have to keep in mind that states with more than one excitation in the ensemble possibly play an important role when inhomogeneity of the eigenenergies are large. This will be a topic of future studies.

An ensemble with a single occupation is described by the product states

$$|\mathbb{1}_n\rangle = |0_0, 0_1, \dots, 0_{n-1}, 1_n, 0_{n+1}, \dots, 0_N\rangle, n = 1, 2 \dots N \quad . \quad (8.3)$$

These vectors mean that none but the n-th two-level-system is occupied. They form a basis of the subspace with a single occupation within the ensemble. They are also eigenvectors of the system if there is no coupling between the two-level-systems.

Each of the two-level-systems has its own set of ladder operators, denoted by adding its label as an index, like in equation 8.2. An en-

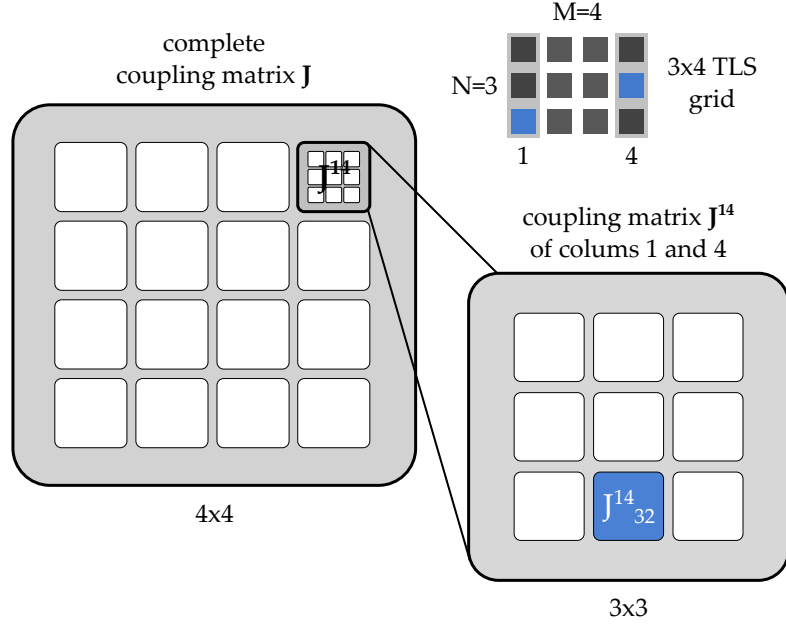


Figure 8.2: The figure illustrates the structure of the coupling matrix J of a coupled ensemble of two-level-systems by example of a 3×4 -grid, as sketched in the upper right. On the top level, J is a 4×4 matrix (left), the entries of which are the 3×3 -sub-matrices J^{mv} (right). These describe the coupling of the columns m and v of the grid. The coupling between n -th two-level-systems in column m with the u -th two-level-system in column v this denoted J_{nu}^{mv} .

semble state $|\mathbb{1}_n\rangle$ is generated from the ensemble ground state $|0\rangle$ by applying the corresponding ladder operator,

$$|\mathbb{1}_n\rangle = \hat{a}_n^\dagger |0\rangle \quad . \quad (8.4)$$

Because we restrict the occupation number in the ensemble to one, we require that $\hat{a}_n^\dagger \hat{a}_m^\dagger \stackrel{\text{def}}{=} 0$. Occupation is removed from the ensemble in an analogous way,

$$|0\rangle = \hat{a}_n |\mathbb{1}_n\rangle \quad . \quad (8.5)$$

The coupling operator of the ensemble is given by the sum of the individual coupling terms as described by eq. 8.2,

$$\hat{J} = \sum_{n,m} \hbar\omega_{nm} \cdot (\hat{a}_n^\dagger \hat{a}_m + \hat{a}_n \hat{a}_m^\dagger) \quad . \quad (8.6)$$

If each state $|\mathbb{1}_n\rangle$ is associated with the energy $\hbar\omega_n$, the total Hamiltonian reads

$$\hat{H} = \sum_n \hbar\omega_n \hat{a}_n^\dagger \hat{a}_n + \hat{J} \quad . \quad (8.7)$$

At this point we must define the geometry of the grid, which determines the coupling energies. The studied system is a plane

of randomly distributed two-level-systems, with normal distributed eigenenergies. In this work, we only consider the inhomogeneity of the eigenenergies. The position randomness is studied in future steps.

Before we include any inhomogeneity, we start with a two-dimensional, rectangular grid of identical two-level-systems. The number of rows is termed N and the number of columns is termed M . We choose a pair-wise isotropic coupling potential proportional to $1/d^3$ where d is the distance between the two-level-systems. This is similar to the interaction of (anti)parallel dipoles. For the present discussion, the choice of the coupling law is of minor importance. It mainly defines the shape of the delocalized states and can be adapted as needed.

To get a matrix representation of the Hamiltonian, we label each two-level-system by its coordinate in the grid, e.g., the two-level-system in the n -th row and the m -th column has the label (n, m) . We also rename the state vectors, $|\mathbb{1}_n\rangle \rightarrow |\mathbb{1}_{nm}\rangle$, to include position information. The coupling energy between two-level-system (n, m) and two-level-system (u, v) is denoted by $\hbar J_{nu}^{mv}$, and depends on the distance of the two members of the grid,

$$J_{nu}^{mv} = -\frac{\omega_c}{\sqrt{(n-u)^2 + (m-v)^2}^3}, \quad n \neq m, u \neq v, \quad (8.8)$$

where ω_c is the coupling rate between next neighbors. Additionally, we define the coupling energy of a two-level-system with itself to be its eigenenergy,

$$\hbar J_{nn}^{mm} = \hbar \omega_{nm},$$

such that we can simply write $\hat{\mathbf{H}} = \hbar \cdot \hat{\mathbf{J}}$. Now we can represent $\hat{\mathbf{J}}$ as an $M \times M$ -block matrix, which is divided into $N \times N$ -sub-matrices \mathbf{J}^{mv} . Each of these sub-matrices contains the coupling constants of two columns of the grid. Figure 8.2 illustrates this scheme. The matrix elements of the Hamiltonian can be expressed as,

$$\hat{\mathbf{H}}_{N \cdot (n-1) + m, N \cdot (u-1) + v} = \hbar \cdot J_{nu}^{mv}. \quad (8.9)$$

To get the delocalized states, the Hamiltonian of the ensemble is diagonalized,

$$\hat{\mathbf{\Omega}} = \mathbf{U}^{-1} \cdot \hat{\mathbf{H}} \cdot \mathbf{U}. \quad (8.10)$$

The entries of the transformation matrix \mathbf{U} yield the delocalized states $|\varepsilon_j\rangle$ as superposition of the localized basis vectors,

$$|\varepsilon_j\rangle = \sum_{\forall n,m} (\mathbf{U}^{-1})_{nm}^j |\mathbb{1}_{nm}\rangle. \quad (8.11)$$

$P_{nm}^j = |(\mathbf{U}^{-1})_{nm}^j|^2$ can be understood as the probability to find the two-level-system at site (n,m) occupied if the coupled ensemble is in

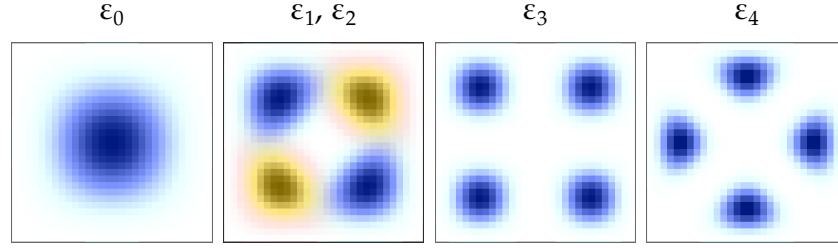


Figure 8.3: Eigenstates of a rectangular grid of two-level-system with a $1/d^3$ -interaction. Each pixel represents the probability to find the corresponding two-level-system occupied. From left to right, the energy of the eigenstates increases. Degenerate states are shown in different color.

the eigenstate $|\varepsilon_j\rangle$. We can visualize $|\varepsilon_j\rangle$ by plotting the occupation probabilities arranged on a grid like the two-level-systems. Figure 8.3 shows the five delocalized states with the lowest energy eigenvalues of a 30×30 grid of coupling two-level-systems.

The first question we like to investigate is how static disorder of the two-level-system eigenenergies does influence the delocalized states.

8.2 DELOCALIZATION AND STATIC SPECTRAL VARIANCE

Delocalization means that the excitation of the ensemble may be found on a large number of sites with significant probability. The larger the number of sites is, the more the state is delocalized. A widely used measure for the degree of delocalization is the inverse participation ratio, which can be imagined as the inverse of the average number of two-level-systems participating in a delocalized state. For a delocalized state $|\varepsilon_j\rangle$ it is defined by [84]

$$\frac{1}{N_j} = \sum_{\forall nm} [(U^{-1})_{nm}^j]^4 . \quad (8.12)$$

In the idealized case of identical eigenenergies of the two-level-systems and a finite coupling potential, the states spread over the whole grid. N_j is then determined by the geometry of the grid and by the coupling potential. However, in real semiconductor systems, the eigenenergies will depend on the local environment. To investigate how the degree of delocalization is influenced by that, we create a map that describes the variation of the eigenenergies depending on the position in the grid. In the simplest case the eigenenergy of each two-level-system is drawn from a normal distribution, but in reality those of neighboring two-level-systems may be correlated, as they share nearly the same environment. We establish a spatial correlation by low pass filtering the distribution of eigenenergies. In this way, various kinds of eigenenergy landscapes can be created and adapted

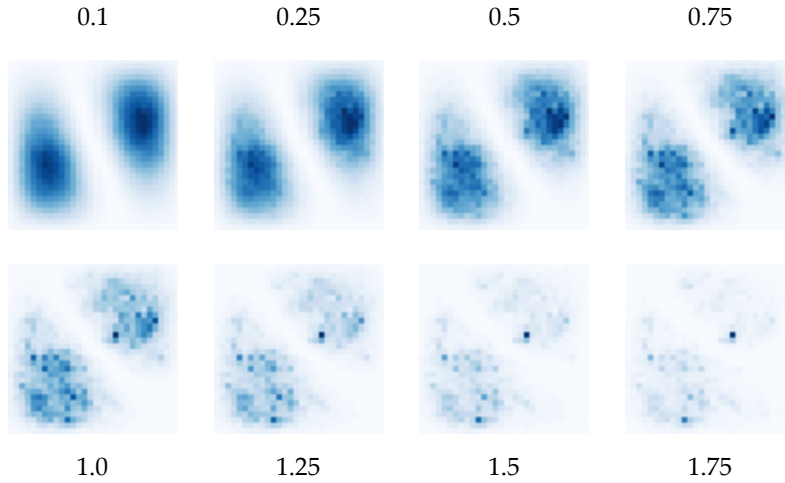


Figure 8.4: Shown is the degradation of a delocalized state with increasing $\Delta\omega/\omega_c$. Shown is the probability that the excitation is found at a given lattice site, separately normalized to the maximum for each subfigure. The numbers next to the patterns denote the corresponding value of $\Delta\omega/\omega_c$.

to the studied systems. This may be especially helpful when the energy landscape in a real system could be manipulated, for example by local strain or by placing material defects in a controlled way.

What happens if the eigenenergy landscape of the grid is not flat? First of all we expect that the influence depends crucially on the ratio between the variance $\Delta\omega$ of the eigenenergies and the coupling strength ω_c . In the limit of very low variance, we find the idealized case of delocalized states defined by the grid geometry and the potential. In the limit of very high variance, the perturbation of the system due to the coupling is so weak that the ensemble eigenstates approximate the single site occupation states, $|\varepsilon_j\rangle \approx |\mathbb{1}_j\rangle$. That is, if $\frac{\Delta\omega}{\omega_c}$ increases, then N_j decreases until only one two-level-system participates to the coupled states. The delocalized states degrade to the localized states. That is demonstrated in fig. 8.4, which shows the degradation of a delocalized state with increasing variance of normal distributed eigenenergies. The ratio $\Delta\omega/\omega_c$ is indicated by the numbers next to the graphs. We see that for $\Delta\omega/\omega_c < 1$, the delocalized state is still determined by the coupling and grid geometry. For larger variance, the excitation tends to localize on a ever smaller number of grid sites.

We use the participation ratio to quantify this behavior. It is not possible to track N_j of an individual state when varying $\Delta\omega$, since the eigenstates of the ensemble for different values of $\Delta\omega$ are not related to each other except that they may look similar. Instead, we consider the average $\langle N_j \rangle$ of the whole ensemble. Figure 8.5a shows $\langle N_j \rangle$ in dependency of $\Delta\omega/\omega_c$ in a double-logarithmic scale. Here we see that the ensemble as a whole degrades. The transition between delo-

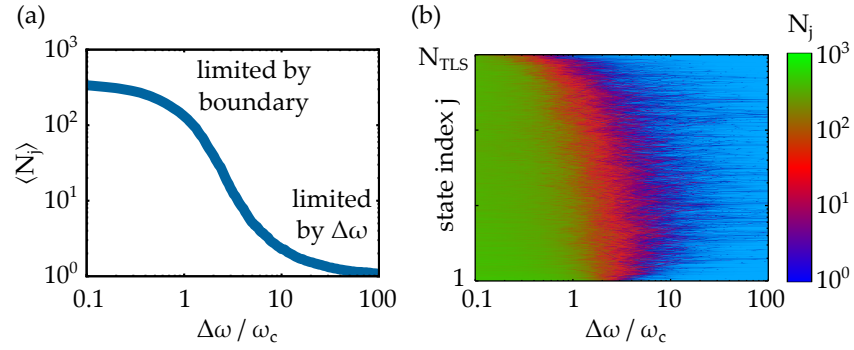


Figure 8.5: **a** shows the average participation ratio $\langle N_j \rangle$ in dependency of $\Delta\omega / \omega_c$. **b** shows the dependency of the participation ratio N_j for each state separately in a color plot. For each value of $\Delta\omega / \omega_c$, the states are ordered by their eigenenergy.

calization, which is determined by the coupling and grid geometry, and localization, which is determined by the local eigenenergy landscape, occurs when $\Delta\omega / \omega_c \approx 1 - 10$.

To some extent it is possible to see how individual delocalized states change when the eigenenergy distribution changes. Figure 8.5b shows N_j in a color plot for each of the delocalized states. The states are ordered along the y-axis according to their eigenenergy. We see that, unless the eigenenergy is high, the transition between delocalization and localization happens for most states within $\Delta\omega / \omega_c \approx 1 - 10$. Note also that the plot has path-like structures and that some states seem to adiabatically change with $\Delta\omega$. This behavior is not very much pronounced since the fluctuations are random and without any spatial correlation. It is related to localization of the excitation to energetic traps, a region where the density of two-level-systems with similar eigenenergies is larger by coincidence. This gets more clear if we consider spatially correlated fluctuations of the two-level-system eigenenergies. Figure 8.6 shows N_j as a function of $\Delta\omega / \omega_c$ for two energy landscapes with correlations of the eigenenergies of neighboring two-level-systems. $\Delta\omega$ has here a different meaning compared to the uncorrelated case. In the former, for every $\Delta\omega$, a new set of eigenenergies was drawn from a normal distribution. But here we like to analyze how the states change for a given energy pattern when its roughness does increase, that is to say, we generate only one pattern of eigenenergies from a normal distribution and then scale it with $\Delta\omega$.

The first pattern is a low-pass filtered normal distribution and shown in figure 8.6a. As we have said, the delocalized states of ensembles for different values of $\Delta\omega$ are not related to each other. But since the spatial pattern of the energy landscape stays the same, the states change adiabatically when $\Delta\omega$ is increased. This is illustrated on the right part of the figure where we show for different values

of $\Delta\omega$ delocalized states with the same index (sorted according to the eigenenergy) laid over the eigenenergy map. The figure shows the transition of the delocalized state into a more localized one. Even though for $\Delta\omega/\omega_c = 0.1$ the state is perturbed, its shape is clearly determined by the grid geometry. In contrast, if $\Delta\omega/\omega_c > 0.9$, it is determined by the local pattern of the two-level-systems eigenenergies. During the transition, the eigenenergy of the delocalized state also changes continuously, both because the scale of the energy map changes and because the state gets more and more localized to a small region of the map. This is better visible in the case of the second energy pattern, shown in figure 8.6b. Here, the eigenenergies of the two-level-systems have been raised or lowered artificially in certain parts of the pattern. In this case, some delocalized states change smoothly over large intervals of $\Delta\omega/\omega_c$ (see fig. 8.6c).

The artificial energy traps lead to the formation of sub-ensembles that are energetically separated from each other. The formation of such a sub-ensemble can be seen on the right side of figure 8.6b, where the delocalized state slowly evolves until it is limited to the trap region. Within the trap boundary the ensemble is still delocalized. Hence, localization can happen on multiple spatial scales. This has interesting implications, i.e., we can think of sub-ensembles that couple to each other, generating complex dynamics on multiple time- and length scales. The localization in the traps is also visible in the color plot of N_j in fig. 8.6b, resulting in a shift of the transition region to larger values of $\Delta\omega$. These are states that are extended within the trap region. Figure 8.6d compares the shape of delocalized states from the regions marked in the color plot by the white circles. We see that states in region A correspond to states in the low-energy trap (blue). The states in region B correspond to the high energy trap (red). The states in region C are located outside the trap region. For each region we averaged over a number of states to show that they all lie within a certain spatial limit.

8.3 OPTICAL EXCITATION OF AN ENSEMBLE

We have optical access to the ensemble via the individual two-level-systems, of which the interaction with optical fields is known. If the optical field couples to the k -th two-level-system at a rate g_k , the interaction can be written as

$$V_{\gamma k} = \left(g_k^* \hat{a}_k^\dagger |0\rangle \langle 0| + \text{h.c.} \right) , \quad (8.13)$$

where *h. c.* denotes the hermitian complex of the former term in the brackets. If a group K of two-level-systems couple to the optical field, the interaction is the sum over all individual interactions,

$$V_\gamma = \sum_{k \in K} \left(g_k^* \hat{a}_k^\dagger |0\rangle \langle 0| + \text{h.c.} \right) . \quad (8.14)$$

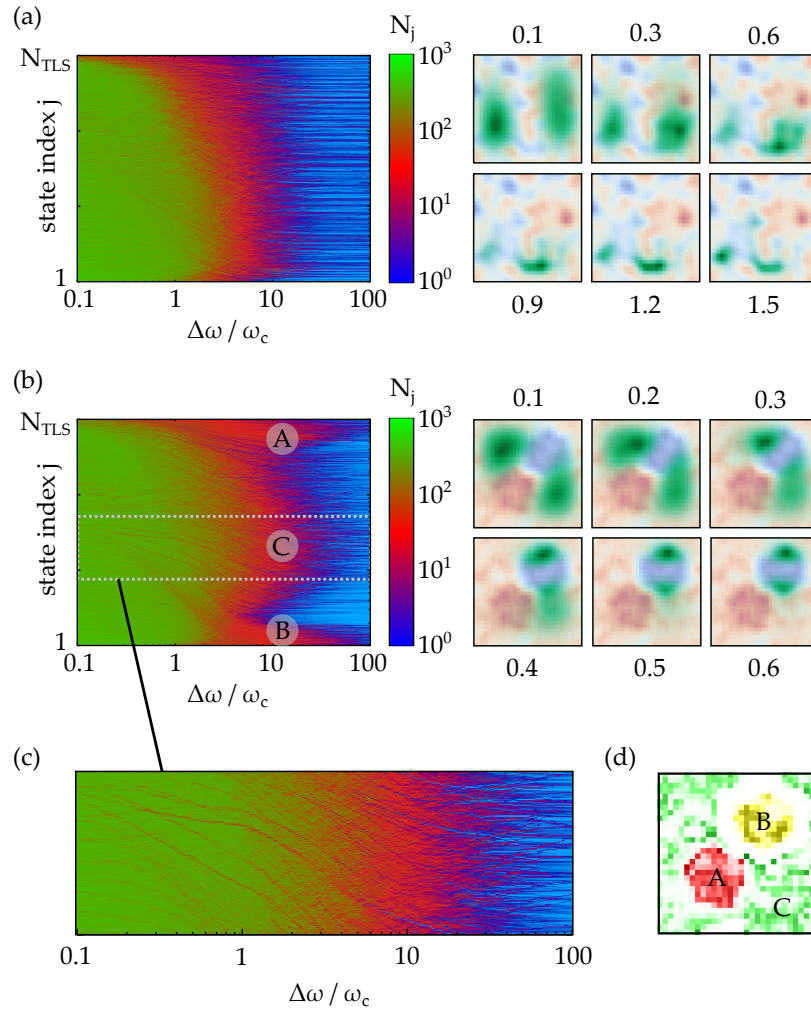


Figure 8.6: This figure shows how the participation ratio N_j and the pattern of the delocalized states depend on the correlation of the eigenenergies of neighboring two-level-systems. **a** shows on the left side, in dependency on $\Delta\omega/\omega_c$, the participation ratio N_j of a rectangular two-level-system grid with locally correlated eigenenergies. On the right, the pattern of the one of the low energy eigenstates of the coupled grid is shown in green, superimposed on the eigenenergy landscape of the grid. The numbers denote the corresponding value of $\Delta\omega/\omega_c$. **b** shows the same, but for a different pattern of eigenenergies including local traps. **c** shows a magnification of the area marked in the color plot in (b) to emphasize the continuous change of the eigenenergies of certain states. **d** shows color coded the averaged pattern of delocalized states within the energy ranges marked by the letters in (b). red, yellow and green color corresponds to states marked by the A, B and C-circle respectively. Clearly, delocalized states with similar eigenenergy correspond to areas with similar eigenenergies of the two-level-systems.

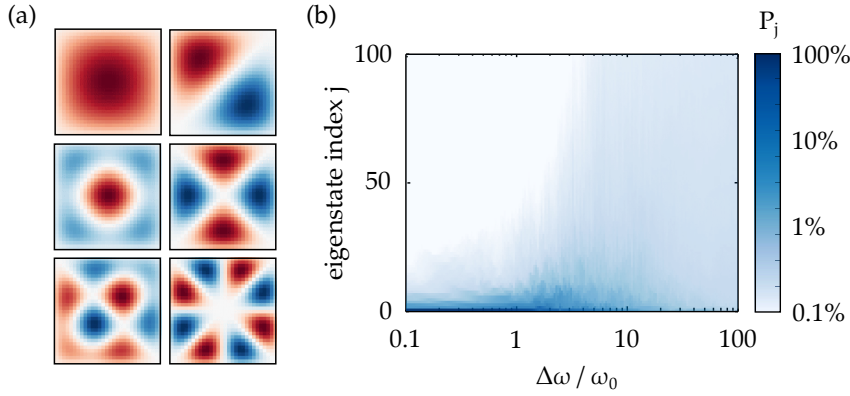


Figure 8.7: **a** Shown is the real part of the eigenvector coefficients $(U^{-1})_{nm}^j$ for a collection of delocalized states of a coupled ensemble of two-level-system. Red and blue colors denote positive and negative sign. For most states, the sum over the ensemble cancels to zero. **b** The color plot shows the probability P_j (see eq. 8.16) that an ensemble with static disorder is found in the delocalized state j after optical excitation. The state index axis is sorted by P_j in descending order (lower state index corresponds to higher P_j).

The transition probability into the delocalized state $|\varepsilon_j\rangle$ is given by the overlap integrals,

$$P_j = |\langle \varepsilon_j | V_\gamma | 0 \rangle|^2 \quad (8.15)$$

$$= \left| \sum_{k \in K} (u_k^j g_k^* + \text{h.c.}) \right|^2. \quad (8.16)$$

This is the coherent sum of the overlap integrals of the two-level-system states and the delocalized states. The fact that the sum is coherent means that interference takes place. The coupling rates with the optical field are complex numbers in general. Assume that they are of the form $g_k = g_0 \cdot \exp(i\phi_k)$, then it is possible to control P_j by adjusting the individual phases. This could be done, for example, by illuminating an ensemble of two-level-systems with a Gaussian laser beam, which has curved wavefronts except in the focal plane[87].

However, it is not clear if an ensemble of semiconductor quantum dots may extend over areas as large or even larger than a diffraction limited laser spot. If it is much smaller than the laser spot, all the ensemble members are excited with the same phase. As a consequence, P_j is zero for almost any delocalized state of an unperturbed ensemble. The individual terms in eq. 8.16 interfere destructively due to symmetry of the delocalized state patterns. That is shown in fig. 8.7a for some of the delocalized states of an ideal 30x30 ensemble. The graphs shows the amplitudes U_{jn} instead the probabilities $|U_{jn}|^2$ where red and blue colors correspond to positive and negative sign. It can be seen at a glance that the sum over the whole ensemble cancels to zero except for the first state.

We expect that inhomogeneity of the two-level-system eigenenergies distort the state patterns such that P_j is finite. This assumption is checked by calculating P_j for all eigenstates of the coupled ensemble while increasing the energy fluctuations just as before. This is shown in figure 8.7b. The state index is sorted by P_j . Only the one hundred states with the highest probability are shown. As expected, P_j is high only for very few delocalized states at small disorders. Only when the states begin to localize the probability to excite them gets higher. In the limit of very high disorder and complete localization of the states to one two-level-system, the probabilities are spread evenly over all states. So it is very hard to excite delocalized states with an extended electric field. Alternatively, near field probes may be used to translate far field optical excitation to a restricted number of ensemble members, for example an gold coated AFM tip can be used to scan the ensemble and find spots that preferably excite a certain group of delocalized states.

How can we measure optically if an ensemble couples at all? We can think of a number of indicators. For example, the luminescence emission lines of J-aggregates do narrow with increasing number of ensemble members[88]. This has also been observed in high density 2D quantum dot ensembles[67], the size of which has been controlled by cutting mesa out of the sample. The narrowing depends on the size of the mesa, which is taken as a proof of a coupled ensemble. What other possible optical probes can we think of?

Anti-bunching of photon emission from different positions in the sample is one possibility. Since the coupling is coherent and only one excitation is allowed in the ensemble, we would expect that we should never find two photons coming from the ensemble at the same time. Anti-bunching from excitons delocalized over macromolecules already has been already observed [89]. If disorder dominates over the coupling, the restriction to a single occupation is no longer fulfilled and anti-bunching should vanish.

Exciting and probing different spots on the sample would also indicate delocalized states. The probability to find emission from the ensemble at the n -th member when it was excited via m -th member is given by

$$P_{nm} = \left| \langle 0 | V_{\gamma m}^\dagger V_{\gamma n} | 0 \rangle \right|^2 \quad (8.17)$$

$$= \left| \langle 0 | V_{\gamma m}^\dagger \sum_j |\varepsilon_j\rangle \langle \varepsilon_j | V_{\gamma n} | 0 \rangle \right|^2 \quad (8.18)$$

$$= \left| \sum_j \left(g_m \cdot g_n^* \cdot U_{jm} \cdot U_{jn}^{-1} + \text{h.c.} \right) \right|^2 . \quad (8.19)$$

Notice that again this is a coherent sum and that interference effects may be observed. The emission from a certain position at the sam-

ple may be controlled by tuning the excitation phase of individual two-level-systems in the grid, enabling us to emit photons preferably at a certain position. Additionally, the emission from different spots should be coherent too. In this case, one would expect optical interference of the emitted photons. Imagine a rod-like ensemble that is excited in the center of the rod. Emitted photons are collected with a far field lens. Lets assume here that the ensemble may decay back into its ground state by emitting photons from either of its ends. This is equivalent to a double slit experiment: we cannot distinguish which path the excitation took in the ensemble. Interference patterns should be visible in the Fourier plane of the imaging objective. Similar experiments have been performed with plasmonic nanorods that coherently emitted photons at their ends due to a non-linear process[90].

8.4 SUMMARY AND OUTLOOK

In the present section we discussed the influence of the eigenenergy distribution of a grid of coupling two-level-systems on the delocalized eigenstates of the grid. In particular, we studied the influence on the shape of the delocalized eigenstates and on the number of two-level-systems that contribute to that state. In an unperturbed grid, with all eigenenergies being identical, the shape is determined by the boundary of the grid and the interaction between the two-level-systems. In our case, the interaction is a $1/d^3$ law, resembling dipole-dipole interaction. On a rectangular grid, it leads to drum-mode type of delocalized states (review fig. 8.3).

In the case of normally distributed eigenenergies without spatial correlation, the delocalized states simply degrade, meaning that the wavefunctions get more and more grainy, while their shape is still determined by the boundary or the grid. When the variance of the eigenenergies grows larger than the coupling energy between the neighboring two-level-systems, the ensemble starts to decouple, meaning that less and less ensemble members contribute to the delocalized states until, eventually, they localize to a single two-level-system. This was shown exemplary in figures 8.4 and 8.5. The transition between delocalization and localization happens in a range where the variance of the eigenenergies is 1–10 times the next neighbor coupling energy. This should be similar for any short ranged interaction like the $1/d^3$ -law.

The situation is different when there is spatial correlation between the eigenenergies of the two-level-systems on the scale of the interaction range. In this case we found that sub-ensembles form with delocalized states that are energetically separated from the rest of the ensemble states. The shape of the delocalized states of the sub-ensembles is defined by the local pattern of the grid eigenenergies, as was shown in figure 8.6. The regions where the eigenenergy differ-

ence between neighboring two-level-systems overcomes the coupling energy from natural borders of the sub-ensembles. The effect should depend very much on the ratio between the length scale of the coupling and the length scale of the eigenenergy correlation.

We found that the optical excitation of an ideal ensemble must be local, as the overlap integrals $|\langle \varepsilon_j | V_\gamma | 0 \rangle|^2$ (see eq. 8.16) that define the probability to excite a delocalized state $|\varepsilon_j\rangle$ average to zero if the excitation phase is homogeneous over the grid. This is due to the high symmetry of the states (compare with fig. 8.7). This restriction is lifted when the eigenenergy disorder grows larger than the coupling strength of neighboring grid sites. However, this situation is similar to coupling to individual two-level-systems, not to the ensemble. We thus have to use probes on length scales smaller than the extension of the delocalized states.

So far, we did only consider static disorder of the eigenenergies of the two-level-systems. As a consequence, the delocalized states are stationary. Relaxation of the delocalized states takes only place when the eigenenergies and the coupling strengths of the two-level-systems fluctuate in time. We can still describe the system in the delocalized picture, if the fluctuations are weak, but they induce a coupling between the delocalized states. In a real system we thus expect that the delocalized states will quickly relax and finally decay to the ensemble ground state.

One idea for future experiments is to induce these fluctuations in a controlled way to induce transitions between delocalized states. We have seen in section 7.2 that in semiconductor sample, local charge carrier clouds can be created with a ultrafast laser pulse and that these charge carriers induce electric fields that Stark-shift the resonance of a quantum dot. One could imagine that if pulses are applied to certain members of the ensemble, transitions into a number of preferred delocalized states can be induced. Imagine two sub-ensembles (similar to the energy traps in fig. 8.6b), separated by an energy barrier that prevents a coupling of the two ensembles. A laser pulse inducing a Dember field could temporally diminish the barrier, allowing a coupling of the ensembles. To do these kind of experiments, we have to further study technologies that allow us to create and structure grids of randomly distributed, coupling emitters.

MODULATION TECHNIQUES FOR CW-SPECTROSCOPY OF SINGLE QUANTUM DOTS

In the last chapters we focused on transient spectroscopy of single quantum emitters, using optical pulses with duration of a few hundred femtoseconds. The real advantage of such a setup is the temporal resolution, giving insight in dynamic processes within the emitter, and the possibility to prepare or manipulate the state of the emitter at wish. The temporal resolution comes at a cost: Spectral resolution is achieved and limited in our setup by using a spectrometer as detector. The emitters we use have linewidths that are by a factor of 5-10 smaller than we can resolve. Aside from preventing us to resolve the emission spectrum of the dots, it also degrades the signal-to-noise ratio. Furthermore, the optical pulses are spectrally broad, making it harder to study resonances individually if in close spectral proximity to each other. In this case they have to be resolved at least spatially, imposing restrictions on the sample structure. To overcome these restrictions we currently add a complementary, continuous-wave spectroscopy experiment with a narrow-line diode laser to the existent optical setup. Sacrificing the temporal resolution, the spectral resolution will be better by a factor 10–100, limited by the spectral width and stability of the laser emission. Depending on the information that we like to have about the quantum dot, either transient spectroscopy or continuous-wave spectroscopy will be used.

Still dealing with resonant spectroscopy, we need to discriminate the emitter signal from the large background of the excitation laser light, requiring a long integration time to beat the laser shot noise. At the same time we have to avoid low frequency noise, which gets more dominant the longer we integrate. This is done by shifting the emitter signal to high frequencies via amplitude modulation or fast scan techniques (see appendix B for an introduction to noise suppression by modulation). As a great deal of the setup design depends on the chosen modulation technique, we did preliminary tests of a number of techniques, which can be divided in two classes: modulation of the relative frequency detuning between the excitation laser and the emitter resonance, and modulation of the relative position of the excitation laser focus and the emitter. Both have to deal with the significant coherence length of the continuous-wave excitation light, which leads to parasitic interference effects that disturb the measurements. In this chapter, we compare the two classes. Section 9.2 discusses the modulation of the detuning between emitter and laser and in sec. 9.3 we discuss the modulation of the relative position of emitter and exci-

tation spot. Before we start with the discussion, we briefly introduce the experimental setup and the signal formation.

9.1 EXPERIMENTAL SETUP AND SIGNAL FORMATION

The central element of the experimental setup is a confocal microscope, illustrated in figure 9.1a. All beams coming from the light sources are mapped confocally to a single spot on the sample. Similarly, any light emitted from this spot is mapped confocally to a number of point detectors. Two pin hole mode filters prevent that other spots on the sample are illuminated by the excitation beams or that light emitted from other spots on the sample is detected. Spatial resolved images can be recorded by moving the sample relative to the focus of the microscope objective while recording the detector readings. This relative motion can be done by both moving the sample or the focus. As our emitters need cryogenic cooling and sit within a microscopy cryostat, we can move the sample either by moving the whole cryostat, which is slow due to its heavy weight, or by moving the sample within the cryostat, which requires actuators that fit within the limited space and work in vacuum at cryogenic temperatures. It is thus much easier to move the confocal spot on the sample, although this has its own drawbacks, as we will see later.

The focal spot is moved using a laser scanner as depicted in figure 9.1b. It is a combination of a tiltable mirror and a 4f-lens system, also termed telecentric system. After the tilt mirror the beam makes an angle with the optical axis. The telecentric system maps this angle to the back-focal-plane of the objective lens, which translates to a lateral shift of the focus on the sample. The telecentric system also guarantees that the beam is centered at the optical axis when crossing the back-focal plane, avoiding clipping while using the full aperture of the objective. Furthermore it ensures that the focus has a symmetric angular spectrum with respect to the optical axis. This is important if the sample is somehow sensitive to the angular spectrum.

The setup supports two operation modes, which are luminescence emission spectroscopy using a diode laser emitting at 532 nm for excitation in combination with a spectrometer plus a single photon counter as detector, and resonant continuous-wave spectroscopy using a narrow-line tunable diode laser in combination with a standard photo diode. The general procedure will be as follows. First, a confocal map of the luminescence emission is recorded with the single photon counter to locate the individual quantum emitters. Then the emitters are pre-selected according to their luminescence spectrum. Finally, resonant spectroscopy is performed on the pre-selected emitters by detecting with the photo diode the intensity reflected by the sample in dependency of the detuning between the laser emission frequency and the exciton resonance.

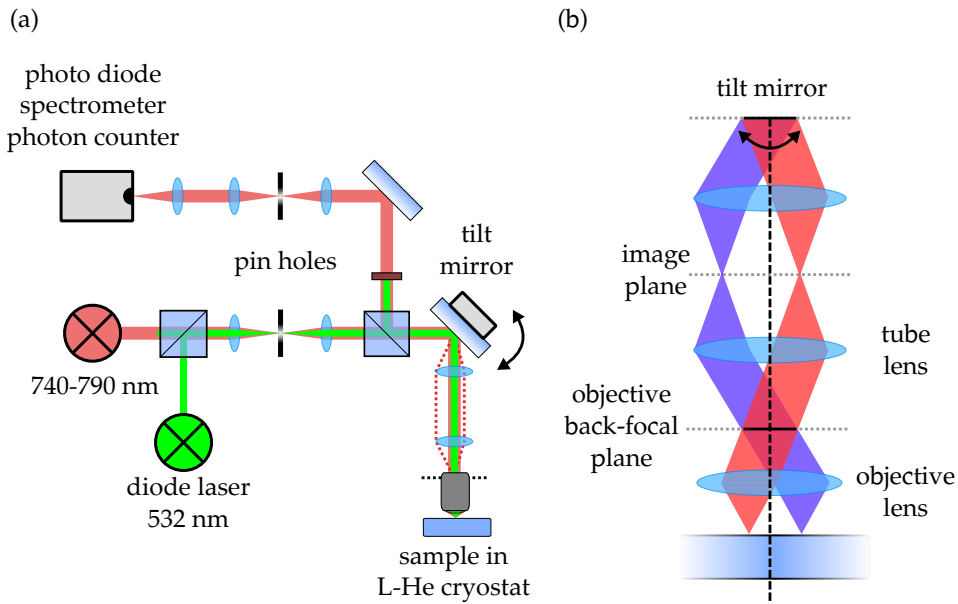


Figure 9.1: Simplified sketch of the continuous-wave spectroscopy setup. **a** shows the beam path. A tunable diode laser emitting at 740-790 nm is used as light source for resonant spectroscopy. A second diode laser emitting at 532 nm is used for luminescence emission spectroscopy. A pin hole is used as a mode filter, after which the beams are confocally mapped to the same spot on the sample surface. The lateral position of the optical focus can be controlled with a tiltable scan mirror in combination with telecentric optics (see sketch in (b)). The light reflected by the sample is again mode filtered with a second pin hole and collected by a number of detectors, including a photo diode, a spectrometer and a single photon counter. **b** sketches the working principle of the telecentric scanner. A 4f-lens system translates the angle induced by the tilt mirror to the back focal plane of the objective lens. The red and blue lines depict the beam path for two different angles. Dashed lines indicate focal planes. The focal points in the image plane are mapped to the sample surface. The beams must trespass the back-focal plane of the objective lens at the optical axis to avoid distortion of the angular spectrum within the focus.

SIGNAL FORMATION Figure 9.2 illustrates the signal formation. In contrast to transient spectroscopy (review fig. 7.2), the quantum emitter is illuminated with a single mode laser beam at frequency ω instead of broad band laser pulses. Of the light coming back from the sample, the main fraction is excitation light reflected from the sample surface. Only a tiny fraction is scattered by the quantum emitter. At the detecting photo diode, both fractions interfere and the intensity of the total field is measured. Given the electric fields of the surface

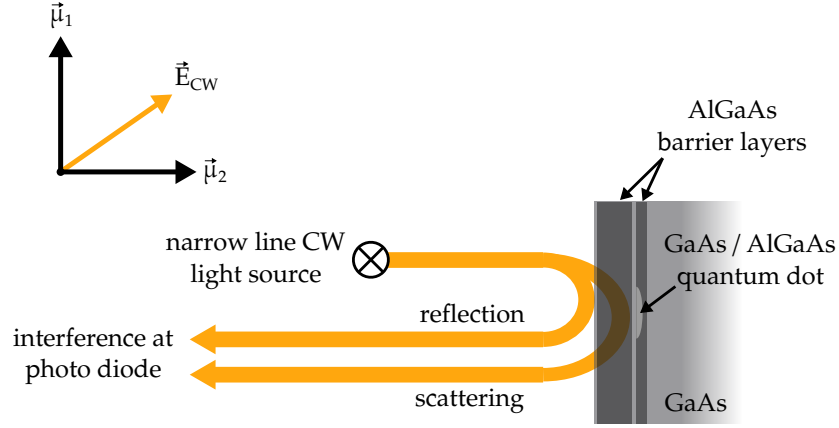


Figure 9.2: This figure illustrates how the the detected signal is formed. Light emitted from the diode laser reaches the sample and is mainly reflected from the surface. A small fraction is scattered by the quantum dot. Both fractions interfere at the detector. The inset in the upper left shows the relative orientation of the exciton dipoles and the optical field polarization. By tweaking the polarization we can select one or the other or both excitons.

reflection and the quantum dot scattering, $\vec{E}_r(\omega)$ and $\vec{E}_{qd}(\omega)$, the detected intensity reads

$$\begin{aligned} I(\omega) &\approx |\vec{E}_r(\omega)|^2 + 2\Re\{\vec{E}_r(\omega) \cdot \vec{E}_{qd}^*(\omega)\} \\ &\approx I_0 \cdot |r(\omega)|^2 + 2 \cdot I_0 \cdot \Re\{r(\omega) \cdot \sigma(\omega)\} \quad , \end{aligned} \quad (9.1)$$

where $r(\omega)$ and $\sigma(\omega)$ are the reflection coefficient of the surface and the scattering coefficient of the quantum dot. We omitted the insignificant, pure scattering term $|\vec{E}_{qd}(\omega)|^2$. In the following sections we will repeatedly speak of *the background* and *the signal*, by which we mean the first and the second term of equation 9.1. Analogous we speak of *background modulation* and *signal modulation* if either the background or the signal changes due to the used modulation technique.

By sweeping the laser frequency with respect to the quantum emitter resonance frequency, a spectrum is recorded. Obviously, we can sweep either the laser emission frequency or the emitter resonance frequency. While the former has the advantage to be technically simple to implement, it has the drawback of changing the optical path, generating a possible background modulation. The latter leaves the optical path unchanged, but is technically demanding and possibly changes the properties of the observed structure. We investigate both alternatives in the following section.

The signal is by orders of magnitude smaller than the background, requiring integration over a certain timespan to lift it above the background shot noise level. The modulation is necessary to suppress the zoo of different deterministic noise sources and stochastic $1/f^\alpha$ -noise at low frequencies, immune against integration. Modulation shifts the

signal to frequencies where these noise sources are insignificant. We use amplitude modulation of the signal in combination with a lock-in amplifier, measuring the complex amplitude ΔI of the detected intensity at the modulation frequency. To get rid of I_0 in eq. 9.1, we also detect the average $\langle I \rangle \approx I_0 \cdot |r(\omega)|^2$ and normalize ΔI with it.

An alternative to lock-in modulation is the fast-scan approach, which is described in the appendix B. The challenge with any modulation scheme is to prevent modulation of the background and of noise. In the following subsections we discuss four different approaches to modulate signal term in equation 9.1. We investigate the modulation of the light source emission wavelength, of the exciton resonance wavelength, the laser focus position and the sample position. Each method has advantages and drawbacks.

9.2 WAVELENGTH MODULATION OF LIGHT SOURCE AND QUANTUM DOT

As the laser frequency is anyway tuned to record the spectrum, the first ansatz to achieve signal modulation is dithering the emission wavelength of the laser within a small interval while tuning the center frequency over the quantum dot resonance. The detected signal then is the derivative of the spectrum at the center wavelength of the dither interval. This technique requires that on frequency scales defined by the spectral width of the quantum emitter emission the background signal does not depend on the frequency of the light source, $I_0 \cdot |r(\omega)|^2 = \text{const.}$

We use an external cavity diode laser in Littman-Metcalf configuration [91]¹. A grating within the cavity provides a high selectivity of the emission wavelength with linewidth below 300 kHz. One of the higher diffraction orders of the grating is used to couple light out of the resonator. The tilt angle of one of the cavity end mirrors is turned to control which spectral component is fed back to the resonator mode. The tilt angle can be modified computer controlled with a stepper motor and a piezo actuator. The mode-hop free tuning range of the emission frequency is 40–50 GHz, fitting the expected quantum dot linewidth of 5–25 GHz. Alternatively, the emission frequency can be tuned rapidly in a small interval by modulating the diode current.

Both methods also change the output power of the laser. We compensate this with a liquid crystal power stabilizer. The stabilizer compensates changes of the emitted intensity up to frequencies of 3 kHz by up to three orders of magnitude. Nevertheless, we found that the intensity at the detector photo diode of the confocal microscope setup changes much stronger with both, the diode current and the voltage of the laser cavity grating piezo actuator. Figure 9.3 shows different

¹ Model LION, Sacher Lasertechnik

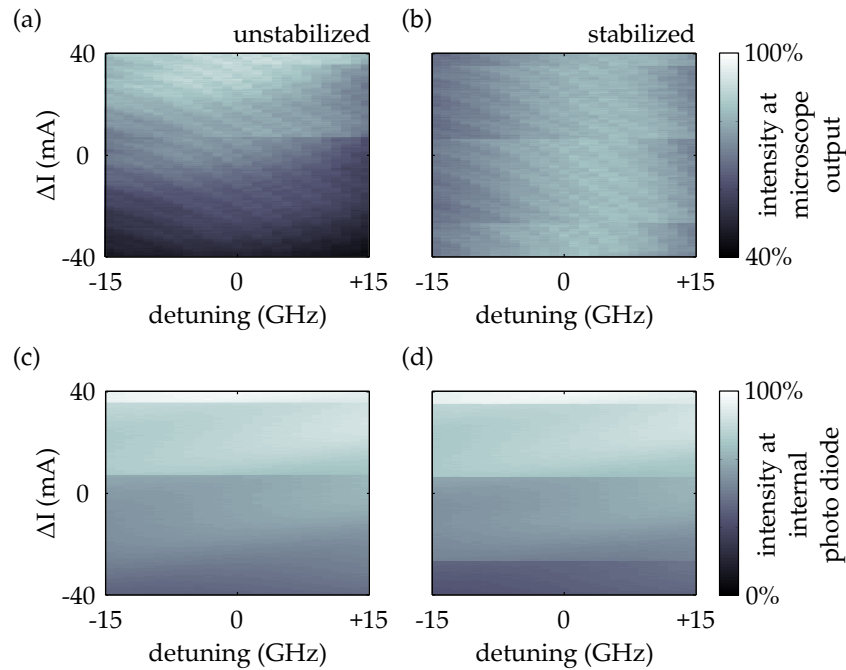


Figure 9.3: **a** These graphs show the intensity of the diode laser light, measured by the photo diode of the confocal microscope, in dependency on the laser diode current and the detuning due to the cavity grating angle. **a** shows the case without stabilization. **b** shows the stabilized case. The power stabilizer is placed right after the laser output. **c** and **d** show the corresponding intensity readings of the internal photo diode in the laser head. Note that they do not show the fringe-like pattern.

measurements of the intensity of the laser emission in dependency of the laser diode current and the frequency detuning as controlled by the cavity grating. Subfigures 9.3a and b compare the intensity, as measured with the photo diode of the confocal microscope, with and without the power stabilizer. Without stabilization the power increases with the diode current as expected. The jump-like features are mode hops where the emission wavelength flips suddenly. Superimposed is a fringe like pattern. While the gradient with the laser diode current is removed by the power stabilizer, the fringe like pattern is not affected. Parallel to the recordings of the emission intensity with the confocal microscope, we recorded the emission intensity also with a photo diode inside the laser head, shown in subfigures 9.3c and d. Of course the power stabilizer has no effect here. Note that there are no fringes visible, which indicates that their origin is due to optics outside the laser head.

Further investigations reveal that the fringes are due to interference of spurious reflections within the optical path, which comes about by the long coherence length of over 500 m. The total intensity at the photo diode depends on the relative phase of all interfering electric fields, which changes with the frequency of the light. For this reason

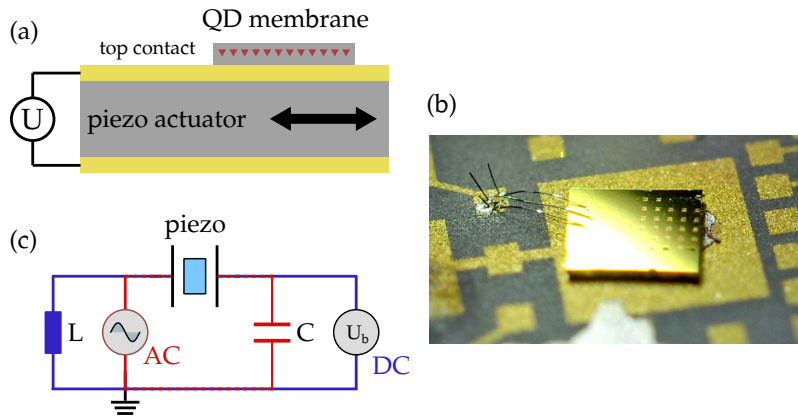


Figure 9.4: **a** illustrates the sample structure. A membrane containing quantum dots is placed on top of a piezo actuator. The piezo crystal is covered with gold electrodes to which a voltage source is connected. **b** shows a photography of the sample, placed on a chip carrier and connected to the voltage source with wires bonded to the top electrode. On the right of the piezo the quantum dot membranes are visible. **c** shows the schematic of the voltage source, described in the text.

it is not possible to modulate the signal by dithering the emission wavelength as it also modulates the background. Up to the present day, we are not able to get the modulation level of the background to less than 1%, far too large to separate the quantum dot response.

Alternatively, we can modulate the quantum dot resonance frequency. As stated before, this is technically more involved as it requires substantial changes to the sample structure. In our case, we use strain within the semiconductor matrix to tune the resonance frequency. For this purpose, the quantum dots are fabricated within a membrane of only a hundred nanometers total thickness. The membranes are transferred to a piezo actuator, which stretches and compresses the membranes[92, 93]. The samples are developed by the group of Oliver G. Schmidt in Dresden. Compared to Stark-shift modulation[68, 69], this has the advantage that we do not need electrodes near the quantum dot. Figure 9.4a illustrates a sketch of the sample structure. The piezo actuator is covered with gold electrodes to which a voltage is applied. A photography of the real sample, mounted to an aluminum nitride chip carrier and electrically contacted via wire bonding, is shown in figure 9.4b. The drive electronics are sketched in figure 9.4c. It contains a DC path (blue) that delivers a high-voltage bias to control the center emission frequency of the quantum dots. The supported voltage range of the piezo is $-200\text{ V} - +600\text{ V}$ between the top and the bottom contact. The AC path (red) allows us to impose a low-voltage modulation on the DC bias with a waveform generator.

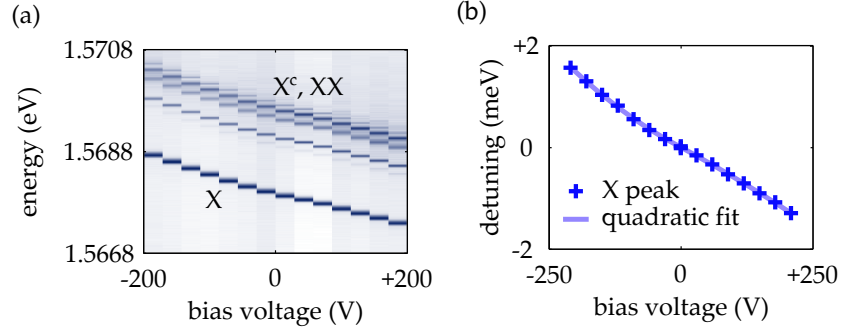


Figure 9.5: **a** shows the piezo voltage-dependent shift of the photoluminescence emission spectrum of a quantum dot within a strained membrane. X denotes the exciton emission, X^c and XX are the charged excitons and bi-excitons. **b** shows the detuning of the exciton peak position with respect to the bias voltage. The voltage dependency is nearly linear with a small quadratic contribution. Fit parameter values can be found in the text.

Figure 9.5a shows how the photoluminescence emission spectrum of a quantum dot within the strained membrane shifts with the bias voltage. Visible are exciton, trion and bi-exciton lines, all shifting according to the applied strain. To determine the energetic shift per applied voltage, we investigate the exciton emission peak position in dependency of the bias voltage (see fig. 9.5b) and fit a quadratic function $ax^2 + bx$ to the data. This is done separately for positive and negative bias voltages. The fit parameter values are

$$\begin{aligned} a_+ &= +0.010 \mu\text{eV}/\text{V}^2, & b_+ &= -5.3 \mu\text{eV}/\text{V} \\ a_- &= -0.003 \mu\text{eV}/\text{V}^2, & b_- &= -5.6 \mu\text{eV}/\text{V} \end{aligned} \quad (9.2)$$

The modulation interval should be on the order of the exciton emission linewidth, which is about 5 – 15 μeV in the as-grown samples, embedded in a bulk crystal. In the membranes, the exciton emission of many dots is broadened above the spectrometer resolution. It is reasonable to assume that in the membranes all dots have a broader linewidth compared to the as-grown crystal. We thus use relatively high modulation depth of 20 – 50 μeV . To avoid changing the laser emission wavelength at all, the whole spectrum of the quantum dot should be recorded by tuning the quantum dot resonance frequency.

The general measurement procedure is thus to locate the quantum dot using confocal maps of the photoluminescence emission and determine the resonance frequency with a spectrometer. The diode laser emission wavelength is then tuned to match the emission wavelength of the quantum dot within the resolution limit of the spectrometer ($\approx 100 \mu\text{eV}$). Afterwards the quantum dot resonance is strain-tuned over the laser emission line while simultaneously modulating by 20 – 50 μeV at a frequency between 0.2 kHz–2 kHz. We check the

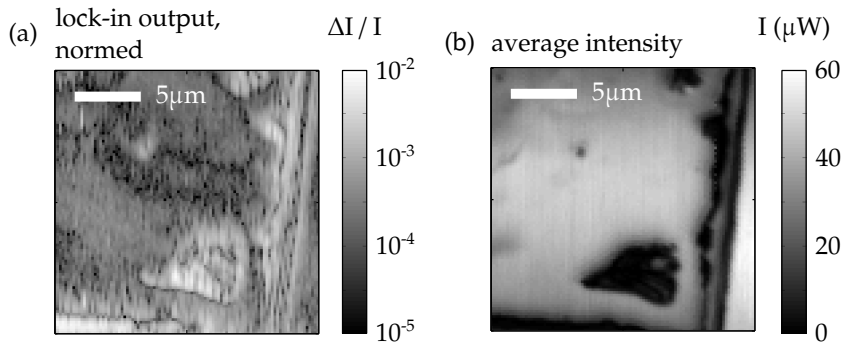


Figure 9.6: **a** shows a spatial map of the differential intensity on top of a GaAs membrane. The membrane sits on a gold covered piezo actuator that induces periodic strain at a frequency of 1.2 kHz. **b** shows the corresponding time averaged intensity.

photoluminescence spectrum to make sure that the laser emission wavelength lies within the tuning interval.

It turns out that the strain modulation generates a strong background modulation on the membrane substrate alone, depending on the position on the membrane, the absolute applied strain and on the focus height. Figure 9.6a shows an example of how $\Delta I/I$ changes with the position on the sample surface. The map is a $20 \times 20 \mu\text{m}^2$ section on the membrane. The modulation depth is $50 \mu\text{eV}$ at a frequency of 1.2 kHz. The center wavelength of the laser is 792 nm. In fig. 9.6b the corresponding average intensity is shown. Clearly, the modulated signal shows features that do not corresponds to a change of the total intensity.

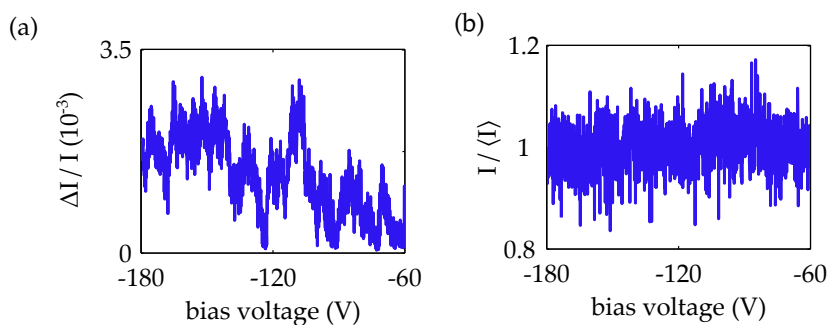


Figure 9.7: **a** shows the differential intensity on the AlGaAs membranes against the bias voltage. The strain is modulated by an equivalent of $50 \mu\text{eV}$ resonance shift at 1.2 kHz. The expected signal strength of the quantum dot is on the order of 10^{-4} . **b** shows the corresponding time averaged intensity.

The dependency of the modulated signal and the total intensity on the bias voltage is shown in figures 9.7a and b. Note that the change

of the differential signal is by one or two orders of magnitude larger than the expected signal of the quantum dot exciton.

Right now the reason for the background modulation is not clarified. We have seen that the modulation background depends on the position on the membrane. Furthermore, we have found (not shown here) that this dependency is very sensitive to the focus. Slight alignments of the focus height, not showing any change of the total intensity, mean drastic changes of the background signal. In the same way the background signal is sensitive to the use of a pin holes in the excitation path or detection path. Considering this and considering that the membrane is not flat and forms, together with the gold covered piezo surface, a multilayer structure, a possible mechanism could be a structural change of this multilayer due to the compression and elongation of the piezo crystal. Assume that the sample is a slab of AlGaAs with a thickness 100 nm on a gold surface, and assume that $n_{\text{AlGaAs}} = 3.38$ and $n_{\text{Au}} = 0.14 + 4.9i$. Then, using eq. 2.11 in part one of this book to calculate the reflectivity of a multilayer structure, a thickness variation of only 0.1 nm would lead to a change in reflectivity of more than 10^{-4} at a wavelength of 792 nm. The conclusion is that with the given sample structure we cannot utilize strain tuning of the exciton resonance energy to modulate the signal.

9.3 POSITION MODULATION OF LASER SPOT AND QUANTUM DOT

We have seen that the modulation of the laser emission frequency and the exciton resonance frequency cannot be used in the presented form. Alternatively, we can use Stark shift modulation, which was shown to work reliably [68, 69, 94]. However, we still want to prevent a direct manipulation of the local environment of the quantum dot. Our next approach is therefore the modulation of the relative position of the quantum dot and the excitation beam, neither of which affords direct manipulation of the sample. It can be realized by either moving the sample or the laser focus. The former has the advantage of an unchanged optical path, with a lesser risk of background modulation. On the other hand, it is technically more demanding in terms of electronics, mechanics and cryogenics because a fast moving actuator has to be brought into the cryogenic environment. Additionally, a laser scanner is already installed in the setup. For this reason, it is reasonable first to investigate modulation of the laser focus position.

FOCUS POSITION MODULATION We perform the modulation of the laser focus with the tilt mirror used to record confocal maps of the sample (review fig. 9.1). The mirror is simply dithered using a waveform generator. The modulation frequency is limited to approximately 200 Hz due mechanical resonances. To get a reasonable mod-

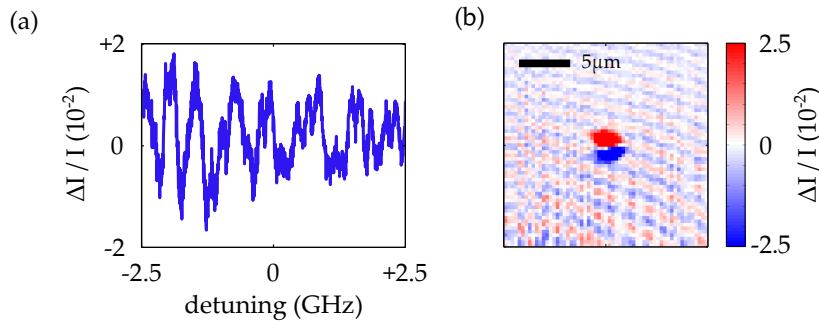


Figure 9.8: **a** shows the differential intensity due to modulation of the lateral laser focus position on the bare substrate in dependency of the laser emission frequency detuning. **b** shows a confocal map of the differential intensity at a fixed laser emission frequency. In the center the signature of a defect on the substrate is seen. Everywhere else we see interference fringes.

ulation depth of the quantum dot signal, the focus must be moved a distance of at least once the size of the diffraction limited focus, which is on the order of $0.5 - 1\mu\text{m}$ depending on the microscope used.

The quantum dot is located spatially and spectrally using its photoluminescence emission. Then the emission frequency of the laser is brought to match with the exciton resonance frequency. The emission wavelength of the laser is swept over the resonance while modulating the focus position. The total intensity is recorded in dependency of the laser emission wavelength. A lock-in amplifier measures the modulated fraction of the intensity.

Figure 9.8a shows the differential intensity in dependency of the laser emission frequency, measured on the bare substrate. We see again background modulation due to interference, the relative amplitude changing considerably when sweeping the laser emission frequency. The background modulation is due to the change of the optical path when the laser focus is modulated along the surface. With the optical path the interference conditions change and thus the detected intensity. Figure 9.8b shows a confocal map of the differential intensity around a defect on the sample surface. The spatial modulation amplitude is $1\mu\text{m}$ in vertical direction, hence the bipolar shape of the defect. On the bare substrate, interference fringes are visible. When tuning the laser emission frequency, the fringes wander along the surface. This leads to the modulated background seen in figure 9.8a. The exact shape of the fringe pattern, its periodicity and amplitude in particular, depends on many parameters such as position of the focus, the alignment of the 4f-lens system, the center emission wavelength. Up to now we have not found a systematic way to reduce the fringe amplitude merely by specific alignment of the optical setup.

One approach to remove the interference fringes is to dither the laser emission frequency in a small interval with a frequency much

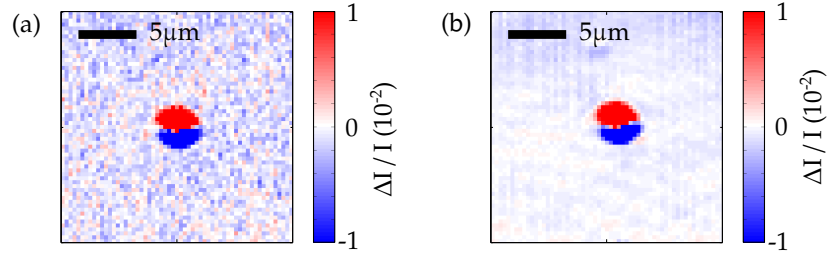


Figure 9.9: **a** shows a confocal map of the differential intensity due to modulation of the laser focus position while dithering the wavelength of the laser emission wavelength at 700 Hz. **b** shows the same for dithering of the laser diode current at 700 Hz.

larger than the modulation frequency of the laser focus. This is equivalent to blurring the fringe pattern in figure 9.8b. We can either modulate the emission wavelength using the piezo actuator of the laser cavity grating or the laser diode current. Figure 9.9a and b show the same map as fig. 9.8b, but this time the the piezo actuator and the laser diode current are dithered with a ramp generator at a frequency of 700 Hz, which washes out the fringes almost completely. However, as this technique only works if the dither interval is smaller than the linewidth of the quantum dots, the question is how large the dither interval has to be in practice, answered by measuring the relative fringe amplitude in dependency laser emission frequency dither amplitude. This involves two steps. First, the fringe amplitude is determined with respect to the laser diode current dither amplitude. Then the we need to determine the transfer function of the diode current and the laser emission frequency. The transfer function is specified by the manufacturer to be approximately 0.17 GHz/mA. We can only roughly check this as the resolution of our spectrometer is limited to 22 GHz. We recorded the spectral position of the laser emission while tuning the laser diode current I_d over a range of 80 mA. For each current value we calculated the weighted average emission wavelength, $\langle f(I_d) \rangle = \sum f \cdot C(f, I_d) / \langle C(f, I_d) \rangle$, where f is the frequency and C is the photon count at this frequency. $\langle f(I_d) \rangle$ is approximately a linear function with slope (-0.09 ± 0.01) GHz/mA, approximately half the nominal value.

Figure 9.10 shows the resulting relative fringe amplitude versus the laser emission frequency dither amplitude. The modulation frequency is 2.56 kHz. We see that the fringe amplitude continuously reduces until the dither interval reaches $3\mu\text{eV}$. This is where the fringes visible in the confocal map shown in fig. 9.8b shift half their period. Afterwards the amplitude rises again and reaches a local maximum. This is where the the fringes shift once their period. This is in agreement with the fringe period seen in the laser emission frequency sweep shown in figure 9.8a. So although we reduce the spectral reso-

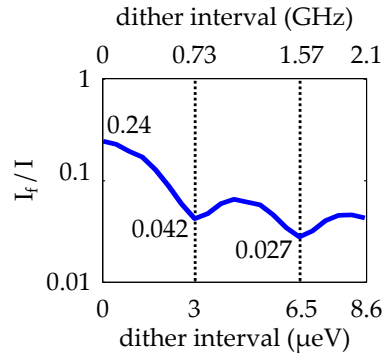


Figure 9.10: Shown is the standard deviation of confocal scans due to fringes in dependency on the dither amplitude of the laser emission frequency.

lution of the laser considerably, it is still enough to resolve the quantum dot resonances. However, we also see that the fringes reduce only by an order of magnitude, and fig. 9.8a indicates that the fringe period changes with the laser emission frequency, which means that the dither interval has to be adapted while taking spectra. The same is true for other parameters, because as stated above, the fringe pattern depends on the particular adjustment of the setup, lateral position of the laser focus, etc. The dithering needs to be adapted to all these parameters, which makes it an unreliable approach.

SAMPLE POSITION MODULATION To prevent the change of the optical path by moving the laser focus we can modulate the sample position instead. This is done with a piezo actuator placed within the cryostat. The sample is mounted on top as depicted in figure 9.11a. Disadvantage of this technique is the reduced thermal conductivity of the piezo crystal compared to direct contact of the sample with the cryostat cold finger. Furthermore, the performance of piezo actuators tend to reduce at cryogenic temperatures, requiring rather large actuators for a given lateral displacement. In exchange, no change has to be done to the sample structure and basically no restrictions are imposed on the sample design, except that it must fit on the actuator.

The actuator is a P-141.10 piezo stack made by PI Ceramic GmbH. Its maximum nominal lateral displacement is $10\mu\text{m}$ at room temperature, and estimated to be $2 - 5\mu\text{m}$ at a temperature of 10 K. In order to not contaminate the piezo actuator on the long term with conducting silver solder, copper plates are glued on top and bottom of the piezo with GE varnish. The sample substrates are glued to the top copper plate with silver solder. Then the complete stack is mounted into the cryostat. The electrical drive is shown in figure 9.11b. The output of an waveform generator is transformed by a factor of 10 to produce the necessary HV voltage of $\approx 200\text{ V}$. The frequency is 100–300 Hz and is limited by the frequency response of the actuator and the transformer.

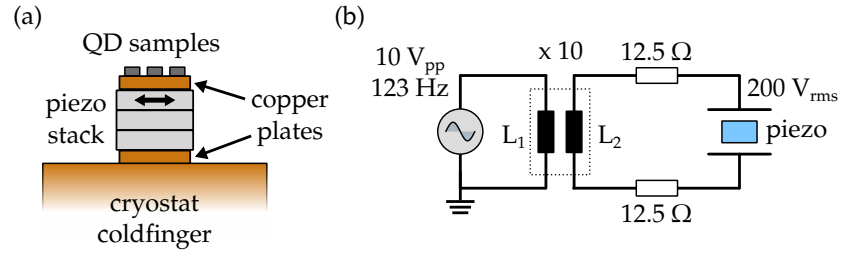


Figure 9.11: **a** shows a sketch of the sample mount with piezo actuator. The piezo displaces its top site in horizontal direction by $2 - 5 \mu\text{m}$ at cryogenic temperatures. **b** shows the electronic drive circuit. A voltage of $0 - 10 V_{\text{pp}}$ at 123 Hz is fed to a $10\times$ step-up transformer. The piezo actuator is connected directly to the secondary transformer winding.

The transfer lines into the cryostat each have a resistance of 50Ω . We use four parallel lines to reduce the total resistance to 12.5Ω . When cooling down, this resistances also guarantee a smooth discharging of the piezo capacitance due to strain relaxation.

First we check again for modulation background. The measurement procedure is as with focus modulation. The laser emission wavelength is tuned while recording the differential intensity due to the sample position modulation. The piezo actuator is driven with a voltage of $10 V_{\text{pp}}$ at 127 Hz . We perform the test at room temperature and at realistic excitation powers, $1 - 10 \mu\text{W}$ at the sample, delivering 100 nW at the photo detector. The detector gain is 10^7 V/W , corresponding to a detector bandwidth of 50 kHz . Figure 9.12 summarizes the results. Graph (a)-(c) shows the unnormalized differential intensity, the total intensity and the normalized differential intensity respectively. The laser emission detuning is given in GHz and meV for convenience. We see that the differential intensity and the total intensity show typical signs of interference fringes. However, in contrast to the approaches discussed before, the fringe amplitudes in the differential signal and the total signal are proportional to each other and cancel in the normalized signal. The standard deviation of the normalized signal is $1.7 \cdot 10^{-5}$, which is by a factor 10-50 below the expected signal strength of the quantum dot. The differential signal was acquired with a time constant of 47 ms with a filter slope of -48 dB/oct , corresponding to a noise equivalent bandwidth of $f_{\text{NEBW}} = 1.1 \text{ Hz}$. The shot noise of laser light with optical power $P = 100 \text{ nW}$ at a wavelength of $\lambda = 770 \text{ nm}$ is

$$\begin{aligned} \sigma_{\text{SN}} &= \sqrt{2 \cdot P \cdot f_{\text{NEBW}} \frac{hc}{\lambda}} \\ &= 0.24 \text{ pW} \end{aligned} \quad (9.3)$$

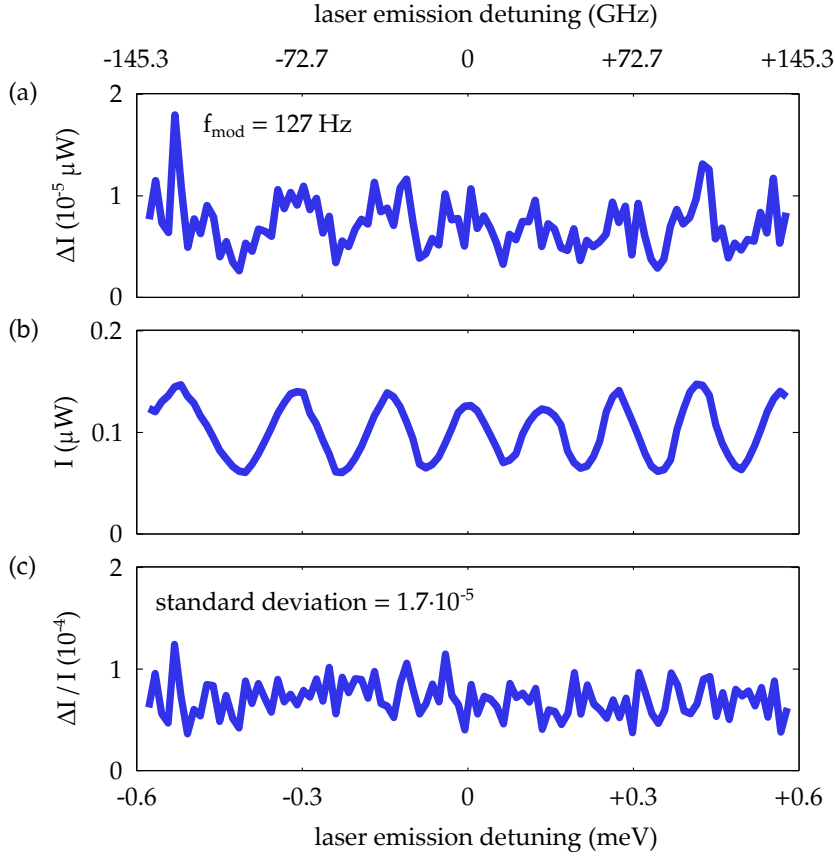


Figure 9.12: This figure shows the modulation background signal while scanning the laser emission frequency. The detuning is given in meV in the lower x-axis and in GHz on the upper x-axis. **a** shows the unnormalized differential signal at the modulation frequency of 127 Hz. **b** shows the total intensity. It shows the typical interference fringes known from other modulation approaches. **c** shows the normalized differential intensity. The fringes seen in (a) and (b) cancel. The standard deviation along the horizontal axis is $1.7 \cdot 10^{-5}$.

For each laser emission frequency the signal was averaged 265 times. Hence, the shot noise level of $\Delta I/I$ is

$$\frac{0.24 \text{ pW}}{\sqrt{256} \cdot 100 \text{ nW}} = 1.5 \cdot 10^{-7} \quad (9.4)$$

The measured signal thus is by a factor of 100 above shot noise. This is due to the low modulation frequency. Figure 9.13 shows the frequency spectrum of the photo diode output voltage, recorded for 320 ms at a sampling rate of 6.4 ksp/s. Different curves refer to different optical powers as denoted in the legend. We see that at the piezo modulation frequency of 123 Hz, used to produce fig. 9.12, the noise level is 1-2 orders of magnitude above shot noise. The noise floor at high frequencies fits to the values expected for shot noise up to a factor of order 1.

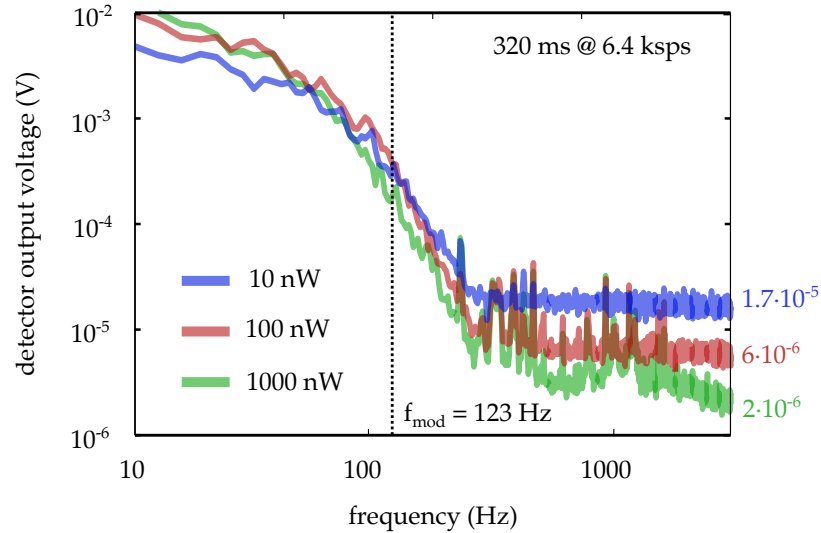


Figure 9.13: This graph shows the noise spectrum of the detected intensity. The sample rate is 6.4 kps. The different colors denote different values of the average detected intensity. The detector gain for 10, 100 and 1000 nW was set to 100, 10 and 1 MV/W respectively. The modulation frequency of 123 Hz used in the experiment is marked by the dashed line.

The figure also shows that at the desired frequency range of a few hundred Hertz, there is a number of deterministic noise sources with relative amplitudes on the order of $10^{-5} - 10^{-4}$. Those can be attributed to vibrations and acoustics, indicating that a higher modulation frequency in the kHz-range is necessary. The modulation amplitude of the used piezo actuator is too low at these frequencies. However, we can artificially double the modulation frequency by modulating the quantum dot position symmetric relative to the laser spot, such that it crosses the laser spot twice per modulation cycle. Care must be taken that the displacement of the quantum dot is large enough. Otherwise the modulation depth will be reduced by this technique.

We performed first test measurements on single self-assembled quantum dots with the available piezo actuator. Figure 9.14a shows a luminescence spectrum typical for the used quantum dots. The experiment is carried out on the isolated exciton line, marked in the spectrum. The linewidth of all investigated quantum dots is below the spectrometer resolution limit of $55 \mu\text{eV}^2$. The piezo drive voltage is $10 V_{pp}$ at a frequency of 143 Hz. Figure 9.14b shows the photoluminescence emission count rate while modulating the quantum dot asymmetrically into the focus. The modulation depth is 83% and proves that the modulation really works.

² Spectrometer: Princeton Instruments SP750, Grating: 1800 l/mm, 500 nm blaze angle, center wavelength 777 nm

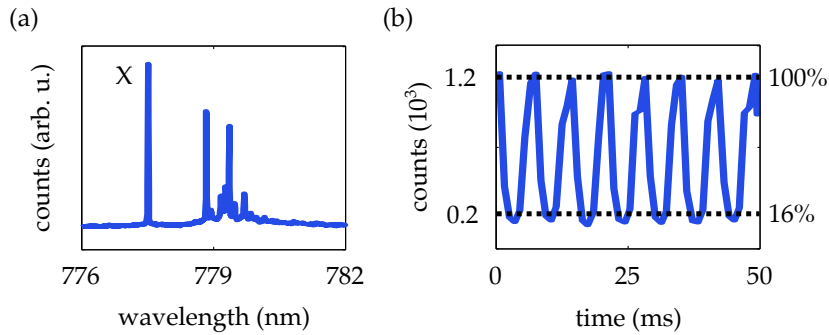


Figure 9.14: **a** shows a typical luminescence spectrum of the quantum dots used in the experiment. **b** shows the luminescence count rate of a single quantum dot while modulating the sample position.

Up to now, we were not able to clearly identify the signature of a quantum dot under resonant excitation. Figure 9.15 shows the differential intensity spectra of two emitters, recorded with different configurations of the modulation scheme. The first one was measured while modulating the emitter position symmetric around the laser spot and locking to the second harmonic frequency. The second one was recorded while modulating asymmetrically, with one of the modulation turning points within the laser focus, and locking to the fundamental frequency. There is signatures that may be due to the excitons of the quantum dots, but right now they are not reproduced reliably neither on the same emitter nor on different ones. Furthermore, we made the experience that the current design of the sample holder is prone to breaks of the joints between the piezo actuator and the cold finger. While this does not seem to be a problem with respect to the modulation, it drastically reduces the thermal contact. We were only in two cases able to cool the quantum dots down to temperatures where they show resolution limited emission. We suspect that the joint breaks during cool-down or warm-up phases or when the sample is modulated. For this reason, without more extended parameter studies, including excitation power, optical polarization and modification of the modulation technique, it is hard to verify that the features observed in fig. 9.15 are signatures of excitons.

Currently we are working on a redesign of the sample holder. A direct heat bridge between the cold finger and the sample carrier could solve the problem of bad heat conductance. For example, a circular net of copper wire strands could provide the necessary heat conductance while keeping the connection flexible as required for proper modulation. Additionally, the current design prevents the usage of a heat shield due to limited space within the cryostat.

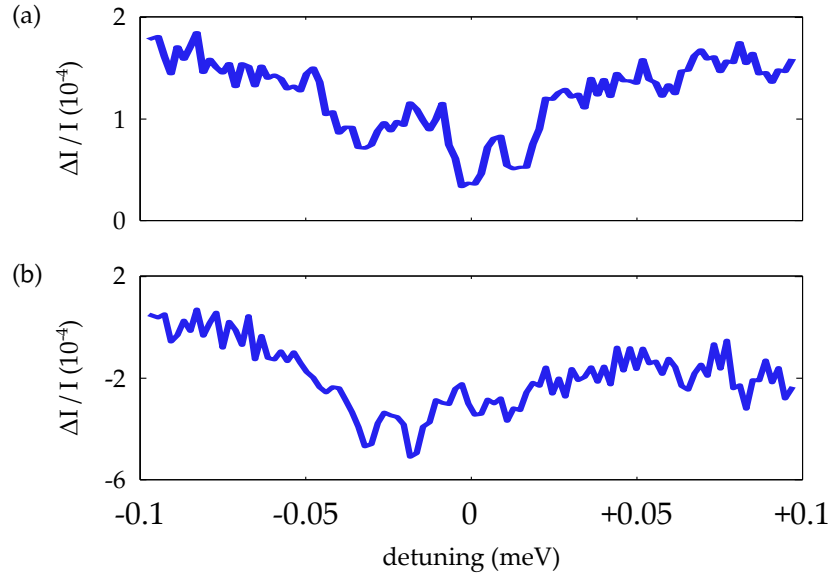


Figure 9.15: Shown are the continuous wave scattering spectra of two different quantum dots. **a** was recorded with a symmetric modulation of the quantum dot relative to the laser focus and at the second harmonic. **b** was recorded with a asymmetric modulation of the quantum dot relative to the laser focus at the first harmonic.

9.4 SUMMARY

In the last sections we investigated four different approaches to modulate the signal of a single quantum dot exciton. The priority was to impose as little restrictions as possible on the sample design. The biggest challenge is to overcome the background modulation due to the modulation of the optical path.

The least invasive techniques, modulation of the optical focus position and modulation of the laser emission frequency, are those where a modulation of the optical path cannot be avoided as it is part of the modulation principle. In the case of laser emission frequency modulation, we found no way to suppress the background modulation, which is by orders of magnitude larger than the signal amplitude. In the case of focus position modulation we were able to suppress the background modulation by one order of magnitude by dithering the emission frequency of the laser. We found, that the required dither amplitudes are on the order of $1 - 2$ GHz, that is $5 - 10 \mu\text{eV}$, still enough to resolve the quantum dot excitons we are currently using in our experiment. Possible next steps is to make the technique more robust and optimize the level of suppression. Up to now, the technique was not tested under realistic conditions, considering excitation power and integration time.

In contrast to modulation of the laser focus position and the laser emission frequency, we investigated two approaches that, nominally,

do not change the optical path. They impose more restrictions on the sample design and are more demanding considering technical realization. Strain-modulation of the sample substrate with a piezo actuator does shift the exciton resonance position. Its advantage is a relatively high cut-off frequency in the kHz range. It works only for membrane samples, but does not require direct modification of the sample structure. We found that with the current design, the strain modulation leads to a strong background modulation, possibly due to a change of the optical properties of the substrate. The current design of the tuning device is thus not suited for continuous-wave spectroscopy.

The last approach we studied is spatial modulation of the sample position. Of all the techniques we tried, it is the only one where no background modulation occurs. Under realistic conditions we reached a noise level of $1.7 \cdot 10^{-5}$, two orders of magnitude above the expected shot noise level. The additional noise can be attributed to the low modulation frequencies of 100-200 Hz, a range where stochastic $1/f^\alpha$ -noise and deterministic noise sources due to acoustics and electronics are significantly larger than shot noise. Hence, the signal to noise ratio should improve drastically at higher modulation frequencies. With the current design, we performed first test measurements of the differential intensity spectrum on quantum dot excitons, but could not find clear evidence that the features found in the spectrum are due to excitons. Systematic studies on quantum dots at low temperatures are hindered due to the error prone mechanics of the actuator mount and bad heat conductance of the piezo crystal. The next step is thus a complete redesign of the modulator stage with focus on higher modulation frequencies and a direct thermal contact between cold finger and the sample. With these modifications, we find no principle reason that spatial modulation of the sample should not work.

SUMMARY AND CONCLUSION

Part two of this thesis is embedded in the large topic of resonant spectroscopy and coherent control of quantum emitters, with the future goal of implementing quantum information processing routines, possibly in large networks of such emitters. Within this broad context, we addressed mainly three sub-topics, namely transient pump-probe spectroscopy of single quantum dots, resonant continuous-wave spectroscopy of single semiconductor quantum dots, and formation of emitter networks.

First we investigated if our particular type of emitter, self-assembled semiconductor quantum dots, is in principle suited to implement coherent control experiments. This was done in chapter 7 by comparing the experimentally determined behavior of the quantum dots and the theoretical behavior of a V-atom in a number of well-known test cases, namely absorption bleaching, perturbed induction decay and Rabi oscillations. We found that in the first two cases, the quantum dots mimic the V-atom very well and that the spectral features found in the experiments can be clearly attributed to distinct processes initiated by particular pulse sequences. Using the theory of the V-atom to reproduce these features, we were able to deduce the optical properties of the quantum dots. We found that the exciton coherence lifetime in our dots is 90 ps and that the population lifetime is 230 ps. Furthermore we were able to show that the unexpected stretching of the Rabi cycles observed with the used quantum dots is not an intrinsic property of the dots, but a consequence of the electric field induced by the Dember effect that quenches the exciton dipole moment via Stark's effect. The Dember effect occurs at the interface of the lower AlGaAs barrier and the GaAs substrate, which can be moved far away from the dot in future samples, eliminating the deviation from the theory. However, our model does explain the stretching only qualitatively. Predicting the strength of Stark's effect using ab-initio calculations of the optical properties of the quantum dot, we would expect a much stronger spectral shift. However, this shift is not observed and further experiments are necessary to clarify this point.

The next subtopic, discussed in chapter 8, was concerned with the formation of networks of randomly distributed, coupling two-level-systems. In a network of identical two-level-systems on a regular grid, the delocalized states are defined by the shape of the grid geometry. For example, the delocalized states of a rectangular grid have drum-like patterns. We studied, how these patterns change when the network

elements have inhomogeneous eigenenergies. We found that the inhomogeneity in general degrades the delocalized network states, leading to localization of the excitation to single network elements. However, if there is local correlation of the eigenenergies, spatially separated sub-networks form within energy traps. Their shape is defined by the local eigenenergy landscape. We also found that the optical excitation must be local, compared to the extension of the states. This could be realized with near field probes and optical nanoantennas.

In chapter 9 we discussed four approaches to implement a modulation scheme in a resonant continuous-wave spectroscopy experiment on the single particle level. We required that the technique is minimally invasive considering the sample design. The four techniques can be divided into modulation of the relative energy of the quantum dot resonance and the light source and into modulation of the relative position of the quantum dot and the excitation spot. We showed that due to the very long coherence length of the light source, a modulation scheme needs to prevent a change of the optical path length. We found that this is true only for the modulation of the sample position, which was realized with a piezo actuator. Using the current design, the technique suffers from insufficient thermal contact and allows only for small modulation frequencies, making it prone to low-frequency noise. Spectral features found in preliminary measurements on single quantum dots could therefore not be safely attributed to exciton resonances. Nevertheless, with further improvements, the technique is the most promising candidate for a non-invasive modulation scheme.

The results on the different subtopics suggest an number of possible follow-up experiments. First of all, the quantitative discrepancy found when modeling the influence of the Dember effect on Rabi oscillation via Stark's effect motivates further investigations of the reaction of our dots to electric fields. Furthermore, the existence of the Dember effect itself opens new possibilities to manipulate the optical properties of the quantum dot on picosecond timescales. We have taken first steps in this direction by nanostructuring the sample substrate, with the goal of confining the photo carrier clouds and thus manipulating the formation of the electric fields. However, the used technique of ion beam milling is too invasive, destroying most of the quantum dots within and close to the exposed area. This was also the case when using protective layers. Other techniques such as reactive ion etching can solve this problem while allowing a controlled structuring of the sample surface. Reactive ion etching can also be used to structure the shape of networks of randomly distributed semiconductor quantum dots. Such samples can be made with a very high density of quantum emitters. Alternatively, instead of shaping the network by removing material, specifically designed metallic antennas could be used to change the distance dependence of the coupling

in a limited area. All this should have impact on the properties of the delocalized network states. Another field of research suggested by our results is the local excitation of such networks using near field probes or nanoantennas. In a coherently coupled network, such excitation should result in a clear signature, mediated to us for example by interfering, anti-bunched single photon emission even from distinct spots of the network.

Part III

APPENDIX

THE JACOBI-ANGER EXPANSION

Here we derive the mathematical identities used in sec. 4.3 to calculate the Fourier components of the detected signal power at the modulation frequency and its second harmonic. The identities used state that the Fourier transform of $f(t) = \cos(\alpha + \beta \cos \omega t)$ at frequencies ω_m and $2\omega_m$ is

$$\mathcal{F}\{f\}(1\omega_m) = -\sqrt{2\pi} \cdot J_1(\beta) \sin \alpha \quad (\text{A.1})$$

$$\mathcal{F}\{f\}(2\omega_m) = -\sqrt{2\pi} \cdot J_2(\beta) \cos \alpha \quad . \quad (\text{A.2})$$

These identities are derived from the Jacobi-Anger expansion[51],

$$e^{iz \cos \theta} = \sum_{n=-\infty}^{n=+\infty} J_n(z) e^{in\theta} \quad . \quad (\text{A.3})$$

where J_n are Bessel functions of the first kind. The first step is to use Euler's equation and represent $\cos(\alpha + \beta \cos \omega t)$ by complex exponentials. Then we use eq. A.3 and replace the complex exponentials by sums over Bessel functions,

$$\begin{aligned} \cos(\alpha + \beta \cos \omega_m t) &= \frac{1}{2} \left(e^{i(\alpha + \beta \cos \omega_m t)} + e^{-i(\alpha + \beta \cos \omega_m t)} \right) \\ &= \frac{1}{2} \sum_{n=-\infty}^{n=+\infty} [J_n(\beta) e^{i\alpha} + J_n(-\beta) e^{-i\alpha}] i^n e^{in\omega_m t} \quad . \end{aligned} \quad (\text{A.4})$$

This is already an expansion of $\cos(\alpha + \beta \cos \omega t)$ into harmonics of $\exp(i\omega_m t)$. The spectral coefficients of $f(t)$ at frequencies ω_m and $2\omega_m$ are found by dropping all the sum terms except for $n = \pm 1, \pm 2$. For the next steps, the following identities are important, which follow from the definition of the Bessel functions,

$$J_{-n} = (-1)^n J_n \quad (\text{A.5})$$

$$J_n(-\beta) = (-1)^n J(\beta) \quad . \quad (\text{A.6})$$

With those we get for $n = \pm 1$

$$\begin{aligned} & \cos(\alpha + \beta \cos \omega_m t)|_{1\omega_m} \\ &= \frac{1}{2} [J_1(\beta)e^{i\alpha} + J_1(-\beta)e^{-i\alpha}] i^1 e^{i\omega_m t} \end{aligned} \quad (\text{A.7})$$

$$\begin{aligned} & + \frac{1}{2} [J_{-1}(\beta)e^{i\alpha} + J_{-1}(-\beta)e^{-i\alpha}] i^{-1} e^{-i\omega_m t} \\ &= \frac{1}{2} [J_1(\beta)e^{i\alpha} - J_1(\beta)e^{-i\alpha}] i e^{i\omega_m t} \end{aligned} \quad (\text{A.8})$$

$$\begin{aligned} & - \frac{1}{2} [-J_1(\beta)e^{i\alpha} + J_1(\beta)e^{-i\alpha}] i e^{-i\omega_m t} \\ &= -2J_1(\beta) \sin \alpha \cos \omega_m t \quad , \end{aligned} \quad (\text{A.9})$$

and for $n = \pm 2$ we get in the same way

$$\cos(\alpha + \beta \cos \omega_m t)|_{2\omega_m} = -2J_2(\beta) \cos \alpha \cos 2\omega_m t \quad . \quad (\text{A.10})$$

Taking the Fourier transform of eq. A.9 and eq. A.10 yields

$$\begin{aligned} \mathcal{F}\{f\}(\omega_m) &= -\sqrt{2\pi} \cdot J_1(\beta) \sin \alpha \\ \mathcal{F}\{f\}(2\omega_m) &= -\sqrt{2\pi} \cdot J_2(\beta) \cos \alpha \quad . \end{aligned} \quad (\text{A.11})$$

NOISE SUPPRESSION BY MODULATION

Noise suppression works either by removing a source of noise or by separating the frequency bands of the noise and the measured signal. The latter approach comes in handy when we cannot remove a source of noise from the apparatus. These almost always exist and turn fun into frustration. To get the fun back, we need to know the spectral characteristic of the noise and means to perform the separation of the frequency bands.

Our setups basically consists of a light source, some optical system and detector electronics. The dominant intrinsic sources of noise that cannot be avoided are $1/f^\alpha$ -noise and shot noise due to photons and electrons. Both are stochastic types of noise.

$f^{-\alpha}$ -noise is dominant at low frequencies only. It is found in many domains and has diverse, often unknown, origins. In electronics, $1/f$ -noise is termed flicker noise and found, for example, in the output operational amplifiers and vacuum tubes. It originates from the statistical fluctuations of the properties of the used materials. Other typical noise sources at low frequencies are vibrations, thermal drifts, or interference from electronic devices (power lines, switching power supplies).

With increasing frequency, $1/f^\alpha$ -noise decreases and is eventually dominated by photon shot noise. In practice, shot noise can be considered white. Thus there will always be a frequency, called corner frequency, where shot noise is larger than $1/f$ noise. This behavior is demonstrated in figures B.1a and b, which show typical time domain signals of white noise and flicker noise respectively. The noise curves are generated artificially: temporal white noise is generated by simply taking the inverse Fourier transform of white noise spectra, that is, complex numbers with unity magnitude and randomized phase. To get temporal flicker noise, the magnitudes of the complex numbers are weighted with an $1/f$ -law. Figure B.1c shows the Fourier transform of a time trace with white noise and flicker noise superposed. At low frequencies we see the characteristic negative slope of the $1/f$ -noise. At some corner frequency the noise floor levels out and white noise dominates. The spectrum of a possible base band signal is shown schematically. In principle it is larger than the shot noise floor, but at low frequencies, it is hidden by the $1/f$ -noise.

The goal, hence, is to separate the signal from noise in the base band. In the next section we introduce two techniques that allow this: *lock-in detection* and *fast scan*. Lock-in modulation is widely used and based on amplitude modulation combined with a phase sensi-

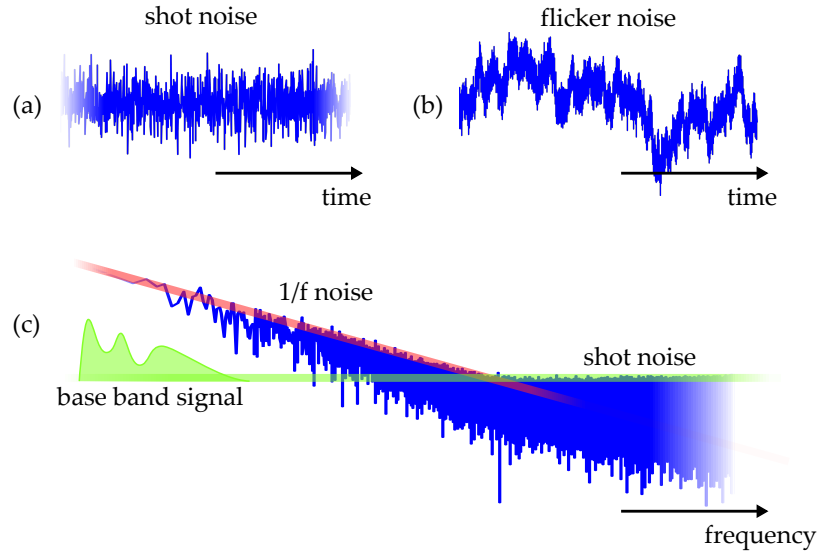


Figure B.1: **a** A computer generated time domain signal limited by white noise. **b** A computer generated time domain signal including flicker noise and white noise. **c** The Fourier transform of (b). The noise floor is limited by shot noise at high frequencies. At low frequencies the characteristic $1/f$ slope of flicker noise is visible. The base band signal imposed on the optical signal (sketched as green shade) is below the noise floor.

tive detector. Fast scan is very similar to noise suppression in oscilloscopes and is convenient whenever the signal waveform is generated by sweeping a control parameter.

B.1 AMPLITUDE MODULATION AND LOCK-IN DETECTION

Amplitude modulation is the mixing of a base band signal y_{BB} with an RF carrier $\cos \omega_m t$,

$$y_{AM}(t) = y_{BB}(t) \cdot \cos \omega_m t$$

The multiplication of two signals in the time domain means convolution of the corresponding Fourier transforms in the frequency domain. In the case of y_{AM} as defined above, this means a delta spike at ω_m convolved with the Fourier transform of y_{BB} . Accordingly, the spectrum of y_{BB} is translated by the modulation frequency ω_m . Figure B.2a illustrates the effect of amplitude modulation in the frequency domain. The baseband signal (indicated in green) would be obscured by the noise. However, due to the frequency translation by ω_m into the RF band it is lifted above the noise floor.

Figure B.2b shows, from left to right, the signal path of an experiment utilizing amplitude modulation. The base band signal is mixed with an RF carrier $\cos(\omega_m t)$ to perform the initial frequency translation. Afterwards, low frequency noise might enter the signal path and

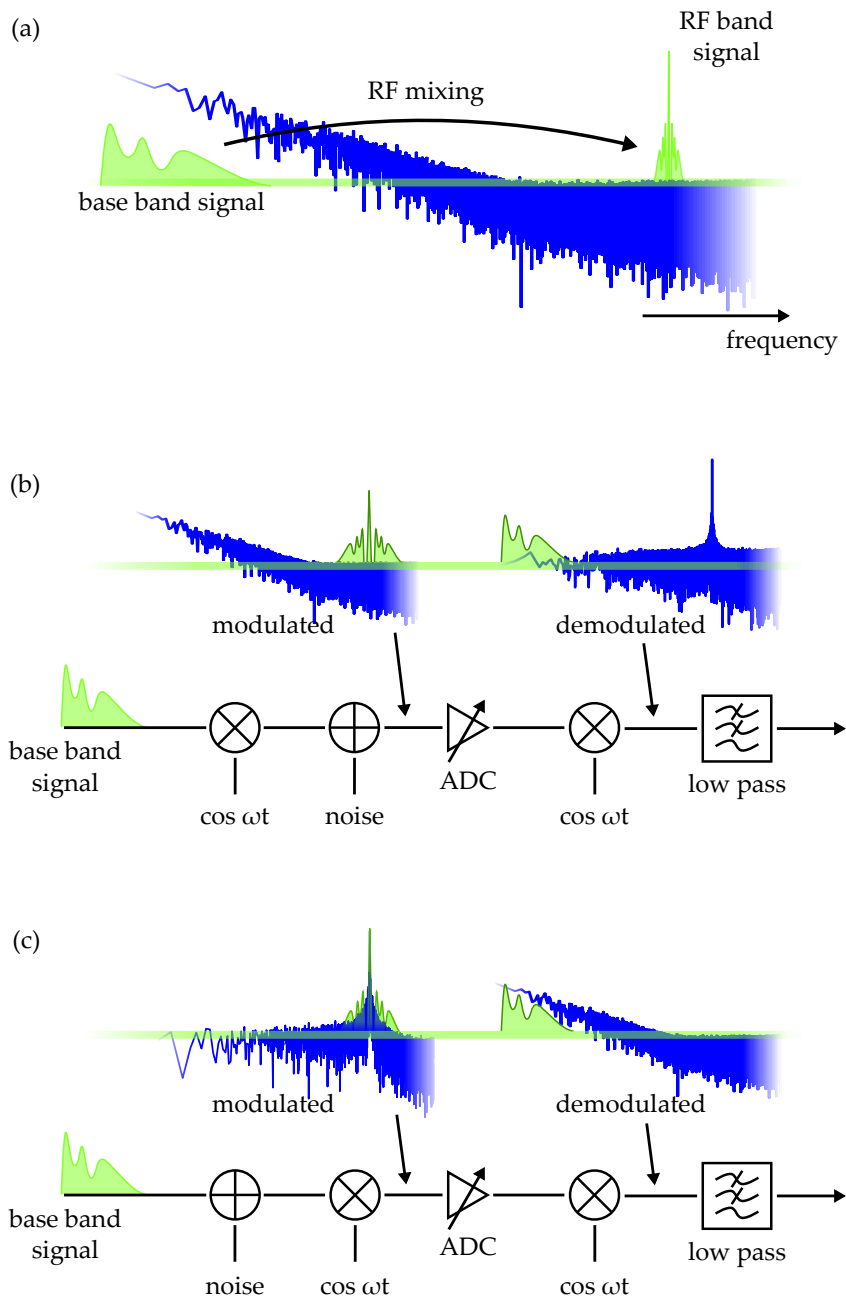


Figure B.2: **a** Lock-in modulation, in essence, is based on the separation of the signal frequency band and the noise frequency band. The separation is achieved by mixing the signal with an RF carrier. **b** Illustration of the signal path in a lock-in detector experiment when low frequency noise is imposed after RF mixing. The insets show the schematically the spectral behavior of the signal (green) and noise (blue) after modulation and after demodulation. **c** The same as in (b) except that the noise is imposed before modulation. In this case the noise frequency band is not separated from the signal frequency band and spoils the noise suppression.

obscure the waveform. The spectrum of the waveform is indicated by the inset after the noise source.

Eventually the waveform reaches an amplifier, an analog-to-digital converter, or a similar device. Idealized, these devices mark the border to a noise free environment. No noise will be added to the waveform afterwards. In practice, the device lifts the signal strength above the level of any noise source that might follow on the remaining signal path.

After amplification, the noise on the waveform must be suppressed and base band signal must be retrieved. The noise suppression is done with a high-Q band pass filter centered around the modulation frequency. The high-Q filtering is done by a trick: Instead of using an expensive filters at the RF band frequency¹, the signal is first demodulated with a second mixer, which has exactly the same frequency as the first mixer. Then the demodulated waveform is low pass filtered with a very low cut-off frequency. This is equivalent to an extremely high-Q tracking band pass filter at the RF band and provides at the same time the demodulated base band waveform. The low frequency noise, in contrast, is translated up to the RF band by the second mixer, as shown in fig. B.2b by the inset after the demodulation. Note that at low frequencies, the noise floor is now flat. The $1/f$ -noise appears as a peak at the RF band. It is removed by the low pass filter. The performance of the filter can be increased by averaging over more modulation cycles. It can be driven to extreme values compared to traditional filters.

There is a very important limitation to this principle: The noise must enter the signal path *after* the initial RF modulation. Otherwise, we cannot separate the noise spectral band from the signal spectral band. This is illustrated in fig. B.2c, where we merely exchanged the first mixer and the noise source. The insets emphasize the change in the spectrum. The noise is translated together with the base band signal to the RF band and in the second mixer stage both are translated back to the LF band. We cannot use the low pass to block the $1/f$ -noise. The lock-in mechanism feeds through modulated noise. Thus, when designing an lock-in detection scheme, we must take care that the relevant noise sources are never modulated together with the base band signal. For example, when the light source in a transmission experiment is modulated, fluctuations of its intensity cannot be filtered with a lock-in detector.

¹ The costs of a filter – analog hardware, number of logic gates, or computation time – are determined by f_T/f_C , the ratio of the transition bandwidth and the filter cut-off frequency.

B.2 NOISE SUPPRESSION BY FAST SCAN

fast scan is another modulation scheme that allows us to suppress low frequency noise. It is very useful whenever a waveform should be recorded while tuning a control parameter. Such measurements, of course, take time because we must integrate for a while for each setting of the control parameter to get rid of high frequency noise. So in practice, we record a time series. The longer the time series is, the more the signal shifts to lower frequencies and the more it is obscured by $1/f$ -noise. To give an example, fig. B.3a shows a time series of a Gaussian obscured by $1/f$ -noise and white noise together with the corresponding frequency spectrum. The spectrum of the Gaussian is indicated by the green line. It is hidden in the $1/f$ -noise.

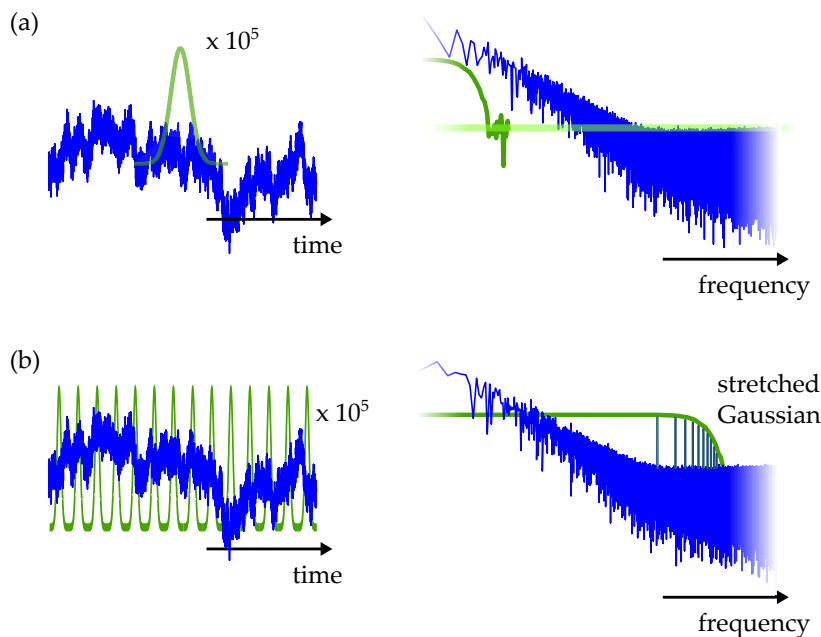


Figure B.3: **a** The temporal evolution of a signal (green) is buried in flicker noise. However, in the frequency domain representation we see that its amplitude is larger than the noise floor at high frequencies. **b** The signal frequency components are brought to the RF band by drastically decreasing the parameter sweep time and repeating the sweep many times. The effect in the frequency domain is shown on the right. The signature of the signal are spikes on the RF noise floor. Their height corresponds to the base band spectrum envelope of the signal (marked green).

As in lock-in detection, fast scan solves this problem by shifting the base band signal to a white noise limited RF band. However, in contrast to amplitude modulation, we do not mix the base band signal with an RF carrier, but use the control parameter to modulate it. The frequency conversion is done by tuning the parameter faster. The spectrum of the base band signal is stretched rather than translated. The total integration time for each parameter value must

be the same as before, required to eliminate high frequency noise. That is done by repeating the parameter sweep many times in a row as indicated in figure B.3b, sketching the modulated time trace and the corresponding frequency spectrum. The spectral signature of the Gaussian appears as spikes distributed over a large spectral interval. The envelope of the spikes corresponds to the stretched spectrum of the Gaussian. The spikes are due to the repetition of the sweep. Their distance is equal to the rate at which the sweep is repeated. Note that the time scale of the noise pattern shown in figures B.3a and b is the same while the time scale of the signal pattern is squeezed. This is the mechanism that separates the frequency bands of noise and signal.

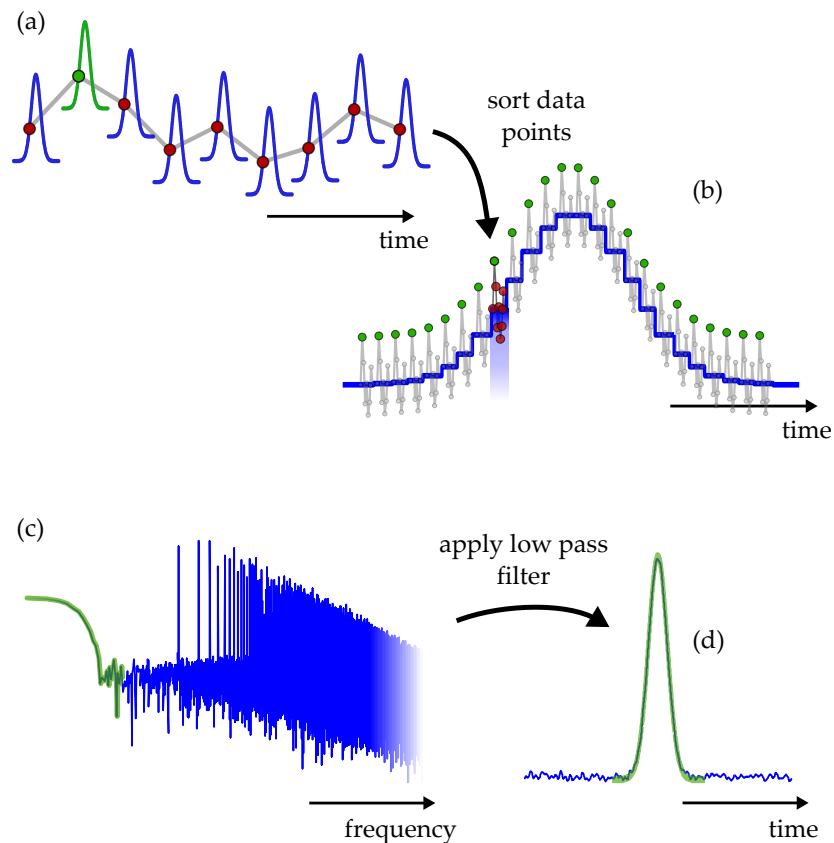


Figure B.4: **a** Schematic sketch of the time evolution in a fast scan measurement. In each scan cycle the signal pattern is repeated, but its baseline is changed by low frequency noise. The red dots mark a set of equivalent points in the scans. Their amplitude change over time. **b** To demodulate the signal, the data points are reordered. The sets of identical points are put in a row. This restores the base band version of the signal. The base line shift of the scans repeats as identical RF noise pattern on each segment. **c** The reordering of the data points effectively is a frequency transposition. The flicker noise appears at high frequencies while the spectral components of the signal are moved back to the base band. **d** The flicker noise is removed with a low pass filter. This leaves us with the shot noise limited signal pattern.

As with amplitude modulation, the waveform is transferred to a noise free environment. After that, the second step is to demodulate the waveform. That is done by averaging all data points that correspond to the same sweep parameter value, like stacking the individual repetitions of the sweeps on top of each other. This directly yields the looked for dependency of the signal on the sweep parameter value.

Why is the stacking the same as demodulation and why does it help against low frequency noise? Let us first discuss demodulation. Figure B.4a shows schematically the modulated waveform. The base line of each sweep is shifted due to low frequency noise. Now the data points are reordered by the stacking: All data points corresponding to the same sweep parameter value are put in a row as shown for the points marked red. By this, all data points initially belonging to a single sweep cycle (marked in green) are distributed over the whole temporal range while data points initially belonging to a single sweep parameter value are squeezed into a small temporal range. The result is the waveform shown in figure B.4b. We see that the parameter sweep is stretched again to a large time interval, that is to say, the waveform is demodulated.

Now let us discuss what happens to the low frequency noise. The effect of low frequency noise is the base line shift of each parameter sweep repetition. In each repetition, the signal amplitude for a given sweep parameter value is different, as indicated by the red dots in figure B.4a. By the stacking, these data points are put in a row and appear as a noisy pattern in a small time interval as illustrated in figure B.4b. Moreover, since the base line shift is constant during each sweep cycle, this noise pattern repeats on each of the resorted time intervals. That is, the low frequency noise is now modulated to high frequencies and can be removed with a low-pass filter.

Expressed in one sentence, the stacking changes the order of the data points such that formerly temporally distant data points are squeezed together in a tiny time interval and temporally close data points are distributed over a large time interval. Figure B.4c shows the spectrum of a waveform like shown in fig. B.4b. The spectral features of the Gaussian are scaled back to low frequencies. The noise frequency band, however, is stretched and appears as spikes in the RF band. The frequency of the first spike corresponds to the scan rate. The averaging corresponds to low pass filtering the reordered data set, that is, the stretched low frequency noise components are removed. The result is presented in fig. B.4d.

Fast scan has the same limitation that lock-in detection has. Modulated noise will be feed through and appear in the output waveform. Additionally, fast scan has more requirements concerning the RF frequency band. Usually, also within the RF bands some sources of noise are apparent such as radio broadcast or RF interference from elec-

tronic devices. With lock-in detectors we can avoid those by choosing another RF carrier. A narrow low noise band is enough. With fast scan we can in principle also change the scan rate, but the frequency comb of the modulated waveform still spreads over a large spectral range. Noise at frequencies of multiples of the scan rate will be demodulated into the base band signal.

The advantage of fast scan is its very simple implementation. Usually, the only requirement is a fast amplifier and a method to quickly sweep the control parameter. Furthermore, fast scan is a very general principle that, in essence, appears in many experimental techniques. For example, oscilloscopes perform fast scan on a periodic waveform. The implicit sweep parameter is the phase. An optical spectrometer, quickly recording spectra repeatedly and averaging them, performs fast scan with the light energy as sweep parameter.

BIBLIOGRAPHY

- [1] C. Wolpert, C. Dicken, L. Wang, P. Atkinson, A. Rastelli, O. G. Schmidt, H. Giessen, and M. Lippitz. "Ultrafast coherent spectroscopy of a single self-assembled quantum dot." In: *physica status solidi (b)* 249.4 (2012), pp. 721–730.
- [2] C. Wolpert, C. Dicken, P. Atkinson, L. Wang, A. Rastelli, O. G. Schmidt, H. Giessen, and M. Lippitz. "Transient Reflection: A Versatile Technique for Ultrafast Spectroscopy of a Single Quantum Dot in Complex Environments." In: *Nano Letters* 12.1 (2012), pp. 453–457.
- [3] T. D. Ladd, F. Jelezko, R. Laflamme, Y. Nakamura, C. Monroe, and J. L. O'Brien. "Quantum Computers." In: *Nature* 464 (2010), pp. 45–53.
- [4] I. Buluta and F. Nori. "Quantum Simulators." In: *Science* 326.5949 (2009), pp. 108–111.
- [5] X. Ma, X. Yuan, Z. Cao, B. Qi, and Z. Zhang. "Quantum random number generation." In: *npj Quantum Information* 2.16021 (2016).
- [6] P. Michler, A. Kiraz, C. Becher, W. V. Schoenfeld, P. M. Petroff, L. Zhang, E. Hu, and A. Imamoglu. "A Quantum Dot Single-Photon Turnstile Device." In: *Science* 290.5500 (2000), pp. 2282–2285.
- [7] M. F. Pascual-Winter, R.-C. Tongning, T. Chanelière, and J.-L. L. Gouët. "Securing coherence rephasing with a pair of adiabatic rapid passages." In: *New Journal of Physics* 15.5 (2013), p. 055024.
- [8] I. Iakoupov and A. S. Sørensen. "An efficient quantum memory based on two-level atoms." In: *New Journal of Physics* 15.8 (2013), p. 085012.
- [9] N. H. Bonadeo, J. Erland, D. Gammon, D. Park, D. S. Katzer, and D. G. Steel. "Coherent Optical Control of the Quantum State of a Single Quantum Dot." In: *Science* 282.5393 (1998), pp. 1473–1476.
- [10] R. J. Gordon and S. A. Rice. "Active control of the dynamics of atoms and molecules." In: *Annu. Rev. Phys. Chem.* 48 (1997), pp. 601–641.
- [11] M. M. Walker, T. E. Dennis, and J. L. Kirschvink. "The magnetic sense and its use in long-distance navigation by animals." In: *Current Opinion in Neurobiology* 12.6 (2002), pp. 735–744.
- [12] W. Wiltschko and R. Wiltschko. "Magnetic orientation and magnetoreception in birds and other animals." In: *Journal of Comparative Physiology A* 191.8 (2005), pp. 675–693.

- [13] D. A. Kishkinev and N. S. Chernetsov. "Magnetoreception systems in birds: A review of current research." In: *Biology Bulletin Reviews* 5.1 (2015), pp. 46–62.
- [14] R. C. Beason and J. E. Nichols. "Magnetic orientation and magnetically sensitive material in a transequatorial migratory bird." In: *Nature* 309 (1984), pp. 151–153.
- [15] D. A. Bazylinski and R. B. Frankel. "Magnetosome formation in prokaryotes." In: *Nature Reviews Microbiology* 2 (2004), pp. 217–230.
- [16] J. F. Stolz, S.-B. R. Chang, and J. L. Kirschvink. "Magnetotactic bacteria and single-domain magnetite in hemipelagic sediments." In: *Nature* 312 (1986), pp. 849–851.
- [17] J. L. Kirschvink. "The horizontal magnetic dance of the honeybee is compatible with a single-domain ferromagnetic magnetoreceptor." In: *BioSystems* 14 (1981), pp. 193–203.
- [18] R. C. Beason, W. Wiltschko, and R. Wiltschko. "Pigeon Homing: Effects of Magnetic Pulses on Initial Orientation." In: *The Auk* 3 (1994).
- [19] S. Johnson and K. J. Lohrmann. "The physics and neurobiology of magnetoreception." In: *Nature Reviews Neuroscience* 6 (2005), pp. 703–712.
- [20] A. Barman, S. Wang, J. D. Maas, A. R. Hawkins, S. Kwon, A. Liddle, J. Bokor, and H. Schmidt. "Magneto-Optical Observation of Picosecond Dynamics of Single Nanomagnets." In: *Nano Letters* 6.12 (2006), pp. 2939–2944.
- [21] J. Li, M.-S. Lee, W. He, B. Redeker, A. Remhof, E. Amaladass, C. Hassel, and T. Eimüller. "Magnetic imaging with femtosecond temporal resolution." In: *Review of Scientific Instruments* 80.7, 073703 (2009).
- [22] J. Xia, P. T. Beyersdorf, M. M. Fejer, and A. Kapitulnik. "Modified Sagnac interferometer for high-sensitivity magneto-optic measurements at cryogenic temperatures." In: *Applied Physics Letters* 89.6, 062508 (2006).
- [23] T. Schumacher, K. Kratzer, D. Molnar, M. Hentschel, H. Giessen, and M. Lippitz. "Nanoantenna-enhanced ultrafast nonlinear spectroscopy of a single gold nanoparticle." In: *Nature Communications* 2.333 (2011).
- [24] P. K. Jain, Y. Xiao, R. Walsworth, and A. E. Cohen. "Surface Plasmon Resonance Enhanced Magneto-Optics (SuPREMO): Faraday Rotation Enhancement in Gold-Coated Iron Oxide Nanocrystals." In: *Nano Letters* 9.4 (2009), pp. 1644–1650.

- [25] N. Qureshi, S. Wang, M. A. Lowther, A. R. Hawkins, S. Kwon, A. Liddle, J. Bokor, and H. Schmidt. "Cavity-Enhanced Magneto-optical Observation of Magnetization Reversal in Individual Single-Domain Nanomagnets." In: *Nano Letters* 5.7 (2005), pp. 1413–1417.
- [26] A. Barman, S. Wang, J. D. Maas, A. R. Hawkins, S. Kwon, A. Liddle, J. Bokor, and H. Schmidt. "Magneto-Optical Observation of Picosecond Dynamics of Single Nanomagnets." In: *Nano Letters* 6.12 (2006), pp. 2939–2944.
- [27] O. L. Muskens, N. Del Fatti, F. Vallée, J. R. Huntzinger, P. Billaud, and M. Broyer. "Single metal nanoparticle absorption spectroscopy and optical characterization." In: *Applied Physics Letters* 88.6, 063109 (2006).
- [28] C. F. Bohren and D. R. Huffman. *Absorption and Scattering of Light by Small Particles*. Wiley, 1983.
- [29] G. Mie. "Beiträge zur Optik trüber Medien, speziell kolloidaler Metallösungen." In: *Annalen der Physik* 330.3 (1908), pp. 377–445.
- [30] P. B. Johnson and R. W. Christy. "Optical constants of transition metals: Ti, V, Cr, Mn, Fe, Co, Ni, and Pd." In: *Phys. Rev. B* 9 (12 1974), pp. 5056–5070.
- [31] J. S. Batchelder and M. A. Taubenblatt. "Interferometric detection of forward scattered light from small particles." In: *Applied Physics Letters* 55.3 (Year), pp. 215–217.
- [32] X. Hong, E. M. P. H. van Dijk, S. R. Hall, J. B. Götte, N. F. van Hulst, and H. Gersen. "Background-Free Detection of Single 5 nm Nanoparticles through Interferometric Cross-Polarization Microscopy." In: *Nano Letters* 11.2 (2011), pp. 541–547.
- [33] B. M. Deutsch and L. Novotny. "Particle Detection Using Dual-Phase Interferometry." In: *Frontiers in Optics 2008/Laser Science XXIV/Plasmonics and Metamaterials/Optical Fabrication and Testing*. Optical Society of America, 2008, FThQ4.
- [34] K. Lindfors, T. Kalkbrenner, P. Stoller, and V. Sandoghdar. "Detection and Spectroscopy of Gold Nanoparticles Using Supercontinuum White Light Confocal Microscopy." In: *Phys. Rev. Lett.* 93 (3 2004), p. 037401.
- [35] K. B. Nahm and W. L. Wolfe. "Light-scattering models for spheres on a conducting plane: comparison with experiment." In: *Appl. Opt.* 26.15 (1987), pp. 2995–2999.
- [36] A. A. Maradudin. *Light Scattering and Surface Roughness*. Springer-Verlag US, 2007.
- [37] S. J. Orfanidis. *Electromagnetic Waves and Antennas*. Rutgers University, 2014.

- [38] M. V. Klein and T. E. Furtak. *Optics*. Wiley, 1986.
- [39] M. F. Erden and H. M. Ozaktas. "Accumulated Gouy phase shift in Gaussian beam propagation through first-order optical systems." In: *J. Opt. Soc. Am. A* 14.9 (1997), pp. 2190–2194.
- [40] M. F. Erden and H. M. Ozaktas. "Accumulated Gouy phase shift in Gaussian beam propagation through first-order optical systems." In: *Journal of the Optical Society of America A* 14.9 (1997).
- [41] S. Feng and H. G. Winful. "Physical origin of the Gouy phase shift." In: *Applied Optics* 26.8 (2001), pp. 485–487.
- [42] B. E. A. Saleh and M. C. Teich. *Fundamentals of Optics*. John Wiley and Sons, Inc, 1991.
- [43] R. G. Newton. "Optical theorem and beyond." In: *American Journal of Physics* 44.7 (1976), pp. 639–642.
- [44] H. S. Bennett and E. A. Stern. "Faraday Effect in Solids." In: *Physical Review* 137.2A (1965).
- [45] J. L. Erskine and E. A. Stern. "Calculation of the M_{23} magneto-optical absorption spectrum of ferromagnetic nickel." In: *Physical Review B* 12.11 (1975).
- [46] J. L. Erskine and E. A. Stern. "Magneto-optic Kerr Effect in Gadolinium." In: *Physical Review B* 8.3 (1973).
- [47] G. X. Du, T. Mori, M. Suzuki, S. Saito, H. Fukuda, and M. Takahashi. "Evidence of localized surface plasmon enhanced magneto-optical effect in nanodisk array." In: *Applied Physics Letters* 96 (2009), p. 081915.
- [48] C. Dicken. *Diploma thesis: Kerr Microscopy of Magnetic Nanostructures*. University of Stuttgart, 2011.
- [49] G. Sagnac. "L'éther lumineux démontré par l'effet du vent relatif d'éther dans un interféromètre en rotation uniforme." In: *Comptes Rendus* 157 (1913), pp. 708–710.
- [50] J. S. Dodge, A. Kapitulnik, and M. M. Fejer. "Magneto-optic measurements with a sagnac interferometer." In: *Ferroelectrics* 162.1 (1994), pp. 387–395.
- [51] M. Abramowitz and I. A. Stegun. *Handbook of Mathematical Functions*. United States Department of Commerce, 1972.
- [52] E. C. Stoner and E. P. Wohlfarth. "A Mechanism of Magnetic Hysteresis in Heterogeneous Alloys." In: *IEEE Transactions on Magnetics* 27 (1948).
- [53] E. Fawcett. "Spin-density-wave antiferromagnetism in chromium." In: *Rev. Mod. Phys.* 60 (1 1988), pp. 209–283.

- [54] J. W. Lau and J. M. Shaw. "Magnetic nanostructures for advanced technologies: fabrication, metrology and challenges." In: *Journal of Physics D: Applied Physics* 44.30 (2011), p. 303001.
- [55] W. T. Z. H. M. Lu and Q. Jiang. "Saturation magnetization of ferromagnetic and ferrimagnetic nanocrystals at room temperature." In: *Journal of Physics D: Applied Physics* 40 (2007), pp. 320–325.
- [56] W. Gong, H. Li, Z. Zhao, and J. Chen. "Ultrafine particles of Fe, Co, and Ni ferromagnetic metals." In: *Journal of Applied Physics* 69.8 (1991), pp. 5119–5121.
- [57] G. Hass and C. D. Salzberg. "Optical Properties of Silicon Monoxide in the Wavelength Region from 0.24 to 14.0 Microns*." In: *J. Opt. Soc. Am.* 44.3 (1954), pp. 181–187.
- [58] M. D. Eisaman, J. Fan, A. Migdall, and S. V. Polyakov. "Invited Review Article: Single-photon sources and detectors." In: *Review of Scientific Instruments* 82.7, 071101 (2011).
- [59] D. A. Simpson, E. Ampem-Lassen, B. C. Gibson, S. Trpkovski, F. M. Hossain, S. T. Huntington, A. D. Greentree, L. C. L. Hollenberg, and S. Praver. "A highly efficient two level diamond based single photon source." In: *Applied Physics Letters* 94.20, 203107 (2009).
- [60] H. J. Krenner, S. Stufler, M. Sabathil, E. C. Clark, P. Ester, M. Bichler, G. Abstreiter, J. J. Finley, and A. Zrenner. "Recent advances in exciton-based quantum information processing in quantum dot nanostructures." In: *New Journal of Physics* 7.1 (2005), p. 184.
- [61] H. J. Kimble. "The quantum internet." In: *Nature* 453 (2008), pp. 1023–1030.
- [62] P. Michler. *Single Semiconductor Quantum Dots*. Springer-Verlag Berlin Heidelberg, 2009.
- [63] R. Nötzel. "Self-organized growth of quantum-dot structures." In: *Semiconductor Science and Technology* 11.10 (1996), p. 1365.
- [64] R. P. Feynman. "Quantum Mechanical Computers." In: *Optics News* 11.2 (1985), pp. 11–20.
- [65] A. J. Ramsay. "A review of the coherent optical control of the exciton and spin states of semiconductor quantum dots." In: *Semiconductor Science and Technology* 25.10 (2010), p. 103001.
- [66] C. Dory, K. A. Fischer, K. Müller, K. G. Lagoudakis, T. Sarmiento, A. Rundquist, J. L. Zhang, Y. Kelaita, and J. Vučković. "Complete Coherent Control of a Quantum Dot Strongly Coupled to a Nanocavity." In: *Scientific Reports* 6.25172 (2016).

- [67] M. Scheibner, T. Schmidt, L. Worschech, A. Forchel, G. Bacher, T. Passow, and D. Hommel. "Superradiance of quantum dots." In: *Nature Physics* 3 (2007), pp. 106–110.
- [68] B. Alén, F. Bickel, K. Karrai, R. J. Warburton, and P. M. Petroff. "Stark-shift modulation absorption spectroscopy of single quantum dots." In: *Applied Physics Letters* 83.11 (2003), pp. 2235–2237.
- [69] A. Högele, S. Seidl, M. Kroner, K. Karrai, R. J. Warburton, B. D. Gerardot, and P. M. Petroff. "Voltage-Controlled Optics of a Quantum Dot." In: *Phys. Rev. Lett.* 93 (21 2004), p. 217401.
- [70] C. Wolpert. *Dissertation: Ultrafast Spectroscopy of Single Quantum Dots*. University of Stuttgart, 2011.
- [71] A. Rastelli, S. Stufliker, A. Schliwa, R. Songmuang, C. Manzano, G. Costantini, K. Kern, A. Zrenner, D. Bimberg, and O. G. Schmidt. "Hierarchical Self-Assembly of GaAs/AlGaAs Quantum Dots." In: *Phys. Rev. Lett.* 92 (16 2004), p. 166104.
- [72] M. Bayer et al. "Fine structure of neutral and charged excitons in self-assembled In(Ga)As/(Al)GaAs quantum dots." In: *Phys. Rev. B* 65 (19 2002), p. 195315.
- [73] L. Allen and J. H. Eberly. *Optical Resonance and Two-Level Atoms*. Dover, 1987.
- [74] R. Balian. *From Microphysics to Macrophysics, Volume 1*. Springer-Verlag Berlin Heidelberg, 2007.
- [75] X. ming Hu, D. Du, G. ling Cheng, J. hua Zou, and X. Li. "Switching from positive to negative dispersion in a three-level V system driven by a single coherent field." In: *Journal of Physics B: Atomic, Molecular and Optical Physics* 38.7 (2005), p. 827.
- [76] G. G. Claude Cohen-Tannoudji Jacques Dupont-Roc. *Atom-Photon Interactions: Basic Process and Applications*. Wiley, 2008.
- [77] H. Dember. "Über eine photoelektronische Kraft in Kupferoxydul-Kristallen." In: *Physikalische Zeitschrift* 32 (1931), p. 554.
- [78] T. Dekorsy, H. Kurz, X. Q. Zhou, and K. Ploog. "Investigation of field, carrier, and coherent phonon dynamics in low-temperature grown GaAs." In: *Applied Physics Letters* 63.21 (1993), pp. 2899–2901.
- [79] T. Dekorsy, T. Pfeifer, W. Kütt, and H. Kurz. "Subpicosecond carrier transport in GaAs surface-space-charge fields." In: *Phys. Rev. B* 47 (7 1993), pp. 3842–3849.
- [80] D. A. B. Miller, D. S. Chemla, T. C. Damen, A. C. Gossard, W. Wiegmann, T. H. Wood, and C. A. Burrus. "Band-Edge Electroabsorption in Quantum Well Structures: The Quantum-Confined Stark Effect." In: *Phys. Rev. Lett.* 53 (22 1984), pp. 2173–2176.

- [81] S. A. Empedocles and M. G. Bawendi. "Quantum-Confined Stark Effect in Single CdSe Nanocrystallite Quantum Dots." In: *Science* 278.5346 (1997), pp. 2114–2117.
- [82] G. Bester. "Electronic excitations in nanostructures: an empirical pseudopotential based approach." In: *Journal of Physics: Condensed Matter* 21.2 (2009), p. 023202.
- [83] M. Pfeiffer, K. Lindfors, H. Zhang, B. Fenk, F. Phillipp, P. Atkinson, A. Rastelli, O. G. Schmidt, H. Giessen, and M. Lippitz. "Eleven Nanometer Alignment Precision of a Plasmonic Nanoantenna with a Self-Assembled GaAs Quantum Dot." In: *Nano Letters* 14.1 (2014), pp. 197–201.
- [84] M. Cho. "Coherent Two-Dimensional Optical Spectroscopy." In: *Chemical Reviews* 108.4 (2008), pp. 1331–1418.
- [85] C. Lienau. "Ultrafast near-field spectroscopy of single semiconductor quantum dots." In: *Philosophical Transactions of the Royal Society of London A: Mathematical, Physical and Engineering Sciences* 362.1817 (2004), pp. 861–879.
- [86] A. G. Curto, G. Volpe, T. H. Taminiau, M. P. Kreuzer, R. Quidant, and N. F. van Hulst. "Unidirectional Emission of a Quantum Dot Coupled to a Nanoantenna." In: *Science* 329.5994 (2010), pp. 930–933.
- [87] D. Dregely, K. Lindfors, M. Lippitz, N. Engheta, M. Totzeck, and H. Giessen. "Imaging and steering an optical wireless nanoantenna link." In: *Nature Communications* 5.4354 (2014).
- [88] F. Würthner, T. E. Kaiser, and C. R. Saha-Möller. "J-Aggregates: From Serendipitous Discovery to Supramolecular Engineering of Functional Dye Materials." In: *Angewandte Chemie International Edition* 50.15 (2011), pp. 3376–3410.
- [89] A. V. Aggarwal et al. "Fluctuating exciton localization in giant pi-conjugated spoked-wheel macrocycles." In: *Nature Chemistry* 5 (2013), pp. 964–970.
- [90] D. Wolf, T. Schumacher, and M. Lippitz. "Shaping the nonlinear near field." In: *Nature Communications* 7.10361 (2015).
- [91] K. Liu and M. G. Littman. "Novel geometry for single-mode scanning of tunable lasers." In: *Opt. Lett.* 6.3 (1981), pp. 117–118.
- [92] R. Trotta, P. Atkinson, J. D. Plumhof, E. Zallo, R. O. Rezaev, S. Kumar, S. Baunack, J. R. Schröter, A. Rastelli, and O. G. Schmidt. "Nanomembrane Quantum-Light-Emitting Diodes Integrated onto Piezoelectric Actuators." In: *Advanced Materials* 24.20 (2012), pp. 2668–2672.

- [93] R. Trotta, E. Zallo, C. Ortix, P. Atkinson, J. D. Plumhof, J. van den Brink, A. Rastelli, and O. G. Schmidt. "Universal Recovery of the Energy-Level Degeneracy of Bright Excitons in InGaAs Quantum Dots without a Structure Symmetry." In: *Phys. Rev. Lett.* 109 (14 2012), p. 147401.
- [94] B. Alén, K. Karrai, R. J. Warburton, F. Bickel, P. M. Petroff, and J. Martinez-Pastor. "Absorption spectroscopy of single InAs self-assembled quantum dots." In: *Physica E: Low-dimensional Systems and Nanostructures* 21.2-4 (2004), pp. 395 -399.

ERKLÄRUNG

Hiermit versichere ich an Eides statt, dass ich die vorliegende Arbeit selbstständig verfasst und keine anderen als die von mir angegebenen Quellen und Hilfsmittel verwendet habe.

Weiterhin erkläre ich, dass ich die Hilfe von gewerblichen Promotionsberatern bzw. -vermittlern oder ähnlichen Dienstleistern weder bisher in Anspruch genommen habe, noch künftig in Anspruch nehmen werde.

Zusätzlich erkläre ich hiermit, dass ich keinerlei frühere Promotionsversuche unternommen habe.

Bayreuth, den 19. September 2016

Christian Dicken

DANKSAGUNG

Zuerst möchte ich meinem Betreuer Prof. Dr. Markus Lippitz für sein Vertrauen in mich und die Möglichkeit danken, nach meiner Diplomarbeit weiterhin an seinem Institut zu bleiben. In all den Jahren gab es bei Ihm immer eine offene Tür, immer einen Ratschlag wenn man ihn suchte und immer die Freiheit, den eigenen wissenschaftlichen Interessen nachzugehen. Dafür bin ich sehr dankbar.

Für das Interesse an meiner Arbeit möchte ich meinem Zweitgutachter Prof. Dr. Jürgen Köhler danken, außerdem Prof. Dr. Martin Axt als Kommissionsvorsitzender und Herrn Prof. Dr. Lothar Kador als Kommissionmitglied.

Ich danke Lijuan Wang, Paola Atkinson and Armando Rastelli von der Gruppe von Oliver G. Schmidt am IFW Dresden für die hervorragenden Halbleiterproben und der Gruppe um Prof. Dr. Gabriel Bester, ehemals am Max-Planck-Institut für Festkörperforschung, für die gute Zusammenarbeit bei der Modellierung unserer Halbleiterquantenpunkte.

Ich möchte meinen Kollegen und Freunden Jonas Albert, Matthias Brandstätter, Markus Pfeiffer, Klas Lindfors, Thorsten Schumacher, Daniela Wolf und Christian Wolpert danken, die all die Jahre an der Universität von Beginn an so sehr bereichert haben. Daran werde ich mich immer erinnern. Darüber hinaus danke ich der ganzen Arbeitsgruppe am EP3 für die schöne Zeit in Bayreuth, insbesondere Robert Weiner, Julian Obermeier, Patrick Knödler und Gerhard Schäfer.

Besonderer Dank gilt meinen Eltern, die mich auf meinem gesamten Weg durchs Leben immer und ohne Bedingung unterstützt haben. Das ist unersetzbar.

COLOPHON

This document was typeset using the typographical look-and-feel `classicthesis` developed by André Miede. The style was inspired by Robert Bringhurst's seminal book on typography "*The Elements of Typographic Style*". `classicthesis` is available for both \LaTeX and \LyX :

<https://bitbucket.org/amiede/classicthesis/>